SYSTEMS, POWER AND ENERGY RESEARCH DIVISION
SCHOOL OF ENGINEERING
UNIVERSITY OF GLASGOW

Peter Collings

Theoretical and Experimental Analysis of an Organic Rankine Cycle

In partial fulfilment of the requirements for the degree of Doctor of Philosophy at the University of Glasgow

ABSTRACT

In order to reduce emissions of carbon dioxide from the energy and transportation sectors, while still providing a reliable and affordable service, innovation in the fields of power generation and energy efficiency is needed. There exists a wide variety of low-temperature heat sources, such as waste heat from industry and transportation, solar thermal, biomass and geothermal, which contain large amounts of energy, but do not have sufficient temperature to be economically viable using traditional power generation techniques. Several technologies have been proposed to utilise these promising resources, of which the Organic Rankine Cycle is widely considered to be the technology with the most potential for large-scale commercial deployment. However, the low driving temperature differential available to Organic Rankine Cycles using these heat sources means that they face several technological challenges, some of which are addressed in this thesis. Firstly, they experience low efficiencies, which means that small absolute changes in efficiency and cost can be proportionally very significant, this makes cycle optimisation to achieve marginal gains a worthwhile exercise. Secondly, there is a lack of suitable working fluids for the Organic Rankine Cycle, meaning that they often have to operate with a fluid that is not tailored for the specific application. Producing tailor-made working fluids to a given heat source and sink temperature could represent a significant field for optimising the performance of ORCs. Thirdly, there is a lack of experimental validation of many theoretical aspects of the Organic Rankine Cycle, particularly for low heat source temperatures and power outputs. This thesis aims to contribute to the body of research on ORC technology by developing an analytical model to design an experimental rig. This rig is used to validate several theoretical predictions, which are then expanded upon to develop a novel method of cycle optimisation in an application with variable heat sink temperatures.

Firstly, a thermodynamic model was developed in MATLAB to analyse a small-scale Organic Rankine Cycle. This model builds on well-established analytical modelling principles that frequently appear in the literature. This basic model was used as a tool to design a lab-scale experimental Organic Rankine Cycle rig, capable of addressing several gaps in the current literature, most notably the lack of research on the impact of a regenerator on the performance of an Organic Rankine Cycle, and the lack of experimental research on the performance of an Organic Rankine Cycle using a working fluid composed of a mixture of two working fluids, in this case r245fa and r134a. The model, its results and the design of the experimental rig are described in detail.

The results from this experimental rig showed an increase in cycle efficiency and cycle output power with increasing heat source temperature and increasing cycle pressure ratio. The use of a regenerative cycle resulted in an increased cycle efficiency, but the extra flow resistance caused by the additional heat exchanger caused the mass flow rate of the cycle to drop, reducing the output power at the same time as reducing the evaporator heat demand and thereby increasing cycle efficiency. The addition of more r134a, which has a lower boiling point, to the working fluid mixture, increased the condenser pressure and thereby reduced the cycle pressure ratio, reducing output power and efficiency. The maximum efficiency achieved was 11.3%, for a regenerative cycle with a heat source temperature of 95°C and a pressure ratio of 4.56:1.

Using the results from the experimental rig, and the model that they validate, the concept for the Dynamic Organic Rankine Cycle is presented. The Dynamic Organic Rankine Cycle was conceived as a solution to a problem identified in the literature, namely that an Organic Rankine Cycle using ambient air as the heat sink cannot fully utilise the driving temperature differential available to it during times of colder ambient temperature, as it must be designed to still function on the hottest day of the year. In order to address this, the Dynamic ORC Concept uses a variable working fluid composition, capable of shifting the composition between one working fluid component and the other by batch distillation in order to change the fluid's bubble and dew points to match the heat sink temperature. The use of working fluid mixtures is in contrast to most current research, which has focused primarily on pure, single-component working fluids. A theoretical analysis of this cycle in MATLAB was carried out, and it was found that the cycle results in substantial increase in year-round power generation from the cycle, of the order of 8-10% for a heat source temperature of 150°C, increasing to 23% and higher for heat source temperatures of 100°C and below, while operating in a continental climate, such as that of Beijing, China. When operating in a climate with less temperature variation, the gains are lower, but still significant.

Structurally, this paper presents a review of the relevant literature to the Organic Rankine Cycle, identifying the knowledge gaps that justify the work carried out. It then reviews the theory of the ORC, and how this was used both to build a computer model for analysis of the dynamic ORC and design the 1kW experimental rig. The experimental results from the rig are then presented and discussed. Finally, the results of the theoretical analysis of the dynamic ORC are presented, and analysed with the aid of the REFPROP fluid properties program to explain the trends observed in the data. Finally, suggestions for further work are made.

ACKNOWLEDGEMENTS

A huge number of thanks are due for the completion of this thesis.

Firstly, to my supervisor Dr. Zhibin Yu, without whose support and guidance at every stage of the process this thesis would never have come close to completion.

To the EPSRC, who funded my research and stipend throughout.

To the academic staff who provided advice and feedback, most notably Profs. Paul Younger and Sandy Cochran, and Drs. Nader Karimi and Enhua Wang.

To the technical staff without whose indispensable work the experimental rig would not have been commissioned, particularly Bernard Hoey, Peter Miller, Brian Robb and Dennis Kearns, and to the administrative staff, especially Elaine MacNamara and Karen Phillips, whose lives I made as difficult as humanly possible.

To Andy McKeown, who made the final year of the PhD immeasurably easier in so many ways.

Finally, to Flo, who I talked to too much, and my family, who I talked to too little. You've kept me sane for the last four years.

DECLARATION

I declare that, unless explicitly stated to be the contribution of others, that this thesis is entirely my own work and has not been submitted for any other degree, at the University of Glasgow or elsewhere.

Elements of this research have previously been published by the author in the following places:

"Modelling and Analysis of a Small-Scale Organic Rankine Cycle System with a Scroll Expander", Peter Collings and Zhibin Yu, Proceedings of the World Congress on Engineering, London, July 2014

"Effect of Working Fluid Mixture Composition on the Performance of an Organic Rankine Cycle", Peter Collings and Zhibin Yu, Proceedings of the 3rd International Seminar on ORC Power Systems, Brussels, October 2015.

"A dynamic organic Rankine cycle using a zeotropic mixture as the working fluid with composition tuning to match changing ambient conditions", Peter Collings, Zhibin Yu and Enhua Wang, Applied Energy 171, June 2016.

"Dynamic Organic Rankine Cycle with a Fixed Expansion Ratio Positive Displacement Expander", Peter Collings and Zhibin Yu, Proceedings of the 12th International Heat Transfer, Fluid Mechanics and Thermodynamics Conference, Málaga, July 2016

"Numerical Analysis of an Organic Rankine Cycle with Adjustable Working Fluid Composition, a Volumetric Expander and a Recuperator", Peter Collings and Zhibin Yu, Energies 10, March 2017.

CONTENTS

NOMENCLATURE

Abbreviations

CFD	Computational Fluid Dynamics
CHP	Combined Heat and Power
DECC	Department of Energy and Climate Change
GHG	Greenhouse Gas
LMTD	Log Mean Temperature Difference
ORC	Organic Rankine Cycle
PD	Positive Displacement
PPTD	Pinch Point Temperature Difference
REFPROP	Reference Properties fluid properties program

Symbols

Bo	Boiling Number
Co	Convection Number
c_p	Specific Heat Capacity
D_h	Hydraulic Diameter
E	Exergy
f	Friction Factor
Fr	Froude Number
g	Acceleration due to Gravity
h	Specific Enthalpy
H	Enthalpy
I	Irreversibility
k	Thermal Conductivity
$\dot{m}$	Mass Flow Rate
Nu	Nusselt Number
P	Pressure
Pr	Prandtl Number
Re	Reynolds Number
s	Specific Entropy
Q	Heat

t	Wall thickness
T	Temperature
u	Flow Velocity
W	Work
x	Quality
α	Heat Transfer Coefficient
β	Plate Chevron Angle
μ	Dynamic Viscosity
v	Kinematic Viscosity
ρ	Density
ψ	Improvement in Annual Power Generation
η	Efficiency

Subscripts

eq	Equivalent
f	Liquid
g	Vapour
tf	Thermal Fluid
wf	Working Fluid

List of Figures

CHAPTER 1- INTRODUCTION

1.1 Background

The International Energy Outlook 2013 (IEO2013) forecasted that world energy consumption will grow by 56% between 2010 and 2040 [1]. Energy supply will still be dominated by fossil fuels until 2040, and there is no sign of a significant fall in their dominance in the foreseeable future [1]. The rapid increase in energy consumption has inevitably caused fuel price increases and environmental challenges. It is widely accepted that greenhouse gas emissions from the burning of fossil fuels are responsible for climate change, which is no longer an abstract concept only discussed by scientists and environmentalists, but a reality of many people's lives. For instance, climate change is likely to be a factor in the stormy weather that hit much of the UK in winter 2013. To avoid dangerous climate change, the United Kingdom has already set a target to cut its greenhouse gas emissions by at least 80% from 1990 levels by 2050 [2] and has increased this commitment under the 2015 Paris agreement [3]. To achieve this ambitious target, we have to either replace the fossil fuel dominated energy supply with low-carbon energy sources or reduce energy demand. Low-carbon energy sources such as wind, solar, tidal, hydro, and wave can partly address these challenges, but are unlikely to dominate the energy supply in the near future due to their intermittence. It is therefore critical to reduce energy consumption by improving the efficiencies of our energy systems and industrial processes. Many current industrial and transportation processes create large amounts of waste heat, which is simply rejected to the environment and lost to the system. At the same time, there exist many large sources of power, such as geothermal, solar and biomass, which have temperatures too low to be economically competitive using current power generation techniques.

1.2 Heat Sources Available

A variety of different heat sources commonly mentioned in literature are presented below.

1.2.1 Waste Heat

Industrial processes such as blast furnaces, ceramic kilns, chemical reactors and so on reject large amounts of waste heat which can no longer be used for the process [3]. This represents a significant financial loss to industry, as well as increasing the associated emissions of pollution both chemical and thermal. Waste Heat is responsible for approximately 4.2% of global

installed ORC capacity, mainly in small-scale applications [4]. Of these, metal production, cement & lime, and glass manufacturing are the most important.

The UK Department of Business Energy and Industrial Strategy [5] report that industrial waste heat represents a total of 47.9TWh/year, or an average power of 5.46GW. Of this resource, 29.6% exists at high temperature (>500°C), 5% exists at medium temperature (250-500°C), and the remaining 65.4% exists at low temperature, or lower than 250°C. Cayer et al [6] report that in Canada, two thirds of primary energy consumption by the eight largest industrial sectors is released as waste heat. Assuming a 10% utilisation rate, this implies a potential annual recovery of 168PJ (an average power of 5.3GW), and reduction in Greenhouse Gas emissions of 11.2MT. Hung et al [7] report that in Taiwan, 88% of waste heat sources are medium to low temperature heat sources, existing at lower than 370°C. In a different paper [8] they state that low grade waste heat accounts for 50% of total heat generated in industry, leading to thermal pollution. Budisulistyo et al [9] estimate that the between 20 and 50% of energy from industry is released as waste heat.

Wang et al [10] point out that waste heat sources do not always form straight lines on a T-H diagram. They can consist of several different waste heat streams, each with their own thermal characteristics, which are normally combined to produce a composite curve, as shown in Figure 1.1. They classified these composite curves into straight, concave and convex curves, and compared ORCs and Kalina cycles being powered by heat sources of each type.

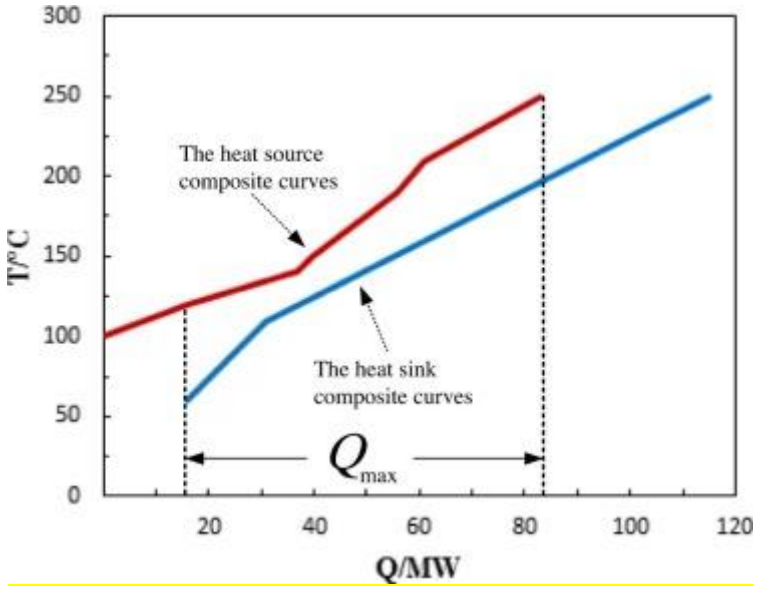

Figure 1.1: Composite curve of an industrial process [12]

1.2.2 Solar Power

Solar power is a niche application for ORCs, with less than 1% of global installed ORC capacity [4]. However, several methods of concentrating solar energy to create useful temperatures for an Organic Rankine Cycle exist. An evacuated tube solar collector consists of glass tubes containing a vacuum. Through these tubes run secondary tubes containing the working fluid and coated in absorbent material, as shown in Figure 1.2 [13].

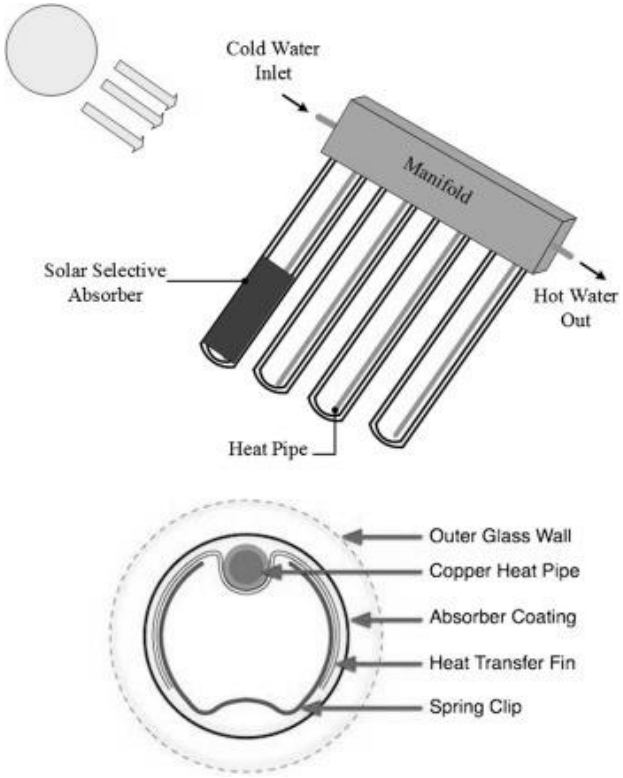

Figure 1.2: Diagram of an evacuated tube solar collector [14]

The temperature of thermal fluid provided by a solar collector will vary throughout the year. Zhang et al [11] reported a thermal fluid temperature for Osaka, Japan of 217.4°C during the summer and 137.0°C during the winter, with an average annual value of 177.4°C. This variation in temperature can cause significant issues for the cycle. If complete evaporation is to be ensured in the winter months, the cycle must either operate with a variable expansion ratio, or run with a significant superheat during the summer months. Both of these introduce technical challenges to the cycle. Wu et al [13] found that they could generate a thermal fluid temperature of 95°C using flat plate solar collectors, and that the overall cost of the cycle was dominated by the solar collectors, meaning that they are the primary target for optimisation of solar-powered ORC systems. Zhang et al [14] presented a 200kW ORC power plant which has been operating in Tianjin, China using parabolic trough collectors, finding a collector

efficiency of 57%, and a first law efficiency of 15% using a maximum cycle temperature of 145°C.

In addition, although higher heat source temperatures increase the efficiency of the ORC, they reduce the efficiency of the solar collector, heat losses to the atmosphere from the collector also increasing with increased thermal fluid temperature. Helvaci et al [15] observed a change in collector efficiency from 60% to 45% over the range of temperatures they investigated, ranging from 40°C to 95°C. This introduces an optimisation conflict to the cycle. The temperature of the thermal fluid provided to the ORC by a solar collector is strongly influenced by the area of the solar collector [11]. Higher temperatures increase the power output of the cycle, but also decrease its effectiveness at utilising the energy contained in the thermal fluid, while also increasing costs.

1.2.3 Geothermal

Geothermal heat sources are a common heat source considered for the application of the Organic Rankine Cycle, with a range of heat source temperatures and cycle configurations appearing in the literature [16] [17] [18] [19]. Tartière et al. report that 74% of global installed ORC capacity is geothermal, although in terms of number of plants this share is smaller, with geothermal systems tending to have a higher power output than other applications. Barbier [20] estimates that around 70% of the global geothermal energy potential exists at temperatures lower than 130°C.

Binary Geothermal Cycles use an ORC, drawing the heat for its evaporator from the primary geothermal fluid. This differs from a single flash cycle, in which the working fluid for the cycle is the geothermal fluid itself. Binary cycles are generally more efficient at lower heat source temperatures [21] [22], as well as generally having longer plant lifetimes due to the fact that the highly aggressive geothermal brine is kept physically separate from the moving parts of the ORC [23]. A large amount of research has been carried out on the application of the ORC to geothermal heat sources. Walraven et al [16] analysed geothermally-powered ORCs with the aim of comparing water- and air-cooled systems. They point out that the parasitic power of air-cooled systems can be twice that of comparable liquid cooling systems, and the capital cost of components 150% those of their equivalents, however, this extra expenditure can be justified in regions where sufficient cooling water is not readily available. They took the details of a geothermal project in Belgium, giving them a heat source temperature of 125°C. Liu et al [17] investigated various typical geothermal heat source temperatures from 80°C to 180°C, while using R245fa as the working fluid. Gu et al [22] estimate the parasitic power in Geothermal

cycles, used to pump thermal fluid, coolant, fans and other auxiliaries, to be about 15% of the total power output.

1.2.4 Bottoming Cycles

ORCs are often used as bottoming cycles for higher-temperature cycles, such as diesel engines, Brayton Cycles or other Rankine Cycles [8] [3] [24] [9] [25] [26] [27]. The systems can be scaled to systems varying in size from road vehicles [24] [27] to large ships [25] [26] or land-based power stations [9] [25] [28] [29]. Roughly 8% of global installed ORC capacity is in the form of bottoming cycles, making them the third most widespread application for the ORC [4].

As with all thermal cycles, these cycles necessarily reject large amounts of heat. Diesel engines reject about 27% of their fuel energy through the exhaust, 20% through the coolant, and 7% through the intercooler [24]. Typical resource temperatures range from 160°C [28]to 380°C [27], with a large variation in between these values [26]. The effects of using ORCs to improve the performance of other thermal cycles has been investigated in the literature. Chen et al [24] reported the use of a bottoming cascade-type ORC capable of increasing the peak thermal efficiency of a diesel engine from 45.3% to 49.5%. Michos et al [25] reported a 9.1-10.2% net reduction in brake specific fuel consumption for a V12 marine diesel engine when a bottoming ORC was added. Eveloy [29] et al recorded an increase in first law efficiency of 12% compared to a gas turbine operating without a bottoming cycle. When using ORCs as bottoming cycles, attention must be paid to the issue of back-pressure, which can reduce the efficiency of the topping cycle, reducing the benefit provided by the bottoming cycle or even cancelling it out completely [24] [25]. Additionally, some topping cycles, such as road vehicle engines, will result in a heat input that varies over time, which can result in the bottoming cycle operating at part-load, negatively affecting its own performance [22].

1.2.5 Biomass

Solid biomass can be used to generate heat in several ways. Pyrolysis and gasification are still to experience widespread commercialisation, and therefore simple combustion is the most widely-used technology [30]. The most common fuels for biomass power generation are wood pellets and waste products such as sawdust [31]. Much previous literature focuses on the use of biomass combustion for trigeneration, or generating electricity, heat and cooling [32] [31] [33]. Biomass plants account for roughly 11% of global installed ORC capacity [4], which makes them the second most common application, after geothermal.

Biomass suffers from lower generated temperatures than most fossil fuels due to a higher moisture content [34]. This requires some of the heat energy liberated by combustion to go

towards drying the fuel. This lower temperature makes it a suitable candidate for ORC applications [30]. The inlet temperatures to power generation equipment reported in literature range from 100°C for a cogeneration application [32] to 210°C [35]. Maraver and Royo [35] report a worldwide capacity of 300MWe as of 2016, with the majority of the individual plants being in the range of 1-2MWe.

1.2.6 Cogeneration

ORC Systems can also be used in Cogeneration or Combined Heat and Power schemes [36] [34]. "Cogeneration" is also a term occasionally used in literature to describe an ORC directly driving a refrigeration system [37] [38]. In the context of this thesis it should be understood to mean combined heat and power generation. Two primary cycle configurations exist for this, firstly, the thermal fluid exiting the hot side of the evaporator can be used to directly meet heat needs. This is best suited for uses such as industrial waste heat, bottoming cycles and biomass, where the energy contained in the thermal fluid would otherwise be lost to the environment. For binary geothermal and solar-powered cycles, using the spent thermal fluid for cogeneration would further reduce its temperature. As the primary fluid for these cycles is usually recirculated through the geothermal borehole or the solar collector, reducing its temperature will tend to cause an increase in the size of these components, which may or may not be offset by the sale of the heat energy.

The second cycle configuration uses the spent coolant of the cycle to meet heating needs. The coolant will have absorbed much of the thermal energy rejected to the working fluid in the evaporator. However, to achieve an adequate coolant outlet temperature can involve increasing the condenser pressure of the ORC, to increase the condensing temperature of the working fluid [33]. This reduction in cycle pressure ratio can reduce the efficiency of the cycle, making the optimisation of CHP ORC systems a nontrivial task. Zhang et al [11] report an expander outlet temperature of 115-181°C for a solar-powered ORC, depending on the local conditions and the season, which is ample for domestic heating applications. Uris et al [33] used a condensing temperature of 100°C, and Al-Sulaiman et al [31] had a minimum condensing temperature of 72°C. Tanczuk et al [34] supplied thermal water to a district heating system at 85°C and received it back at 50°C . It is apparently that these temperatures are significantly above those of most real-world heat sinks, which will cause the efficiency of the ORC to suffer.

1.3 Available Conversion Technologies

There are a number of competing technologies for extracting useful energy from low-temperature heat sources. These include the Stirling Cycle [39], the inverted Brayton Cycle [39], Thermoelectric Conversion [39] and the Kalina Cycle.

1.3.1 Stirling Cycle

The Stirling cycle has several specific cycle configurations, but all share the same basic principle. A fluid volume is physically displaced between hot and cold reservoirs by the action of a displacer. As the fluid moves between the hot and cold ends, it expands and contracts, driving a piston to produce power.

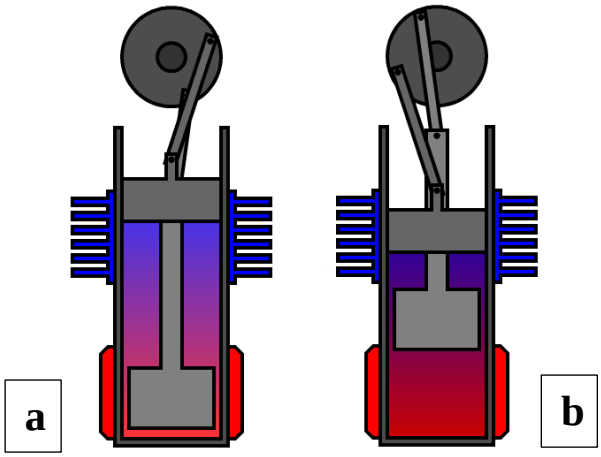

Figure 1.3: Cut-away diagram of a Beta-Stirling Engine in operation [40].

Figure 1.3 shows this principle graphically. Figure 1.3 (a) shows the displacer at the hot end of the cylinder, displacing the fluid towards the cold end. This causes heat to be removed from the system, cooling the working fluid and causing it to contract, moving the piston downwards. Figure 1.3 (b) shows the same Stirling engine with the displacer towards the cold end of the cylinder. The fluid is displaced towards the hot end, causing it to heat up and expand, pushing the piston back up, its reciprocating motion turning the crankshaft.

Bianchi and De Pascale [39] state that Stirling Cycles suffer from low efficiency due to highly irreversible expansion and displacement processes, and is therefore inferior to Organic Rankine Cycles at lower temperatures, where marginal gains and losses are significant.

Cotana et al [41] performed a comparison of an ORC and a Stirling Cycle for application to a 300kW gasified biomass project. They found that although the Stirling Cycle produced more

power at the relatively high temperatures produced by the gas burner, its increased capital cost compared to the ORC meant that the overall payback period was the same for both systems.

Jradi and Riffat [32] also report that the Stirling Cycle, while capable of greater efficiency under certain operating conditions than the Organic Rankine Cycle, experiences lower efficiency at low heat source temperatures, while requiring a higher capital cost, making it a less desirable solution for utilising low-temperature waste heat.

1.3.2 Inverted Brayton Cycle

The Brayton Cycle is a thermal cycle that operates entirely in the vapour phase, and can operate as either an open or a closed cycle. Bianchi and De Pascale [39] analysed this cycle for a range of heat source temperatures and found that for heat source temperatures of less than about 300°C it was difficult for the extracted work in the expander to exceed the work expended in the compressor, let alone achieve high efficiencies.

1.3.3 Direct Thermoelectric Conversion

Bianchi and De Pascale [39] mention Thermoelectric conversion in passing, but state that it is currently only suitable for extremely small power outputs, of the order of a couple of watts.

Chen et al briefly discuss it in the context of waste heat recovery from diesel engines, but discount it as being too inefficient in comparison with ORCs under the same conditions [24].

1.3.4 Kalina Cycle

The Kalina cycle is essentially a variation on the zeotropic Organic Rankine Cycle. For its working fluid it uses a mixture of water and ammonia. Due to the large temperature difference between the boiling points of these fluids there is a large temperature change during the phase change of the fluid. This means that for many heat sources the Kalina Cycle will not produce a pure vapour at the exit of the evaporator, but instead a fluid mixture. This is then separated, the vapour portion being directed through the expander, and the liquid portion bypassing the expander. A schematic diagram of three configurations of Kalina Cycle is shown in Figure 1.4. All share the same basic structure of separating out the vapour from the evaporator outlet for expansion, with the primary difference between them being the configuration of the recuperative heat exchangers.

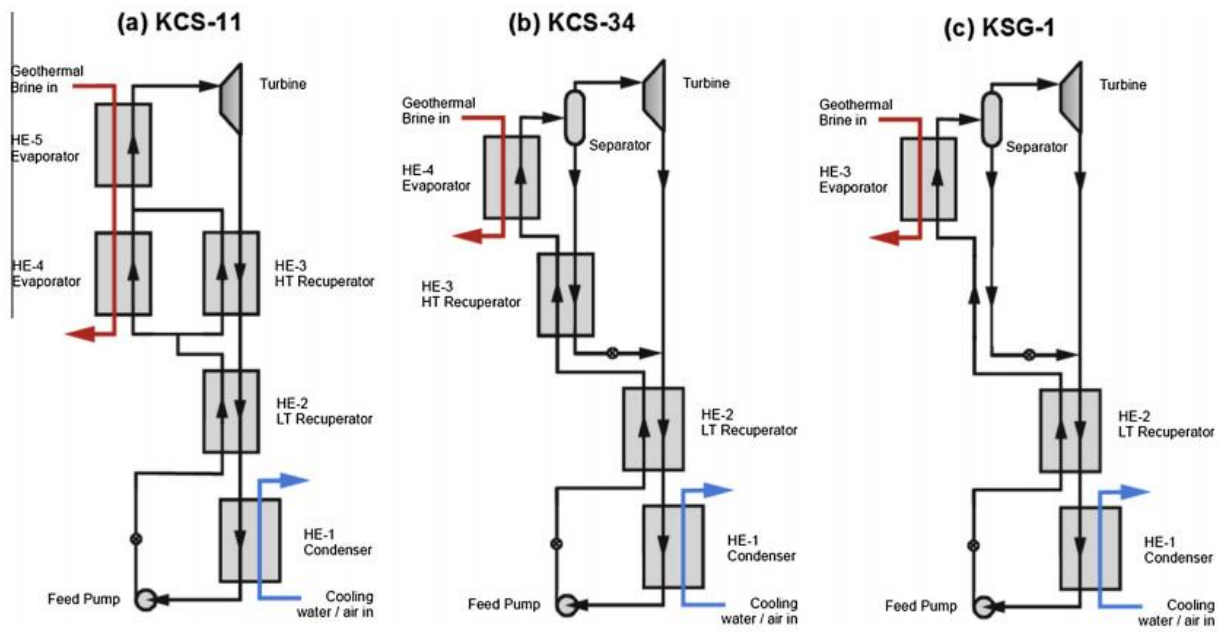

Figure 1.4: Schematic Diagram of three different configurations of Kalina Cycle [42]

The Kalina Cycle has been compared to the ORC for power generation by several authors. Nemati et al [43] found that the although the Kalina Cycle had a lower turbine size parameter than the ORC, the ORC performed better overall due to a simpler overall cycle configuration, lower operating pressure (11 bar as opposed to 46 bar), and feeding a superheated vapour rather than a saturated vapour into the expander led to more reliable performance.

Lin et al [44] concluded that the ORC outperformed the Kalina Cycle in terms of net power generation over a range of low-temperature heat source conditions ranging from 100°C to 200°C.

Zare and Mahmoudi [45] compared the ORC and Kalina Cycles for use as bottoming cycles for the gas turbine of a small nuclear reactor. They also concluded that the ORC was the better cycle, due to higher efficiency, lower complexity, lower pressure during operation and the potential to superheat the vapour at the expander inlet.

Di Pippo [46] calculated using a second law analysis that operating Kalina Cycles only showed a 3% improvement in power compared to ORCs using the same heat source, while being of significantly higher complexity.

However, Fu et al [47] concluded that the Kalina cycle showed a greater specific net power output than comparable ORCs for utilisation of heat sources above 150°C, and that this advantage increased with increasing heat source temperatures. This is possibly due to the

increased temperature glide during phase change. They also mention the greater required operating pressure for a Kalina Cycle compared to an equivalent ORC.

Wang et al [10] compared the thermodynamic performance of the ORC and Kalina cycles for multi-stream waste heat recovery from industry, finding that the Kalina Cycle had a higher thermodynamic performance than the ORC for straight and concave composite curves of heat source temperature, whereas the ORC had a higher performance for convex composite curves. This is most likely due to the shapes of the evaporating curves for the two cycles, with the Kalina cycle having a higher glide and zero superheat compared to most ORCs, giving better thermal matching in the evaporator.

1.4 The Organic Rankine Cycle

The Rankine Cycle consists of four major processes [48] [8]. Starting from the condenser outlet, the fluid exists in a subcooled, liquid state. It is pressurised by a pump and fed into an evaporator, where it is boiled at a constant pressure. From there, it passes through an expander, where its pressure drops, and energy is extracted as mechanical work. This work can be used to either directly power a process, or be converted into electrical energy. Finally, any excess heat energy left after the expansion process, most often latent heat of vaporisation, is removed in a condenser, leaving it as a subcooled liquid and closing the cycle. These processes are plotted on , a T-s diagram in Figure 1.6, and a P-h diagram in Figure 1.7

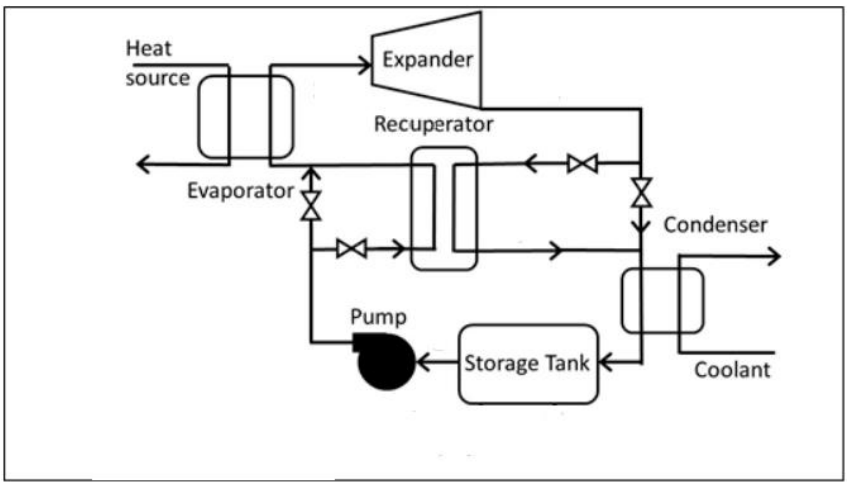

Figure 1.5: Block diagram of the Organic Rankine cycle

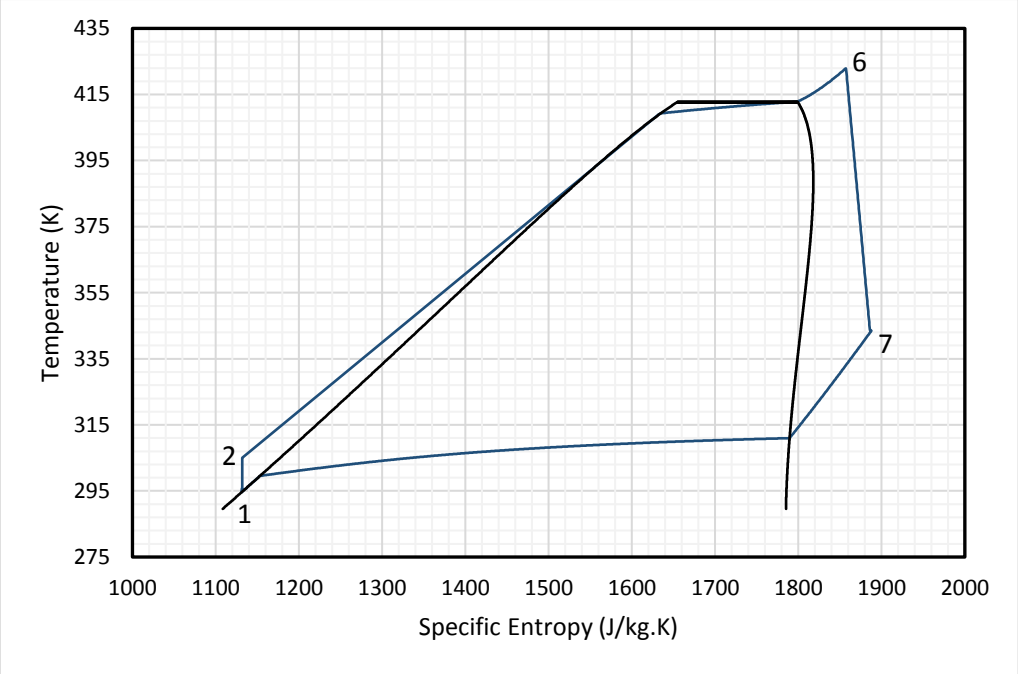

Figure 1.6: T-s diagram of the Organic Rankine Cycle

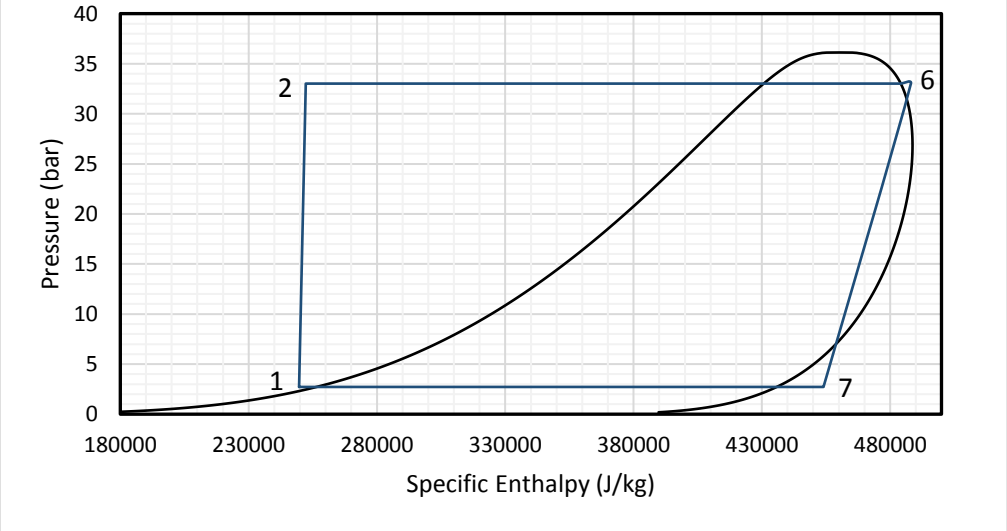

Figure 1.7: P-h diagram of the Organic Rankine Cycle

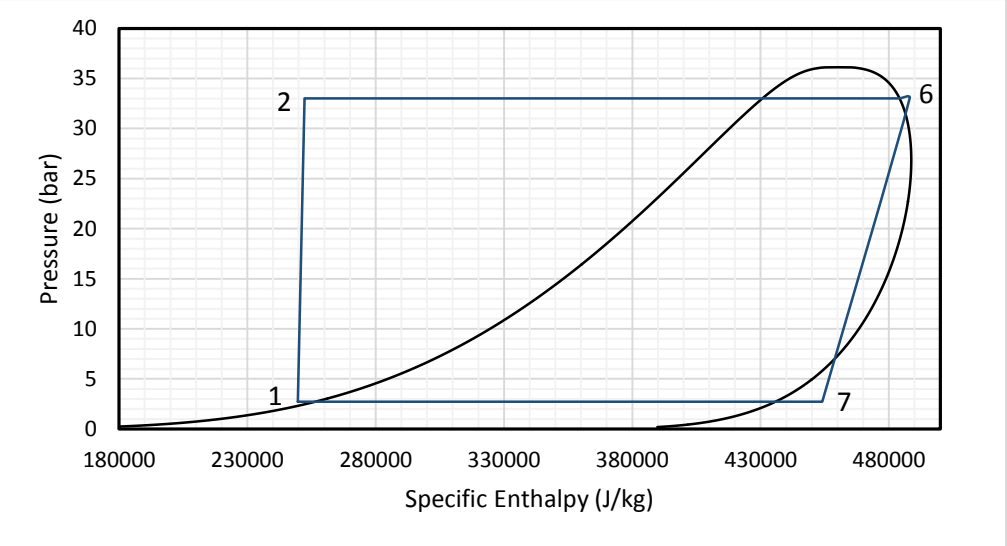

Figure 1.5 and Figure 1.7 show the Organic Rankine Cycle plotted on T-s and P-h diagrams. Beginning with state 1, the pump inlet, there is a compression process to state 2, increasing the temperature and the entropy of the working fluid. Then an isobaric heat addition process from state 2 to state 6, incorporating a phase change. From state 6 to 7 the fluid passes through the expander, decreasing in temperature, pressure and enthalpy, while increasing in entropy. From state 7 to state 1 the fluid passes through the condenser, undergoing an isobaric heat rejection process, decreasing in temperature, enthalpy and entropy.

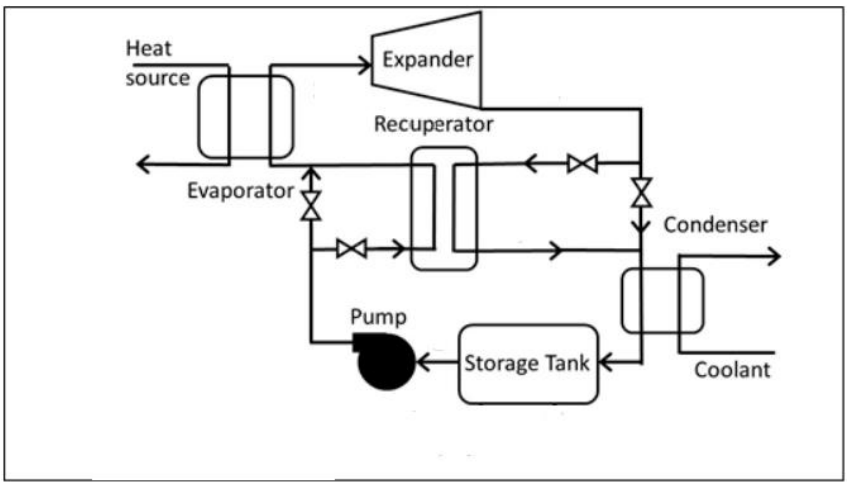

Figure 1.8: Block diagram of the Organic Rankine cycle

Traditional Organic Rankine Cycles using water as the working fluid are not economically competitive at heat source temperatures below about 370°C [49] [50] [51], so instead organic fluids can be used. These fluids have several advantages over water as a working fluid, as will

be described in chapter 2. Bianchi and De Pascale [39] concluded that the ORC is significantly more efficient than both the Inverted Brayton Cycle and the Stirling Cycle at low temperatures. Larjola [3] states that the ORC is the most effective cycle for converting low-grade heat sources to useful energy. Tancszuk et al [34] report that the ORC is not particularly sensitive to changing loads, with technological minimum loads extending as far down as 20-30% of the nominal load, making them suitable for use in applications where off-design conditions are likely to be encountered, particularly solar and bottoming cycles.

1.5 Current Challenges to ORC Implementation

1.5.1 Low Efficiency

As demonstrated in the previous section, the Organic Rankine Cycle is used for heat source temperatures in the range of 80°C to 350°C. This gives it an inherently low Carnot efficiency compared to cycles using higher heat source temperatures. Cayer et al [6] achieved a maximum first law efficiency of 8.8% with a Transcritical CO_2 cycle with a heat source temperature of 99°C. Dai et al [52] performed a parametric optimisation of an Organic Rankine Cycle for a heat source temperature of 145°C. The first law efficiency of the cycles varied from 11.5% to 13%. Liu et al [53] performed an off-design theoretical analysis of an ORC system using a simulated waste heat source, achieving a maximum first law efficiency of 6.47% from a 200°C heat source

Experimentally, Shao et al [54] achieved an efficiency of 5.5% using a 140°C heat source. Miao et al [55] built a system using a scroll expander and R123 as the working fluid, which could achieve 6.1% thermal efficiency using a 150°C heat source.

The implications of these published results are twofold, firstly, that the efficiency of Organic Rankine Cycles tends to be low, and that experimental results demonstrate far lower efficiencies than theoretical predictions. Due to the inherently low efficiency of cycles using lower-temperature heat sources, small absolute changes in the efficiency can have results that are proportionally very significant on the viability of the system.

1.5.2 High Cost

As a result of low efficiencies, Organic Rankine Cycle systems tend to have high costs compared to other forms of power generation. The primary reason for this is that the low specific enthalpy drop in the expander means that the other components of the cycle, pumps, heat exchangers and support systems, must be relatively larger compared to a system utilising a greater driving temperature difference. Muratori et al [56] provided a comparison of current energy generation capital costs in the United States. Oil ($750/kW), Natural Gas ($1,050/kW) and Onshore Wind ($2,000/kW) have the lowest average capital cost for the methods analysed. In contrast, Quoilin et al [57] report a capital cost for ORCs starting at roughly $2,600/kW for full systems, increasing to over $8,000/kW for the more expensive systems. Higher ORC efficiencies will tend to reduce the capital cost of the cycle.

1.5.3 Lack of Suitable Working Fluids

Due to a combination of factors, there is a lack of suitable working fluids for Organic Rankine Cycles. This is in spite of the fact that the working fluid selection is considered a key area for the optimisation of ORC systems [58]. Many of the older, chlorine-containing compounds such as R-11 and R-12 have been phased out due to the Kyoto protocol, and have been replaced by lighter fluorine-based refrigerants with lower critical temperatures, exemplified by R134a. While these compounds are well-suited to refrigeration their low boiling temperatures make them less appropriate for the higher temperatures encountered by ORCs. While options do exist, notably r245fa, used in many analyses and experimental rigs [17] [59] [60] [61] [62] and Pentane, used in the commercial ORC unit from Ormat [56], the lack of a large choice of options means that a fluid cannot always be picked that is appropriate to the particular heat source and sink of a system.

One proposed solution to this issue is the use of working fluid mixtures. When two fluids are mixed together a blend is formed with boiling and condensing temperatures between those of the component fluids. It is possible that working fluid blends could be developed to fill the gaps between existing working fluids, giving increased cycle efficiency. Additionally, fluid blends can exhibit a phenomenon called “glide”, whereby the fluid undergoes a change in temperature while it changes phase, unlike pure fluids, which change phase isothermally [62]. Such fluids are called zeotropic. The presence of glide can result in better temperature matching in the heat exchangers of an ORC and therefore reduce irreversibility and increase the utilisation of heat sources [58] [63]. In spite of these potential advantages, there is a lack of research, particularly experimental, on the effects of using a zeotropic working fluid in the ORC.

1.6 Research Areas and Motivation for this Thesis

1.6.1 Theoretical and Experimental Analysis of Small-Scale ORCs

The previous section demonstrated that real-world ORCs do not generally perform to the level predicted by thermodynamic analysis. In order to understand why this is the case, a thermodynamic MATLAB model linked to REFPROP 9.1 [64] was developed, and used in the design of a 1kW experimental ORC rig, using r245fa as the working fluid and a scroll-type device as the expander. Little in-depth experimental work has been carried out on small-scale ORCs and it was hoped that by understanding what causes the deviations from theoretical behaviour that strategies for reducing these losses could be minimised. The design and construction of the rig are discussed in chapters 4 and 5, and the results in chapter 6.

1.6.2 Experimental Analysis of Zeotropic ORCs

Although there is a body of theoretical analysis of ORCs using zeotropic working fluids there is very little experimental work on zeotropic working fluids. By designing and building the lab-scale rig in such a way that it could operate with a variety of working fluid blends, and have the composition of its working fluid changed after commissioning, several theoretical predictions about the performance of the zeotropic ORC could be tested. The most important of these were whether the temperature glide did indeed increase the heat source utilisation of the cycle, and whether the zeotropic working fluid adversely affected the heat transfer coefficient in the heat exchangers. The results for the zeotropic fluids are analysed and compared to the pure fluid in chapter 6.

1.6.3 Theoretical Analysis of the Dynamic ORC

ORCs using low-temperature heat sources will only have a small differential between the hot and cold reservoirs. This means that any changes in the temperature of the heat sink, for example, due to ambient temperature variations for a cycle using an air-cooled condenser, will have a large proportional effect on the driving temperature differential of the cycle. Building on the concept of using a zeotropic mixture as the working fluid and the theoretical model developed during the design of the experimental rig, a dynamic ORC is presented, capable of changing the composition of its working fluid during operation to ensure an optimal composition at all times for a heat sink of variable temperature. As ORCs tend to suffer from low thermal efficiencies, marginal gains such as this have the potential to cause a significant increase in the lifetime power generation of a system. The Dynamic ORC concept is presented in detail in chapter 7, with the results of theoretical modelling.

CHAPTER 2- LITERATURE REVIEW

In this section the main trends in Organic Rankine Cycle research are presented, broken broadly down into cycle optimisation, working fluid selection, expanders and cycle configuration. With this review of the latest trends in ORC research, the motivation for the research carried out in this thesis is presented.

2.1 Cycle Optimisation

Various methods exist to optimise the configuration of the Organic Rankine cycle, and several of these are outlined below.

2.2 Monte Carlo Simulation

Monte Carlo Simulation is a "brute force" method of cycle optimisation, although for systems with many independent variables it can be the best way of obtaining an optimal solution. The Monte Carlo method identifies a number of key parameters and assigns them a random value within a specified range. The simulation is then run with the chosen parameters, and the results stored. A new set of parameters is chosen, again at random, and the simulation is run again. Given a large enough number of iterations, the Monte Carlo simulation should, generate a probability density function for the output parameters of the cycle. The best-performing cycle configuration with respect to the selected objective function can then be selected from this set of generated results. The number of simulations required to generate a large enough population depends on several factors, primarily the number of independent variables being used for the simulation, and the range within which the variables are being simulated. A large number of parameters being varied, and a large range over which the parameters are varied will require a larger number of Monte Carlo iterations to produce an acceptable optimum solution. The point at which a solution is "good enough" can be obtained by several methods, for example, the percentage error from the mean [65]. The distribution of the parameters fed into the Monte Carlo simulation can take a number of forms [66] [67] [68] [69], for example, a normal or log-normal distribution is often used to model an uncertain input into a system. The required number of iterations required can be reduced by the use of Latin Hypercube Sampling. Whereas random sampling will produce acceptable results given a large enough number of iterations, there is the likelihood that by pure random generation, a large number of input cases will be similar to or duplicates of each other. Latin Hypercube Sampling takes into account the previous inputs generated and ensures that they are not repeated [70]. It is primarily used for generating a truly representative set of scenarios for uncertain input parameters.

For optimisation purposes, uniform or discrete distributions are more commonly used. The Monte Carlo method, when contrasted with the classical "one at a time" method, gives a more global picture of the sensitivity of the cycle to different parameters by varying them simultaneously [70].

Monte Carlo simulation has been extensively used in the analysis of ORC systems [69] [70] [71] [72]. Zhang et al [69] used a 1000-iteration Monte Carlo simulation to analyse an ORC operating as a bottoming cycle for an internal combustion engine (ICE), varying the ambient temperature, the power output of the ICE and the pinch point temperature difference in the heat exchangers.

Frutigera et al [70] performed a Monte Carlo simulation of an ORC to determine the effect of the uncertainty of the calculated working fluid parameters. Their model had ten degrees of freedom, two related to the operating conditions and a further 8 related to the working fluid properties. Their model took 400 cases with the inputs determined using Latin Hypercube Sampling.

2.3 Genetic Algorithm

The Genetic Algorithm is one method by which the cycle can be optimised, and has been used by several sources [52] [73] [74] [75] [76] [77].

The algorithm is an optimisation method based on the principle of natural selection. The algorithm creates a population of potential solutions, defined by a "chromosome" and discards those producing the worst values of the selected fitness function, before creating a new population based on the survivors from the previous generation. Due to the fact that it is directed by selection pressures and discards members of the population with weak fitness functions, it has the potential to produce an optimal solution with fewer iterations than the brute force method employed by Monte Carlo Simulation, saving on processing time.

Various fitness functions have been selected for genetic algorithm optimisation. Wang et al [74] used the capital cost of the cycle and the exergy efficiency. Frutigera et al [70] used the Net Present Value of the cycle. Kai et al [75] used the net power output per unit mass flow of thermal fluid. Feng et al [76] used the exergy efficiency and the heat exchanger area per unit power output, itself a proxy for total system cost. Sadeghi et al [77] used the energy efficiency and exergy destruction rate.

The most basic form of the genetic algorithm simply eliminates the worst-performing members of the population and creates a new population based on "mutation" operators, which generate a new set of parameters within a given range of those of the survivors.

More advanced genetic algorithms can use "crossover" operators, which "breed" the survivors together to create a new population based on the parameters of the survivors. While more complicated, this can result in faster convergence.

One possible limitation of the genetic algorithm is that with an insufficient starting population, the solution can potentially converge at a local minimum by eliminating members of the population whose descendants would ultimately have produced a better solution.

2.4 Working Fluid Selection

Working fluid selection for the Organic Rankine Cycle is a complicated process, and often requires trade-offs depending on which objective function is being prioritised by the system designers [78] [79]. For example, Zhang et al [59] found that R123, R600, R245fa, R245ca and R600a produce the best results in terms of thermal and exergy efficiency, R218, R125 and R41 perform best at recovering the maximum amount of heat from a given source, R152a, R134a, R600 and R143a required the lowest heat exchanger area, and R152a, R600, R600a, R134a, R143a R125 and R41 all performed well in terms of overall Levelised Energy Cost for the system under the conditions analysed.

No single fluid can be characterised as the "best" for the Organic Rankine Cycle, as the choice of fluid depends strongly on the application and the cycle conditions. Lakew and Bolland [60] found that the highest power for heat sources below 160°C was given by R227ea, but that R245fa outperformed it for heat sources greater than this temperature.

Dai et al [52] found that R236ea produced the highest heat source utilisation for a 145°C heat source, but that the highest first law efficiency was achieved using R113. Hung [7] found that the refrigerants required higher flow rates than hydrocarbon working fluids to achieve the same power output from a cycle. Combined with a generally higher cost for refrigerants than hydrocarbons, he concludes that this will make hydrocarbons the more attractive option for larger capacity systems. Zhang et al [69] found that hydrocarbon working fluids gave a higher power output from a given heat source than refrigerants.

2.4.1 Wet and Dry Working Fluids

The wetness or dryness is a common categorisation of working fluid types [79] [8] [8] [52], according to the shape of the saturation curve on a T-s diagram. Wet fluids have a negative slope on the vapour side of the curve, implying that the drop in temperature due to isentropic expansion will tend to override the drop in pressure, causing a reduction in superheat, or condensation of the working fluid. Isentropic working fluids have an infinite slope, meaning that an isentropic expansion will cause no phase change and no change in the superheating of the fluid. Dry fluids have a positive slope on the vapour side of the curve, meaning that the decrease in pressure overrides the decrease in temperature, and isentropic expansion causes the superheat to increase. These three cases are shown graphically in Figure 2.1.

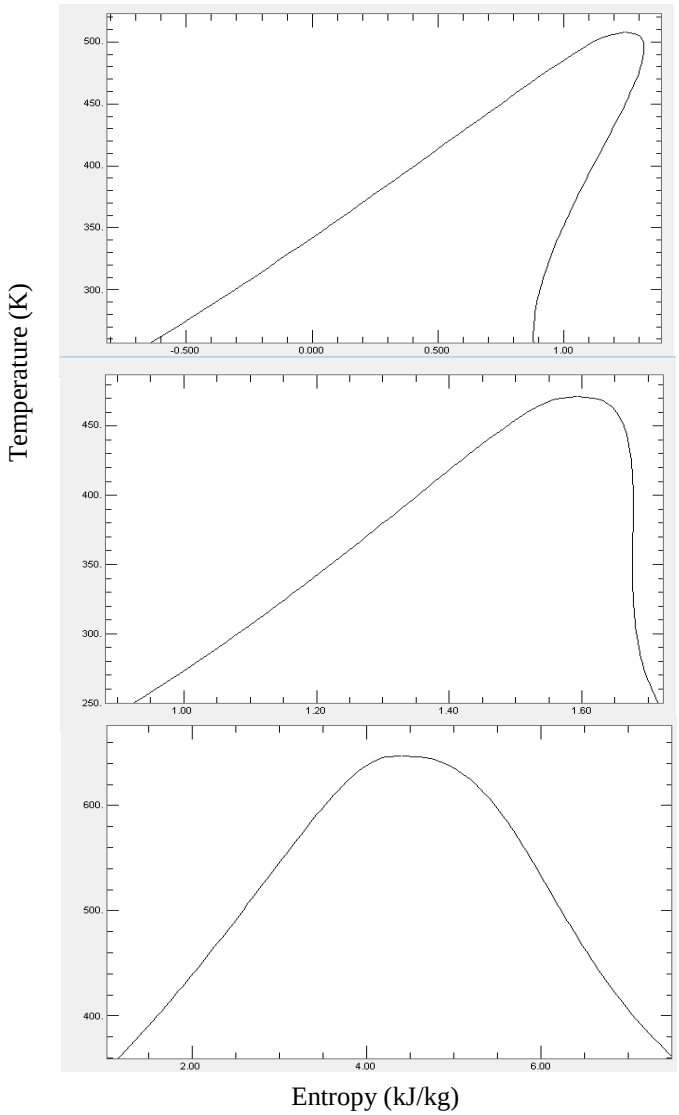

Figure 2.1: T-s diagrams of different types of fluids generated using REFPROP 9.1 [80]. From top to bottom, dry (hexane), isentropic (R-11) and wet (water)

Theoretically, isentropic fluids produce the greatest efficiency for an Organic Rankine Cycle, all other factors being equal [8]. Wet Fluids suffer from condensation inside the expander if the expansion ratio is too great. Condensation of the working fluid can damage turbine blades, and reduce the isentropic efficiency of the device [79] [78] [81]. This means that wet working fluids require a degree of superheat to be applied at the expander inlet to ensure that condensation does not occur [7] [52]. Allowing superheat at the expander inlet implies that the cycle is not operating at the maximum possible pressure ratio for the given working fluid and heat source, which will reduce the efficiency of the cycle. Additionally, at low temperatures, there may not be a sufficient temperature difference between the hot and cold reservoirs to operate the cycle with superheat, making wet fluids unattractive in the region in which ORCs tend to operate [7].

Dry working fluids suffer from the opposite effect. As the fluid expands isentropically, the vertical line on the T-s diagram moves away from the vapour side of the saturation curve. This results in superheat at the expander outlet. This means that there is some amount of thermal energy in the working fluid after expansion that has not been utilised, adding to condenser load and reducing efficiency [78]. This can be mitigated to some degree by incorporating a regenerator into the cycle.

In practice, the expansion process is never fully isentropic [8]. Expansion losses such as leakage, heat transfer out of the expander, heat transfer between the hot and cold sides of the expander, turbulence, friction and entry and exit losses all mean that the isentropic efficiency of the expander is below 100%. The effect of this in terms of wet and dry fluids is that even for an isentropic fluid, the increase in entropy during expansion will lead to an increase in superheat. This means that for a non-regenerative cycle, the ideal working fluid will be slightly wet. This was noticed by Hung et al [82]. They also note that the wetter fluids have a higher specific enthalpy drop as they expand, which reduces the size and required stages of expansion devices.

Figure 2.2 shows how the expansion process varies with changing isentropic efficiency. The red line is the dew side of the saturation dome. The black line represents an ideal, isentropic expansion process, with no entropy increase. As the isentropic efficiency drops below this, the entropy increases across the expander, leading to increased expander outlet temperature compared to the idealised isentropic case.

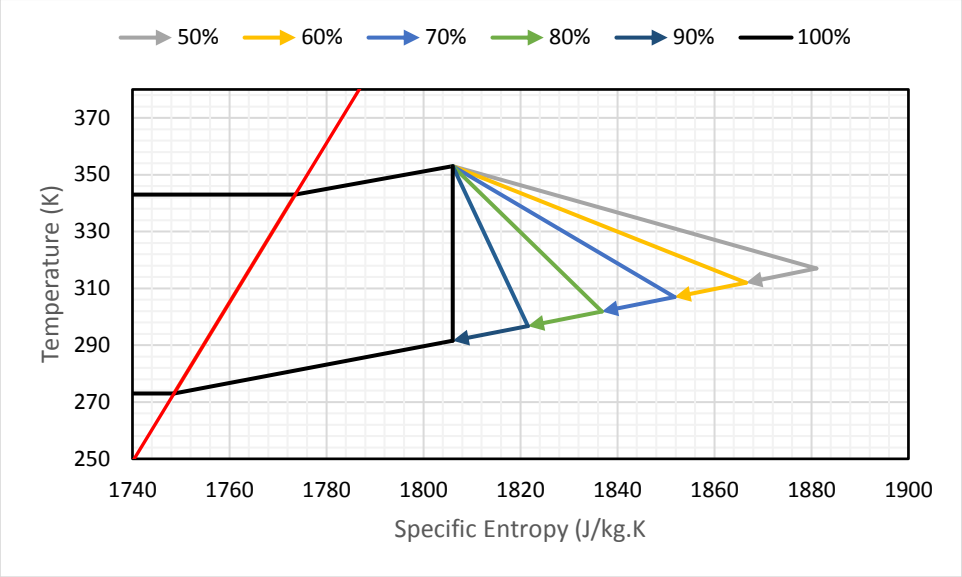

Figure 2.2: Illustration of how the expansion process varies with changing isentropic efficiency

2.4.2 Thermophysical Properties

2.4.2.1 Volumetric Expansion Ratio

One of the primary advantages of Organic Working Fluids over water is that they exhibit a far smaller volumetric expansion than water in the pressure and temperature ranges in which ORCs are generally utilised, sometimes by an order of magnitude [48]. This means that simpler and cheaper expanders can be used, which can greatly drive down total system cost, given that the expander tends to be a major contributor to the overall capital cost of a system.

2.4.2.2 Latent Heat of Vaporisation

High latent heat of vaporisation increases the work done in the expander, while also increasing the amount of energy required for the evaporator.

Additionally the higher the latent heat, the lower the slope of the heating fluid must also be on a Temperature-Energy diagram [3]. This corresponds to a higher flow rate of the heating fluid and a lower temperature drop. Depending on the heat source used, this can be a major consideration. For sources such as solar thermal or some geothermal, where the heating fluid can simply be recirculated, a higher flow rate of thermal fluid will result in a slightly higher capital cost in terms of pumping and piping, and might be acceptable if an increase in efficiency can result. For waste heat sources, where the fluid is not generally recirculated, a higher temperature drop in the heating fluid as it passes through the hot side of the ORC evaporator is desirable to maximise the amount of heat utilised, and therefore a smaller latent heat of vaporisation of the working fluid results in a more economically viable cycle [48].

In thermodynamic terms, a lower latent heat of vaporisation results in better thermal matching between the two fluid streams in the heat exchanger, resulting in lower irreversibility and increasing second law efficiency [3] [78] [79]. It also allows for a greater temperature drop in the thermal fluid, increasing heat source utilisation, an important metric of cycle performance for certain ORC applications.

When designing a system, lower enthalpy of vaporisation can be achieved most simply by selecting a working fluid that operates closer to the critical point, as the majority of saturation domes narrow with increasing temperature, as shown in the sample T-h diagram for R245fa, shown in Figure 2.3.

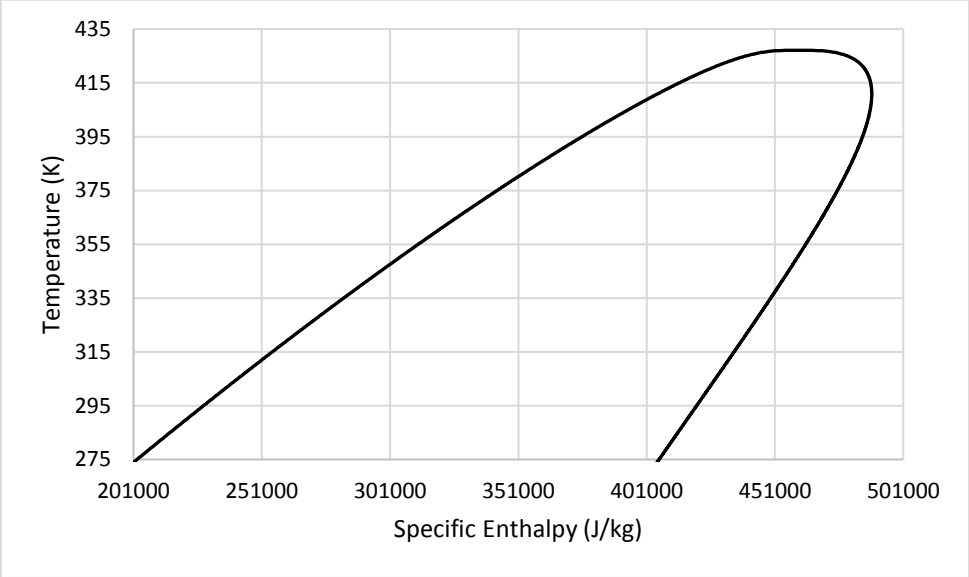

Figure 2.3: T-h diagram for R245fa

2.4.2.3 Density

Density has several implications in terms of practical system design. Low density necessitates higher volume flow rates in the system to obtain the same amount of power. This increases pressure losses in heat exchangers and pipes, and increases the size of turbomachinery [78] [83] [62]. In contrast, higher density allows more compact system design [84].

2.4.2.4 Specific Heat

A low liquid specific heat is noted in the literature [85] to decrease pump work and thereby increase the net work of the cycle, increasing its efficiency. However, further research from Borsukiewicz-Gozdur has failed to identify this trend [86].

2.4.2.5 Critical Temperature

The critical temperature has a significant effect on the pressure ratio of the cycle. Liu et al [79] state that the thermal efficiency of a cycle is a weak function of the critical temperature of the fluid. Invernizzi et al [87] concluded that the pressure ratio across the expander in an ORC is a function of the acentric factor of the molecules of the working fluid, and the fluid's critical temperature. For a fixed evaporation and condensation temperature, higher critical temperatures generally result in higher efficiencies, as the superheat at the expander inlet can be minimised [78]. However, the higher the critical temperature of the working fluid, the lower the condenser pressure must be for a given heat sink. This leads to lower densities, larger components, and higher capital costs [83] [21]. Condenser pressures below atmospheric pressure also risk contamination of the working fluid from leakage [21] [27].

Additionally, fluids operating close to their critical temperatures tend to have lower enthalpies of vaporisation, with all of the advantages outlined in 2.4.2.2..

2.4.2.6 Boiling Temperature

The boiling point of the working fluid should ideally be between 0°C and 100°C for ease of handling, and to avoid needing extremely low or high pressures in the condenser, assuming the coolant used is close to ambient temperature [78]. From a thermodynamic and cycle efficiency point of view, the boiling point of the working fluid should be tailored to the heat source and sink temperatures. A low boiling point means that the pressure must be raised to a high level to minimise superheat and increase cycle efficiency. This can push the cycle into a supercritical region. A high boiling point means the evaporator pressure cannot be raised as high for the same heat source while still ensuring complete evaporation of the working fluid. This restriction enforced on the cycle's pressure ratio limits the efficiency.

Hung [7] reports that the efficiency of a cycle increases with increasing boiling point, for a given heat source temperature

2.4.2.7 Freezing Point

The freezing point of the fluid must be higher than the cycle's lowest temperature [78].

2.4.2.8 Molecular Weight

For a momentum-based expander such as a turbine, molecular weight corresponds to the turbine efficiency [78]. Heavier molecules tend to have lower speed and fewer stages, reducing capital costs for the cycles [22]. However, a fluid with a high molecular weight and a high critical pressure will require a greater heat transfer area.

Hung [7] found a weak inverse correlation between the molecular weight of a working fluid and the irreversibility in the evaporator of the cycle.

2.4.2.9 Molecular Complexity

Molecular complexity is an influencing factor on several different properties of the working fluid. Firstly, more complex molecules tend to be drier working fluids [78], having a smaller, positive slope on the vapour side of the saturation curve of a T-s diagram. This means that they tend to have a higher superheat at the expander outlet, and all other things being equal, will have a lower efficiency for a non-regenerative cycle than a comparable isentropic or dry fluid.

Molecular complexity also has an effect on the isentropic efficiency of a turbine, primarily due to the fact that for homologous compounds, the molecular complexity increases with increasing molecular weight [78].

2.4.2.10 Viscosity

A low viscosity is desirable to reduce pressure losses in piping and heat exchangers [78]. A low viscosity also increases the Reynolds number, which improves convective heat transfer performance, reducing the necessary size of heat exchanger [62].

2.4.2.11 Thermal Conductivity

High thermal conductivity increases the conductive heat transfer coefficient in heat exchangers and thereby reduces their minimum size, leading to savings in capital cost [78]. However, thermal conductivity does not in itself affect the thermodynamic performance of a system.

2.4.2.12 Fluid Mixtures

Most research on Organic Rankine Cycles has focused on pure working fluids. A pure working fluid will change phase at a constant temperature, as latent heat is absorbed. This results in a horizontal region on a T-s diagram. In general, the thermal fluid used in the hot side of ORC evaporators and the coolant on the cold side of ORC condensers, do not undergo a phase change as they pass through the heat exchanger. This results in a mismatch in temperature profiles between the hot and cold sides of the heat exchanger, which reduces utilisation of the heat source, similarly to the lever effect discussed in the section on latent heat of vaporisation.

Fluid mixtures of two of more components with differing boiling points do not change phase at a constant temperature. Instead, they exhibit a temperature variation during phase change [62], a phenomenon known as “glide”. This temperature glide has several related advantages:

-It allows better temperature matching in heat exchangers, reducing the irreversibility and increasing the exergy efficiency.

-It moves the bubble point downwards relative to the dew point. This means that either the evaporator pressure can be increased, increasing cycle efficiency, or the temperature change of the thermal heating fluid increased, increasing heat source utilisation, depending on the priorities of the individual system. It also allows for a reduction in required coolant flow rate for a given heat rejection rate and pinch point temperature difference. This allows fan or pump power to be reduced, and minimises the use of scarce water in drier regions of the world [88]. It also allows for the UA of heat exchangers to be potentially reduced compared to an equivalent cycle using a pure fluid. However, when evaluating the usefulness of this reduction in terms of system capital cost, the effect of using a fluid mixture on the heat transfer properties of the fluid must also be considered.

Fluid mixtures also exhibit bubble, dew, and critical points in between the respective properties of their member components. This allows tailor-made blends to be produced for individual applications, increasing efficiency.

An additional benefit of a zeotropic mixture used as a working fluid is that by increasing the temperature of the dew point relative to the bubble point and introducing glide, the temperature differential between the expander exhaust and the fluid flowing into the evaporator is increased [89] [63]. This increases the amount of energy available for use by a regenerator, which can improve the efficiency of the cycle.

There is some debate over the effect of zeotropic working fluids on the efficiency of Organic Rankine Cycles. Several sources state that a zeotropic mixture leads to a slight loss in the first low efficiency of a cycle under certain operating conditions [89] [63] [90]. However, in many applications the first law efficiency is less important to the overall cycle than factors such as heat source utilisation, so zeotropic fluids may be more suited to these applications. Heberle et al [88] reported that the second law efficiency of fluid mixtures increased by 15% compared to pure fluids, due to better temperature matching in the heat exchangers. Venkatarathnam and Murthy [91] report an increase in both the efficiency and power output of an ORC using zeotropic fluids, especially for applications with a heat source temperature of less than 250°C.

While heat transfer coefficients are not considered in detail in this thesis, there is some research that suggests that zeotropic mixtures perform more poorly in this regard [78] [62], which would increase the necessary size of heat exchangers compared to a similar system using a pure working fluid. Baik et al [62] suggest that this is because of diffusion resistances arising from

the changing fluid composition of both phases and propose a correction factor based on Bell and Ghaly. They estimated the heat transfer coefficient of the zeotropic mixture to be 8-15% lower than that of a pure working fluid.

2.4.2.13 Supercritical and Transcritical Cycles

A supercritical ORC is an ORC that operates above the critical pressure and temperature of the working fluid. A transcritical cycle is an ORC that operates with part of the cycle above the critical point, and part of the cycle below it [92] [62] [84]. This does require a fluid with a sufficiently low critical temperature compared to the heat source temperature, so as to ensure the expansion process does not bring the fluid under the saturation dome in the expander. CO_2 is a commonly used working fluid for transcritical cycles due to its moderate critical pressure and stability under high temperature and pressure conditions [92] [84].

Supercritical fluids do not undergo a definitive phase change from liquid to vapour, instead gradually changing density as the temperature is increased. Therefore they avoid the problems caused by a temperature mismatch in the evaporator, in much the same way as using a zeotropic working fluid does [92] [6] [22] [62]. For transcritical cycles, this only applies to the evaporator, as the condenser will still be operating under subcritical conditions [78]. This requires either an increase in flow of coolant, or an increase in the condensing temperature, reducing the Carnot efficiency of the cycle. Zeotropic transcritical cycles have been considered by some to overcome this issue, by adding temperature glide in the condensation phase, and the lack of a defined phase change in the evaporator [62]. However, when the comparison metric is defined by heat exchanger area, as in Baik et al's work [62], the zeotropic cycle only performs marginally better than a transcritical cycle using a pure working fluid, due to the reduced heat transfer coefficient introduced by the zeotropic fluid.

Transcritical Cycles often require higher pressures than a comparable subcritical cycle, and therefore experience higher pumping and expansion losses [62]. This can offset the gains in other objective functions. The higher temperatures and pressures associated with a transcritical cycle may also lead to low stability, high flammability and corrosive tendencies [21].

It is sometimes difficult to compare transcritical cycles and their subcritical counterparts, as concepts like evaporating temperature and pressure have no meaning under supercritical conditions. Chen et al [92] suggest using the mean heat addition temperature when comparing cycles to ensure both are operating under comparable conditions.

Baik et al [62] [61] investigated and compared several subcritical and transcritical cycles, and concluded that due to reducing the temperature mismatch, transcritical zeotropic cycles could utilise heat sources better than comparable subcritical cycles using pure working fluids such as R134a and r245fa, albeit with lower cycle first law efficiencies.

Cayer et al [6] compared supercritical and transcritical cycles using CO_2, Ethane and R125. They found that the performance of the fluids varied depending on which parameters were prioritised, and which operating conditions were used. The highest Specific Net Power and Net Power Output were given by Ethane, the highest thermal efficiency, lowest Heat Exchanger Area and lowest relative capital cost per kW by R125, with CO_2 giving intermediate performance.

Gu et al [22] compared three working fluids (Propane, R125 and R134a) for a supercritical cycle with a geothermal heat source temperature of 230°C. They found R134a to produce the highest first and second law efficiencies, of 12% and 55.7% respectively.

2.4.2.14 Environmental Considerations

Several sources [48] [15] [78] [84] identified three primary environmental considerations for the selection of Organic Working Fluids, these being Ozone Depletion Potential (ODP), Global Warming Potential (GWP) and Atmospheric Lifetime (ALT). R-11, R-12, R-113, R-114 and R-115 have already been phased out due to their high ODP [22], and are therefore not suitable candidates for ORC systems, in spite of often having favourable thermodynamic properties. Further working fluids such as R-21, R-22, R-123, R-124, R141b and R142b are due to be phased out over the coming decades, as although their ODP is lower than those refrigerants already phased out, their GWP is still considered to be too high.

The ASHRAE refrigerant safety classification has also been identified as being a good indication of how dangerous a fluid is considered [78], focusing on key properties such as non-corrosive [7], non-flammable [7] [22] and non-toxic [7] [84]. However, it has been pointed out that these are often merely desirable characteristics, and not always absolutely necessary. For example, alkanes such as n-pentane and isopentane are often used for low-temperature applications in spite of their flammability, as they are safe so long as they are kept away from sources of ignition [48]. Some applications require different environmental considerations to others. For example, automotive bottoming applications generally have more stringent requirements for non-flammability and non-toxicity than static cycles due to the increased risk

posed to the cycle by vehicular collisions, meaning fluids such as CO_2 have attracted more attention than hydrocarbons and ammonia [84].

2.5 Expander Selection

The expander selection is a critical part of the Organic Rankine Cycle, and different expander types are better suited to different working fluids and cycle operating conditions. Several categories of expander exist, divided into the two broad categories of velocity/momentum based (i.e. turbines) and volume-based, which includes all positive displacement devices such as screw, scroll and rotary vane expanders [78]. In general, positive displacement expanders are used for lower power, lower speed applications than turbines [81].

The most common metric used for the comparison of expansion devices is their isentropic efficiency. The Carnot cycle assumes isentropic expansion of the working fluid between the high and low pressure states [7]. In reality, a variety of factors cause the expansion process to deviate from this idealised situation, resulting in an increase in entropy.

The isentropic efficiency of an expansion process is a measure of how close the actual process resembles the ideal case, and is given by the equation [7]:

$$\eta_{isentropic} = \frac{h_{initial} - h_{final}}{h_{initial} - h_{ideal}} \tag{2.1}$$

Where h_{ideal} is the enthalpy at the end of the expansion process, assuming isentropic expansion.

Often in analysis of ORCs, the isentropic efficiency is simply assumed to be a certain value, without considering the more in-depth reasons why this might be the case. For example, Baik et al [62] and Mago et al [93] assume a value of 80%. Chen et al assumed 70% for their research, based on existing literature [92] [84]. Dai et al [52] assumed an isentropic efficiency of 85%. Bianchi and De Pascale took a value of 75% [39]. Gu et al [22] took a slightly different approach, and used an isentropic exponent of 1.3 for the expansion processes of Propane and R134a.

2.5.1 Turbines

ORC turbines have some specific design considerations that set them apart somewhat from turbines used in traditional Rankine Cycle plants, summarised by Bao et al [78] as follows:

> -Organic fluids have greater molar mass than water, and therefore a correspondingly lower speed of sound. This means that extra care must be taken to ensure that the flow

does not become supersonic, which leads to losses in isentropic efficiency due to shock wave formation.

-Under certain temperature conditions, ORC turbines will have a higher expansion ratio and lower enthalpy drop than a traditional steam turbine.

-Organic fluids tend to have a higher density than water, so turbines can be smaller for the same amount of power generated.

-Due to this compactness, and resulting reduced rotational inertia, ORC turbines are slightly more at risk of overspeed during load shedding

-Many Organic Fluids are dry fluids, which reduces the risk of droplet formation in the turbine, and the associated problems that this can cause.

-Some other properties of certain Organic Fluids, such as cost, toxicity or flammability, mean that leakage and contamination is a more serious concern. Bao et al recommend using gas as the sealing medium and adopting a double-face seal.

The literature generally recommends the use of single-stage radial inflow turbines, as these perform better than their competitors in a number of areas, as outlined by Sauret et al [94].

-They can be optimised for different thermal resources with only minor modifications.

-Variable inlet guide vanes allow higher-efficiency operation under off-design conditions.

-They are less sensitive to inaccuracies in the blade profile, which means that they are more scalable, losing less isentropic efficiency as the size of the turbine decreases.

-They are more robust, and therefore better suited to working with higher-density organic working fluids, especially under supercritical conditions.

-They are easier to manufacture, as the blades are attached to the hub, and also exhibit higher dynamic stability.

There is some research, both practical and theoretical, into turbines as expansion devices for the Organic Rankine Cycle.

Compared to positive displacement devices, turbines generally have higher efficiencies and better compactness, while being more expensive. Axial variants can also benefit from higher expansion ratios by adding sequential stages [95].

Fiaschi et al [96] compared several radial expanders under different conditions and working fluids, and concluded that R134a gave the highest isentropic efficiency of the fluids considered, with 0.85. Li et al [97] performed an analysis of heat loss from turbine expanders, which is one of the key contributors to low isentropic efficiency.

Teng et al [98] researched waste heat recovery from automotive applications, where the quality and quantity of waste heat available to an ORC varies widely, and came to the conclusion that turbines were not suitable for this sort of variable-temperature heat recovery, as it leads to inefficiency, and droplet formation inside the turbine.

Song et al [99] analysed the performance of a Tesla turbine applied to an Organic Rankine Cycle, finding a maximum isentropic efficiency of 70%, although the efficiency with organic working fluids under standard cycle operating conditions was calculated to be not more than 38.7%. They also found that the Tesla turbine was very sensitive to the properties of the working fluid, particularly viscosity and density.

Fiaschi et al [100] performed a 3D CFD analysis of a 5kW radial turbine. They concluded that the main source of isentropic inefficiency in such a turbine was blade loading, followed by clearance losses. Disk and skin friction had only small effects. The most effective way of reducing losses due to blade loading and clearance is by tighter proportional tolerances, which explains why turbines become less isentropically efficient at smaller power outputs.

Turbines become less suited to low-power applications, as the required tolerances are high, and they require a gearbox, due to their high rotational speed. Gearboxes increase capital cost, and can introduce parasitic losses into a system which increase as the scale becomes smaller [101] [81].

Kang [95] designed a two-stage radial turbine for use in an ORC using R245fa as the working fluid, achieving an isentropic efficiency of 85%.

Nguyen et al [102] developed a small-scale Organic Rankine Cycle using a radial turbine and high-speed alternator, recording an isentropic turbine efficiency of 49.8%.

Turbines can operate at a pressure ratio of up to 70:1 [81]. Although Gu et al note that high pressure ratios can lead to low isentropic efficiencies, as is the case in single flash geothermal systems [22].

2.5.2 Scroll Expander

A scroll expander consists of two helical scrolls, one is the rotor, and the other the stator. As the rotor rotates, it creates a closed volume between its points of contact with the stator. This volume increases in size through each rotation due to the increasing separation of rotor and stator, and eventually reaches the exit port, where it leaves the expander.

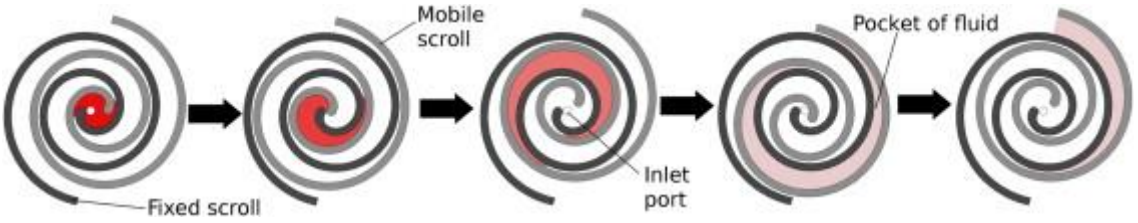

Figure 2.4: Diagram of mode of operation of a scroll expander [103]

Scroll expanders deviate from isentropic behaviour due to several major factors. Firstly, over- and under-expansion losses occur when the ratio of specific volumes between the high and low pressure sides is not equal to the expander's own in-built volume ratio [104]. This can occur in one of two ways. Firstly, under-expansion losses are the most intuitive. These occur when the in-built volume ratio of the expander is smaller than the ratio of specific volumes either side of it. In this case, the fluid will still have the capacity to do useful work on leaving the expander, but this capacity will remain unused, and the fluid will undergo an isenthalpic throttling process as it exits the expander [104]. The opposite case is that of over-expansion. This occurs when the in-built volume ratio of the expander is greater than the ratio of specific volumes either side of it. In this case, the fluid trapped in the expansion volume between the two scrolls will reach a lower pressure than that in the discharge line. Work will then have to be done by the expander to repressurise this fluid so it will flow into the discharge line [104] [15]. These two processes are illustrated on a P-V diagram in Figure 2.5.

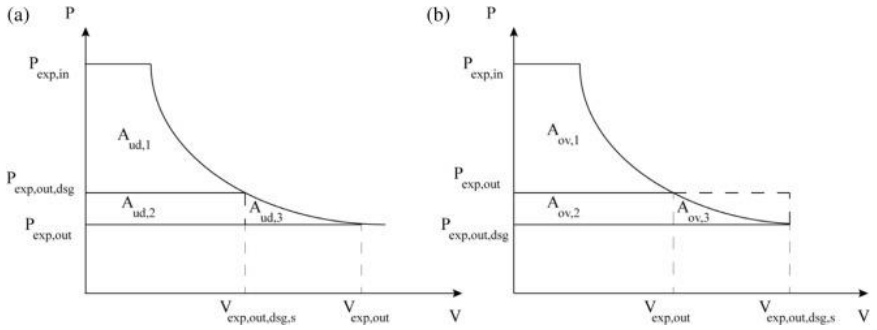

Figure 2.5: Isentropic expansion processes in the case of a) under expansion and b) over expansion [15]

Even in the case of perfectly-expanded fluids, there still exist some losses in expanders. These include leakage around the edges of the scroll due to imperfect seals, especially at high pressure differences [105], heat losses from the hot surfaces of the expander, fluid losses due to turbulence and inlet and outlet losses, mechanical losses such as tip friction and bearing losses, and conduction of heat through the scrolls themselves. Lemort et al [106] surmised that the main cause of loss of efficiency in a scroll expander was leakage past the scrolls, with mechanical losses and supply pressure drop also having an effect. This means that the isentropic efficiency of scroll expanders tends to peak at around 70%. Fukuta et al [107] reported an isentropic efficiency of 55%. Huff and Rademacher [105] 42%, Yanigasawa et al [108] 60%, Zanelli and Favrat [109] 65% using R134a. Lemort et al [106] achieved a maximum experimental isentropic efficiency of 68% while validating a semi-empirical model, and also noted the sharp drop off at low imposed pressure ratios due to over-expansion losses.

Scroll expanders are mechanically simple, reliable and relatively scalable [106].

2.5.3 Screw Expander

Screw Expanders are a relatively mature technology for Organic Rankine Cycle applications [78]. They come in two varieties, single-screw and twin screw. Both types of screw expander operate on the same basic principle. A volume of vapour is trapped in an expansion chamber formed by the geometry of the screw or screws. The motion of the screws then enlarges this chamber until the trapped vapour reaches an exit port.

In a single screw expander, this volume is created by meshing the main screw rotor with peripheral gate rotors. The rotation of the screw tends to move the trapped volume from one end of the screw to the other, expanding as it goes, until it reaches the discharge port located on the outside wall of the expansion chamber. A diagram of a single-screw expander can be seen in Figure 2.6. Fluid enters the screw through a port at the point marked A. As the screw turns under the pressure of the enclosed fluid, the trapped volume both expands and moves along the axis of the expander, as shown at positions B and C.

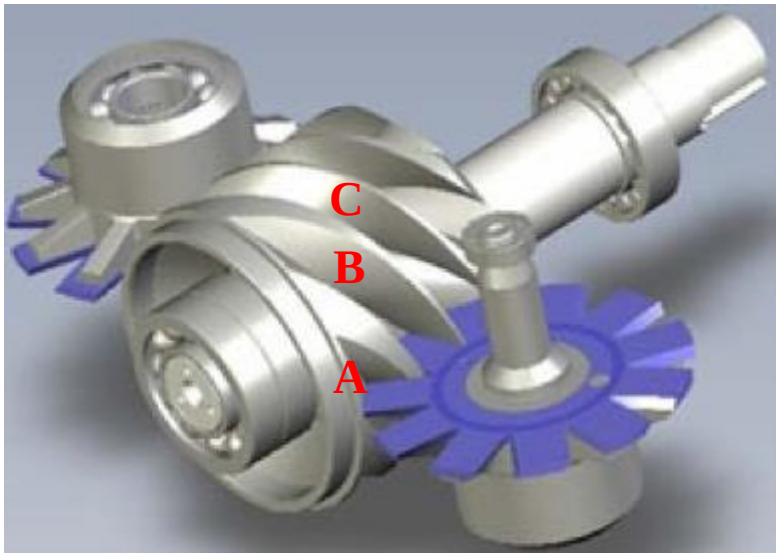

Figure 2.6: Diagram of a single-screw expander, minus housing, adapted from [110]

A twin screw expander operates in much the same way, except the volume of vapour is trapped between two counter-rotating screws, instead of using gate rotors. In both cases the effect is the same, the trapped volume moves along the length of the screws, its volume increasing as it moves, before being released when it reaches the outlet port.

Both of these technologies have a maximum expansion ratio defined by their geometries. However, they also have the interesting and useful potential for operation with a variable expansion ratio, potentially reducing the effects of over- and under-expansion. Variable expansion ratio is achieved simply by utilising a sliding cover for the outlet port. Sliding the cover partially over the outlet port means that the trapped fluid volume takes longer to reach the outlet port, and therefore expands more. Sliding it completely back means that the trapped fluid reaches the outlet port earlier, and therefore expands less. The principles of operation of such a variable-displacement screw expander are described by Wu et al [111]. They found that the variable-displacement screw expander allowed the cycle to respond to varying pressure ratios and working fluid mass flow rates and increases the overall energy generation of the cycle under such varying input conditions. Additionally, the experimental results seem to indicate that this has been achieved with little to no decrease in the isentropic efficiency of the expansion process, as the response of the cycle to changing heat source and sink temperatures was roughly linear, as is the Carnot efficiency of the cycle. If the isentropic efficiency of the expansion process was being affected greatly by the sliding of the valve, this would not be the case.

The principal challenges in the operation of screw expanders are that they require high tolerances of manufacture to reduce leakage [81], and also can experience lubrication problems due to high running speeds and tight clearances. This means that they are not particularly scalable to small sizes, and become prohibitively expensive for low-power applications.

Screw expanders, as all positive displacement devices, suffer in terms of isentropic efficiency due to internal leakage, inlet and outlet losses, internal and external heat losses, and mechanical losses.

Screw expanders are a common research area in the literature. Tang et al [112] developed a thermodynamic model for a twin-screw expander, and investigated the effect of several parameters on the performance of that expander, finding a maximum isentropic efficiency of 88%, decreasing to 60% as the expander speed increased. They attributed this loss in isentropic efficiency to a corresponding loss in volumetric efficiency as the rotational speed of the screw increased. Ziviani et al [113] presented experimental data and a semi-empirical model of a single-screw expander, finding a maximum isentropic efficiency of 64.7%. They found that the major contributors to isentropic efficiency losses were friction losses, followed by suction pressure drops and leakages. Giuffrida [114] performed a semi-empirical analysis of a screw expander applied to an ORC, and found that leakage flow could be almost 25% of the expander flow, and that thermal losses from the expander were also significant. They also found that increasing the pressure ratio on the expander increases its isentropic efficiency. Zhang et al [115] developed and tested a single-screw expander for use in a bottoming ORC cycle attached to a diesel engine exhaust with a temperature of 550 °C, developing a power of 10kW and with an overall efficiency of 57.88%.

2.5.4 Reciprocating Piston Expander

Piston expanders have several issues that have hindered their uptake into ORC applications. They are high-complexity devices with many moving parts [81], and high precision requirements, especially for components such as cams and valves. They require careful balancing due to the rotation of asymmetric and off-centre masses around the crankshaft, and experience high friction losses between the cylinder and piston rings, with associated lubrication problems. They also experience pulsations in output, a consequence of the granular nature of valve opening and closing.

However, they also feature several advantages in comparison to other expanders. They can achieve high in-built volume ratios, they can ingest liquid with few problems, and are capable of withstanding high temperatures and pressures in operation [116].

Isentropic efficiency is reduced by high entry and exit losses as fluid passes through the valves [81], as well as the usual factors affecting positive displacement devices. Oudkerk et al [116] identified internal leakage at low rotational speeds as being of particular significance, while at higher rotational speeds, entry losses and mechanical inefficiencies dominated. Zha et al [117] reported an isentropic efficiency of 50% for a rolling-piston expander using CO_2. Zhang et al [118] achieved an isentropic efficiency of 62% using a double-acting free piston expander, also using CO_2 as their working fluid. Oudkerk et al [116] achieved a calculated isentropic efficiency of 70%, but a shaft efficiency of just 53%, due to mechanical losses.

Reciprocating pistons can be used as variable displacement expanders through the use of a swash plate. A swash plate type piston expander does away with the traditional crankshaft, and instead uses an angled plate [119] [116] [120]. The pistons are attached to the swash plate with ball joints, and the swash plate itself connects to a rotating driveshaft that passes through its centre point. By firing each cylinder sequentially, the swash plate is caused to rotate, turning the driveshaft. Torregrosa et al [119] ran a swash plate piston expander at a pressure ratio of 20 between the high and low sides.

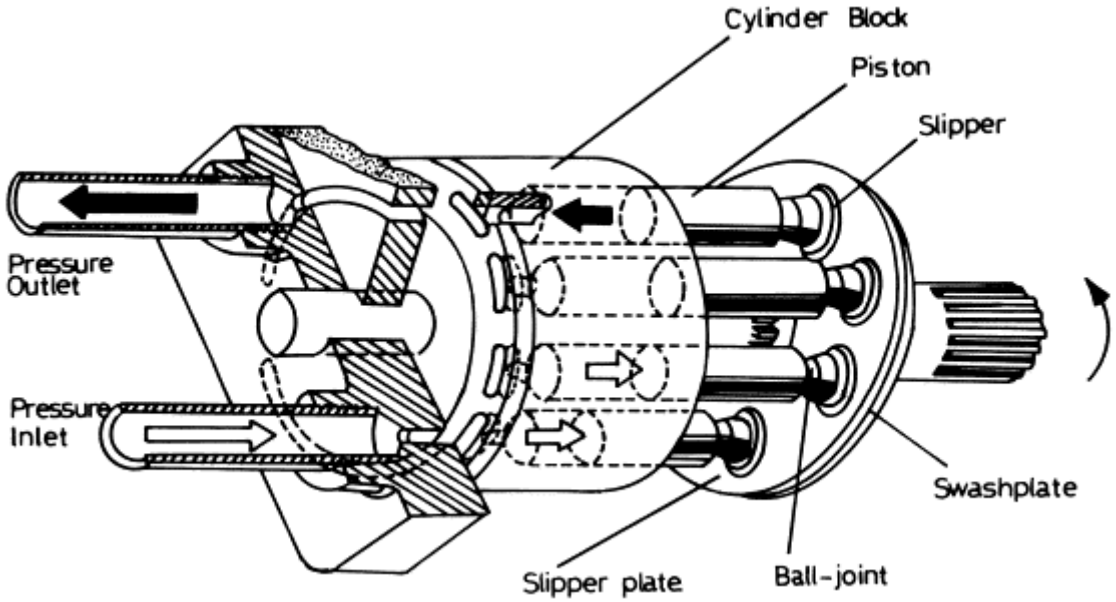

Figure 2.7: Diagram of a swash plate piston device [121]

Variable displacement can be introduced into a swash plate piston expander by varying the angle of the swash plate. The greater the angle of the swash plate, the greater the displacement the pistons of the expander can achieve. As the clearance volume of piston expanders is quite small, the volumetric ratio can theoretically be adjusted a large amount with only a small change in the angle of the swash plate.

2.5.5 Rotary Vane Expander

Rotary Vane Expanders consist of a circular chamber, with a rotor offset from the centre. This rotor incorporates several vanes, which extend from the rotor hub to the edges of the chamber, either through centrifugal force or spring loading. Spring loading tends to reduce leakage at the vane tip, while introducing complexity, a component vulnerable to fatigue [122] and increasing the mechanical losses due to friction due to the increased reaction force between vane tips and cylinder wall [123]. The location of the inlet port at the side of the chamber closest to the rotor hub means that the volume trapped between two sequential blades increases at the trapped fluid moves towards the other side of the chamber, where it is exhausted.

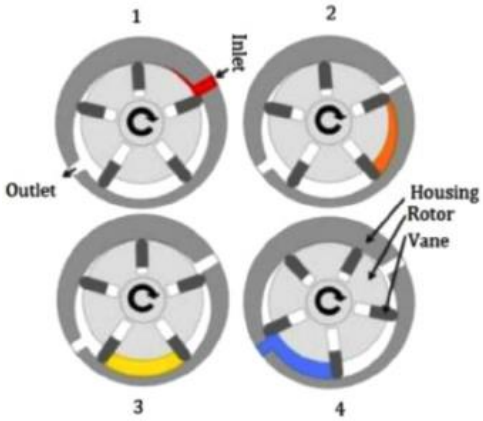

Figure 2.8: Diagram of the operation of a rotary vane expander [124]

Variable expansion ratio can be achieved with rotary vane expanders by changing the offset of the rotor hub. The smaller the offset of the rotor hub, the smaller the ratio of the outlet volume to the inlet volume, and therefore the smaller the in-built volume ratio. The literature reveals that rotary vane expanders are suited to operation at in-built expansion ratios of up to 10:1 [81].

Rotary vane expanders are mechanically quite simple, operate at reasonably low speeds, eliminating the need for a gearbox, and can tolerate some degree of droplet formation [81] [118]. They are also relatively insensitive to changes in operating speed, making them suitable for certain ORC applications with varying availability of heat source, such as solar or some

types of waste heat [81]. In general, friction losses are low, although leakage losses can be quite high [122]. Badr et al [81] [123] found that the greatest losses occurred at the inlet, with the majority of the remaining losses due to leakage, while identifying heat transfer and frictional losses as additional areas for improvement. They also found that the sealing between the vane tip and the cylinder wall was suboptimal, with some degree of rebound occurring leading to leakage, a phenomenon they termed "vane chatter". This finding was backed up by Toji et al [125].

Isentropic efficiencies vary between 70% and 95% under laboratory conditions [126]. Badr et al [81] report an efficiency of 70% with significant potential for improvement. Yang et al [122] report an experimental isentropic efficiency of 23% for CO_2, with serious leakage problems, evidenced by a low volumetric efficiency.

2.5.6 Comparison of Technologies

The right expander for a given application will depend on a number of factors. These include allowable expansion ratio, compatibility with working fluids, especially for those expanders that require extensive lubrication, isentropic efficiency of the expansion process, performance under off-design conditions, tolerance of droplet formation, reliability, complexity and cost. For example, screw expanders and turbines have many favourable properties, but require high manufacturing tolerances, which makes them uneconomical for smaller systems. Scroll expanders have a limited expansion ratio, but are mechanically simple, can often run unlubricated, and are scalable to small sizes.

Quoilin et al [103] performed a comparison of turbine, screw and scroll expanders for various heat sources and power outputs, as shown in Figure 2.9. It can be seen that for higher power applications, turbines are the best performing technology for all heat source types. Screw expanders are more suited to intermediate power levels, with the exact classification of what constitutes an "intermediate" power depending on the heat source. For all technologies, scroll expanders performed the best at the lowest power outputs.

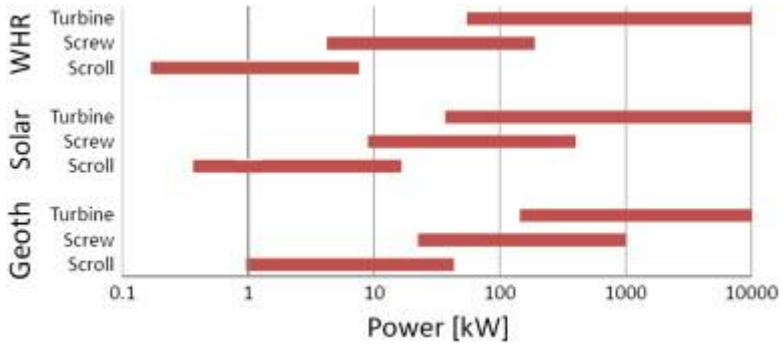

Figure 2.9: Optimum Expander operating map for three expander types and three heat sources [103].

2.6 Cycle Operating Conditions

2.6.1 Evaporator and Condenser Pressure

Higher pressure ratios tend to result in higher efficiencies for the Organic Rankine Cycle [7] [78]. However, it is clearly not feasible to increase the pressure ratio to an arbitrarily large value. Increasing the evaporator pressure too high will increase stress on the system, as well as increasing the boiling point of the fluid. If the boiling point of the fluid is increased to above the heat source temperature, the system will no longer function. Therefore, the optimum evaporator pressure for an ORC, particularly one using a dry or near-isentropic working fluid, is the saturated pressure at the turbine inlet temperature [52]. This will also increase the density of the fluid, reducing necessary flow rates and increasing heat transfer coefficients in the evaporator [7], which will tend to reduce its size. Additionally, legal requirements in many countries limit the maximum pressure in the system to 20 bar, so this is a common evaporator pressure limit [48] [127].

Condensing pressure is limited primarily by two factors. A large negative gauge pressure in the condenser could result in leakage into the system from the surrounding air. This will reduce the efficiency of the cycle and contaminate the working fluid [78] [15]. Reduced pressure will also reduce the density of the working fluid, which will increase the size of some components, and also increase flow losses in pipes and heat exchangers.

Increasing the condensing pressure will reduce the differential between the evaporating and condensing temperatures, reducing the efficiency of the cycle [22].

Several sources [22] [128] note that close to the critical point of the working fluid, large changes in pressure can result from small changes in temperature, leading the system to become

unstable. In this region, the vapour side of the saturation dome for many dry fluids also has a convex shape. This means that if there is only a small amount of superheat present, the expansion can cause the fluid to pass back under the saturation dome for a time, even though the overall shape of the curve is that of a dry fluid. They recommend not operating ORCs near the critical point, in spite of any theoretical thermodynamic benefits this might bring.

Hung [7] reported that the irreversibility in the evaporator of an ORC decreases with decreasing evaporator pressure for a given heat source, provided no superheat at the expander inlet is applied. This is due to the fact that the lower the evaporator pressure, also the lower the evaporating temperature. With a fixed heat source temperature, this increases the mismatch between the two fluid streams. When the heat source temperature was held at a constant value relative to the evaporating temperature, the irreversibility increased with increasing evaporator pressure.

2.6.2 Heat Source Temperature

The heat source temperature is a major driver of the efficiency of a cycle. The higher the heat source temperature, the higher the Carnot efficiency of a cycle for a given heat sink, and therefore, as a general rule, the higher the first law efficiency of the cycle using that heat source.

Cayer et al [6] found that both the efficiency and the specific work of a cycle increased monotonically with increasing heat source temperature.

Subbiah and Natarajan [21] found that small increases in heat source temperature can result in substantial increases in the Thermal Fluid Utilisation of a cycle by increasing the superheat of the working fluid and improving thermal matching in the evaporator. They recommend topping up the geothermal fluid's temperature by the use of a "hybrid cycle".

Hung et al [8] found that the efficiency of the cycle increases for wet fluids with increasing heat source temperature, but decreases for dry fluids, when the evaporator pressure is fixed. This corresponds to increasing the superheat of the cycle. They do note that the exact effects depend on the particular slopes of the isobaric curves in the superheated region of the T-s diagram

2.6.3 Heat Sink Temperature

Hung [7] demonstrated that the efficiency of a cycle using dry fluids increases with decreasing condenser exit temperature. This is because of the implied decrease in condensing pressure, increasing the pressure ratio of the system.

2.6.4 Maximum Cycle Temperature

Organic Fluids become chemically unstable at high temperatures [7], and can decompose. This decomposition into lighter products affects the boiling, condensation and expansion processes, and in general will adversely affect the thermal performance of the cycle [129]. Most organic fluids are unsuitable for use above about 600K [130]. The actual temperature at which organic working fluids lose their thermal stability depends strongly on the pressure, conditions, and presence of any contamination. Invernizzi et al [131] recommend that R134a, R245fa, Siloxanes, Pentane and Cyclopentane not be used above 300°C.

The Maximum Cycle Temperature, sometimes also referred to in literature as the "Turbine Inlet Temperature", can also affect the performance of several key indicators of cycle performance. Dai et al [52] found that for many Organic Fluids operating at their optimum pressure, by increasing the turbine inlet temperature actually reduced the heat source utilisation of the cycle.

2.6.5 Superheat at Expander Inlet

The superheat at the expander inlet is determined by the evaporator pressure and the maximum cycle temperature, itself a weak function of heat source temperature. Increasing the superheat can increase the utilisation of a given thermal source, but reduce the first law efficiency of a cycle [7]. It also increases the irreversibility in the evaporator [93].

Saleh et al [48] found that increasing the superheat of a cycle (by changing the working fluid) caused a small increase in efficiency. However, this increase could be improved if a regenerator was used to recover the increased thermal energy in the working fluid at the expander outlet which is introduced by the increase in superheat.

2.6.6 Expansion Device Considerations

The cycle operating conditions are in some cases constrained by the choice of expansion device.

For turbines, parameters such as tip speed, rotational speed, specific speed and maximum Mach number all determine the operational viability of the device [132]. High tip speed increases the stage specific work of a turbine, but also increases the stress on the materials from which the turbine is constructed. The optimum rotational speed depends on the bearing capacity and deviations from this optimum speed will result in reductions in isentropic efficiency. If the Mach number becomes greater than about 0.85, it can result in local choking of the flow as it passes through the turbine, also reducing its isentropic efficiency. This limitation in Mach

number constrains the maximum pressure ratio with which the turbine can deal. These limitations can result in the actual optimum cycle operating point differing from the theoretical thermodynamic optimum.

Positive displacement expanders are limited by their internal geometry, specifically their in-built volume ratio and swept volume [132]. The maximum in-built volume ratio is generally smaller than 5, due to greater volume ratios placing larger stress on the components. To obtain greater volume ratios, it is possible to string multiple expanders together in series. However, this does result in greater capital cost to the system and will suffer from diminishing returns.

2.6.7 Regenerative Cycles

Many cycles use a regenerator, or internal heat exchanger to increase first law efficiency by reducing evaporator heat demand relative to expander power [88] [52] [133].

When the working fluid exits the expander, particularly when the working fluid is dry or isentropic, such as n-perfluoropentane, it may still have some degree of superheat [48]. This superheat must be removed in the condenser before returning the working fluid to the pump inlet. In a basic, non-regenerative or non-cogenerating ORC, this energy is simply lost to the system.

The Regenerator is a heat exchanger that uses this superheat to preheat the working fluid between the pump outlet and the evaporator. By doing so, it reduces the heat demand in the evaporator without having any effect on the power of the expander. This increases the efficiency of the cycle, at the cost of increased complexity, and increased pressure drop. The way in which the regenerative section fits into the larger cycle is shown in a T-s diagram in Figure 2.10, and a T-h diagram of the fluid streams inside the heat exchanger for another case is shown in Figure 2.11.

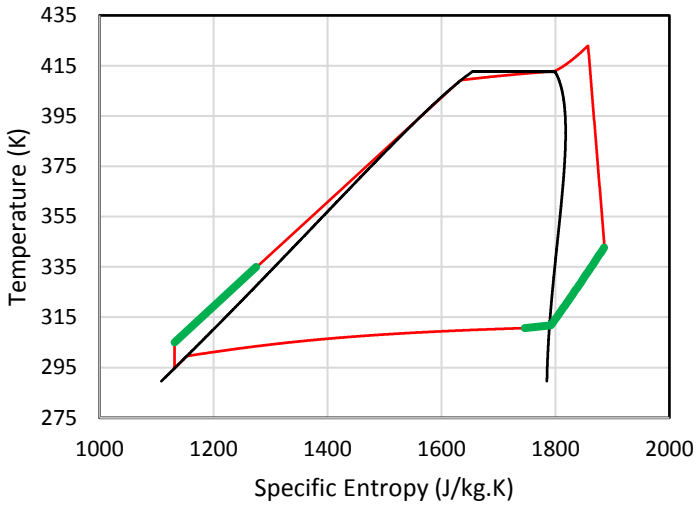

Figure 2.10: T-s diagram of a regenerative Organic Rankine Cycle using a zeotropic working fluid. The portions of the cycle that occur in the regenerator are highlighted as thicker green lines.

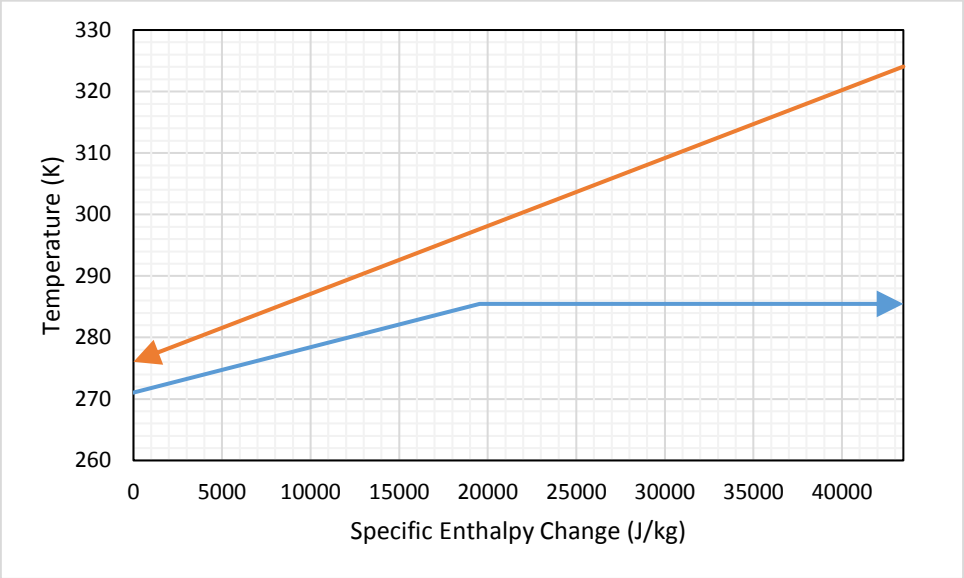

Figure 2.11: T-h diagram of the hot and cold fluid streams inside a regenerator. In this case, there is a phase change on the cold side, and the pinch point occurs at the cold side inlet, although this is not always the case.

Cayer et al [6] [134] found that when the total heat exchanger area is used as the objective function, a regenerator does not improve the performance of the cycle, as the net increase in heat exchanger area outweighs the increase in First Law Efficiency. Mago et al [135] observed an increase in first law efficiency, second law efficiency, and heat source utilisation with the

addition of a regenerator. Baik et al [61] report that a regenerator can increase the first law efficiency of a cycle, but does not generally produce any improvement in the heat source utilisation. This result was also shown analytically by Bianchi and de Pascale [39] and Dai et al [52]. This occurs because the heat source utilisation depends on the power output of the expander, and the temperature drop of the thermal fluid from the heat source. A regenerator will not affect the expander power at all, and the effect on the heat source temperature drop will most likely be zero except in the case where the energy transferred in the regenerator is enough to cause a phase change in the working fluid on the cold side. This is only the case for extremely dry working fluids, or cycles running with a very large degree of superheat at the expander outlet. This specific instance was noted by Heberle et al [88] for a cycle using R227ea at heat source temperatures above 120°C. The overall effect is to move the pinch point to the right on the T-Δh diagram, allowing a greater slope of the thermal fluid line. This effect can be seen in Figure 2.12 on the following page. The top figure shows a cycle in which the regenerator does not cause a phase change. The pinch point is located at the bubble point of the fluid, so changing the enthalpy transfer in the regenerator will change the outlet temperature of the thermal fluid without changing the slope of the grey line, which depends on the flow rate of the thermal fluid. The bottom figure shows a cycle in which the regenerator does cause a phase change. In this case, the pinch point has moved to the regenerator outlet/evaporator inlet. The slope of the grey line now depends on the enthalpy at the regenerator outlet.

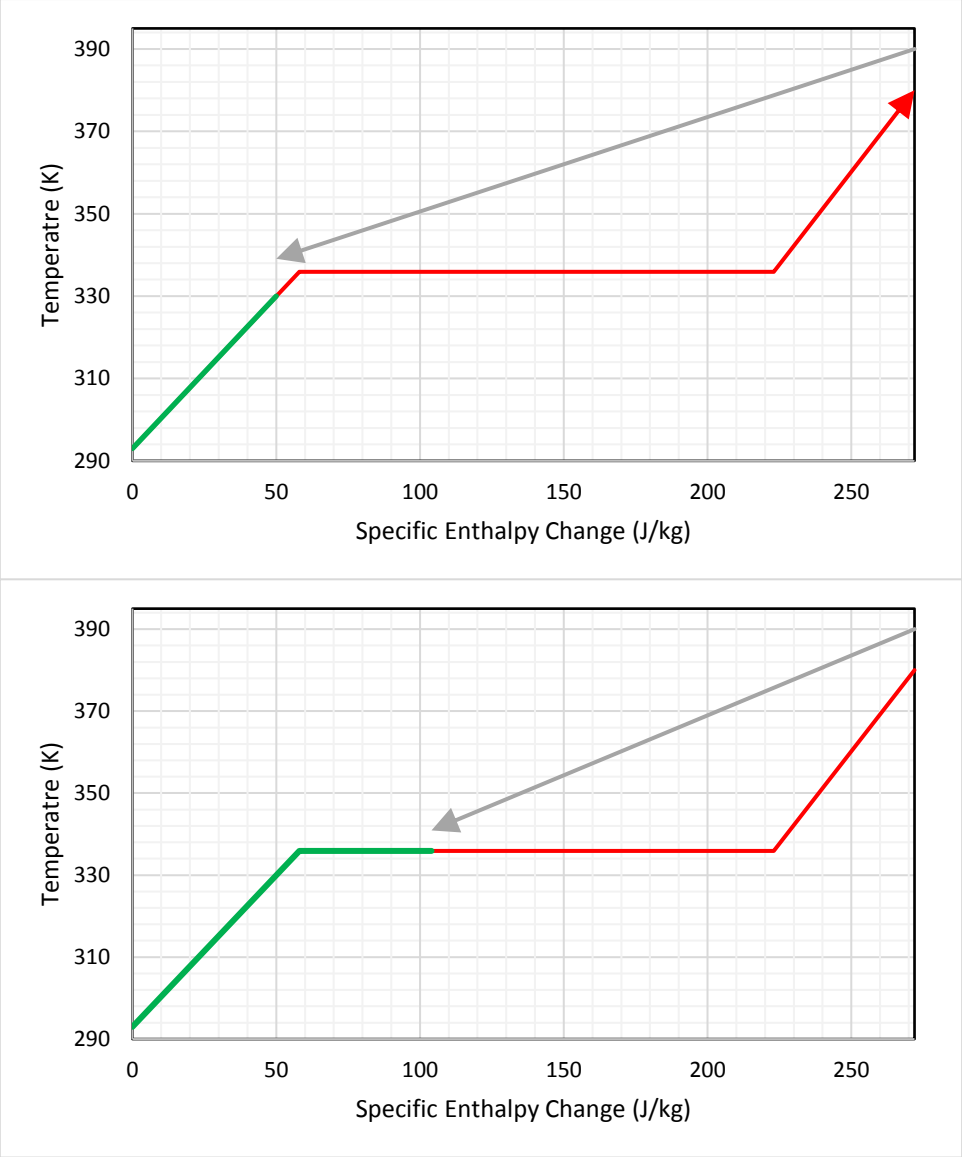

Figure 2.12: Comparison of the pinch point diagrams for a regenerator that does not cause a phase change (top) and one that does cause a phase change (bottom)

The implication of these results is that the value of a regenerator to an Organic Rankine Cycle is determined by the particular application and which objective function is being used. For a "free" heat source such as waste heat from industry or bottoming cycles, heat source utilisation is highly valued, more so than the first law efficiency of the cycle, as any heat carried away in the thermal fluid stream is lost to the system. For cycles such as geothermal or solar thermal, heat source utilisation is not quite so important, as even if the majority of the available energy contained in the working fluid is not used by the cycle, this will merely result in higher return temperatures to the geothermal source or the solar collector, which reduces necessary heat exchanger area compared to a cycle that makes more full use of the heat source.

2.7 Previous Experimental Research

There exists a substantial body of experimental research on the Organic Rankine Cycle. However, there are a number of key research areas that have not been fully explored in previous literature. In this section the latest trends in experimental research on the ORC will be reviewed, and the current knowledge gaps identified. A summary of the research is presented in Table 2-1.

Peris et al [136] analysed a commercial ORC module for CHP applications, focusing on the first law efficiency obtainable, calculated from the electrical output and thermal input, achieving a maximum net electrical efficiency of 8.8%, and a maximum isentropic efficiency for the expander of 65%, increasing with higher pressure ratios. Wang et al [137] designed and constructed a low-temperature solar ORC system using r245fa as the working fluid, using a rolling-piston expander with an average isentropic efficiency of 45.2%, achieving a maximum electrical efficiency of 4.2%. Pu et al [138] performed a study on a small-scale ORC system using pure r245fa and pure HFE7100 as the working fluids and a micro-turbine with an isentropic efficiency of 60% as the expander, generating a maximum of 1979W, achieving a maximum efficiency of 4.01%. Yun et al [139] built an experimental ORC system with two parallel scroll expanders, exhibiting a maximum isentropic efficiency of 62%. This cycle achieved a maximum first law efficiency of 7.5%. Quoilin et al [140] built an experimental rig with a scroll expander using R123 as the working fluid, achieving a maximum cycle efficiency of 9.9% and a maximum expander isentropic efficiency of 67.5%. Navarro-Esbrí et al [141] achieved a maximum first-law efficiency of 8.3% using a scroll expander, and the low-GWP working fluid HFO-1336mzz-Z. Eyerer et al [142] performed experiments on an experimental rig using the low-GWP fluid R1233zd-E, and a scroll expander with a maximum isentropic efficiency of 64%, achieving a maximum efficiency of 4.98%. Muhammad et al [143] performed research on a 1kW experimental rig using r245fa as the working fluid and a scroll expander with a maximum isentropic efficiency of 77%, achieving a maximum thermal efficiency of 5.75%. Li et al [144] constructed a 6kWe electrical rig using R123 as the working fluid, comparing the regenerative and non-regenerative configurations of the cycle, achieving a maximum efficiency of 7.98%, 1.6% higher than that of the non-regenerative cycle. Jung et al [145] tested a zeotropic mixture of R245fa and 365mfc and achieved a maximum thermal efficiency of 3.1%. Abadi et al [146] constructed a 1kW ORC rig using both pure R245fa and a zeotropic mixture of [60% R245fa:40% R134a], obtaining a maximum first law efficiency of

7%, while reporting that the zeotropic mixture improved heat source utilisation, while decreasing output power and cycle efficiency.

Table 2-1: Comparison of experimental Organic Rankine Cycles reported in the literature

Author	Working Fluid	Configuration	Heat Source Temp	Expander	Power	Efficiency
Peris et al [136]	R245fa	Regenerative	165°C	Scroll	7.5 kWe	8.8%
Wang et al [137]	R245fa	Non-Regenerative	115°C	Rolling Piston	1.73kWe	4.2%
Pu et al [138]	Pure R245fa/ Pure HFE7100	Non-Regenerative	100°C	Micro-turbine	1.979kWe	4.01%
Yun et al [139]	R245fa	Non-Regenerative	120°C	Scroll	3.5kWe	7.5%
Quoilin et al [140]	R123	Non-Regenerative	165°C	Scroll	1.8kW	9.9%
Navarro-Esbrí et al [141]	HFO-1336mzz-Z	Regenerative	160°C	Scroll	1.1kWe	8.3%
Eyerer et al [142]	R1233zdE	Non-regenerative	130°C	Scroll	0.4kWe	4.98%
Muhammad et al [143]	R245fa	Non-regenerative	135°C	Scroll	1.01kWe	5.75%
Li et al [144]	R123	Regenerative	130°C	Turbine	6kW	7.98%
Jung et al [145]	R245fa/ 365mfc	Non-regenerative	160°C	Scroll	0.47kWe	3.1%
Abadi et al [146]	R245fa/R134a	Non-regenerative	120°C	Scroll	1.4kWe	7%

From this information it is clear that although there is a body of research on the Organic Rankine Cycle, it is principally concerned with pure working fluids and non-regenerative

cycles. A survey of the literature revealed that there does not appear to be any previous experimental research comparing the regenerative and non-regenerative cycles in the same system, and although a number of authors have investigated zeotropic working fluids there were no systematic studies investigating how the performance of the cycle progressively changes across a range of working fluid compositions.

2.8 Summary

In this section, the current body of literature with regard to Organic Rankine Cycles has been summarised. The key areas focused on today are the optimisation of the cycle parameters, the working fluid and the expansion devices. There is a general lack of practical research into the performance of the ORC and in particular into the performance of the ORC with zeotropic working fluid mixtures. This justifies one of the primary goals of this thesis; to design, build and test a practical lab-scale ORC rig capable of varying its working fluid composition, heat source temperature, operating pressures and cycle configuration.

Also little analysed is the problem of Organic Rankine Cycles under varying conditions of heat sinks. ORCs operating under variable heat sources or at off-design conditions, such as bottoming cycles, have been presented in the literature previously, but the effect of a varying heat sink temperature on the cycle has so far only really been analysed for the case of heat pumps. Therefore, the research in this thesis into the effect of changing heat sink temperature, and the potential solution in the form of the Dynamic ORC, also makes a novel contribution to the body of literature.

CHAPTER 3- THEORY AND MODELLING OF ORC POWER PLANTS

In this section, the theory and mathematics behind ORC power plants as used in this thesis will be discussed. The relevant equations will be presented, as well as some typical values for the primary parameters of the cycle encountered in the literature. Firstly the thermodynamic parameters of the cycle are laid out, followed by the equations for heat transfer in the heat exchangers, and finally the equations used to size and estimate the power requirements for a distillation system to change working fluid composition. It also presents some equations for specific parameters developed for this thesis, as well as the rationale for their development. Leading on from this the MATLAB models used in the generation of results are detailed.

3.1 Thermodynamics

3.1.1 First Law Efficiency

Also commonly termed Thermal Efficiency, this is the simplest analysis of the cycle, and is used in a wide range of sources [92] [21] [7]:

$$\eta_{cycle} = \left(\frac{W_{expander} - W_{pump}}{Q_{evaporator}}\right) \tag{3.1}$$

It is simply the useful net work done by the cycle, divided by the heat energy required by the evaporator to achieve that work. It does not take into account the amount of energy contained in the heat source and how effectively the cycle utilises it , the theoretical Carnot efficiency of the cycle, or the economic implications of achieving this efficiency, so can therefore be rather limited as a tool for in-depth thermodynamic analysis of an ORC system [92]. However, it is intuitive, and useful for comparing similar systems, so therefore is widely used.

For Organic Rankine Cycles, the first law efficiency is typically in the range of 6% to 13%, depending on the heat source temperature and the particular applications of the cycle. Cayer et al [6] achieved a maximum first law efficiency of 8.8% with a Transcritical CO2 cycle. Dai et al [52] performed a parametric optimisation of an Organic Rankine Cycle for a heat source temperature of 145°C. The first law efficiency of the cycles varied from 11.5% to 13%. Iglesias Garcia et al [147] compared various cycles using a heat source temperature of around 60°C, with a theoretical first law efficiency of 8%. Zeyghami [148] analysed various working fluids across a range of heat source temperatures. For a heat source temperature of 150°C, first law efficiencies were between 7.7% and 8%. For a heat source temperature of 200°C, first law efficiencies were between 11.9% and 12%, and for a heat source temperature of 200°C the first law efficiencies were between 14.6% and 15.3%.

The first law efficiency of a cycle is most useful for analysis in applications where the heat source is very large in comparison to the required power demand, i.e. an undersized power conversion system. A cycle optimised for first law efficiency will not make the most effective use of a limited heat source, but when the heat source is not the limiting factor a cycle with a high first law efficiency will generally have smaller component sizes and therefore a lower capital cost than a system optimised along other lines.

This work expands on the principle of first law efficiency to introduce a new parameter, the "effective first law efficiency", given by:

$$\eta_{effective} = \left(\frac{W_{expander} - W_{pump} - Q_{ancillaries}}{Q_{evaporator}}\right) \quad (3.2)$$

This uses a similar formula to that for first law efficiency, but with the net power adjusted to take into account ancillaries to the cycle. These ancillaries can include such things as circulation pumps or fans for thermal fluid and coolant, but in the context of this thesis, it is primarily used to determine the energy used for distillation of the working fluid in a dynamic ORC. It should be noted that the energy required for distillation is not necessarily parasitic power. This will depend on the particular heat source used. If it is waste heat from industry, biomass or a bottoming cycle, the energy contained in the thermal fluid will be rejected to the environment after passing through the hot side of the evaporator, and will be lost to the system. Therefore it could be used to power the distillation process with no loss to the system. For cycles such as solar and geothermal, where the thermal fluid is often recirculated, the energy used for distillation will manifest itself as a drop in the feed temperature to the heat source, requiring more energy to reheat and therefore representing a parasitic loss to the system. The same applies if the waste heat from the system is to be used as part of a combined heat and power scheme.

3.1.2 Second Law/Exergy Efficiency

The concept of exergy is based on the idea that certain types of energy are more thermally useful than others. For example, even if a large amount of thermal energy is available in a given heat source, if it is at low temperature, the Carnot efficiency of any thermal cycle utilising it will be relatively lower than one using a higher, but smaller heat source temperature.

Exergetic Efficiency takes this into account by considering the "quality" of the heat source. Higher temperature, lower entropy heat sources have more exergy than lower temperature, higher entropy ones.

In any real thermal process, exergy, unlike energy, is destroyed due to the second law of thermodynamics. For example, in transferring heat from a hot fluid to a cold fluid in a heat exchanger, the temperature mismatch between the hot and cold sides means that the cold fluid will always have a lower quality of heat than the hot one at the end of the process [6]. This can be minimised, if not entirely eliminated, by better thermal matching of the fluids within the heat exchanger. In expanders, heat loss due to imperfect insulation, mechanical inefficiencies, and thermal and fluid leakage cause the actual power produced by the system to be less than that lost by the working fluid as it passes through [149] [150].

Several competing definitions of Exergy Efficiency exist. Subbiah et al [21] defined it simply as the net output work of the cycle, divided by the amount of energy available to the cycle in the thermal fluid

$$\eta_{exergy} = \left(\frac{\dot{m_{ORC}}(W_{expander} - W_{pump})}{\dot{m}_{thermal\ fluid}(\Delta h_{thermal\ fluid}) - T_0(\Delta s_{thermal\ fluid})}\right) \tag{3.3}$$

Dai et al [52] performed a more in-depth approach, defining the exergy at a given state point as:

$$E_i = \dot{m}\big((h_1 - h_0) - T_0(s_1 - s_0)\big) \tag{3.4}$$

Where T_0 is the temperature of the dead state. Knowing the exergy at every state point of the cycle allows the destruction in each component to be evaluated, by comparing the exergy before and after the working fluid passes through it. This allows the components responsible for the most exergy destruction to be specifically identified.

They then define the exergy efficiency of the cycle as:

$$\eta_{exergy} = \frac{E_{in} - \Delta I - E_{out}}{E_{in}} \tag{3.5}$$

Using this definition, they calculated exergy efficiencies for a heat source temperature of 145°C ranging from 29% to 35.4%.

Heberle et al [90] defined the Irreversibility of each component in the cycle as:

$$\dot{I} = \dot{m}T_0\left[(s_b - s_a) - \frac{h_b - h_a}{T_{min,component}}\right] \tag{3.6}$$

For the heat exchangers, where $\dot{m}$ is the mass flow rate of the working fluid, the subscripts b and a represent the inlet and outlet of the component, respectively, and $T_{min,component}$ represents the minimum temperature of the component, and, for the Pump and Expander.

:

$$\dot{I} = \dot{m}T_0[(s_b - s_a)] \tag{3.7}$$

Most sources performing an exergy analysis of the ORC have found that the majority of exergy destruction occurs in the evaporator [7] [52]. Typical exergy efficiencies are higher than first law efficiencies. Cayer et al [6] achieved a maximum exergetic efficiency of 60.5% with a Transcritical CO_2 cycle. Zeyghami [148] reported an exergetic efficiency varying from 46.4% for a heat source temperature of 150°C, increasing to 58.3% for a heat source temperature of 250°C, the rise being attributed to better thermal matching inside the evaporator. Seyedkavoosi et al [151] performed an exergy-based optimisation of a bottoming ORC, obtaining a maximum theoretical exergy efficiency of 45% for a heat source temperature of 470°C.

3.1.3 Heat Source Utilisation and Specific Power

Several linked concepts describe the ability of an Organic Rankine Cycle to utilise the heat source available to it.

Cayer et al [6] named it "Specific Net Output", and noted that for "free" heat sources, such as waste heat, it was more important to maximise this parameter than the First Law and Second Law efficiencies of the cycle. They recommend achieving this by reducing the evaporator pressure, lowering the temperature at the pinch point and allowing more of the energy of the thermal fluid to be transferred to the working fluid. They did, however, find that increasing this parameter also results in increasing heat exchanger area, increasing the capital cost of the system.

Liu et al [79] defined the "Total Heat Recovery Efficiency" quantity mathematically as:

$$\eta_T = \frac{W_{net}}{\Delta H_{thermal\ fluid}} \tag{3.8}$$

This does take into account more than just the first law efficiency of the cycle, also allowing for the efficiency of the heat transfer process in the evaporator, but does not account for the fact that much thermal energy may still be rejected with the thermal fluid, and therefore it does not give a full picture of the heat source utilisation.

A similar concept, the cycle power output for a given, fixed heat source, was used by Chen et al [92] to compare transcritical and subcritical ORCs.

Dai et al [52] used the concept of Specific Net Power to examine how well a cycle utilises its heat source. This is expressed as:

$$\dot{W}_{specific} = \frac{W_{net}}{\dot{m}_{thermal\ fluid}} \tag{3.9}$$

They found that this was affected greatly by the choice of working fluid, even if the first law efficiency did not show any particularly large variations over their considered range. The greatest thermal fluid utilisation recorded was for R236ea.

This definition of thermal fluid utilisation is highly dependent on the exact parameters of the heat source. For geothermal fluids, the pressure and salinity of the fluid will affect the shape of its curve, and there is the possibility it will condense or even freeze depending on its initial temperature and the temperature of the coolant. For solar energy, the thermal fluids tend to include things like nitrate salts. Waste heat can take several forms, such as liquid water for cooler sources like machinery coolant or hot gases for hotter sources like engine exhaust. Both of these things will greatly affect the flow rate of the thermal fluid and the position of the pinch point. To ensure an even comparison of different cycles, the MATLAB model assumed that the heat source was water, pressurised to ensure it did not undergo a phase change.

A cycle optimised for specific power will make better use of a heat source that is limited, or that costs money to generate, although optimising specific power can be mutually exclusive to optimising first law efficiency with respect to several parameters, for example, evaporator pressure, and therefore a cycle optimised for maximum specific power may have a higher capital cost than if it was optimised for first law efficiency.

3.2 Heat Exchangers

3.2.1 Thermal Balance Model

It is generally assumed in thermodynamic analysis of heat exchangers that there is no heat loss from heat exchangers to the environment, therefore all of the thermal energy lost by the fluid on the hot side is assumed to be absorbed by the cold side. With the thermal fluid on the hot side assumed to be pressurised water with no phase change, this gives the equation:

$$\dot{m}_{cycle}(h_{out} - h_{in}) = \dot{m}_{tf} c_{p,tf}\left(T_{tf\ in} - T_{tf\ out}\right) \tag{3.10}$$

Where the subscript "*tf*" refers to the thermal fluid. In general, the state points in the cycle, along with the thermophysical properties and inlet temperature of the thermal fluid will already be known, leaving the outlet temperature and mass flow rate of the thermal fluid to be calculated using this equation.

3.2.2 Pinch Point Model

In order to calculate the mass flow rate on the hot side of the heat exchanger and therefore the thermal fluid outlet temperature, a pinch point model is used.

Some simple analysis of evaporators assume that there is no temperature drop in the thermal fluid as it passes through the hot side of the evaporator [7], treating the heat source as isothermal. However, this is rarely true [79], and for the modelling carried out for this thesis, a more in-depth approach was taken, analysing the temperature drop in the thermal fluid and using a pinch point limitation to set a minimum flow rate for it.

Pinch point analysis centres on the fact that heat will always flow from a hot reservoir or fluid stream to a colder one. Therefore, in a heat exchanger, the hot stream must at all points be warmer than the cold stream. As outlined in the previous section, it is assumed that there is no heat loss from the system and that all energy lost by the hot fluid is absorbed by the cold fluid. When two flows of this type are plotted on a T-Q diagram, as in Figure 3.1, it can be seen that the temperature differential between the two streams varies along the length of the heat exchanger. The closest point, i.e. the location along the heat exchanger with the smallest gap between hot and cold streams, is known as the Pinch Point. The wider the pinch point temperature difference, the smaller the required heat exchanger area, but also the lower the average temperature of heat addition to the cycle and the higher the average temperature of heat rejection, which will reduce its Carnot efficiency [48]. The optimum pinch point temperature difference is something that depends heavily on the particular parameters being optimised for a given ORC.

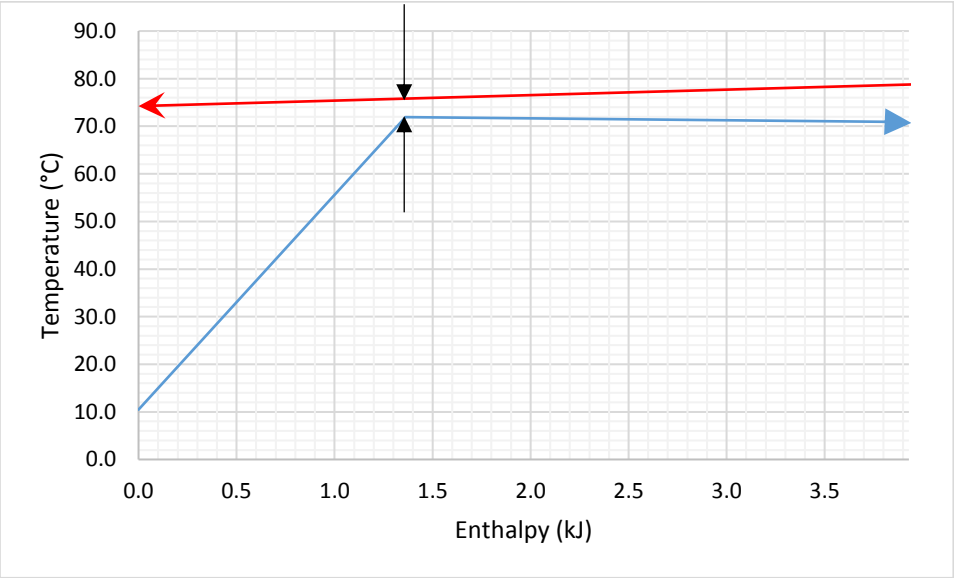

Figure 3.1: Sample T-H diagram for an evaporator with the pinch point marked

Baik et al [62] used a pinch point temperature difference of 10°C for high temperature applications, although they mention that this can drop to 3°C for lower temperature applications, referencing several sources [6] [134]. Subbiah and Natarajan [21] analysed a subcritical ORC under a range of conditions. They found that reducing the pinch point temperature difference had only a small effect on the efficiency and work output of the cycle, but did have a large effect on the heat exchanger area and therefore the overall system cost. The output work of the cycle per kg of geothermal fluid was increased from 9 kJ/kg to 11kJ/kg as the pinch point temperature was reduced from 10°C to 4°C. Chen et al [84] used a pinch point temperature difference of 10°C for their evaporator and condenser, and a pinch point temperature difference of 5°C for their regenerator. Dai et al [52] used a pinch point temperature difference of 8°C. Heberle et al [88] used a pinch point temperature difference of 5°C for all heat exchangers. Zhang et al [69] varied the pinch point temperature difference between 5°C and 25°C. Liu et al [17] investigated various pinch point temperatures from 2°C to 21°C.

Regardless of the pinch point temperature difference used in the cycle, the process for calculating the mass flow rate and temperature difference in the thermal fluid uses the same equations.

For evaporators the temperature of the thermal fluid at the pinch point is calculated using the equation:

$$T_{tf,\ pinch\ point} = T_{wf4} + \Delta T_{pinch\ point} \tag{3.11}$$

Where T_{wf4} is the bubble point temperature of the working fluid.

The change in enthalpy up to this point can be calculated by multiplying the change in specific enthalpy by the mass flow rate.

$$H_x = \dot{m}(h_x - h_3) \tag{3.12}$$

Where the subscript x denotes a given point along the heat exchanger, and h_3 is the specific enthalpy of the working fluid at the inlet of the cold side of the heat exchanger.

Knowing the enthalpy change between two given points allows the mass flow rate of the thermal fluid to be calculated using the equation:

$$\dot{m}_{tf} = \frac{H_6 - H_4}{C_{p,tf} * (T_{tf6} - T_{tf4})} \tag{3.13}$$

Where the subscript *4* refers to the bubble point of the working fluid, and the subscript 6 refers to the exit of the working fluid from the heat exchanger.

For a condenser, the process is similar, according to the following equations:

$$T_{tf,\ pinch\ point} = T_{wf9} - \Delta T_{pinch\ point} \tag{3.14}$$

$$H_x = \dot{m}(h_x - h_1) \tag{3.15}$$

And

$$\dot{m}_{tf} = \frac{H_8 - H_9}{C_{p,tf}(T_{tf8} - T_{tf9})} \tag{3.16}$$

Regenerators are a special case of heat exchanger in this analysis, as they can have a phase change on either the hot side, cold side, or neither side of the heat exchanger. In this thesis, a solution for the regenerator was obtained numerically rather than analytically.

3.3 Heat Transfer

The process of heat exchange in the evaporator, condenser and regenerator of Organic Rankine Cycles has been an object of research for many papers.

The actual heat transfer in the heat exchangers is a complicated process, strongly dependent on local flow characteristics, heat exchanger geometry and fluid properties. A comprehensive analysis of the heat transfer would require a full CFD analysis, which is computationally expensive and does not lend itself well to iterative processes such as cycle optimisation. Instead, the heat transfer process is usually analysed using predetermined semi-empirical correlations. Each correlation has a certain range of validity, outside of which its accuracy is not guaranteed.

Most correlations are of the form:

$$Nu = c_1 Re^{c_2} Pr^{c_3} \left(\frac{\mu_m}{\mu_w}\right)^{c_4} \tag{3.17}$$

Where *Nu* is the Nusselt number, or the ratio of the convective to conductive heat transfer coefficients, given by:

$$Nu = \frac{\alpha D_h}{k} \tag{3.18}$$

Where α is the overall heat transfer coefficient of the fully-developed flow, D_h is the characteristic length, in this case the hydraulic diameter, and k is the thermal conductivity of the liquid phase.

μ_m is the dynamic viscosity in the bulk flow, and μ_w is the dynamic viscosity at the wall. *Re* is the Reynolds number, or the ratio of inertial to viscous forces in the fluid flow, given by:

$$Re = \frac{\rho u D_h}{\mu} \tag{3.19}$$

Where ρ is the density of the fluid, u is the velocity of the fluid, μ is the dynamic viscosity of the fluid, and D_h is the characteristic diameter in the region of analysis, generally plate separation or pipe diameter in the case of heat exchangers.

Pr is the Prandtl number is the ratio of viscous diffusion to thermal diffusion. It is given by:

$$Pr = \frac{c_p \mu}{k} \tag{3.20}$$

Where c_p is the specific heat of the fluid, μ is the dynamic viscosity of the fluid and k is thermal conductivity of the fluid.

Once the Nusselt number for each side of the heat exchanger at a given location is known, the overall heat transfer coefficient U can be calculated according to the equation:

$$\frac{1}{U} = \frac{1}{\alpha_{cold}} + \frac{t}{k} + \frac{1}{\alpha_{hot}} \tag{3.21}$$

Where the subscripts cold and hot denote the hot and cold streams in the heat exchanger, t is the thickness of the heat exchanger wall, and k is the conductivity of the wall material, taken as 400 W/m.k for copper.

Dovíc et al [152] developed a correlation for the heat transfer coefficients in chevron plate heat exchangers, valid for chevron angles from 28° to 65° and Reynolds Numbers from 2-10,000.

García-Cascales et al [153] compared and assessed a number of different correlations for heat transfer coefficients applied to both evaporation and condensation. They also highlight that different correlations might have different performances for different stages of the heat exchanger, that is to say, a correlation that produces a good correlation for the preheating stage may not provide a satisfactory correlation for the two-phase or superheating stage of the heat exchanger.

For evaporation, they looked at the following correlations:

The Chisholm and Wanniarachchi correlation [154], which has an experimentally-verified accuracy of 15-20% for Reynolds Numbers above 1000 and a chevron angle between 30° and 120°. It is given by:

$$Nu = 0.724\left(\frac{6\pi}{\beta}\right)^{0.646} Re^{0.583} Pr^{\frac{1}{3}} \tag{3.22}$$

Where β is the chevron angle of the corrugated plates in radians.

The Kim correlation [155] is given by:

$$Nu = 0.295 Re^{0.64} Pr^{0.32}\left(\frac{\pi}{2} - \beta\right)^{0.09} \tag{3.23}$$

The Wanniarachchi correlation [156] is claimed by the authors to produce a satisfactory solution in all three flow regions of a plate heat exchanger, and is given by:

$$Nu = j_{Nu} Pr^{\frac{1}{3}}\left(\frac{\mu_m}{\mu_w}\right)^{0.17} \tag{3.24}$$

Where j_{Nu} is an asymptotic function of the Reynolds number.

The Bogaert and Bölcs correlation [157] is given by:

$$Nu = B_1 Re^{B_2} Pr^{\frac{1}{3}} e^{\left(\frac{6.4}{Pr+30}\right)}\left(\frac{\mu_m}{\mu_w}\right)^{\frac{0.3}{(Re+6)^{0.123}}} \tag{3.25}$$

Where B_1 and B_2 are constants that depend on the Reynolds number.

These equations serve to demonstrate that, for Plate Heat Exchangers, the range of possible correlations is extremely large, and many of the correlations depend on very specific conditions of geometry, working fluid and flow, many of which many be unknown during preliminary thermodynamic analysis of ORC systems.

3.3.1 Correlations for single-phase flow

García-Cascales et al's results [153] suggest that the most satisfactory correlations for heat transfer coefficient are, for single-phase flow, the Kim correlation, given by:

$$Nu = 0.295 Re^{0.64} Pr^{0.32}\left(\frac{\pi}{2} - \beta\right)^{0.09} \tag{3.26}$$

3.3.2 Correlations for Boiling

For boiling, the Yan-Lin correlation [158], given by:

$$Nu = 1.926 Pr_f^{\frac{1}{3}} Bo_{eq}^{-0.3} Re_{eq}^{0.5} \left[(1 - x) + \left(\frac{\rho_f}{\rho_g} \right)^{0.5} \right] \quad (3.27)$$

Where the subscript f represents the saturated liquid and the subscript g represents the saturated vapour phase. Bo_{eq} is the equivalent Boiling Number, given by:

$$Bo_{eq} = \frac{q''_w}{G_{eq} h_{fg}} \quad (3.28)$$

And Re_{eq} is the equivalent Reynolds Number, given by:

$$Re_{eq} = \frac{G_{eq} D_h}{\mu_f} \quad (3.29)$$

Where q''_w is the heat flux at the wall, h_{fg} is the enthalpy of vaporisation, D_h is the hydraulic diameter and μ_f is the dynamic viscosity of the fluid at the wall. G_{eq} is an equivalent mass flux, and is given by:

$$G_{eq} = G \left[1 - x + x \left(\frac{\rho_f}{\rho_g} \right)^{0.5} \right] \quad (3.30)$$

Where G is the mass velocity in kg/s m^2 and x is the vapour fraction of the working fluid. As this correlation contains the Boiling Number, which requires the heat flux at the wall as an input, it requires an iterative solution to calculate. The Yan-Lin correlation is experimentally verified for a Reynolds Number from 2000-10000.

An alternative correlation, one that does not include the boiling number and is therefore is less computationally demanding is that proposed by Klimenko [159] [160]:

$$Nu = 0.087 (Re_m)^{0.6} Pr_l^{\frac{1}{6}} \left(\frac{\rho_v}{\rho_l} \right)^{0.2} \left(\frac{\lambda_w}{\lambda_l} \right)^{0.09} \quad (3.31)$$

Where the subscript l denotes saturated liquid, the subscript v denotes saturated vapour, the subscript w denotes the wall. Re_m is the Reynolds number of the mixture, given in this case by:

$$Re_m = \frac{w_m b}{\nu_l} \quad (3.32)$$

Where ν_l is the kinematic viscosity of the saturated liquid phase.

w_m is the two-phase mixture velocity, given by:

$$w_m = \frac{\dot{m}}{\rho_l} \left(1 + x \left(\frac{\rho_l}{\rho_v} - 1 \right) \right) \quad (3.33)$$

Where $\dot{m}$ is the total mass flow rate.

b is the Laplace Constant, given by:

$$b = \sqrt{\frac{\sigma}{g(\rho_l - \rho_v)}} \tag{3.34}$$

Where σ is the surface tension of the liquid phase and g is acceleration due to gravity.

This method has been shown to produce values for the Nusselt number comparable to other correlations requiring iterative solutions [161].

3.3.3 Correlations for Condensation

The best correlation for condensation heat transfer coefficient is given by the Kuo, Lie, Hsieh and Lin Correlation [162] [163].

$$\alpha_{tp} = \alpha_f \left[0.25 Co^{-0.45} Fr_f^{0.25} + (75 Bo^{0.75})\right] \tag{3.35}$$

Where α_f is the heat transfer coefficient for the liquid phase and is given by:

$$\alpha_f = 0.2092 \left(\frac{\lambda_f}{D_h}\right) Re_f^{0.78} Pr_f^{\frac{1}{3}} \left(\frac{\eta_{fm}}{\eta_{fw}}\right)^{0.14} \tag{3.36}$$

In which λ_f is the thermal conductivity of the liquid phase, D_h is the hydraulic diameter, η_{fm} is the dynamic viscosity of the liquid phase in the bulk of the fluid, and η_{fw} is the dynamic viscosity of the liquid phase close to the wall.

Co is the convection number and is given by:

$$Co = \left(\frac{\rho_g}{\rho_f}\right) \left(\frac{(1-x)}{x}\right) \tag{3.37}$$

Fr_f is the Froude number of the liquid phase and is given by:

$$Fr_f = \frac{G^2}{\rho_f^2 g D_h} \tag{3.38}$$

An alternative version that does not include the Boiling Number, and therefore can be calculated without the need for an iterative solution, while still producing an acceptable solution, is the Han, Lee and Kim correlation [164]. This is given by:

$$Nu = Ge_1 Re_{eq}^{Ge_2} Pr^{1/3} \tag{3.39}$$

Where Ge_1 and Ge_2 are geometric coefficients given by:

$$Ge_1 = 11.22\left(\frac{p_{co}}{D_h}\right)^{-2.83}\left(\frac{\pi}{2}-\beta\right)^{-4.5} \quad (3.40)$$

$$Ge_2 = 0.35\left(\frac{p_{co}}{D_h}\right)^{0.23}\left(\frac{\pi}{2}-\beta\right)^{1.48} \quad (3.41)$$

Where p_{co} is the pitch of the heat exchanger.

3.3.4 Geometric properties of heat exchangers

Dovíc et al [152] provided a common range of values for the geometric properties of plate heat exchangers, which are presented in Table 3-1, and are of the same order as the values provided by Imran et al [165].

Property	**Minimum Value**	**Maximum Value**	**Nominal Value**
Pitch Angle β (°)	15°	60°	45°
Corrugation depth b (mm)	2mm	2mm	2mm
Corrugation pitch p_{co} (mm)	4mm	8mm	6mm
Hydraulic Diameter (mm)	3.2mm	7mm	3.6mm
Plate Thickness (mm)	0.8mm	1.2mm	1mm

Table 3-1: Typical geometric parameters for plate heat exchangers

The width of the heat exchanger was calculated using the flow velocity. When designing a heat exchanger, the flow velocity is a highly controllable parameter, a lower flow velocity can be achieved by the addition of greater flow width, either by including more heat exchangers in parallel, or by increasing the number of plates, and therefore channels, per heat exchanger. The flow velocity for the liquid phase used to calculate this was taken to be 0.6m/s, as an average of the typical values given in [166] and verified with [167]. Determining the heat exchanger width in this way allowed the calculation to be valid over a wide range of powers, as ultimately the acceptable pressure drops and heat transfer coefficients are determined by the velocity of the fluid and the turbulence that this causes, so velocities are more constant across a range of heat loadings than heat exchanger widths are.

3.4 Pressure Losses

The pressure drops in heat exchangers and pipework are commonly assumed to be negligible in cycle analysis [62] [88] [70] [61]. This is for the same reasons of complexity as for the heat transfer coefficients, full CFD analysis often being impractical as part of ORC analysis. However, as for the heat transfer coefficients, semi-empirical correlations have been developed to estimate the pressure drop in the heat exchanger within the range for which the correlations are valid.

The correlations generally give a friction factor *f* which is related to the pressure drop according to the following equation [168]:

$$f = \frac{\Delta P D_H}{2L\rho u^2} \tag{3.42}$$

Where *L* is the length of the channel.

For single-phase flow, Kim [157] did not publish a correlation, so the Wanniarachchi correlation [158] for friction factor is used instead, given by:

$$f = (f_l^3 + f_t^3)^{\frac{1}{3}} \tag{3.43}$$

Where:

$$f_l = 1774(\beta)^{-1.026}(\beta)^2 Re^{-1} \tag{3.44}$$

$$f_t = 46.6(\beta)^{-1.08}(\varphi)^{1-p} Re^{-p} \tag{3.45}$$

$$p = 0.00423(\beta) + 0.0000223(\beta)^2 \tag{3.46}$$

Where φ is an area scaling factor, and

For evaporation, the Yan-Lin correlation for pressure drop is given by:

$$f = 6.947 * 10^5 Re_{eq}^{-1.109} Re^{-0.5} \tag{3.47}$$

For Re_{eq}<6,000, and:

$$f = 31.21 Re_{eq}^{0.04557} Re^{-0.5} \tag{3.48}$$

For Re_{eq}>=6,000.

For condensation, the Kuo et al correlation for pressure drop is given by:

$$f = 21{,}500 Re_{eq}^{-1.14} Bo^{-0.085} \tag{3.49}$$

These correlations can be used to estimate the pressure drops in heat exchangers, similarly to how the corresponding correlations can be used for the heat transfer coefficients.

3.5 Theory of Distillation

This thesis also addresses aspects of distillation, which is used in the Dynamic Organic Rankine Cycle concept to adjust the working fluid composition. The equations for the sizing and power requirements of an appropriate distillation system are presented below.

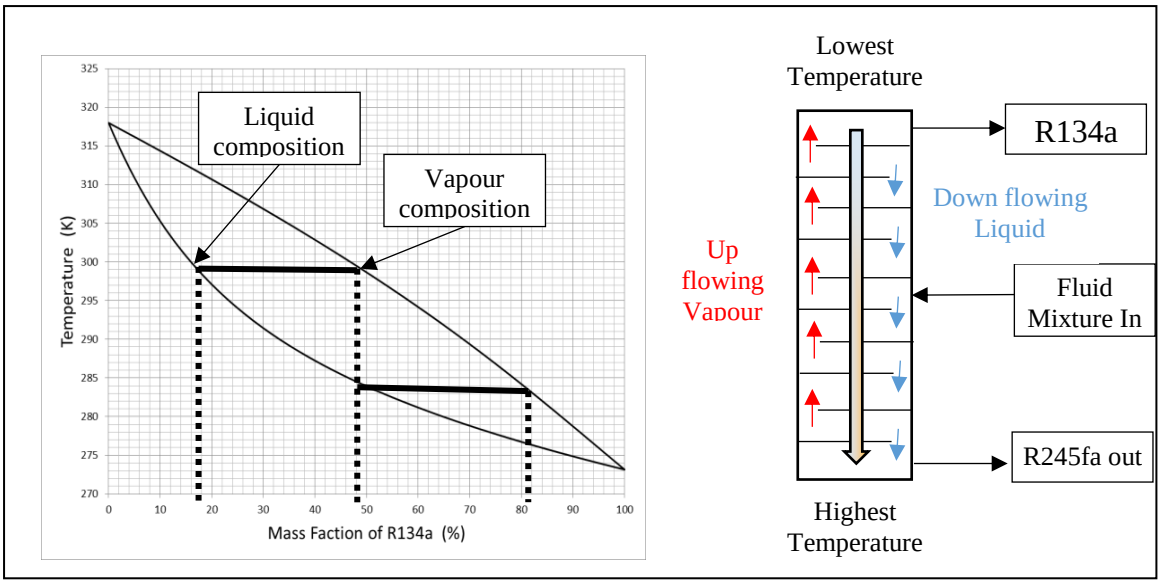

Figure 3.2: Glide curve diagram for R245fa and R134a showing the distillation process, alongside a schematic diagram of a distillation column showing its operation

Figure 3.2 demonstrates the principle behind the distillation process. The temperature decreases up the column, and the blended working fluid is injected half way up. As seen in the glide curve diagram, at any given temperature, the composition of the vapour and liquid phases can be obtained. The design of the column is such that the vapour flows upwards due to buoyancy, whereas the liquid rains towards the bottom of the column due to gravity. Each tray in the distillation column exists at a different temperature, with the cooler trays located towards the top, allowing liquid richer in R245fa to rain out even as its concentration in the overall fluid decreases. Eventually, the vapour at the top of the column has been almost completely depleted of R245fa, and the liquid at the bottom has had almost all of the R134a driven out of it, leaving nearly pure liquid R245fa at the bottom of the column, and nearly pure R134a vapour at the top.

3.5.1 Number of Trays Required

The number of trays theoretically required for a distillation can be obtained by using Fenske's Equation [169]

$$N_{min} = \frac{\log\left[\left(\frac{x_D}{1-x_D}\right)\left(\frac{1-x_B}{x_B}\right)\right]}{\log \alpha_{ave}} \tag{3.50}$$

where x_D is the proportion of the more volatile component in the distillate, x_B is the proportion of the more volatile component in the bottoms, and α is the relative volatility of the feed. This result can, as a rule of thumb, be doubled to give the actual number of trays required [27].

The number of trays in the distillation system is correlated with the purity of the product of the distillation, as shown in Figure 3.3. Increasing the number of trays increases the purity of the product, at the cost of increased capital expense for the system.

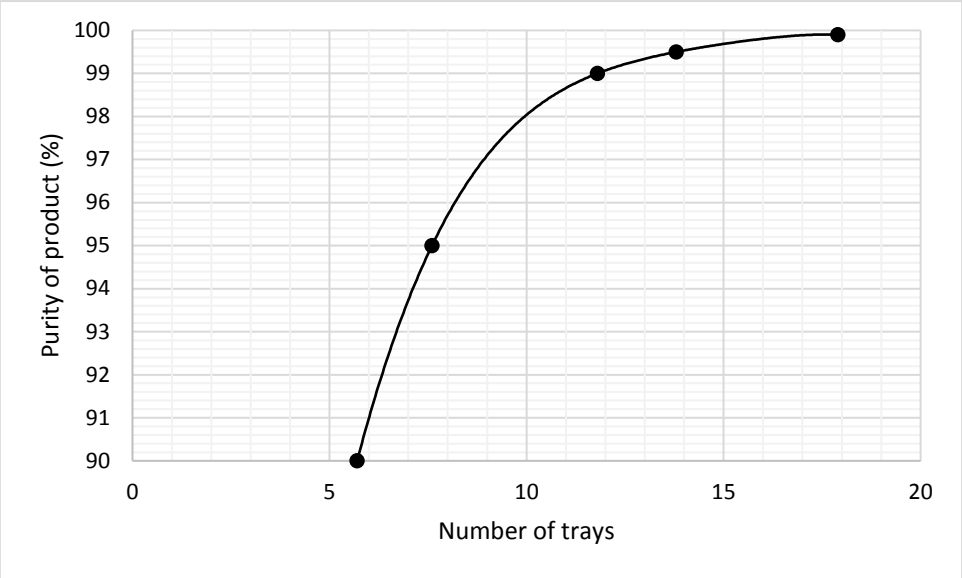

Figure 3.3: Effect of number of trays on product purity

3.5.2 Energy Required for Distillation

Distillation processes require an input of energy in order to vaporise the fluid before its introduction into the distillation column. Most designs also incorporate a reboiler and condenser at the ends of the column, which reintroduce fluid to the column. This reintroduced fluid, known as reflux flow when it is distillate and vapour boil-up when it is bottoms, mixes with the fluid undergoing distillation and minimises the column size. This arrangement is shown in Figure 3.4.

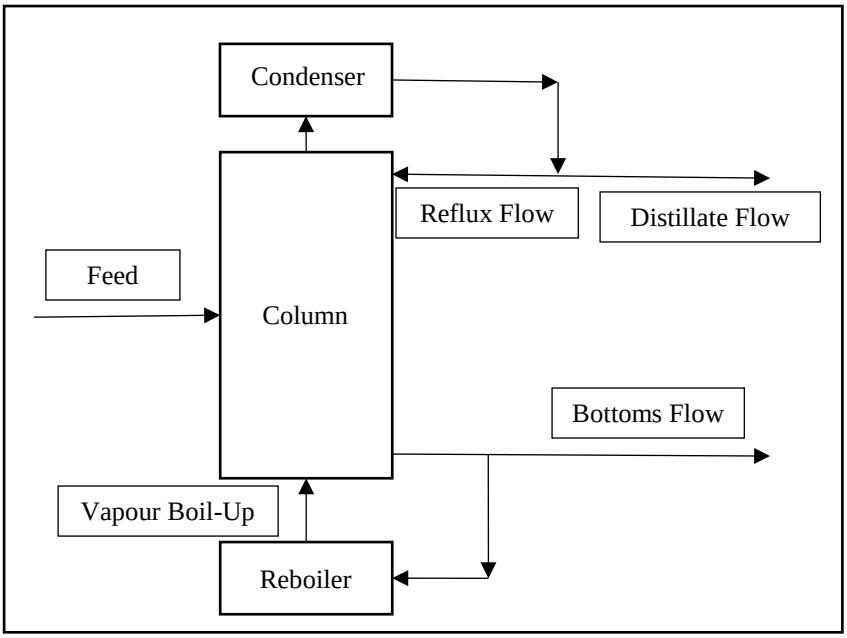

Figure 3.4: Distillation Column with Condenser and Reboiler

The reflux and vapour boil-up flows are generally expressed as a ratio, compared to the distillate and bottoms flow respectively.

$$Boil - up\ Ratio = \frac{V}{B} \tag{3.51}$$

$$Reflux\ Ratio = \frac{R}{D} \tag{3.52}$$

Where V is the vapour boil-up flow, B is the bottoms flow, R is the reflux flow and D is the distillate flow.

The higher the reflux and boil-up ratios, the lower the number of plates needed, and therefore the lower the capital cost of the system. However, increasing these ratios also increases the energy requirement for a given amount of pure product [170]. Therefore a compromise must be reached between the two. The exact compromise will depend on the operation of the system, the capital cost, the value of the products and the thermal properties of the fluid. Typical values in the literature range from 1 to 3 [171].

The total energy requirement of the distillation column is therefore the energy required to vaporise the fluid mixture before its introduction to the column, plus the energy required in the reboiler, which is given by the latent heat of vaporisation of the working fluid, multiplied by the vapour boil-up flow rate.

The amount of fluid that needs to be removed from the system in order to achieve the correct fluid composition can be calculated using the principles of dilution. If the component being removed from the system is treated as a solute at a given concentration, the following formula can be used to calculate the dilution factor required to bring the fluid composition to the required value:

$$V_1 C_1 = V_2 C_2 \tag{3.53}$$

Where V represents volume and C represents concentration. The concentrations before and after the temperature change are known from the glide curve diagram, so the ratio of volumes before and after dilution can be determined. Assuming the total system charge remains the same, the amount of fluid that must be added to the system to result in the new concentration can then be calculated. For example, if the required dilution factor is 3, 2/3 of the original system charge must be removed to leave adequate space for the dilution of the remainder to the appropriate concentration.

3.6 MATLAB Routine

3.6.1 Naming Convention

The naming convention for the points in the cycle were as follows:

Point 1: The pump inlet

Point 2: The pump outlet

Point 3: The Regenerator Cold Side Outlet. If no regenerator is specified, this point is the same as point 2.

Point 4: The bubble point inside the Evaporator or Regenerator Cold Side.

Point 5: The dew point inside the Evaporator or Regenerator Cold Side.

Point 6: The evaporator outlet/expander inlet

Point 7: The expander outlet

Point 8: The Regenerator Hot Side Outlet. If no regenerator is specified, this point is the same as point 7.

Point 9: The Dew point inside the Condenser or Regenerator Hot Side

Point 10: The Bubble point inside the Condenser or Regenerator Hot Side

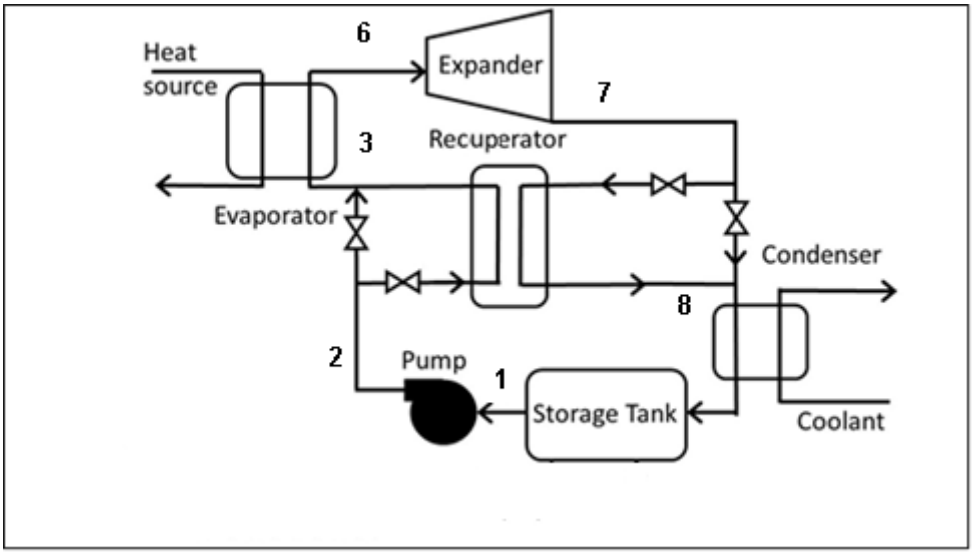

Figure 3.5: Schematic Diagram of Cycle with state points numbered. States 4, 5, 9 and 10 are saturation points inside heat exchangers and are not shown in this figure.

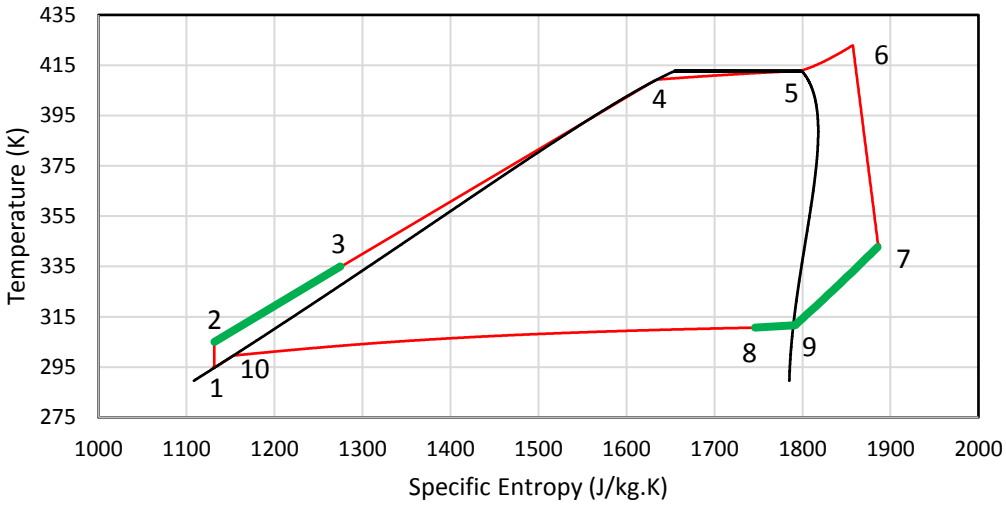

Figure 3.6: T-s diagram of the cycle showing the naming convention for the state points. The thicker green lines on the plot represent the portion of the cycle that occurs in the regenerator.

Figure 3.5 and Figure 3.6 show these naming points graphically. It should be noted particularly that in Figure 3.6, because of the phase change on the cold side of the regenerator, point 8 actually falls after point 9.

3.6.2 REFPROP Fluid Properties Program

The REFPROP Fluid Properties Program [80] was used to provide the thermophysical data of the working fluids. Provided with two thermodynamic properties, it can return any others on its extensive list of properties, with a few exceptions. For example, temperature and pressure

are enough to fully define a liquid or vapour phase fluid, but are insufficient on their own to define a fluid under its saturation dome, some information on enthalpy, entropy, or vapour quality is needed. REFPROP can be called by MATLAB using a simple function. Although there is a degree of uncertainty associated with the fluid properties returned by REFPROP, they were treated as single deterministic values for ease of analysis in this project.

Other methods are available, such as the Cubic Equation of State [48], the BACKONE equation of state [48] Peng Robertson Equation of State [70], DIPPR 801 AIChE database [70] [130], or other mathematical predictions of fluid properties [79]. The accuracy of these equations of states vary, with BACKONE producing better results than the cubic EOS, for example. However, REFPROP's ease of use, capacity to analyse fluid mixtures, and the possibility of simple integration into MATLAB meant that it was deemed the most appropriate for the cycle modelling.

3.7 Assumptions of the modelling

Several assumptions were made in the development of this model. These assumptions are commonly used in ORC analysis:

-The system is assumed to be perfectly insulated, with no transfer to the environment except through the heat exchangers [48] [70] [8].

-The pressure losses in pipes and heat exchangers were assumed to be negligible [70] [62] [61] [88].

-The effects due to velocity, compressibility and changes in elevation were assumed to be negligible [70] [6].

-The work required to move thermal fluid through the hot side of the evaporator and coolant through the cold side of the condenser were both assumed to be negligible in comparison with the amount of power produced by the system.

-The system is assumed to operate at a steady state, with no transient effects occurring [70] [6] [43] [52].

All of the assumptions simplify the model and reduce processing time. However, each of them has several other justifications underlying its adoption in the model.

The first two of these assumptions are considered justified in the context of the theoretical model, as heat and pressure losses are particular to the individual pipework and its geometry.

As well as being difficult and inaccurate to predict the physical configuration of a theoretical system, such specific details would hinder a general comparison of the effects of changing various parameters on a theoretical cycle.

The third assumption is considered justified as the changes in elevation are once again a very specific aspect of a physical system, and their inclusion would compromise a fair general comparison. The flow velocities in a physical system are well below the speed of sound in the working fluid, so velocity and compressibility effects can safely be discounted.

The fourth assumption, that the work required to move the thermal fluid through the heat exchangers is negligible compared to the power generated by the cycle, was considered justified for the same reasons. The flow rate of the thermal fluid depends on the composition of the coolant or heating fluid, and its source. For example, an artesian geothermal well will not require additional power to force the brine through the heat exchanger, whereas hot gas from and industrial process might do.

The fifth assumption, that the system operates at a steady state, was considered justified as the theoretical analysis of the cycle is taken over the period of hours or days, whereas transient effects from dynamic flow conditions stabilise over the course of seconds, and thermal equilibrium is reached over the course of minutes, meaning the majority of the time the cycle will be operating under steady state conditions.

3.8 Model Shell

The shell of the model is where several values are initialised and the functions are called. Different shells can be used depending on the particular application.

The heat source temperature is set by the user, while the heat sink temperature is contained in an array pulled from an excel spreadsheet. This allowed the value of the heat sink temperature to be swept across a range, or for real-world climate data to be used. The minimum temperature of the cycle was set to 5K above the heat sink temperature.

The shell progressed through the array of heat sink temperatures, generating a fresh set of data for each value.

The condenser pressure is set based on the heat sink temperature, calculated using REFPROP as follows:

$$P_{condenser}=\text{refpropm}(\text{'p'}, \text{'t'}, T_{heat\ sink}+7, \text{'q'}, 0, Fluid1, Fluid2, Ratio)$$

This gives a subcooling of 2K at the pump inlet, to allow for an adequate NPSH to be provided.

Similarly, the evaporator pressure is set based on the heat source temperature, calculated as follows:

$$P_{evaporator}=\text{refpropm}(\text{'p'}, \text{'t'}, T_{heat\ source}-10, \text{'q'}, 1, Fluid1, Fluid2, Ratio)$$

After the basic cycle model has been called, the mass flow rate of the working fluid can be calculated. This is done by dividing the desired cycle power by the specific enthalpy drop across the expander.

$$\dot{m}_{wf} = \frac{W_{expander}}{\Delta h_{expander}} \tag{3.54}$$

3.9 Basic Model

The core of the MATLAB model is the basic model, which is called using a function called "BasicCycle2Pressures". A block diagram of this function is given in Figure 3.7.

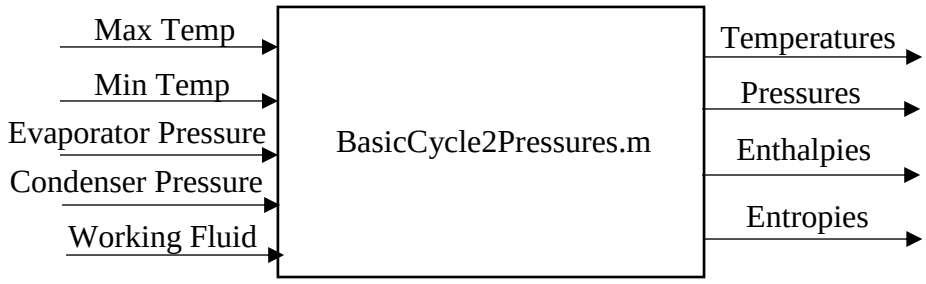

Figure 3.7: Block Diagram of the "BasicCycle2Pressures.m" function

The fluid properties at State 1 can be determined as follows:

The temperature T_1 is equal to the minimum temperature of the cycle, one of the input variables, and the pressure P_1 is the condenser pressure, another of the input variables. The enthalpy and entropy, h_1 and s_1, can be calculated using the "refpropm.m" function, called as follows:

$$h_1=\text{refpropm}(\text{'h'}, \text{'t'}, T1, \text{'P'}, P1, Fluid1, Fluid2, Ratio)$$

s_1=refpropm('s', 't', T1, 'P', P1, Fluid1, Fluid2, Ratio)

The pressure at state 2 is the evaporator pressure, one of the input variables. The temperature, enthalpy and entropy must be calculated using the equation for isentropic efficiency.

$$\eta_{pump} = \frac{h_{2,isentropic} - h_1}{h_2 - h_1} \tag{3.55}$$

Where $h_{2,isentropic}$ is calculated using the refpropm function as follows:

$h_{2,isentropic}$=refpropm('h', 'p', P2, 's', s1, Fluid1, Fluid2, Ratio)

And the isentropic efficiency of the pump was set to 70%.

This allows h_2, the enthalpy at the pump outlet to be calculated, and knowing this, s2 and T2 can be calculated using the refpropm function:

s_2 =refpropm('s', 'p', P2, 'h', h2, Fluid1, Fluid2, Ratio)

T_2 =refpropm('t', 'p', P2, 'h', h2, Fluid1, Fluid2, Ratio)

State 3 is the exit to the cold side of the regenerator. It is set to be equal to state 2 in this function, and is later modified by the regenerator function.

State 4 is the bubble point of the working fluid at evaporator pressure, and can be obtained directly from REFPROP as follows:

T_4 =refpropm('T', 'p', P2, 'q', 0, Fluid1, Fluid2, Ratio)

h_4 =refpropm('h', 'p', P2, 'q', 0, Fluid1, Fluid2, Ratio)

s_4 =refpropm('s', 'p', P2, 'q', 0, Fluid1, Fluid2, Ratio)

State 5 is the dew point at evaporator pressure, and can be obtained from REFPROP similarly:

T_5 =refpropm('T', 'p', P2, 'q', 1, Fluid1, Fluid2, Ratio)

h_5 =refpropm('h', 'p', P2, 'q', 1, Fluid1, Fluid2, Ratio)

s_5 =refpropm('s', 'p', P2, 'q', 1, Fluid1, Fluid2, Ratio)

Where 'q' in both cases refers to the quality of the fluid, with 0 being a saturated liquid and 1 being a saturated vapour.

State 6 is the evaporator inlet, T_6 is the maximum cycle temperature, and P_6 is the evaporator pressure, both of which are inputs to the function. The enthalpy and entropy can be calculated using REFPROP as follows:

h_6 =refpropm('h', 't', T6, 'p', P2, Fluid1, Fluid2, Ratio)

s_6 =refpropm('s', 't', T6, 'p', P2, Fluid1, Fluid2, Ratio)

State 7 is the evaporator outlet. As for the pump outlet, the condition of the working fluid here can be calculated using the equation for isentropic efficiency:

$$\eta_{expander} = \frac{h_6 - h_7}{h_6 - h_{7,isentropic}} \tag{3.56}$$

Where $h_{7,isentropic}$ is given by:

$h_{7,\ isentropic}$ =refpropm('h', 'p', P1, 's', s6, Fluid1, Fluid2, Ratio)

And the isentropic efficiency of the expander was set to 70%.

Knowing h_7, s_7 and $T_{7\ can}$ then be calculated as follows:

s_7=refpropm('s', 'p', P1, 'h', h7, Fluid1, Fluid2, Ratio)

T_7=refpropm('t', 'p', P1, 'h', h7, Fluid1, Fluid2, Ratio)

State 8 is the outlet of the hot side of the regenerator, and is set equal to state 7 for now.

State 9 and state 10 are the dew and bubble points at condenser pressure, given by:

T_9 =refpropm('T', 'p', P1, 'q', 1, Fluid1, Fluid2, Ratio)

h_9 =refpropm('h', 'p', P1, 'q', 1, Fluid1, Fluid2, Ratio)

s_9 =refpropm('s', 'p', P1, 'q', 1, Fluid1, Fluid2, Ratio)

T_{10} =refpropm('T', 'p', P1, 'q', 0, Fluid1, Fluid2, Ratio)

h_{10} =refpropm('h', 'p', P1, 'q', 0, Fluid1, Fluid2, Ratio)

s_{10} =refpropm('s', 'p', P1, 'q', 0, Fluid1, Fluid2, Ratio)

With the temperature, pressure, enthalpy and entropy known at each point in the cycle, the outputs of the function can be returned.

3.10 Regenerator Function

The Regenerator function is called after the Basic Cycle function, and modifies the previously unused values for points 3 and 8. A block diagram of the operation of this function is shown in Figure 3.8

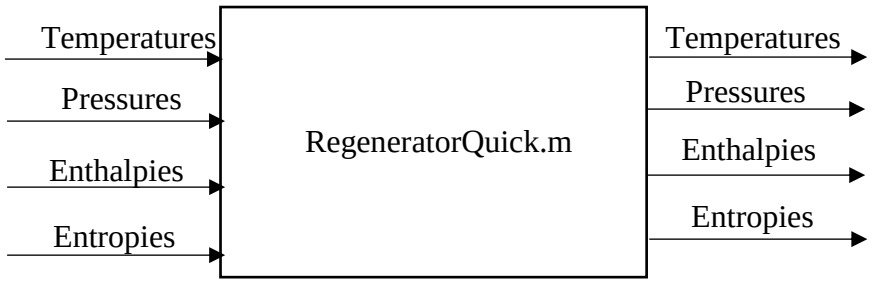

Figure 3.8: Block Diagram of the "RegeneratorQuick.m" function

The Regenerative Model works on the basis of a pinch point analysis between the hot stream leaving the expander and the cold stream leaving the pump. The inlet temperature to the hot side is always the expander outlet temperature, and the inlet temperature to the cold side is always the pump outlet temperature. The outlet temperature from each side of the regenerator will vary depending on how much enthalpy is transferred from the hot side to the cold side.

Initially, the program assumes there is zero enthalpy transfer between the streams. This means the inlet temperature and outlet temperature for the hot stream are the same, as are the inlet and outlet temperatures for the cold side. This means that the pinch point temperature difference between the two fluid streams is simply the difference between the expander outlet temperature and the pump outlet temperature.

The program then gradually increases the enthalpy transfer between the two streams. Assuming no losses to the surroundings, any enthalpy lost by the hot side must be absorbed by the cold side. The greater the enthalpy transfer, the greater the overlap between the two streams. The program takes 100 points along a temperature-enthalpy curve for the two streams, and compares the temperature difference at each of them. It then takes the lowest value of this and uses it as the pinch point temperature difference. It continues to increase the enthalpy transfer until this value is smaller than the value of allowable pinch point temperature difference. This process is shown graphically in Figure 3.9.

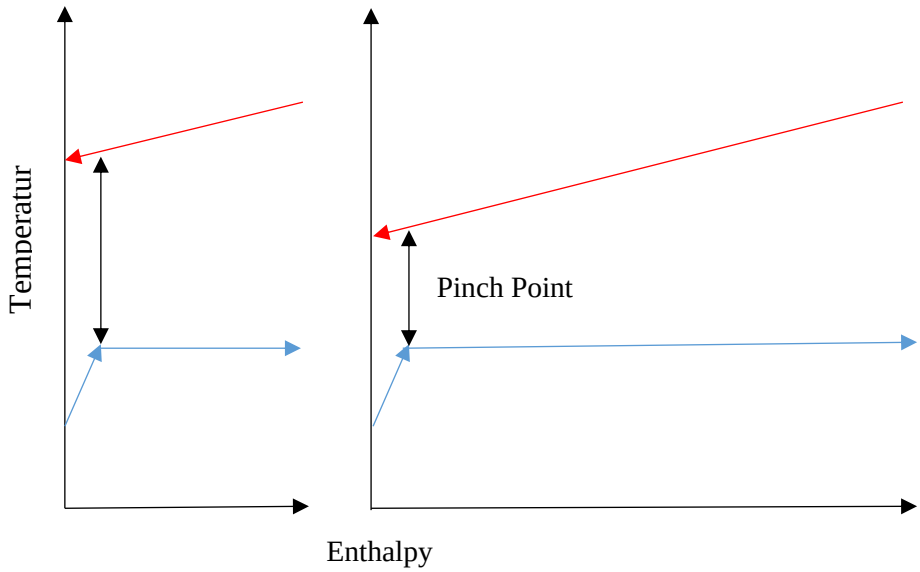

Figure 3.9: Progression of the regenerator model, showing how increasing the enthalpy transfer closes the pinch point temperature difference.

This gives a value for the enthalpy change in the regenerator, so h_3 and h_8 can be calculated by:

$$h_3=h_2+h_{regenerator} \tag{3.57}$$

$$h_8=h_7-h_{regenerator} \tag{3.58}$$

And the temperatures and entropies calculated by:

T_3 =refpropm(‘T’, ‘p’, P2, ‘h’, h3, Fluid1, Fluid2, Ratio)

s_3 =refpropm(‘s’, ‘p’, P2, ‘h’, h3, Fluid1, Fluid2, Ratio)

T_8 =refpropm(‘T’, ‘p’, P1, ‘h’, h8, Fluid1, Fluid2, Ratio)

s_8 =refpropm(‘s’, ‘p’, P1, ‘h’, h8, Fluid1, Fluid2, Ratio)

The new arrays for temperature, pressure, enthalpy and entropy can then be returned by the function.

3.11 Pinch Point Model for Heat Exchangers

The evaporator and condenser functions took in the flow rate, enthalpy, temperature and pressure data for the main cycle, and returned the thermal fluid outlet temperature and the thermal fluid flow rate, as shown in Figure 3.10.

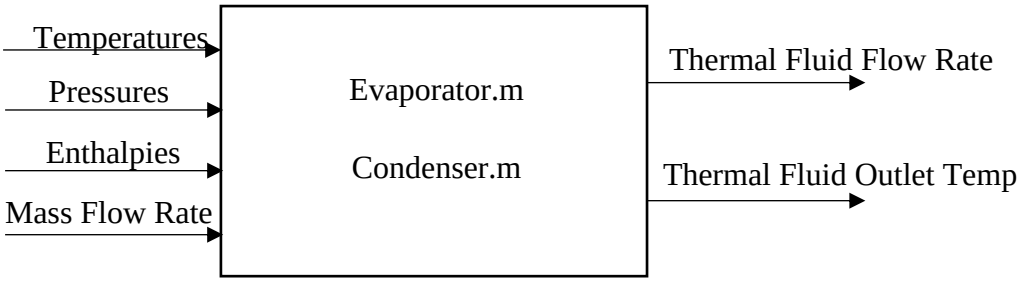

Figure 3.10: Block diagram of the heat exchanger functions

The temperature profile of the working fluid on the T-H diagram as it passes through a heat exchanger is fixed by the operating conditions of the cycle. The inlet temperature of the heating or cooling fluid is also fixed. For the hot fluid it is the temperature set as one of the boundary conditions of the cycle. For the cold fluid, it is the ambient temperature fed to the cold side of the condenser. It is assumed that all heat transfer occurs between the two fluids, i.e. that no heat is absorbed from or rejected to the environment.

In both cases, the only variable in the system left unconstrained is the flow rate of the thermal fluid. The program initially assumes this to be zero, which for the evaporator gives an infinite temperature change in the thermal fluid to provide the energy to heat up the working fluid. The flow rate is then gradually increased, and the temperature difference at each 100 points along the length of the evaporator is calculated by the program, with the minimum being taken as the pinch point temperature difference. Initially this is a negative value, which is physically impossible, but as the flow rate of thermal fluid increases, the required temperature drop to provide the same amount of energy to the working fluid decreases. Eventually the slope will be such that the thermal fluid line will lie completely above the working fluid line, the pinch point temperature difference will become positive and reach the desired value, and the corresponding flow rate of thermal fluid can be calculated. This process is shown graphically in Figure 3.11.

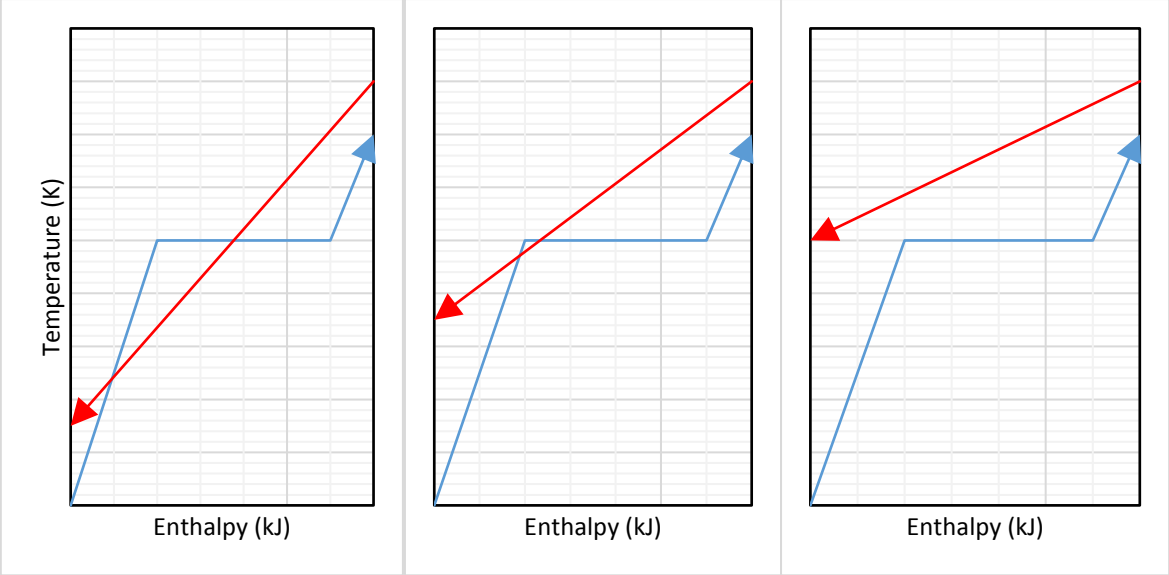

Figure 3.11: Illustration of how increasing the flow rate of the thermal fluid can open the pinch point in an evaporator

The process is the same for condensers, except that because the coolant is absorbing heat from the working fluid, the coolant line on the T-H diagram moves downwards with increasing flow rate until the desired value of pinch point temperature difference is reached.

With the values for the thermal fluid mass flow rate and outlet temperature known these values can then be returned by the function.

3.12 Dynamic Model

The dynamic model was used to analyse a dynamic Organic Rankine Cycle as outlined in Chapter 1. This required the use of a different shell for the MATLAB routine.

In this shell the array of heat sink temperatures was read in from an excel file containing maximum, minimum and average daily temperature data [172]. The hourly temperature profile can be estimated by assuming a sinusoidal variation in the temperature over the course of the day. The relevant equation to generate this sinusoidal curve is:

$$T_{hourly} = T_{minimum} + \left(\frac{T_{maximum} - T_{minimum}}{2}\right)\left(1 + \sin\left(\left(\frac{2\pi * hour}{24}\right) - \left(\frac{\pi}{2}\right)\right)\right) \quad (3.59)$$

Where *hour* represents the number of the hours elapsed in the day, starting from 1 at 00:00hr.

The type of profile this generates is shown in Figure 3.12. The sinusoidal shape of the daily temperature curve can be seen, as can the slight discontinuities between days.

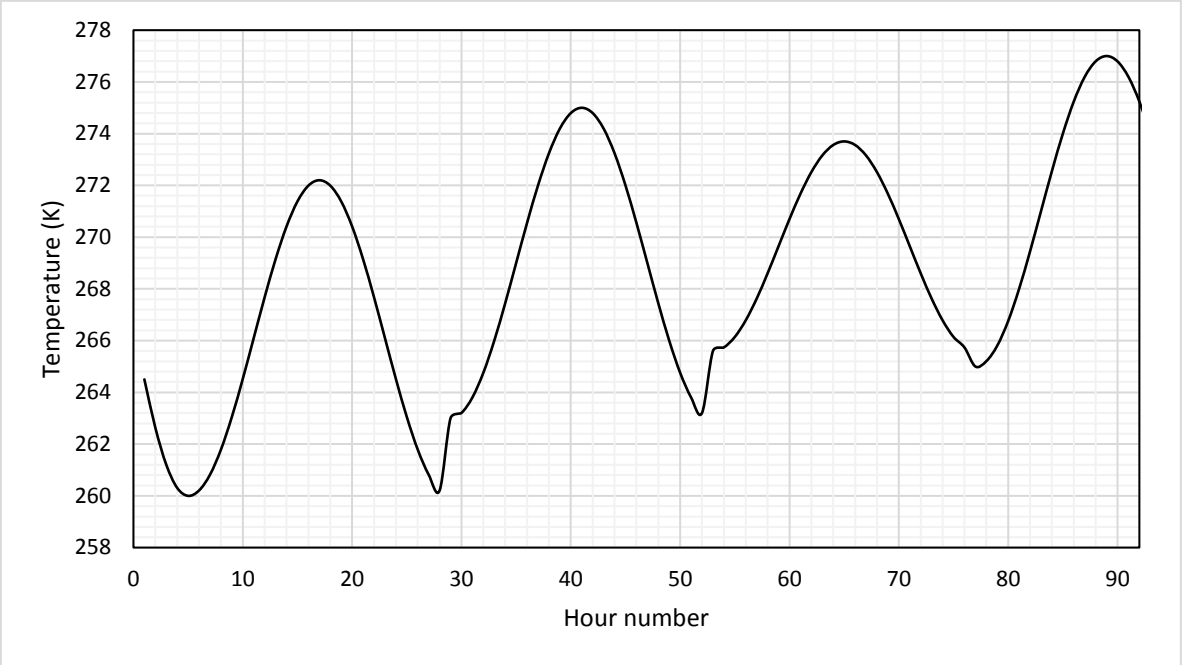

Figure 3.12: Temperature profile over a 4 day period in spring, approximated as a sinusoid

The condenser pressure was fixed according to the maximum yearly temperature, calculated using REFPROP:

$$T_{max}=\max(\text{TemperatureArray}) \tag{3.60}$$

$$P_1=\text{refpropm}(\text{‘p’, ‘t’, } T_{max}+7, \text{‘q’, 0, Fluid1}) \tag{3.61}$$

Where Fluid1 is the component of the working fluid with the higher boiling point. This gives the required condenser pressure to ensure that the working fluid is liquid at the pump inlet on the hottest day of the year.

Knowing the condenser pressure, the bubble and dew curves for the two component fluids at this pressure can then be calculated and made into an array, as plotted in Figure 3.13.

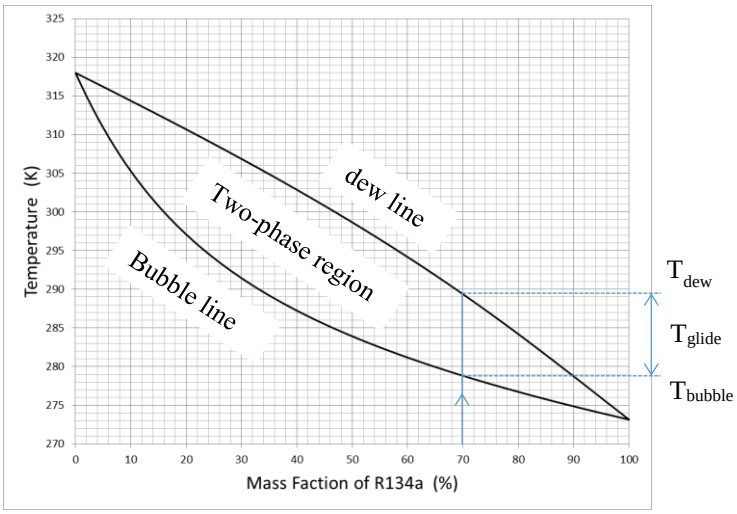

Figure 3.13: Glide curves for r245fa and r134a for a pressure of 2.9 bar

With the bubble curve known, the program can then begin to work through the array of ambient temperatures. For each ambient temperature, it selects the fluid composition from the bubble curve array that corresponds to the ambient temperature, plus an allowance for the pinch point temperature difference.

Knowing the working fluid composition, the heat source and sink temperatures and the condenser and evaporator pressure, the basic cycle, regenerator and heat exchanger functions could be called as normal.

3.13 Validation of the Model

The predictions of the theoretical model were compared against experimental data from the literature.

Firstly the model was applied to the results of Kang et al. [97] and the results compared in Table 3-2. It can be seen that the theoretical predictions of the model line up closely with the experimental results, with deviations of less than 1% from the experimental values in most cases. The largest deviations are observed at the exit of the expander, where assumptions about the isentropic efficiency of the expander have the greatest effect.

Table 3-2: Comparison of model's prediction to the results of Kang et al. [97].

State point		Model	Kang's experiments	
1 (Pump inlet)	T (K)	303	303	0.00%
	P (bar)	1.78	1.78	0.00%
	h (kJ/kg)	239.1	239	-0.04%
	s (kJ/kg K)	1.135	1.14	0.40%
2b (saturated liquid)	T (K)	350.6	350	-0.16%
	P (bar)	7.32	7.32	0.00%
	h (kJ/kg)	305.4	305	-0.13%
	s (kJ/kg K)	1.337	1.34	0.22%
2c (Saturated Vapour)	T (K)	350.6	350	-0.16%
	P (bar)	7.32	7.32	0.00%
	h (kJ/kg)	460	460	0.00%
	s (kJ/kg K)	1.778	1.78	0.11%
3 (Expander Inlet)	T (K)	353	353	0.00%
	P (bar)	7.32	7.32	0.00%
	h (kJ/kg)	462.9	463	0.02%
	s (kJ/kg K)	1.786	1.79	0.22%
4 (Condenser Inlet)	T (K)	318.2	321	0.87%
	P (bar)	1.78	1.78	0.00%
	h (kJ/kg)	441	444	0.68%
	s (kJ/kg K)	1.799	1.75	-2.80%

3.14 Summary

In this chapter the relevant equations for the Organic Rankine Cycle are presented, for the thermodynamic analysis of the system and its heat exchangers, and also a more detailed approach analysing the heat exchangers using semi-empirical correlations. The theoretical model of the rig developed in MATLAB is then described, explaining how the relevant equations are used by the program. Finally, the accuracy of the theoretical model as it applies to the experimental rig was discussed and validation of the theoretical model provided. In Chapter 4 the design of the experimental rig using these methods will be discussed, and in Chapter 5 the results of the theoretical analysis of the Dynamic Organic Rankine Cycle.

CHAPTER 4- DESIGN AND CONSTRUCTION OF THE EXPERIMENTAL RIG

In this section the specification of the components of the experimental rig are presented, and the components sourced to meet these specifications discussed. The construction, testing and commissioning of the rig are then discussed.

4.1 Specification of Components

The critical performance parameters and required specifications of the components of the rig were developed using the theoretical model outlined in Chapter 3. This produced the following specifications for the rig under optimum conditions:

Table 4-1: Specifications of the rig

State	**Temperature**	**Pressure**	**Enthalpy**	**Entropy**	**Density**
	K	Bar(a)	kJ/kg	kJ/kg.K	kg/m^3
Pump In	285	1.1	215.24	1.054	1374
Pump Out	286	12	216.90	1.057	1374
Expander In	372	12	474.48	1.794	69
Expander Out	319	1.1	443.56	1.836	5.81

Pump Enthalpy	kJ/kg	1.66
Evaporator Enthalpy	kJ/kg	257.58
Expander Enthalpy	kJ/kg	30.92
Condenser Enthalpy	kJ/kg	228.32
Volume Flow Rate	m^3/s	0.00072
Mass Flow Rate	kg/s	0.0496
Power Output	W	1533

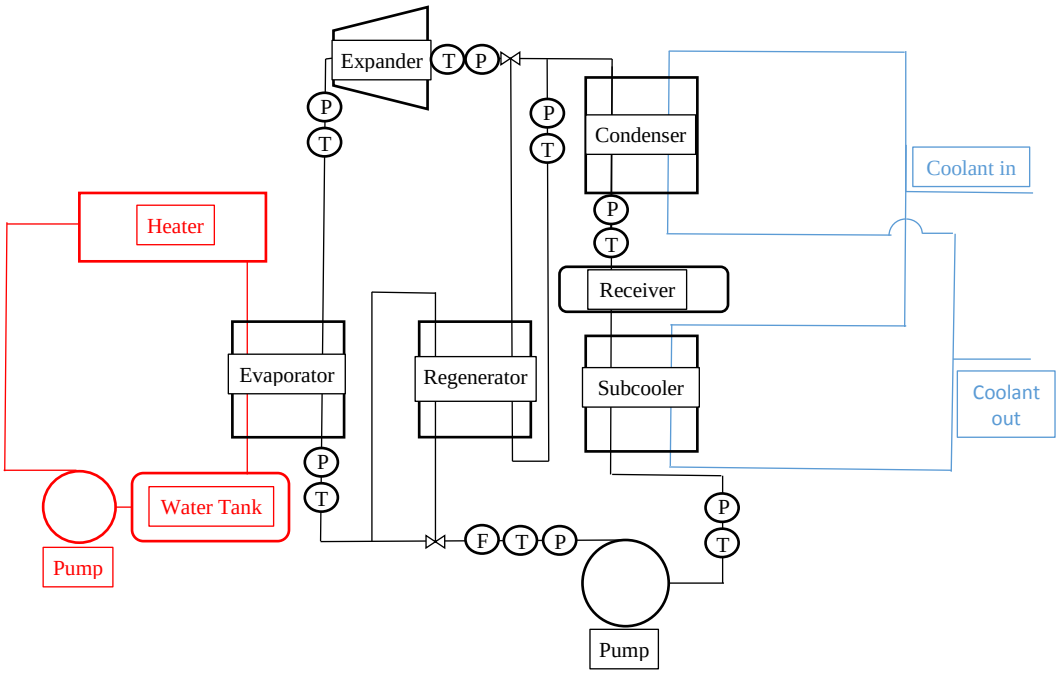

Figure 4.1: Schematic Diagram of the ORC Rig

Figure 4.1 shows a schematic diagram of the ORC rig and support systems. The red loop denotes the heater system. An insulated buffer tank holds water, which is circulated through the heater, which raises its temperature prior to being passed through the hot side of the evaporator.

The black line indicates the refrigerant loop. The pump circulates the working fluid, causing it to flow either directly into the evaporator, or through the regenerator to the evaporator, after which it is in the vapour phase, and flows to the expander. After the expander, the fluid then flows either to the condenser, or through the regenerator, then the condenser, after which it is in the liquid phase, and drains into the receiver. This rig also features a subcooler, which further cools the refrigerant leaving the condenser to ensure adequate subcooling at the pump inlet to help prevent cavitation.

The blue line indicates the coolant loop, which is branched from the building's cold water supply, and flows directly to both the condenser and subcooler in parallel.

4.1.1 Expander

Small-scale expanders are not widely commercially available, with much of the currently available experimental research having to resort to modifying compressors for this purpose

[150]. For this reason, the expander was considered the critical component around which to build the cycle.

Figure 4.2: Airsquared E15H022A-SH scroll expander

The expander selected for the cycle was an off-the-shelf E15H022A-SH from Airsquared, shown in Figure 4.2. It has a nominal output of 1 kWe, making it a suitable size for small-scale lab applications. It is a fully-contained unit using a magnetic coupling to transfer power from the rotor of the expander to the generator, meaning no dynamic seals, which cuts out one significant leak path from the system. It has also been tested under a wide variety of inlet pressures and is known to be compatible with refrigerants. Its ability to operate unlubricated also removes a degree of complexity from the system and allows fair comparison of cycle conditions without any extra variables introduced by the presence of lubricating oil in the working fluid. Figure 4.3 shows the variation in expander power and isentropic efficiency with varying inlet pressure and rotational speed, showing a peak power of 2000W and a peak isentropic efficiency of 75%.

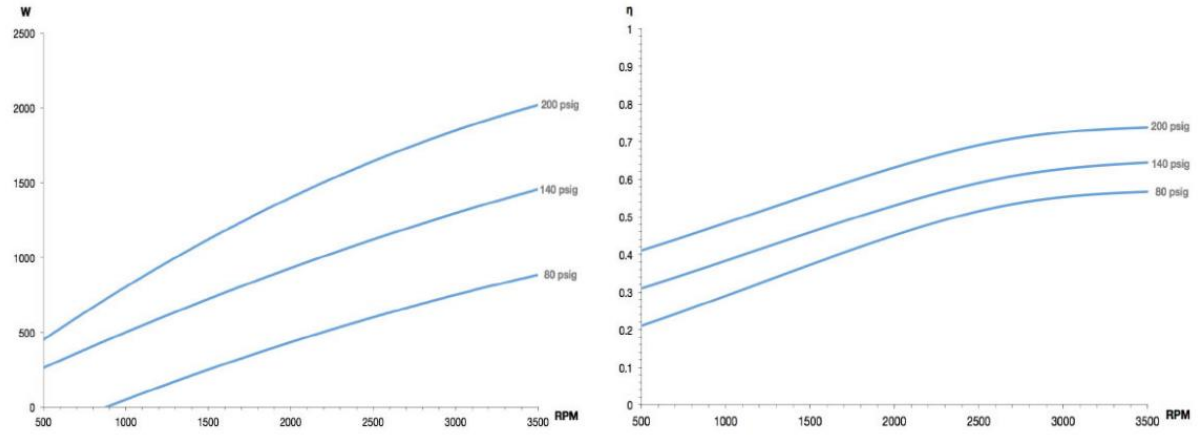

Figure 4.3: Performance curves of the Scroll Expander with varying rotational speed and inlet pressure for R245fa, provided by the manufacturer.

4.1.2 Working Fluid

The selection of working fluid was dictated by the choice of expander. The chosen expander has been tested by the manufacturer with R134a and R245fa. As the vapour pressure of R134a at room temperature is 4.86 bar, the volume ratio of the expander is 3.5, and the maximum inlet pressure is 13.8 bar, if the cycle were to use R134a as the working fluid, it would have to run permanently in under-expansion mode. Therefore R245fa, which has a higher boiling point, and therefore a lower vapour pressure, was chosen as the working fluid.

25kg of R245fa was purchased from BOC, and Chilli Refrigeration Services were contracted to charge the rig using it. An overall system charge of 7kg was found to be sufficient to provide an adequate NPSH to the pump.

15kg of R134a was also purchased to test refrigerant blends. It was found that blends of up to 30% R134a could be used in the rig without exceeding the pressure limitation of the expander during normal operation.

4.1.3 Heat Source

The heat source chosen was a MLH18L (S) electric water heater, manufactured by ExHeat, similar to that shown in Figure 4.4. In the interest of safety, the heating water was not pressurised, limiting the maximum temperature of the water to 100°C. The total heating capacity of the unit is 18kW.

Figure 4.4: Core of an MLH-series electric water heater from ExHeat

The temperature of the fluid flowing to the system can be controlled by use of a CN32PT-305-DC Controller supplied by Omega. This is a microprocessor-based PID controller that regulated the power supplied to the heater to maintain the set output temperature, as monitored by a thermocouple at the heater outlet.

Figure 4.5: Interface of the PID Temperature Controller

A 25 litre buffer tank is included in the system to minimise fluctuations in temperature. This is also open to the atmosphere to avoid a dangerous build-up in pressure in the event of the safety systems on the heater fail and the temperature of the water rises to above its boiling point. Any steam generated will simply bubble out of the system instead of increasing the internal pressure.

The hot water is circulated by a Grundfos UPS2 15-50/60 domestic central heating pump, shown in Figure 4.6 and rated to a maximum flow rate of 3.3 m^3/hour, and a maximum fluid temperature of 95°C.

Figure 4.6: Grundfos UPS2 15-50/60 central heating pump

Figure 4.7 shows the assembled heating rig located behind the Organic Rankine Cycle rig, with the three primary components, the water heater, water tank and circulation pump, labelled.

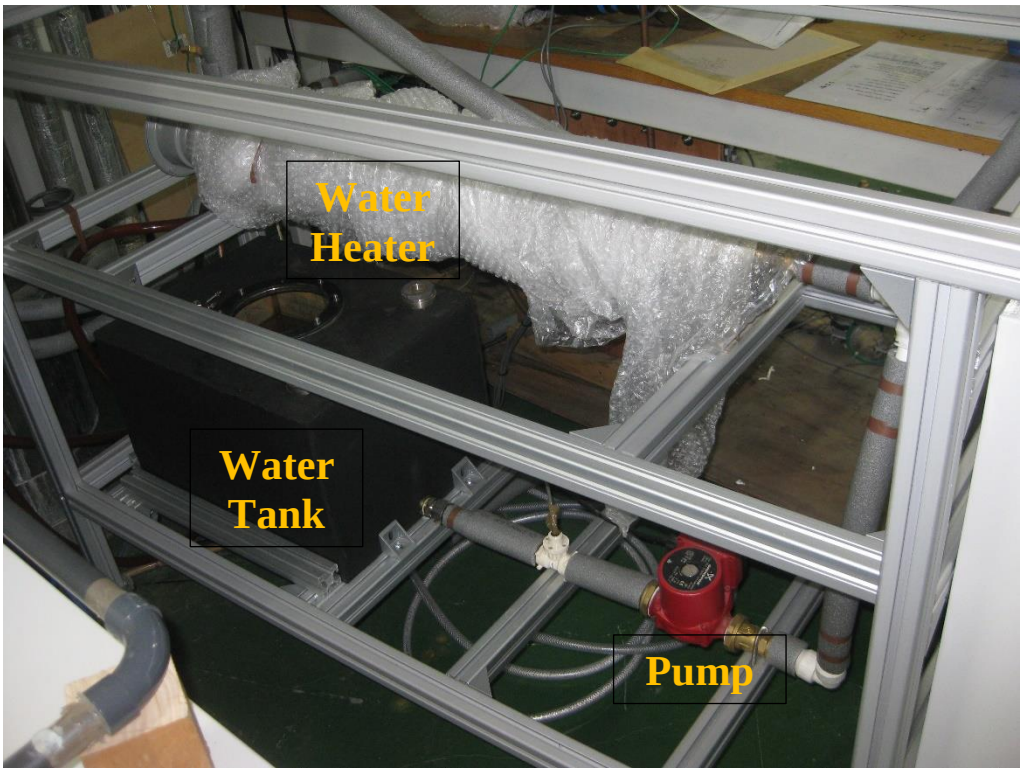

Figure 4.7: Labelled Diagram of the Heating Rig

4.1.4 Working Fluid Pump

The maximum mass flow rate of the system was calculated to be 0.07kg/s. This figure was arrived at by taking the maximum volume flow rate of the expander ($20cm^3$/rev * 3600 rev/min), and the density of r245fa at the expander inlet under normal operating conditions ($23kg/m^3$, calculated using REFPROP). The maximum pressure provided by the pump could not exceed the rated pressure of the expander, which gave a value for the maximum pressure head the pump would need to provide. This allowed the pump to be specified. In addition to the mass flow rate, the type of pump needed to be chosen. Due to the fact that R245fa is known to have some compatibility issues with common sealing materials, particularly elastomers, as shown in Figure 4.8, a diaphragm pump was chosen, due to the diaphragm's ability to isolate the working fluid from much of the pump materials.

Plastics				
Application	**% Weight Delta**	**% Length Delta**	**% Width Delta**	**%Thickness Delta**
Acetal	Negligible	Negligible	Negligible	Negligible
Acrylic	Dissolving			
HDPE	Negligible	Negligible	Negligible	Negligible
Nylon	Negligible	Negligible	Negligible	Negligible
Polycarbonate	Negligible	Negligible	Negligible	Negligible
Polyetherimide	Negligible	Negligible	Negligible	Negligible
Polypropylene	Negligible	Negligible	Negligible	Negligible
PET	Negligible	Negligible	Negligible	Negligible
PVC	Negligible	Negligible	Negligible	Negligible
PVDF	Negligible	Negligible	Negligible	Negligible
PTFE	Negligible	Negligible	Negligible	Negligible
Elastomers				
Application	**% Weight Delta**	**% Length Delta**	**% Width Delta**	**%Thickness Delta**
Butyl Rubber	Negligible	Negligible	Negligible	Negligible
Fluoroelastomer	76.5	24.8	26.9	27.7
EPDM	Negligible	Negligible	Negligible	Negligible
Epichlorohydrin	10.4	3.7	3.4	25.5
EthylenePropylene	1.2	0.8	Negligible	Negligible
Neoprene	Negligible	Negligible	Negligible	Negligible
Nitrile Rubber	4.2	Negligible	Negligible	Negligible
Silicone	6.0	Negligible	Negligible	2.4
Urethane	20.5	2.3	5.0	9.1

Notes: Fluoroelastomer: "Viton A": Trademark of DuPont Dow Elastomers
Nitrile Rubber: "Buna N"
PTFE: "Teflon": Trademark of the E. I. du Pont de Nemours and Company
PVDF: "Kynar": Trademark of Arkema Inc.
Polyetherimide: "Ultem": Trademark of The General Electric Company

Figure 4.8: Material compatibility of r245fa with common sealing materials [173].

Figure 4.9: Hydra-Cell G20 Pump of the type used for the rig, albeit with a stainless steel pump head rather than polypropylene

The pump used in the cycle is a Hydra-Cell G20 Diaphragm Pump with a polypropylene head as shown in Figure 4.9, fed by mains electricity through a frequency inverter. It can provide up to 17 bar at its outlet, and a maximum volume flow rate of 3.79l/min, which corresponds to a mass flow rate of 0.088kg/s, meeting the demands of the cycle.

The speed of the pump could be changed manually at the inverter, shown in Figure 4.10, which directly affected the speed of the motor driving the pump. Changes in pump speed resulted not only in an increase in flow rate, but also in the pressure ratio imposed on the cycle.

Figure 4.10: Lenze SMV Inverter of the type used to control the speed of the working fluid pump

The nature of the pump as a positive displacement device does cause a pulsing of the flow. This was found not to cause major problems with the power generation of the cycle. However, at certain frequencies, a large amount of vibration did occur in the pipework.

4.1.5 Heat Exchangers

Brazed Plate Heat Exchangers, supplied by Sondex, were chosen for use in the cycle, due to their compactness, versatility, and pressure resistance. The exchangers were first characterised by maximum temperature, operating pressure and heating duty calculated using a first-law thermodynamic analysis, and Sondex sized them using their in-house analysis software.

Table 4-2: Specifications of the evaporator

Evaporator Specifications		
Hot Side Inlet Temperature	°C	60-95
Cold Side Inlet Temperature	°C	10
Hot Side Outlet Temperature	°C	50-85
Cold Side Outlet Temperature	°C	55-90

Hot Fluid		Water
Cold Fluid		R245fa
Hot Flow Rate	kg/s	0.2
Cold Flow Rate	kg/s	0.1
Hot Pressure	Bar	1
Cold Pressure	Bar	5-10

Table 4-3: Specifications of the regenerator

Regenerator Specifications		
Hot Side Inlet Temperature	°C	35-50
Cold Side Inlet Temperature	°C	10
Hot Side Outlet Temperature	°C	15-20
Cold Side Outlet Temperature	°C	30-45
Hot Fluid		R245fa
Cold Fluid		R245fa
Hot Flow Rate	kg/s	0.1
Cold Flow Rate	kg/s	0.1
Hot Pressure	Bar	1-1.5
Cold Pressure	Bar	5-10

Table 4-4: Specifications of the condenser

Condenser Specifications		
Hot Side Inlet Temperature	°C	35-50
Cold Side Inlet Temperature	°C	5-8
Hot Side Outlet Temperature	°C	12-15
Cold Side Outlet Temperature	°C	10-112
Hot Fluid		R245fa
Cold Fluid		Water
Hot Flow Rate	kg/s	0.1
Cold Flow Rate	kg/s	0.3
Hot Pressure	Bar	1-1.5
Cold Pressure	Bar	1

Figure 4.11: Brazed Plate Heat Exchanger of the type used in the experimental rig

The details of the heat exchanger are given in Table 4-5.

Table 4-5: Details of the chosen heat exchanger

Sondex SL-14-30	
Type	Brazed Plate Heat Exchanger
Maximum Operating Pressure	34 bar
Maximum Temperature	185°C
Length	172mm
Width	42mm
Number of Channels	30

Four heat exchangers were included in the cycle, an evaporator, a regenerator, a condenser, and an additional post-cooler after the liquid reservoir to ensure a subcooled liquid entering the pump. A pair of inline check valves could be opened and closed to redirect the main flow of working fluid directly to the evaporator and condenser, or to divert it through the regenerator.

4.1.6 Cooling System

On-site cooling was available in the James Watt South engineering building. The building has an air-cooled chiller which provides cold water at a temperature of between 7 and 12°C, which was piped through the cold side of the heat exchangers. No additional cold water circulation pumps were required for the cooling system.

4.1.7 Instrumentation

4.1.7.1 Temperature

K-type thermocouples were selected as being sufficiently accurate for the chosen temperature range, based on the manufacturer information provided and shown in Figure 4.12. A probe-type design as in Figure 4.13 was chosen to allow the thermocouple to be inserted directly into the flow of working fluid or water via a compression fitting, giving higher accuracy than an adhesive thermocouple placed on the outside of the copper pipe.

TOLERANCE OF THERMOCOUPLES

ANSI/ASTM	°C			°F		
	Temperature Range	Standard	Special	Temperature Range	Standard	Special
T	-200° to -67° -67° to -62° -62° to 125° 125° to 133° 133° to 370°	± 1.5% T ± 1° ± 1° ± 1° ± 0.75% T	± 0.8% T* ± 0.8% T* ± 0.5° ± 0.4% T ± 0.4% T	-328° to -88° -88° to -80° -80° to 257° 257° to 272° 272° to 700°	± 1.5% (T – 32) ± 1.8° ± 1.8° ± 1.8° ± 0.75% (T – 32)	± 0.8% (T – 32)* ± 0.8% (T – 32)* ± 0.9° * ± 0.4% (T – 32) ± 0.4% (T – 32)
J	0° to 275° 275° to 293° 293° to 760°	± 2.2° ± 2.2° ± 0.75% T	± 1.1° ± 0.4% T ± 0.4% T	32° to 527° 527° to 560° 560° to 1400°	± 3.96° ± 3.96° ± 0.75% (T – 32)	± 1.98° ± 0.4% (T – 32) ± 0.4% (T – 32)
E	-200° to -170° -170° to 250° 250° to 340° 340° to 870°	± 1% T ± 1.7° ± 1.7° ± 0.5% T	± 1°* ± 1°* ± 0.4% T ± 0.4% T	-328° to -274° -274° to 482° 482° to 644° 644° to 1600°	± 1% (T – 32) ± 3.06° ± 3.06° ± 0.5% (T – 32)	± 1.8°* ± 1.8°* ± 0.4% (T – 32) ± 0.4% (T – 32)
K	-200° to -110° -100° to 0° 0° to 275° 275° to 293° 293° to 1260°	± 2% T ± 2.2° ± 2.2° ± 2.2° ± 0.75% T	— — ± 1.1° ± 0.4% T ± 0.4% T	-328° to -166° -166° to 32° 32° to 527° 527° to 560° 560° to 2300°	± 2% (T – 32) ± 3.96° ± 3.96° ± 3.96° ± 0.75% (T – 32)	— — ± 1.98° ± 0.4% (T – 32) ± 0.4% (T – 32)
N	0° to 275° 275° to 293° 293° to 1250°	± 2.2° ± 2.2° ± 0.75% T	± 1.1° ± 0.4% T ± 0.4% T	32° to 527° 527° to 560° 560° to 2300°	± 3.96° ± 3.96° ± 0.75% (T – 32)	± 1.98° ± 0.4% (T – 32) ± 0.4% (T – 32)
R or S	0° to 1260° 1260° to 1480°	± 1.5° ± 0.25% T	± 0.6° ± 0.1% T	32° to 1112° 1112° to 2700°	± 2.7° ± 0.25% (T – 32)	± 1.08° ± 0.1% (T – 32)
B	870° to 1700°	± 0.5% T	± 0.25%	1600° to 3100°	± 0.5% (T – 32)	± 0.25% (T – 32)
C**	0° to 426° 426° to 2315°	± 4.4° ± 1% T	— —	32° to 800° 800° to 4200°	± 8° ± 1% (T – 32)	— —

Figure 4.12: Ranges and tolerances of various thermocouple calibration types [176]

Figure 4.13: Mineral-Insulated probe-type thermocouple as used in the experimental rig

In total, 12 separate thermocouples were included in the system, at the pump inlet, the pump outlet, the evaporator inlet, the evaporator outlet (expander inlet), expander outlet, condenser

inlet, cold water inlet, cold water outlet, hot water inlet, and hot water outlet. In addition to these 11 thermocouples used for analysis, a twelfth thermocouple was included at the outlet of the water heater and connected to the PID controller, both allowing the controller to set the temperature, and acting as a backup to the heater's own internal thermocouple to prevent the water temperature exceeding 100°C.

4.1.7.2 Pressure

Pressure was measured using PX319 and PX419 series transducers, supplied by Omega. The details of this series of pressure transducers are provided in Table 4-6 and Table 4-7, and an image of the pressure transducers in Figure 4.14 and Figure 4.15: PX-419 Pressure Transducer

Table 4-6: Details of the PX-319 series pressure transducer

PX-319 Series	
Output	15-30 Vdc at 10mA
Excitation	9-30Vdc
Error Band (1-20 bar)	1% of absolute
Compensated Temperature	0-85°C
Maximum Pressure	200 bar
Connection	¼" NPT male

Figure 4.14: PX-319 Pressure Transducer

Table 4-7: Details of the PX-419 series pressure transducer

PX-419 Series	
Output	100mV at 5mA
Excitation	9-30Vdc
Error Band (1-20 bar)	0.08% of absolute

Compensated Temperature	-29-85°C
Maximum Pressure	69 bar
Connection	¼” NPT male

Figure 4.15: PX-419 Pressure Transducer

The pressure transducers were connected to the system with a standard ¼” NPT male threaded fittings. Five separate pressure transducers were included in the system, one at the pump outlet, one at the evaporator inlet, one at the expander inlet, one at the expander outlet, and one at the pump inlet. The multitude of pressure measurements allowed the pressure drops in the heat exchangers and pipework to be estimated, as well as calculate the derived thermodynamic properties of the working fluid at each point in the cycle.

4.1.7.3 Flow Rates

The flow of both heating and working fluids were measured by pulse output flow meters connected directly inline with the main flow of thermal or working fluids. The pulse output generated was converted directly to a flow rate by the data acquisition card.

An FPD2002 positive displacement flow meter (Figure 4.16) provided by Omega was used to measure the flow rate of the working fluid in the system. The primary challenge in sourcing an appropriate flow meter was to find a model that would provide sufficient accuracy at low mass flow rates. The details of the flow meter are given in

Table 4-8.

Table 4-8: Details of the FPD2000 series flow meter

FPD2000 Series Flow Meter	
Output	Pulse (2000/litre)
Input	10-28Vdc, 8mA @ 12 Vdc, 12mA @ 24Vdc
Maximum Temperature	204°C
Compensated Temperature	-40 - 85°C
Maximum Pressure	345 bar
Accuracy	±0.5%
Flow rate range	0.04-7.5 l/min
Connection	¼" NPT (Female)

Figure 4.16: FPD2002 Flow Meter

The flow rate of the hot water was measured by a 220-100-V-75-B FT2 Hall Effect flow meter (Figure 4.17) supplied by Titan Pumps. Its details are given in Table 4-9

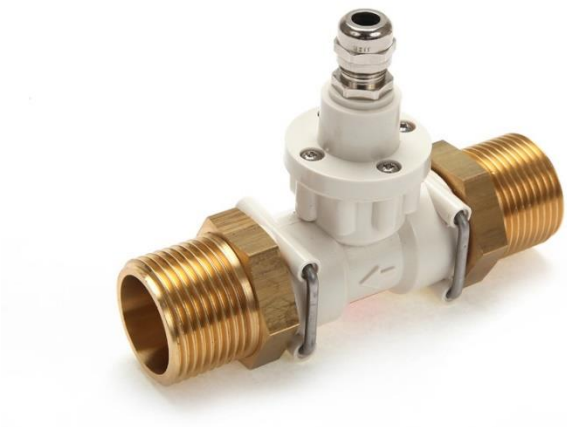

Figure 4.17: 220-100-V-75-B FT2 flow meter

Table 4-9: Details of the FT2 series flow meter

FT2 Series Flow Meter	
Output	Pulse (165/litre)
Input	5-24 Vdc
Maximum Temperature	125 °C
Compensated Temperature	-15 - 125°C
Accuracy	±0.75%
Flow rate range	6-100 l/min

4.1.7.4 Data Acquisition

Data from the temperature, pressure and flow rate sensors was fed to a computer using a DAQTEMP 14A data acquisition system, via a PCI plug-n-play card.

The data acquisition system features 14 thermocouple channels, 7 voltage channels, with a range of 0.156-10V, and 4 pulse channels, which allows the temperature, pressure and flow rate data to be simply collected and fed to the computer.

The signals received by the computer were interpreted using DAQView software. Each of the channels was configured using the calibration data for each sensor provided by the manufacturer, so the value of the relevant parameter could be displayed in intuitive units, instead of as a voltage or pulse output. A screencap of the data acquisition interface is presented in Figure 4.18.

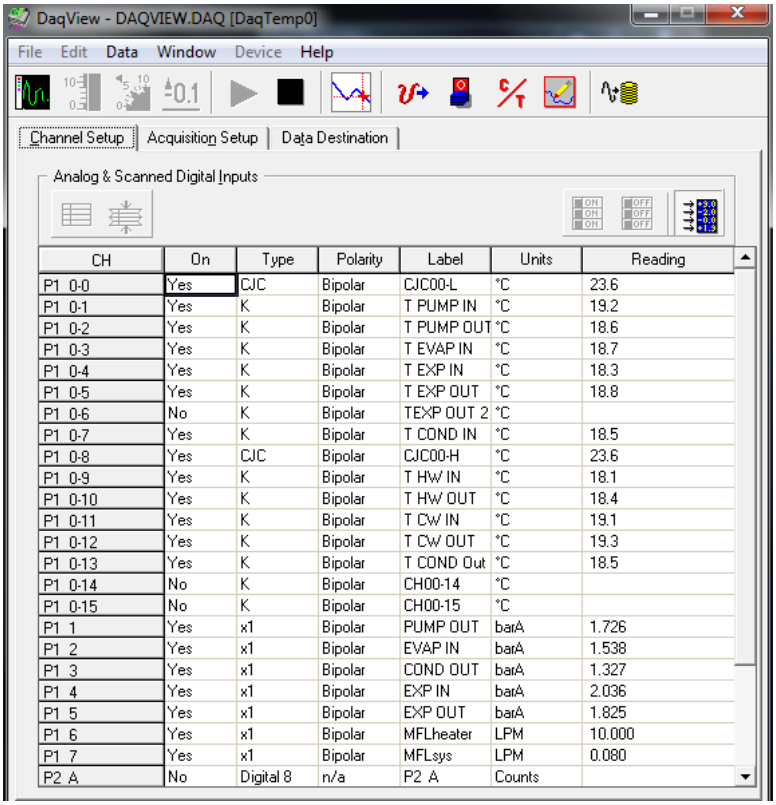

CH	On	Type	Polarity	Label	Units	Reading
P1 0-0	Yes	CJC	Bipolar	CJC00-L	°C	23.6
P1 0-1	Yes	K	Bipolar	T PUMP IN	°C	19.2
P1 0-2	Yes	K	Bipolar	T PUMP OUT	°C	18.6
P1 0-3	Yes	K	Bipolar	T EVAP IN	°C	18.7
P1 0-4	Yes	K	Bipolar	T EXP IN	°C	18.3
P1 0-5	Yes	K	Bipolar	T EXP OUT	°C	18.8
P1 0-6	No	K	Bipolar	TEXP OUT 2	°C	
P1 0-7	Yes	K	Bipolar	T COND IN	°C	18.5
P1 0-8	Yes	CJC	Bipolar	CJC00-H	°C	23.6
P1 0-9	Yes	K	Bipolar	T HW IN	°C	18.1
P1 0-10	Yes	K	Bipolar	T HW OUT	°C	18.4
P1 0-11	Yes	K	Bipolar	T CW IN	°C	19.1
P1 0-12	Yes	K	Bipolar	T CW OUT	°C	19.3
P1 0-13	Yes	K	Bipolar	T COND Out	°C	18.5
P1 0-14	No	K	Bipolar	CH00-14	°C	
P1 0-15	No	K	Bipolar	CH00-15	°C	
P1 1	Yes	x1	Bipolar	PUMP OUT	barA	1.726
P1 2	Yes	x1	Bipolar	EVAP IN	barA	1.538
P1 3	Yes	x1	Bipolar	COND OUT	barA	1.327
P1 4	Yes	x1	Bipolar	EXP IN	barA	2.036
P1 5	Yes	x1	Bipolar	EXP OUT	barA	1.825
P1 6	Yes	x1	Bipolar	MFLheater	LPM	10.000
P1 7	Yes	x1	Bipolar	MFLsys	LPM	0.080
P2 A	No	Digital 8	n/a	P2 A	Counts	

Figure 4.18: Screencap of the instrumentation interface

Test runs performed saved the data to a .csv file, which could then be analysed in Microsoft Excel. The data for temperature, pressure and flow was used directly, and the values of enthalpy and entropy could be inferred using the REFPROP plug-in for Excel.

4.1.7.5 Power Consumption

Two power readings were taken. The power consumed by the resistive load on the generator was measured using an Elcontrol digital power meter with LCD display as shown in Figure 4.19, mounted in the control box.

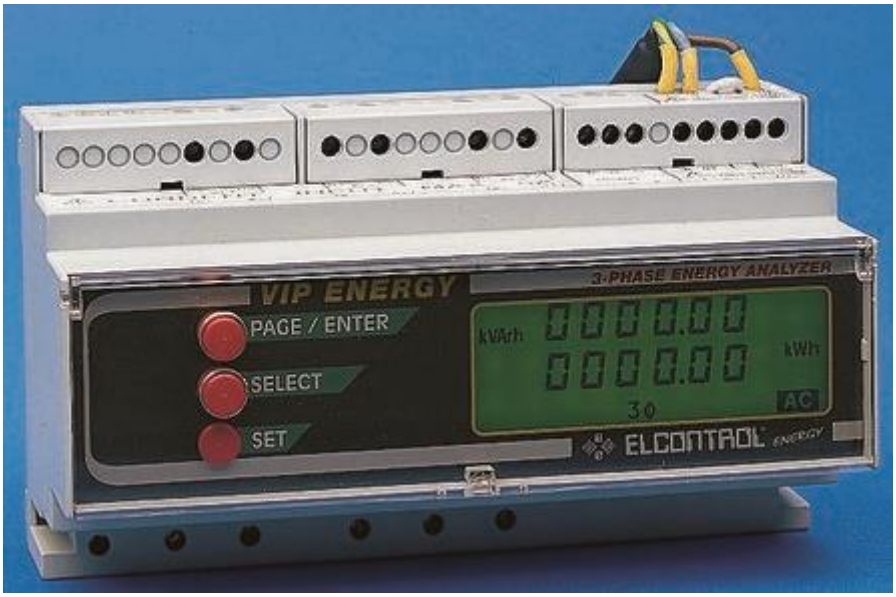

Figure 4.19: Elcontrol power meter

The power consumed by the inverter and the pump was measured by an ABBC11 digital power meter as shown in Figure 4.20, also mounted on the control box.

Figure 4.20: ABB C11 Digital Power Meter

Both power readings were noted manually at the end of each test run, as the signals were not noisy or subject to pulsations from the pump, and so did not need to be averaged to obtain a precise value.

4.2 Pressure and Leak Testing

The rig was fabricated by Star Refrigeration, and tested to a pressure of 18.9 bar on the high side and 15.4 bar on the low side for one hour. Upon delivery, an extended pressure test

revealed some leakage of pressurised air from the system over the timescale of several days to a week. Charging and commissioning of the rig was delayed until the source of any leaks could be identified.

Initial investigations using bubbling leak test fluid revealed observable leaks at several of the threaded and compression fittings attaching thermocouples and pressure transducers to the cycle. While the replacement of these fittings did slow down the leakage, the problem still persisted. At this point Argus Refrigeration were contracted to locate and seal any remaining leaks using an electronic leak sniffer and a small charge of R410a. This identified several further small leaks at threaded fittings, which were repaired. However, the rig still proved not to be tight after this, so Chilli Refrigeration Services were contracted to perform a leak test using a charge of fluorescent dye. Upon inspection with an ultraviolet light, the source of the final leaks was narrowed down to the threaded fittings of the heat exchangers. These leaks were repaired and the cycle retested, resulting in an acceptable pressure tightness for charging the system with refrigerant.

4.3 Safety Features

The rig incorporated several safety features to protect both the equipment and the operators.

4.3.1 Control Interlocks

Several electronic interlocks were placed in the control system to avoid the rig from reaching a dangerous state.

Firstly the heater could not be switched on unless the hot water circulation pump was running. This was to ensure a flow of water through the heater, ensuring that no "hot spots" formed, and avoiding unintentional boiling of the water inside the heater.

Secondly, two separate thermocouple interlocks were in place. The heater's internal thermocouple was set to 95°C, meaning that it would shut off its heating elements if the temperature exceeded that. Additionally, the control system for the rig took an input from a thermocouple at the exit of the heater, and would cut the power to the heater if this reading exceeded 95°C.

Thirdly, there was a pressure interlock built into the control system. If the pressure at the working fluid pump outlet, as read by the pressure transducer there, exceeded 14 bar, power to the pump would be cut.

4.3.2 Mechanical Safety Features

Two primary mechanical aspects of the rig were also intended to prevent a dangerous build-up of pressure anywhere in the system.

Firstly the storage tank for the hot water was large, and open to the atmosphere. This allowed any steam accidentally generated in the boiler to bubble through the water and condense, and more importantly, the fact that the tank was open to the air means that any steam will escape to the atmosphere, instead of being trapped and increasing the pressure inside the hot water circuit.

Secondly the system contained four separate pressure relief valves set to open at a gauge pressure of 14 bar. These valves were directed downwards and away from the user of the rig. As r245fa is heavier than air, in the event of a pressure relief valve opening, the risk of asphyxiation is minimised.

4.4 Commissioning

The commissioning of the rig was carried out by Chilli Refrigeration services, using a Javac XTR Pro refrigerant recovery machine as shown in Figure 4.21. This drew the system down to vacuum to remove air and moisture from the inside of the refrigerant loop. Liquid refrigerant was then added from a cylinder to the system via a charge port between the receiver and the pump. Initially the low pressure inside the system led to the vaporisation of any working fluid added, but as more fluid was added, the pressure eventually increased to a level where liquid refrigerant could exist. As more liquid was added after this point, it flowed downwards through gravity to the inlet of the pump.

The working fluid pump was left running during this process. Initially no fluid was drawn through the pump as it was in the vapour phase due to the low pressure. Even as liquid began to pool above the pump, the pressure caused by the weight of the fluid was insufficient to provide the net positive suction head to the pump, so the pump cavitated instead of pulling in liquid. As the liquid level above the pump increased so did the net positive suction head. The reading from the flow meter, located at the pump outlet, was observed throughout. When it indicated that there was a flow of liquid through this part of the rig, it was an indication that the level of liquid was high enough to provide adequate NPSH to the pump to avoid cavitation. The mass of the refrigerant charge in the system was measured using a refrigerant scales placed underneath the refrigerant cylinder during the charging process. It was found that a charge of 7kg was sufficient to allow the pump to operate.

Figure 4.21: Javac XTR Pro Refrigerant Recovery Unit

4.5 Completed Rig

Figure 4.22 shows a labelled diagram of the completed experimental rig, showing the principal components and their layout.

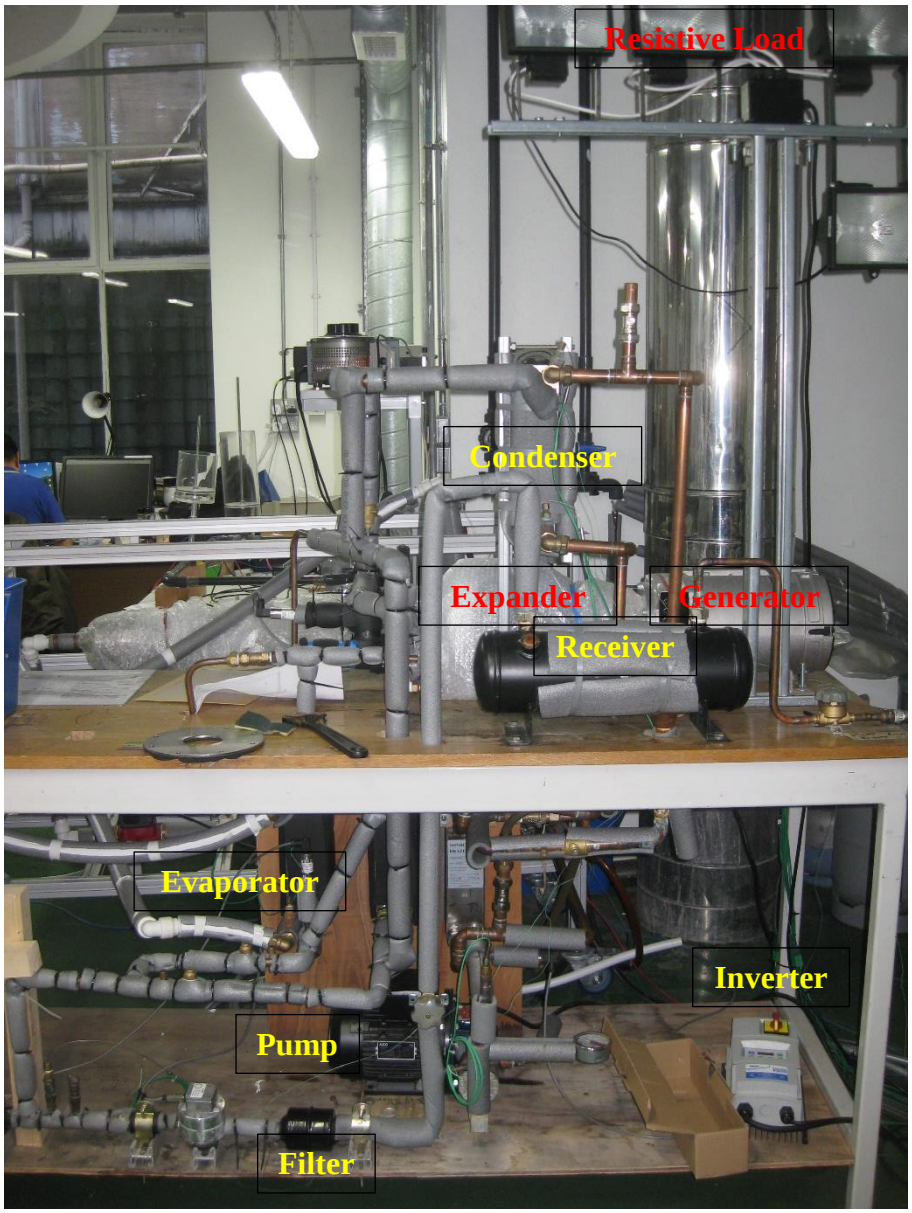

Figure 4.22: Labelled diagram of the completed experimental rig

4.6 Summary

In this chapter the design and specifications of the rig were presented. The components selected for the rig are shown, and their performances given. How they meet the requirements identified in the design of the rig is also discussed. In the following chapter the results generated by the experimental rig are presented and discussed.

CHAPTER 5- EXPERIMENTAL RESULTS

In this chapter, firstly the test methodology for the experiments is laid out. The parameters varied and the values measured are presented and the justification for each of these given. Several derived parameters are also used in the analysis of the results. The equations for these and the rationale behind using them are also given.

For the results themselves, firstly non-regenerative cycles are examined. The flow of working fluid was passed directly to the evaporator and condenser. Tests were carried out across a range of heat source temperatures and for two pump speeds. The observed trends in first law efficiency were then analysed with respect to the obtained data of temperatures, pressures and flow rates, as well as the derived values of enthalpy changes across components.

Next, regenerative cycles are examined. The flow was directed through the regenerator for these tests, recovering heat from the expander exhaust. As for the non-regenerative cycles, the trends in efficiency were analysed and explained with the measured and derived information about the cycle.

Finally, the effect of working fluid composition on both regenerative and non-regenerative cycles was analysed. Again, the measured and derived information about the cycle was used to explain the trends in working fluid composition.

5.1 Validation of the Theoretical Model

The lab-scale rig developed using the experimental model was used to validate the thermodynamic accuracy of the model, and the results of this validation are presented below in both graphical and tabular form.

5.1.1 For Pure Working Fluids

Four cases of cycle operating conditions using r245fa were taken to validate the model for pure working fluids demonstrating two heat source temperatures at two difference pump speeds.

Table 5-1: Validation of theoretical model for pure working fluids

	60°C, 20Hz			75°C, 20Hz			95°C, 20Hz			95°C, 40Hz		
	Model	Rig	Error	Model	Rig	Error	Model	Rig	Error	Model	Rig	Error
T1	281.1	281.1	0.0%	282.4	282.4	0.0%	281.4	281.4	0.0%	281.5	281.5	0.0%
T2	283.2	283.2	0.0%	284.4	284.4	0.0%	284.5	284.5	0.0%	283.1	283.1	0.0%
T3	282.6	282.6	0.0%	283.5	283.5	0.0%	283.8	283.8	0.0%	317.2	317.2	0.0%
T4	322.1	320.8	-0.4%	348.0	344.9	-0.9%	325.1	325.5	0.1%	346.3	350.1	1.1%

T5	322.1	319.9	-0.7%	348.0	343.9	-1.2%	325.1	326.3	0.4%	346.3	348.7	0.7%
T6	331.5	331.5	0.0%	348.1	343.7	-1.3%	366.2	366.2	0.0%	360.6	360.6	0.0%
T7	312.2	313.9	0.5%	313.0	318.5	1.7%	348.4	342.1	-1.8%	330.1	331.3	0.4%
T8	312.2	307.8	-1.4%	313.0	314.9	0.6%	348.4	332.9	-4.4%	330.1	331.3	0.4%
T9	293.1	292.8	-0.1%	295.2	295.4	0.0%	296.6	294.9	-0.6%	298.3	296.9	-0.5%
T10	293.1	292.2	-0.3%	295.2	295.7	0.1%	296.6	291.3	-1.8%	298.3	293.8	-1.5%
P1	1.2	1.2	0.0%	1.3	1.3	0.0%	1.1	1.1	0.0%	1.2	1.2	0.0%
P2	3.3	3.3	0.0%	6.9	6.9	0.0%	3.6	3.6	0.0%	6.6	6.6	0.0%
P3	3.3	3.3	0.0%	6.9	6.5	-5.3%	3.6	3.6	-1.3%	6.6	7.5	14.1%
P4	3.3	3.2	-4.0%	6.9	6.3	-7.7%	3.6	3.7	1.2%	6.6	7.2	10.2%
P5	3.3	3.1	-6.6%	6.9	6.2	-10.1%	3.6	3.7	3.8%	6.6	7.0	6.3%
P6	3.3	3.0	-9.1%	6.9	6.0	-12.5%	3.6	3.8	6.4%	6.6	6.7	2.4%
P7	1.2	1.2	0.0%	1.3	1.3	0.0%	1.4	1.4	0.0%	1.5	1.5	0.0%
P8	1.2	1.2	0.0%	1.3	1.3	0.0%	1.4	1.4	0.0%	1.5	1.5	0.0%
P9	1.2	1.2	-1.1%	1.3	1.3	0.5%	1.4	1.3	-6.2%	1.5	1.4	-5.1%
P10	1.2	1.2	-3.4%	1.3	1.3	1.6%	1.4	1.1	-18.6%	1.5	1.2	-15.4%
h1	210.2	210.2	0.0%	211.8	211.8	0.0%	210.6	210.6	0.0%	210.7	210.7	0.0%
h2	213.0	213.0	0.0%	214.6	214.6	0.0%	214.6	214.6	0.0%	212.9	212.9	0.0%
h3	212.1	212.1	0.0%	213.5	213.4	0.0%	213.7	213.7	0.0%	258.2	258.2	0.0%
h4	264.8	263.0	-0.7%	301.6	297.1	-1.5%	269.0	269.5	0.2%	299.2	304.7	1.8%
h5	440.2	438.6	-0.4%	458.3	455.5	-0.6%	442.3	443.2	0.2%	457.2	458.8	0.3%
h6	450.0	450.8	0.2%	458.4	455.7	-0.6%	485.2	484.8	-0.1%	473.5	473.1	-0.1%
h7	437.0	438.5	0.3%	437.4	442.6	1.2%	471.1	465.0	-1.3%	453.2	454.4	0.3%
h8	437.0	439.3	0.5%	437.4	443.8	1.4%	471.1	465.9	-1.1%	453.2	409.1	-9.7%
h9	419.1	418.8	-0.1%	420.7	420.8	0.0%	421.7	420.4	-0.3%	422.9	421.8	-0.2%
h10	225.8	224.6	-0.5%	228.6	229.2	0.2%	230.4	223.4	-3.1%	232.6	226.8	-2.5%
hEvap	237.0	237.8	0.3%	243.8	241.1	-1.1%	270.6	270.2	-0.1%	260.5	260.2	-0.1%
hPump	2.8	2.8	0.0%	2.8	2.8	0.0%	4.0	4.0	0.0%	2.3	2.3	0.0%
hExpander	13.0	12.3	-5.5%	21.0	13.2	-37.3%	14.1	19.8	40.7%	20.3	18.7	-7.6%

Table 5-1 shows a comparison between the theoretical model and the results from the experimental rig, along with the percentage error between them. Although most of the readings for temperature, pressure and enthalpy are close to each other for all of the cycles considered, and the enthalpy changes across the pump and the evaporator are within 1.1% of the

experimental values for all cases, the value for the enthalpy change across the expander shows a significant effort in some cases, ranging from 5.5% to 40.7%.

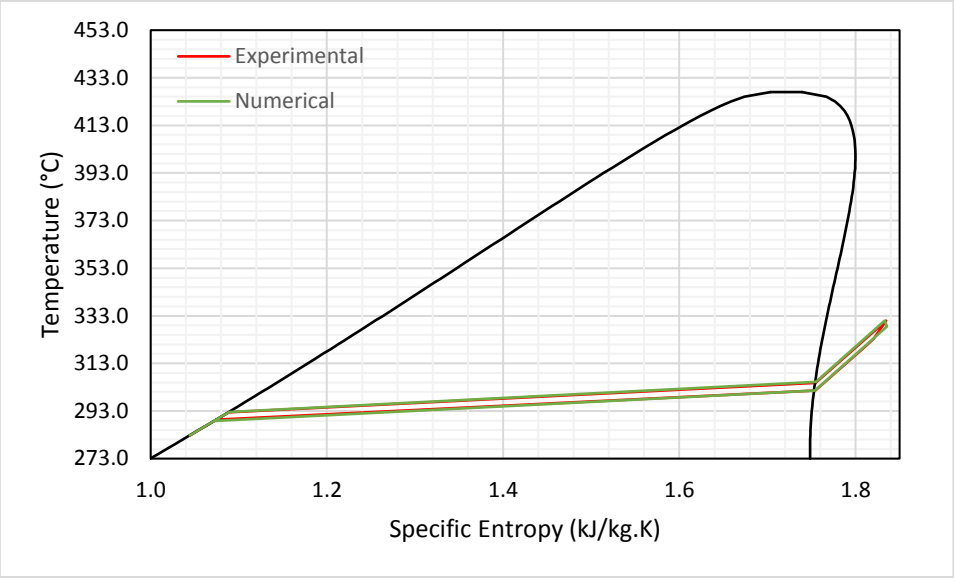

Figure 5.1: T-s diagram of the cycle for a pump speed of 20Hz and a heat source temperature of 60°C. The error for expander enthalpy in this case was 5.5%.

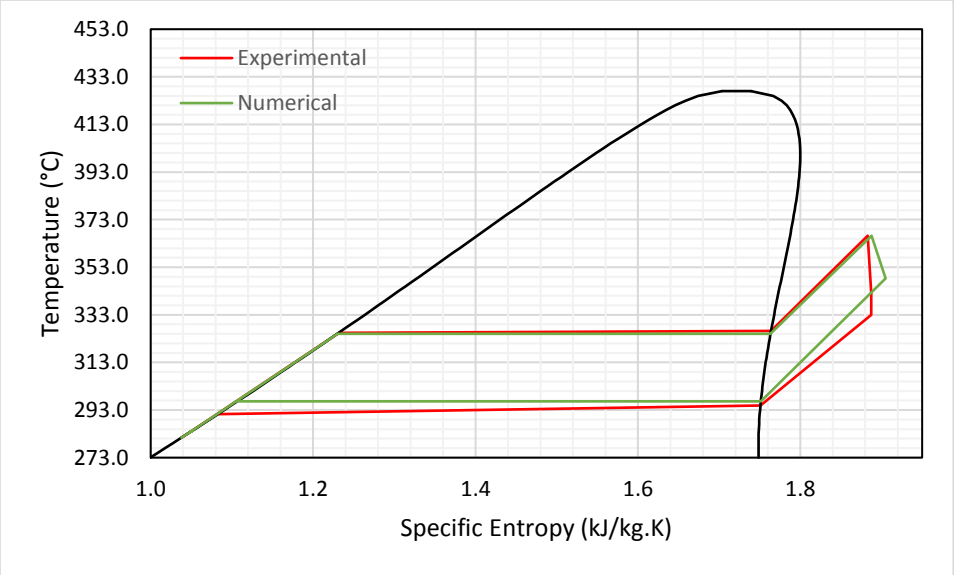

Figure 5.2: T-s diagram of the cycle for a pump speed of 20Hz and a heat source temperature of 95°C. The error for expander enthalpy in this case was 40.7%.

Figure 5.1 and Figure 5.2 show T-s diagrams for the two most extreme cases of this. It can be seen that the expansion process in Figure 5.1 closely matches between the experimental and theoretical results, whereas in Figure 5.2 the experimental results exhibit a much greater temperature drop across the expander, perhaps due to increased thermal leakage. In other

words, it is hard to tell whether the discrepancy between the experimental results is due to an inaccuracy in the model, or due to a flaw in the design or operation of the rig leading to escape of heat. Addressing this question is an interesting avenue for future research.

5.1.2 For Working Fluid Mixtures

Again, four cases were taken for fluid mixtures, and these cases are displayed in Table 5-2

Table 5-2: Validation of model for a working fluid mixture of 80% R245fa and 20% R134a

	60°C, 20Hz			70°C, 20Hz			90°C, 20Hz			90°C, 40Hz		
	Model	Rig	Error	Model	Rig	Error	Model	Rig	Error	Model	Rig	Error
T1	282.7	282.7	0.0%	281.0	281.0	0.0%	280.6	280.6	0.0%	282.3	282.3	0.0%
T2	284.6	284.6	0.0%	283.1	283.1	0.0%	284.5	284.5	0.0%	284.1	284.1	0.0%
T3	290.8	290.8	0.0%	281.6	281.6	0.0%	283.7	283.7	0.0%	321.9	321.9	0.0%
T4	292.6	292.5	-0.1%	323.2	326.8	1.1%	304.6	304.2	-0.1%	333.6	335.6	0.6%
T5	305.2	304.9	-0.1%	334.1	325.7	-2.5%	316.5	316.6	0.0%	343.9	344.3	0.1%
T6	331.0	331.0	0.0%	335.4	335.4	0.0%	361.0	361.0	0.0%	362.0	362.0	0.0%
T7	328.5	323.3	-1.6%	313.1	303.5	-3.1%	350.1	345.2	-1.4%	335.4	336.2	0.2%
T8	328.5	319.4	-2.8%	313.1	303.0	-3.2%	350.1	338.0	-3.5%	335.4	336.2	0.2%
T9	301.6	301.6	0.0%	302.4	301.5	-0.3%	300.1	299.4	-0.3%	304.0	303.1	-0.3%
T10	288.8	289.3	0.2%	289.6	286.7	-1.0%	287.2	284.0	-1.1%	291.3	288.6	-0.9%
P1	2.1	2.1	0.0%	1.9	1.9	0.0%	1.8	1.8	0.0%	2.0	2.0	0.0%
P2	2.3	2.3	0.0%	5.7	5.7	0.0%	3.3	3.3	0.0%	7.4	7.4	0.0%
P3	2.3	2.3	0.1%	5.7	6.4	13.1%	3.3	3.3	-1.2%	7.4	8.0	8.5%
P4	2.3	2.3	-0.6%	5.7	6.2	9.9%	3.3	3.4	1.6%	7.4	7.8	4.9%
P5	2.3	2.3	-1.3%	5.7	6.0	6.6%	3.3	3.5	4.4%	7.4	7.5	1.2%
P6	2.3	2.2	-2.0%	5.7	5.9	3.4%	3.3	3.6	7.2%	7.4	7.2	-2.4%
P7	2.0	2.0	0.0%	2.1	2.1	0.0%	1.9	1.9	0.0%	2.2	2.2	0.0%
P8	2.0	2.0	0.0%	2.1	2.1	0.0%	1.9	1.9	0.0%	2.2	2.2	0.0%
P9	2.0	2.0	0.6%	2.1	2.0	-3.1%	1.9	1.9	-2.8%	2.2	2.1	-2.9%
P10	2.0	2.1	1.6%	2.1	1.9	-9.2%	1.9	1.8	-8.3%	2.2	2.0	-8.8%
h1	212.4	212.4	0.0%	210.1	210.1	0.0%	209.6	210.1	0.2%	211.8	211.8	0.0%
h2	214.8	214.8	0.0%	212.9	212.9	0.0%	214.8	215.0	0.1%	214.3	214.3	0.0%
h3	223.0	223.0	0.0%	211.1	211.1	0.0%	213.7	213.9	0.1%	265.2	265.2	0.0%
h4	225.4	225.1	-0.1%	267.1	272.1	1.9%	241.4	242.1	0.3%	281.9	284.6	1.0%
h5	425.4	425.1	-0.1%	445.5	447.1	0.3%	433.4	434.4	0.2%	452.0	452.3	0.1%

h6	450.3	450.4	0.0%	446.9	446.4	-0.1%	478.3	482.6	0.9%	472.3	472.7	0.1%
h7	448.5	443.6	-1.1%	433.6	424.4	-2.1%	469.7	467.4	-0.5%	454.9	455.6	0.2%
h8	448.5	439.8	-1.9%	433.6	426.3	-1.7%	469.7	468.5	-0.3%	454.9	455.6	0.2%
h9	422.8	422.8	0.0%	423.4	422.7	-0.1%	421.8	421.2	-0.1%	424.5	423.9	-0.1%
h10	220.4	221.0	0.3%	221.4	217.6	-1.7%	218.3	215.0	-1.5%	223.6	220.0	-1.6%
hEvap	235.5	235.6	0.0%	234.0	233.5	-0.2%	263.5	267.6	1.5%	258.0	258.3	0.1%
hPump	2.4	2.4	0.0%	2.8	2.8	0.0%	5.2	5.0	-4.3%	2.6	2.6	0.0%
hExpander	1.8	6.9	380%	13.3	22.0	65.4%	8.6	15.2	76.8%	17.5	17.1	-2.1%

Again it can be seen that for most of the absolute values of temperature, pressure and enthalpy the errors are small, and that for the heat exchangers, the values of enthalpy change are extremely accurate. However, the value for the enthalpy change across the expander still shows a high degree of discrepancy between the experimental and theoretical results.

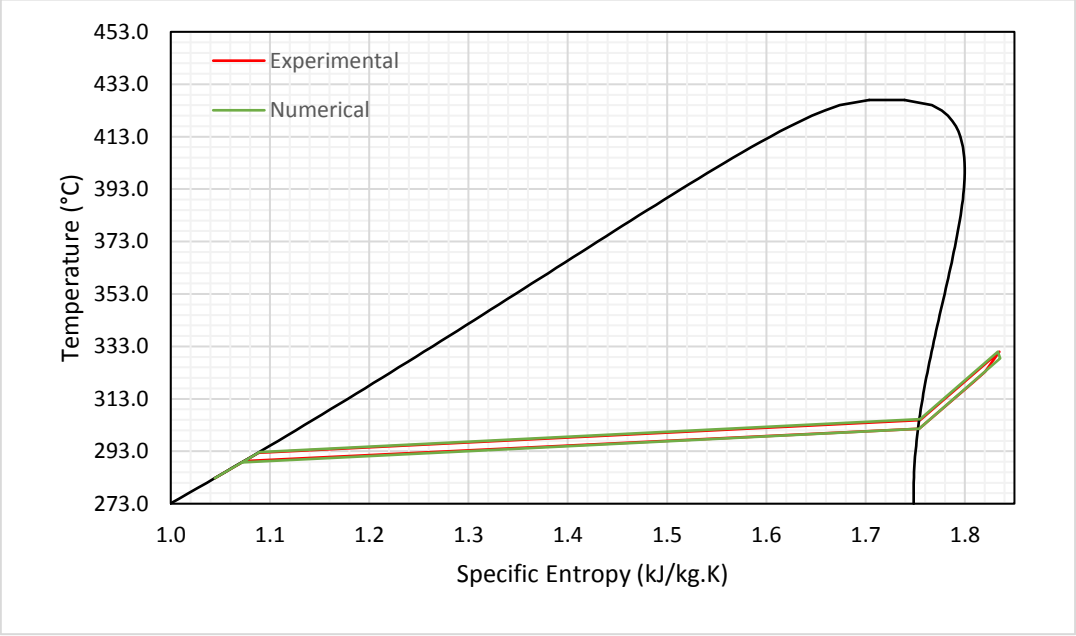

Figure 5.3: T-s diagram of experimental and theoretical results for a working fluid composition of 80% R245fa:20% R134a, a heat source temperature of 60°C and a pump speed of 20Hz. The error in expander enthalpy change for this cycle is 280%

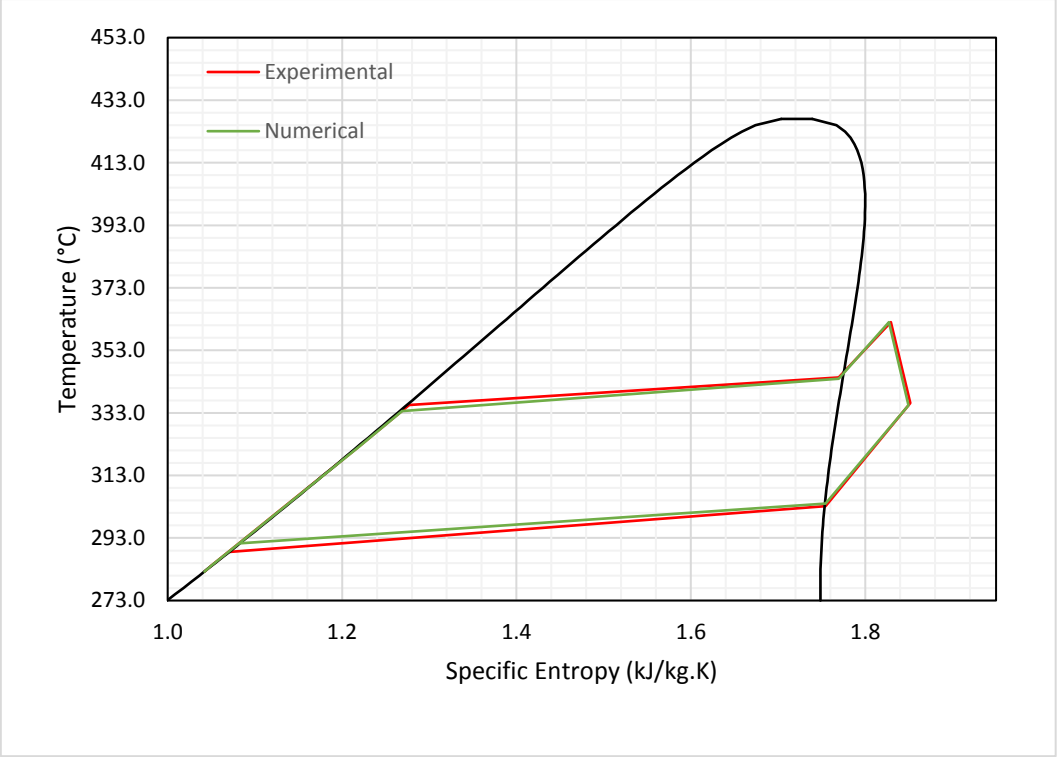

Figure 5.4: T-s diagram of experimental and theoretical results for a working fluid composition of 80% R245fa:20% R134a, a heat source temperature of 90°C and a pump speed of 40Hz. The error in expander enthalpy change for this cycle is 2.1%.

Figure 5.3 and Figure 5.4 show the T-s diagrams for two cycles using working fluid mixtures. Once again it is clear that the expansion process is the major source of error between the theoretical model and the experimental rig. In Figure 5.3 the discrepancy is proportionally extremely significant due to the very small enthalpy drop across the expander. In Figure 5.4, the most accurate of the comparisons, the discrepancy is small.

This validation highlights that while the theoretical model developed is highly accurate in many cases, its results for the expansion process are not always reliable, due to the fact that they do not simulate such phenomena as leakage of fluid past the scrolls, or loss of heat from the surface of the expander. To ensure the accuracy of the model, measures must be taken to improve its forecasting, and also the rig may be modified to reduce these sources of error, for example by adding more insulation to its surface, or by allowing tests to run for a longer period of time to ensure that thermal equilibrium has been reached. The results of the validation shown in Table 3-2, as well as the agreement in the isentropic efficiency figures with Figure 4.3 suggest that the model is still acceptably accurate for steady-state conditions with high enthalpy drops across the expander.

5.2 Test Methodology

The state of the rig for each test was defined by five factors:

-The Working Fluid Composition, which was determined by the initial charging of the rig. The refrigerant cylinder was placed on a scales, attached to the charging ports on the charging machine and the rig, and refrigerant was added to the system until the pump was flooded. With the initial mass of the refrigerant in the system known the composition of the working fluid could be changed to the desired value by the addition of the appropriate amount of the secondary working fluid. The working fluid compositions considered in this thesis ranged from [100% R245fa; 0% R134a] to [70%R245fa; 30% R134a] by mass. At higher mass fractions of R134a the evaporator pressure would rise above the rated pressure of the expander, so these could not be tested with the current experimental setup.

-The Hot Water Temperature, which was set by the temperature controller installed in the control box, and described in Chapter 5. This was limited to below 100°C due to the use of water at atmospheric pressure as the thermal fluid. The minimum hot water temperature for the cycle to run and the generator to synchronise was found to be 60°C. Tests were carried out with hot water temperatures at 5°C intervals between these two values.

-The Pump Speed. The speed of the pump controlled both the mass flow rate of the working fluid and the pressure ratio of the cycle. As the pump was a positive displacement device the speed of the pump motor was directly correlated to the volume flow rate of the working fluid. Assuming no significant changes in the density of the liquid entering the pump, this means that the speed of the pump motor was also directly linked to the mass flow rate. A higher mass flow rate resulted in a higher back pressure from the expander, increasing the pressure ratio of the cycle. The speed of the pump was controlled by an AC inverter, supplied by mains electricity which could vary the frequency of AC supplied to the pump from 20Hz to 60Hz. It was found during testing that a pump speed above 40Hz resulted in a heat exchanger loading that was too great for the electric heater to provide a constant temperature of hot water to the evaporator. Therefore supply frequencies of 20Hz and 40Hz were used to generate results for this thesis.

-The Regenerator: The flow of working fluid could either be routed from the pump directly to the evaporator, or else passed through the cold side of a regenerator. Similarly, the working

fluid at the outlet of the expander could be directed straight to the condenser or passed through the hot side of the regenerator. The flow path of the fluid was controlled by four ball valves which could be opened and closed to redirect the working fluid to the desired path. Each combination of parameters was tested with the rig in regenerative and non-regenerative mode.

Each of these variables was set at the start of a test and the rig left running at a steady state for 20 minutes before readings were taken. This was to allow all components in the rig to reach thermal equilibrium, as during early tests it was found that the thermal mass of the components meant that the cycle still had not reached a steady state before this point.

Data was collected using a DAQTEMP 14A data acquisition system. This logged data at a predetermined interval (in this case 10 seconds) to a .csv file which could then be processed using Microsoft Excel. For calculating the steady-state operating conditions of the system, the final 12 readings in each run, representing 2 minutes of continuous operation, were averaged to give representative values for power, temperature, pressure and flow rate. REFPROP 9.1 was used to calculate values of density, enthalpy and entropy from these values. The measurement uncertainties as presented in Chapter 5 were included in these results.

5.3 Considered Parameters

Several derived parameters were considered in the analysis of the results. Numbering of states is as described in Figure 3.6.

Firstly, the measured efficiency, given by

$$\eta_{measured} = \frac{W_{net}}{\dot{m}_f(h_6 - h_3)} \tag{5.1}$$

Where W_{net} is the power output from the generator given by the power meter in the rig's control box, less the pump power, $\dot{m}_f$ is the mass flow rate of the working fluid, calculated from the flow meter, h_6 is the specific enthalpy at the expander inlet, calculated using REFPROP from measured pressure and temperature data, and h_3 is the specific enthalpy at the evaporator inlet, again calculated from measured temperature and pressure data. This means that the measured efficiency is the power delivered to the resistive load, divided by the thermal energy imparted to the working fluid in the evaporator

Secondly, the calculated efficiency, given by:

$$\eta_{calculated} = \frac{(h_6 - h_7) - (h_2 - h_1)}{(h_6 - h_3)} \quad (5.2)$$

Where h_7 is the calculated specific enthalpy at the expander outlet. Therefore the calculated efficiency is the thermal energy lost by the working fluid as it passed through the expander.

The losses in the expander and the generator, which include over- and under-expansion losses, leakage past the scrolls, thermal conductivity, both through the scrolls and into the mass of the expander and the environment, as well as mechanical and electrical losses in the transmission and generator, were given as a percentage:

$$Expander\ Losses = \frac{\eta_{calculated} - \eta_{measured}}{\eta_{calculated}} \quad (5.3)$$

The isentropic efficiency of the expansion process was calculated using the equation:

$$\eta_{isentropic} = \frac{h_6 - h_7}{h_6 - h_{7,isentropic}} \quad (5.4)$$

Where $h_{7,isentropic}$ is the ideal enthalpy at the expander outlet, assuming no entropy increase across the expander.

5.4 Pump power consumption

The power consumed by the pump and inverted was directly correlated to the speed of the inverter. The frequency inversion process was highly inefficient, leading to large pump losses relative to the expander power, as shown in Figure 5.5. The power consumed by the pump had to be subtracted from the expander power in order to give a net efficiency.

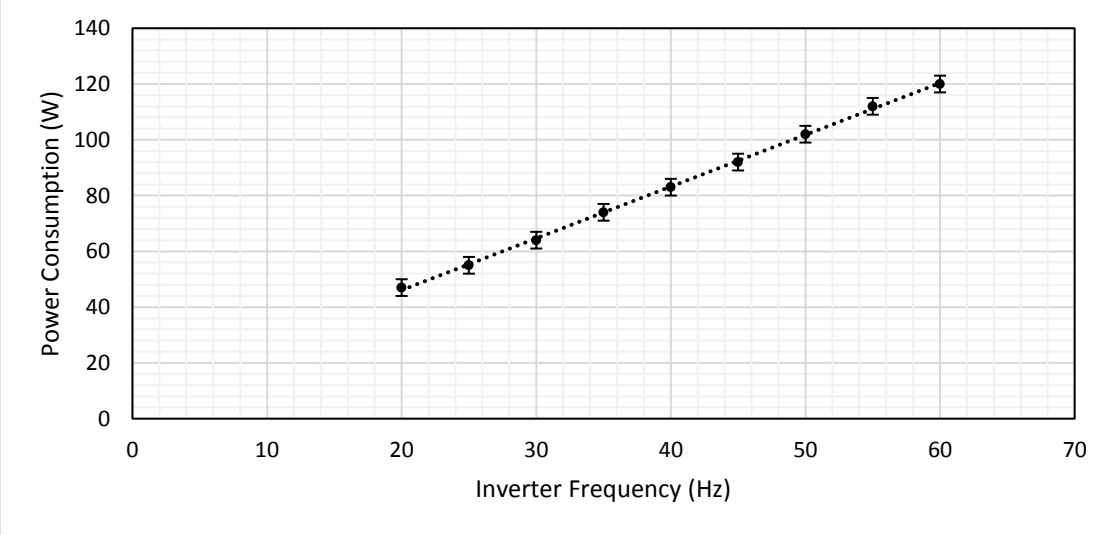

Figure 5.5: Variation in Inverter Power Consumption for a range of pump speeds

5.5 Non-regenerative cycles

The cycle was run in a non-regenerative configuration at two different pump speeds, 20Hz and 40Hz, for a range of heat source temperatures from 60°C to 95°C. Additional pump speeds could not be tested due to excessive vibration in the rig when the pump was operating near its resonant frequency.

5.5.1 Pump Speed 20Hz

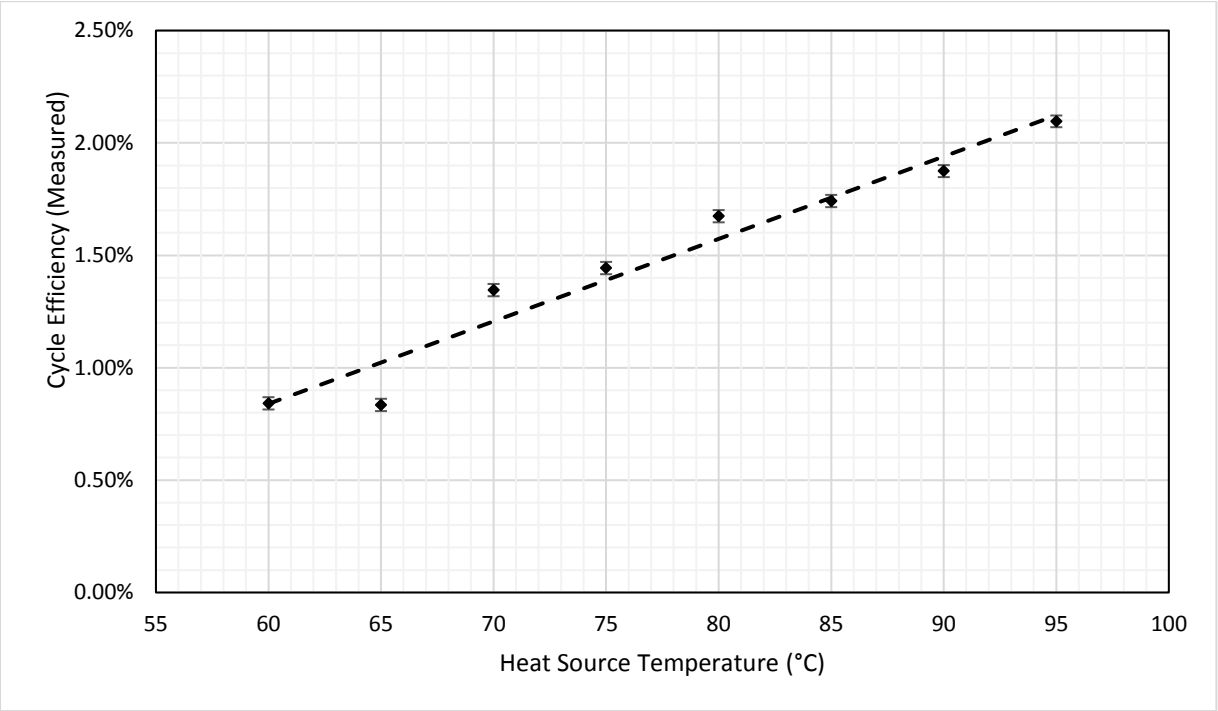

Figure 5.6: Variation in the measured first law efficiency of the rig in a non-regenerative configuration with varying heat source temperature for a pump speed of 20Hz

Figure 5.6 shows how the measured efficiency of the cycle is affected by the heat source temperature for a pump speed of 20Hz. A clear upward trend can be seen from the data, although there is some scatter in the results. The overall effect of the instrumentation inaccuracy on the results is relatively small in comparison to both their absolute value and the differences between them. The maximum value of measured efficiency is 2.1%. To account for this observed trend, several other parameters must be considered.

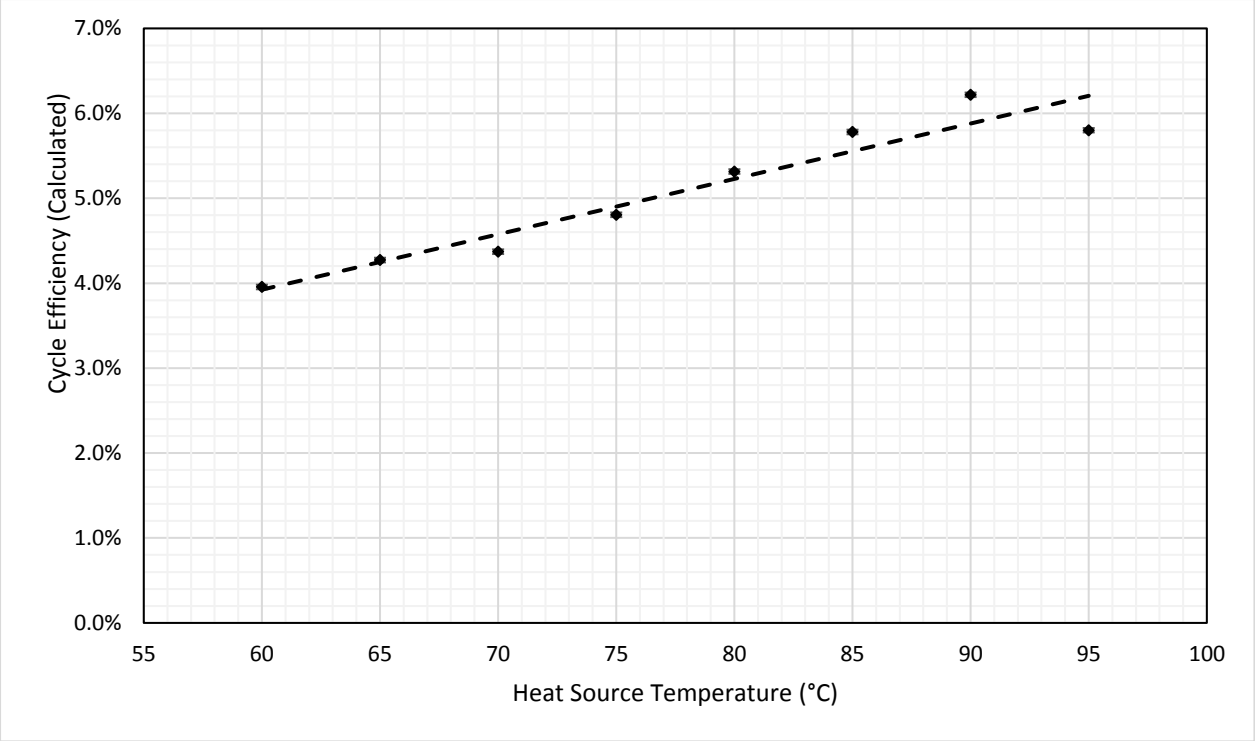

Figure 5.7: Variation in the calculated first law efficiency of the rig in a non-regenerative configuration with varying heat source temperature for a pump speed of 20Hz

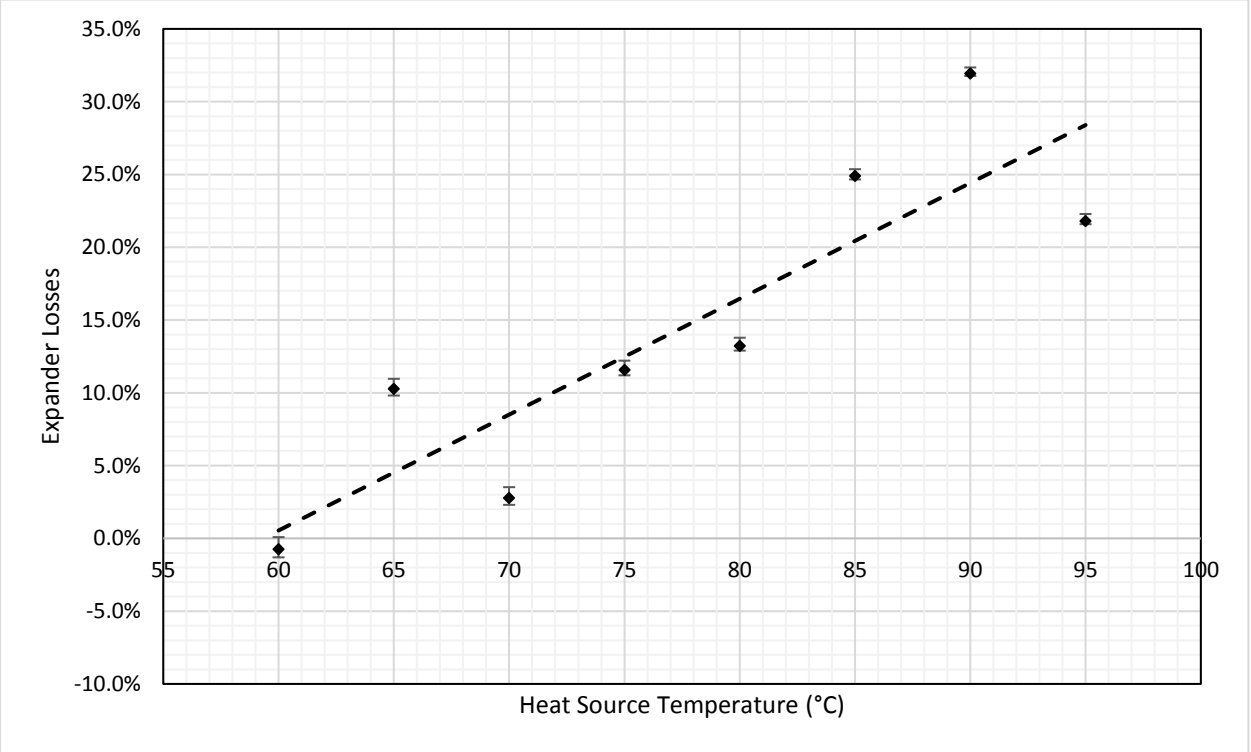

Figure 5.8: Variation in the expander losses of the rig in a non-regenerative configuration with varying heat source temperature for a pump speed of 20Hz

Figure 5.7 shows the variation in the calculated efficiency with varying temperature, and Figure 5.8 shows the variation in expander losses under the same conditions. The calculated efficiency is in general higher than the measured efficiency, and shows a steeper upward trend, with a highest value of 6.22%. The main reason for this is thought to be the disparity between the calculated and measured pump power. The maximum calculated pump power based on the enthalpy change across the pump is 36W. This is compared to a measured pump power consumption of 50W to 80W in the speed range considered in this thesis. With a power output of 70-95W from the cycle at a pump speed of 20Hz, the discrepancy between the calculated and measured pump power is highly significant. Whether this disparity is caused by an overestimation in the isentropic efficiency, mechanical losses, or losses in the inverter is impossible to say with the current experimental setup, and merits further investigation. The expander losses also show an increasing trend with increasing heat source temperature. There are several potential explanations for this, which will now be discussed.

Firstly, and most intuitively, the increased heat source temperature could be leading to increased conduction losses from the expander. Although the expander is well-insulated, heat losses are inevitable, and will be greater at a higher heat source temperature, so the working fluid will lose energy as it passes through the expander that is not transmitted to the electrical load. This is shown graphically in the two T-s diagrams for heat source temperatures of 60°C and 95°C, shown in Figure 5.9 and Figure 5.10 respectively.

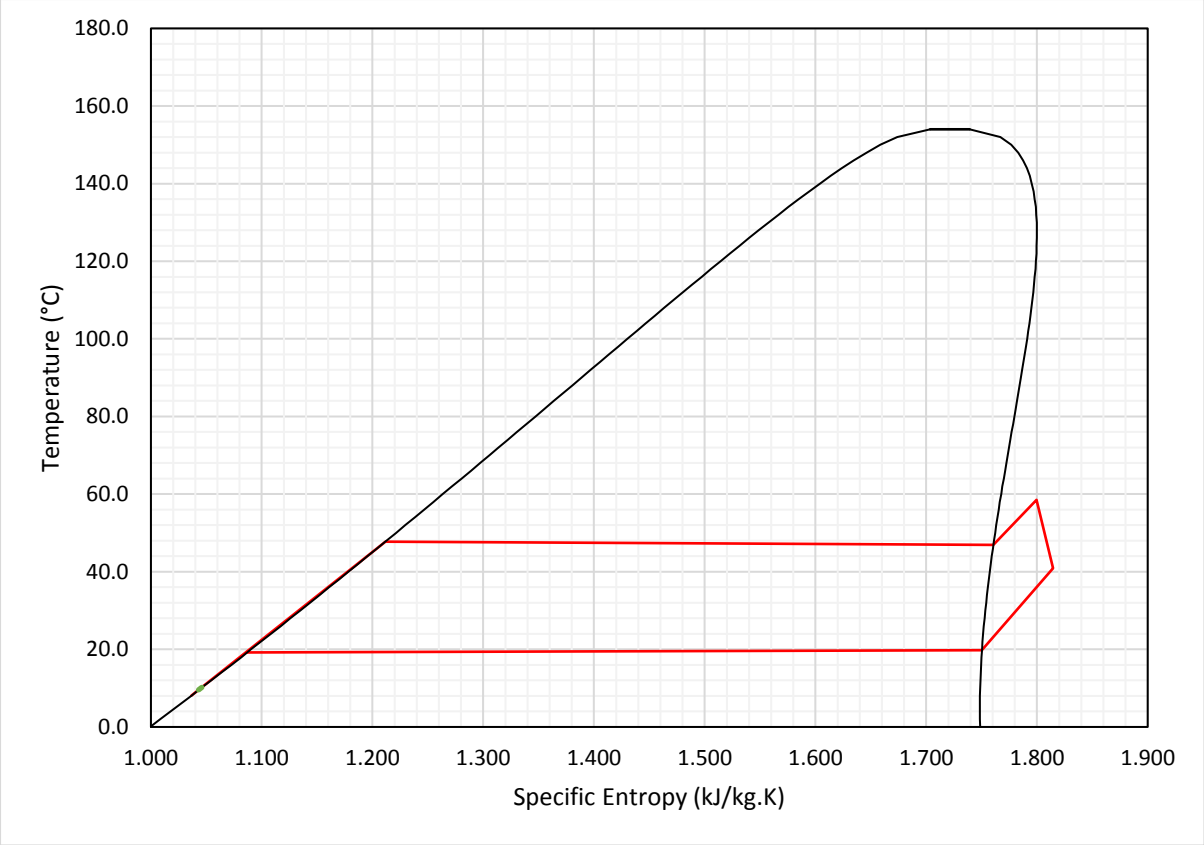

Figure 5.9: T-s diagram for a heat source temperature of 60°C, for a non-regenerative cycle with the pump speed set at 20Hz.

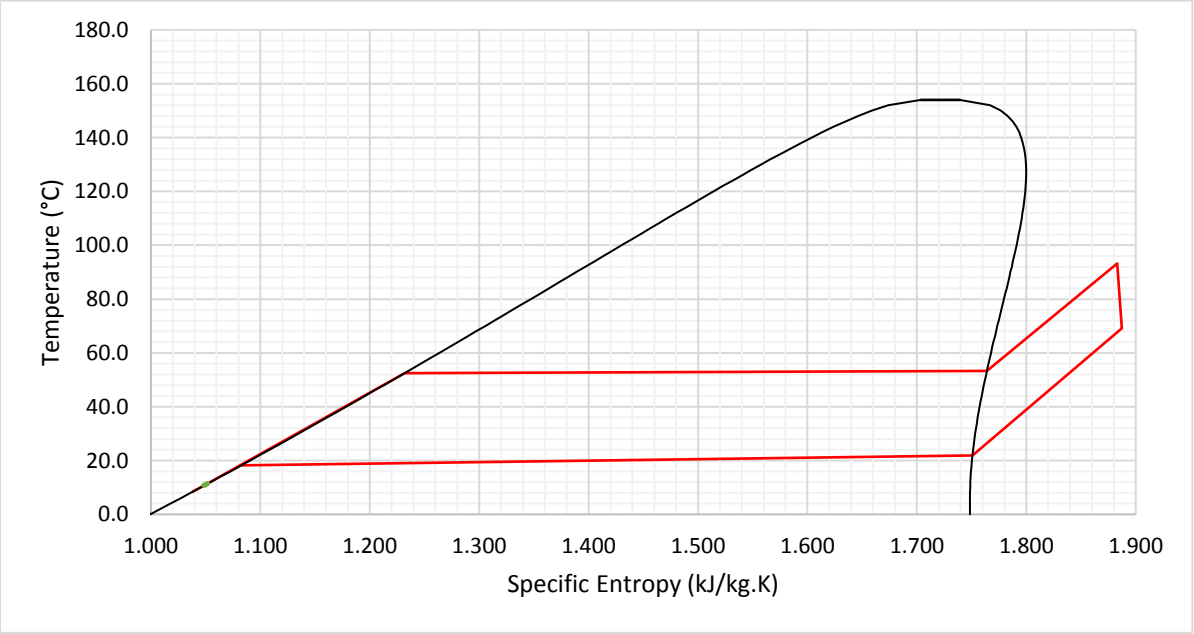

Figure 5.10: T-s diagram for a heat source temperature of 95°C, for a non-regenerative cycle with the pump speed set at 20Hz.

Secondly, a changing pressure ratio could be leading to differing over- or under-expansion losses for the cycle as the heat source temperature changes.

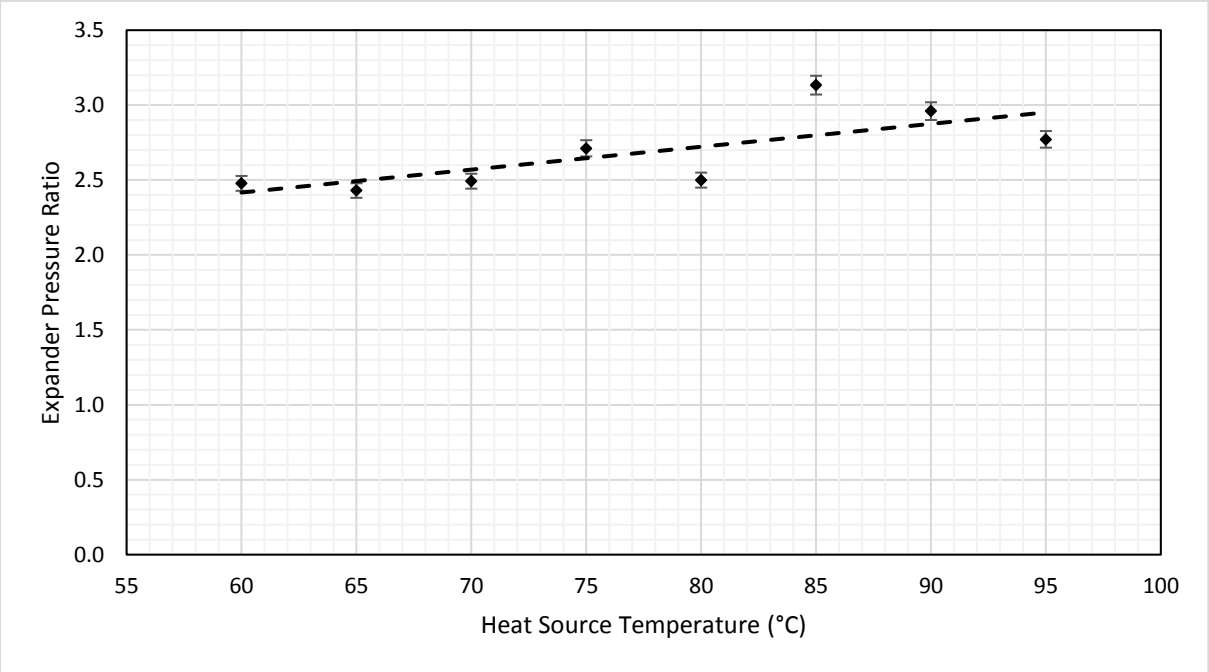

Figure 5.11: Variation in Cycle Pressure Ratio with varying heat source temperature for a non-regenerative cycle and a pump speed of 20Hz

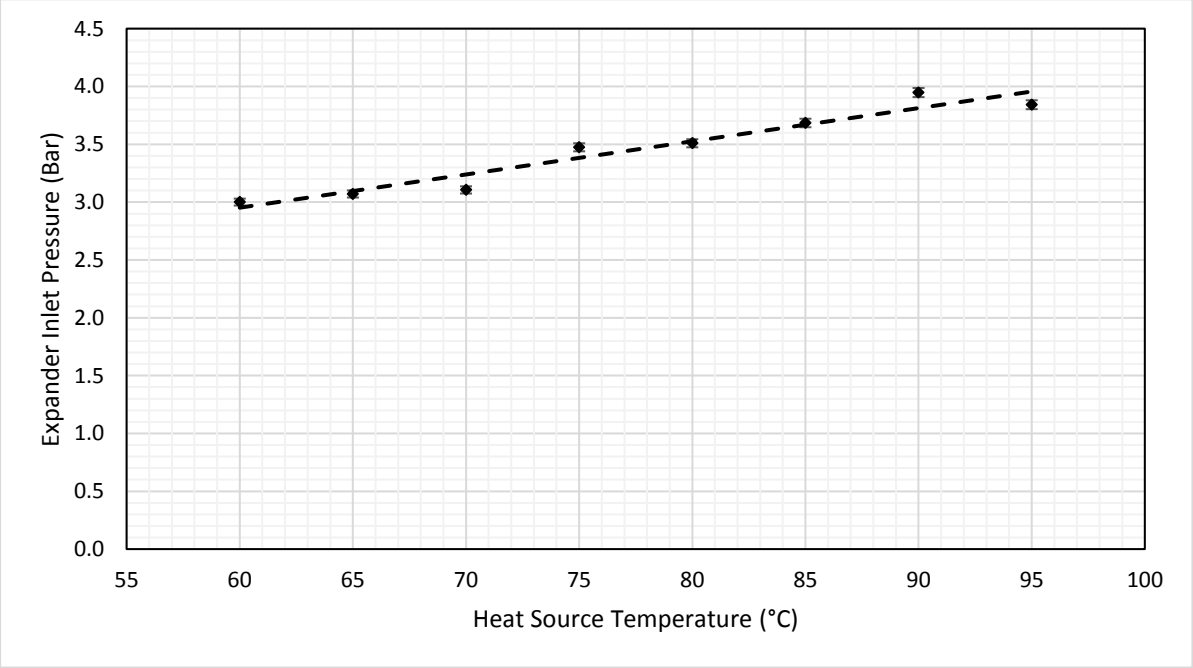

Figure 5.12: Variation in Expander Inlet Pressure with varying heat source temperature for a non-regenerative cycle and a pump speed of 20Hz

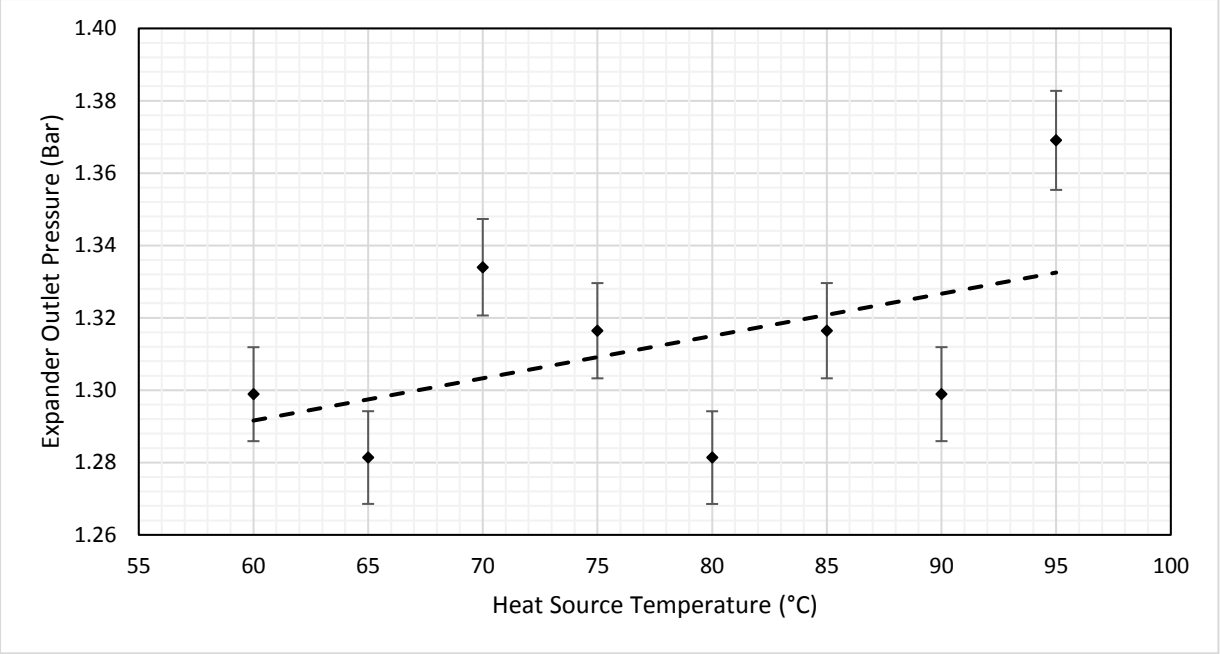

Figure 5.13: Variation in Expander Outlet Pressure with varying heat source temperature for a non-regenerative cycle and a pump speed of 20Hz

Figure 5.11, Figure 5.12, and Figure 5.13 show the variation in the pressure ratio of the cycle, the expander inlet pressure, and the expander outlet pressure with varying heat source temperature. It can be seen that the general trend for the pressure ratio is to increase, with the expander inlet pressure rising more quickly than the expander outlet pressure as the vapour pressure of the working fluid increases with increasing temperature. For all heat source temperatures, the pressure ratio across the expander is below 3.5, so the fluid will always exit the expander in an over-expanded condition. As the pressure ratio increases, it more closely approaches the expander's in-built ratio of 3.5, so therefore over-expansion losses should actually be decreasing with increasing temperature, this is borne out by the increasing trend in the isentropic efficiency of the expansion process as shown in Figure 5.14.

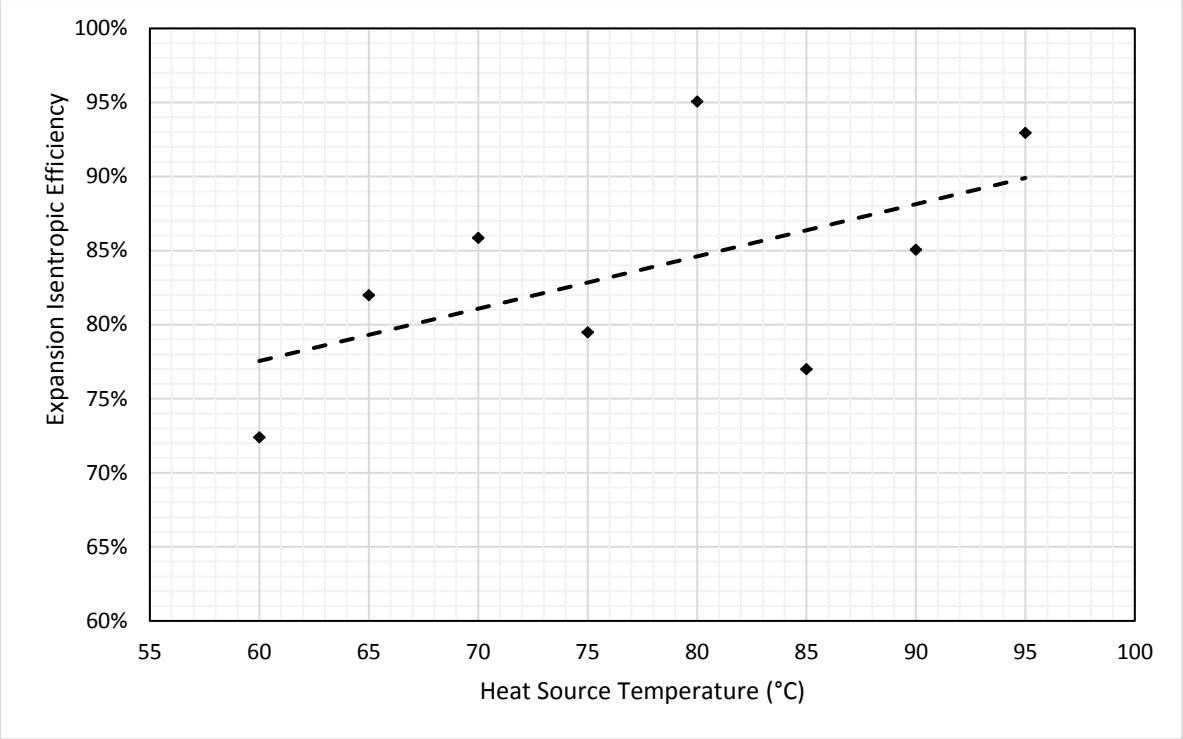

Figure 5.14: Variation in the Isentropic Efficiency of the expansion process with varying heat source temperature for a non-regenerative cycle with a pump speed of 20Hz

Thirdly, an increase in mechanical losses could be responsible for the discrepancy between the calculated and measured results. As the expander is a positive displacement device, the rotational speed is a function of the mass flow rate and the fluid specific volume at the expander inlet. These two parameters are plotted in Figure 5.15 and Figure 5.16. It can be seen that there is a slight increasing trend in the working fluid mass flow rate, and a decreasing trend in the fluid specific volume. This means that there will be a greater volume of fluid passing through the expander the higher the heat source temperature becomes, which will lead to an increased expander rotational speed and potentially increased mechanical losses.

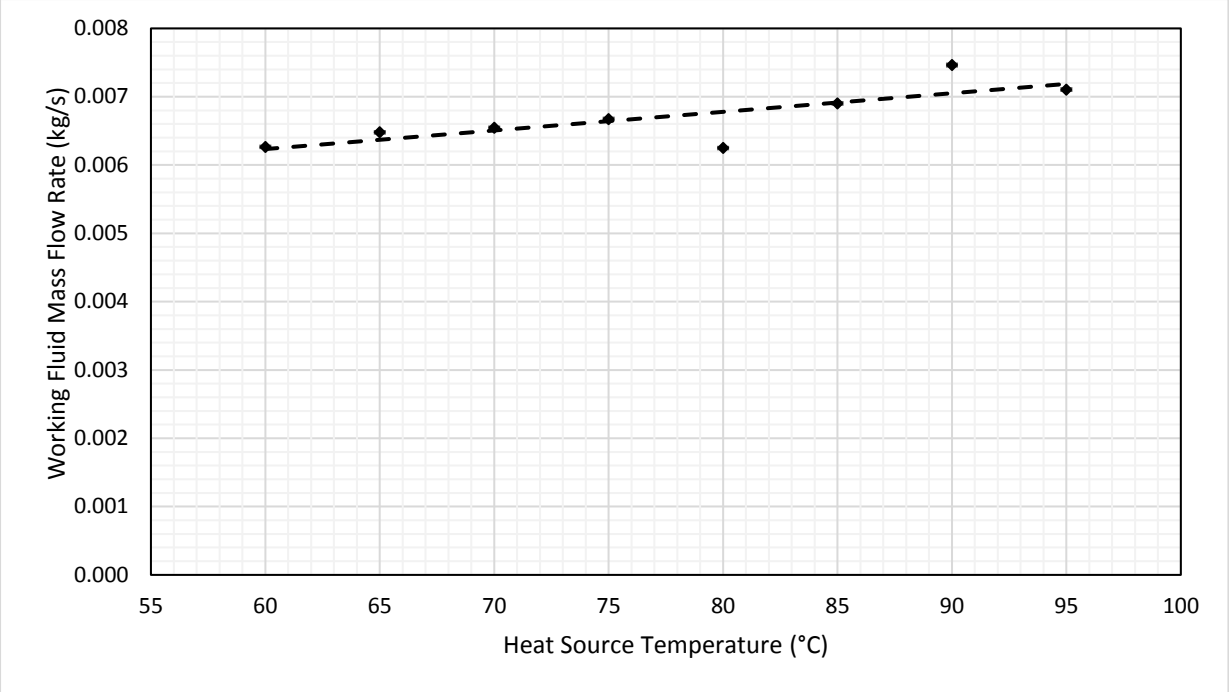

Figure 5.15: Variation in working fluid mass flow rate with changing heat source temperature for a nonregenerative cycle with a pump speed of 20Hz

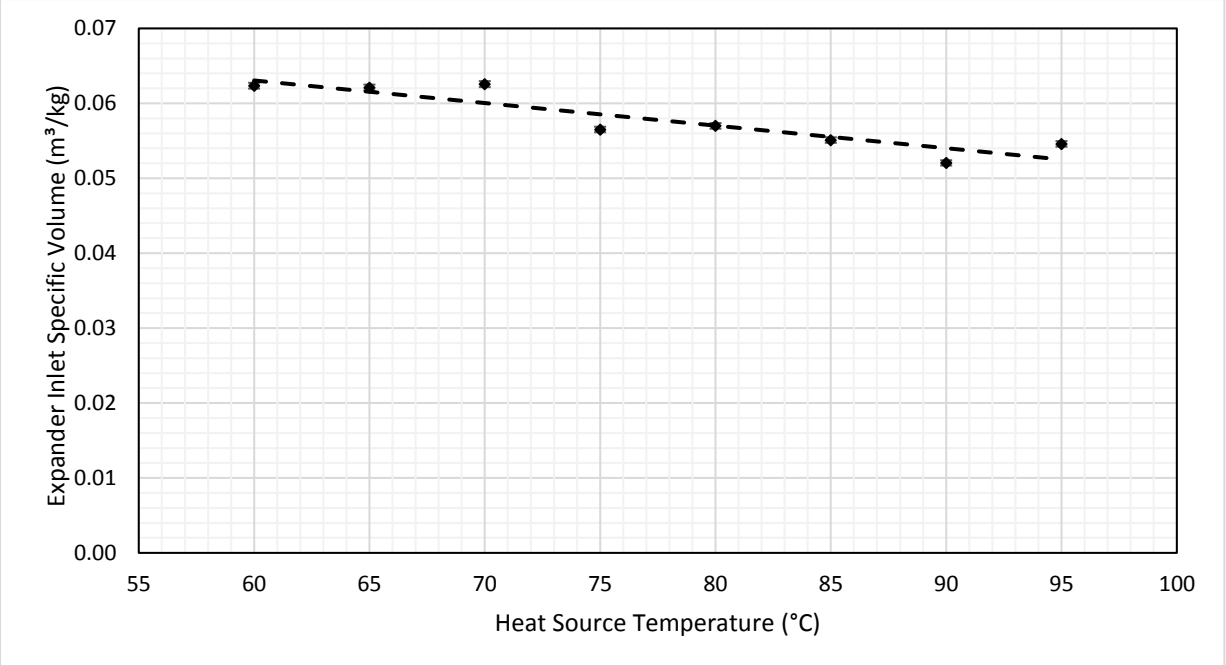

Figure 5.16: Variation in Expander Inlet specific volume with increasing heat source temperature for a non-regenerative cycle and a pump speed of 20Hz

From these figures, it seems most likely that the discrepancy between the calculated and measured first law efficiencies is due to increased heat losses from the expander, possibly

exacerbated by increased mechanical losses due to greater rotational speed. This agrees with the experimental and theoretical analysis performed by Quoilin et al [142].

As there was a pressure transducer at both the inlet and outlet of the evaporator, the pressure losses across the heat exchanger could also be evaluated. This information is plotted in Figure 5.17.

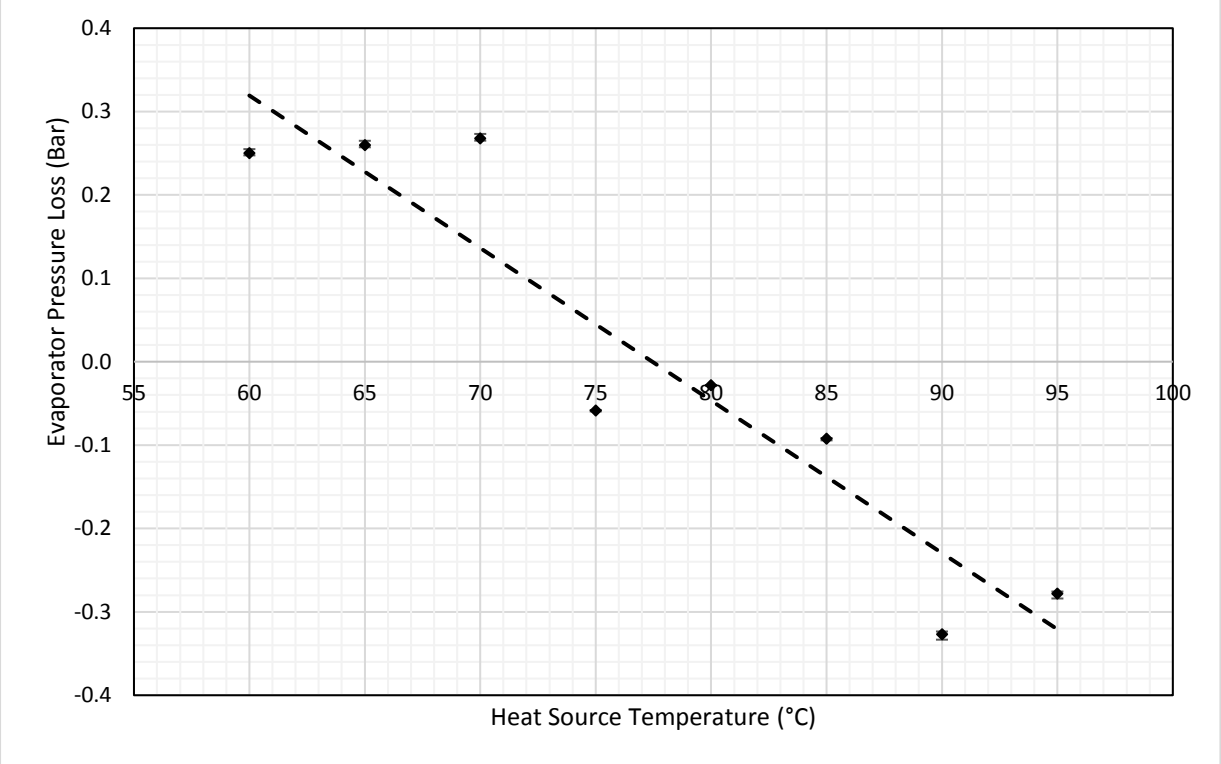

Figure 5.17: Variation in evaporator pressure losses with varying heat source temperature for a non-regenerative cycle with a pump speed of 20Hz.

It can be seen that at the lower heat source temperatures the pressure loss across the evaporator is positive, in other words, the pressure at the outlet of the evaporator is lower than at its inlet. However, there is a downward trend in this plot, and at higher heat source temperatures this value is negative, indicating that there is actually an increase in the working fluid pressure as it passes through the evaporator. This is most likely due to two conflicting effects in the evaporator, firstly the viscous and friction losses in the fluid flow as it passes through the exchanger, which tends to reduce the pressure, and secondly, the increased temperature increasing the pressure of the vapour due to thermal expansion. As the temperature rises, the second effect begins to dominate.

The data collected also allowed for the temperature profiles inside the heat exchangers to be inferred. Several pinch point diagrams for different heat source and sink temperatures are shown in the following figures.

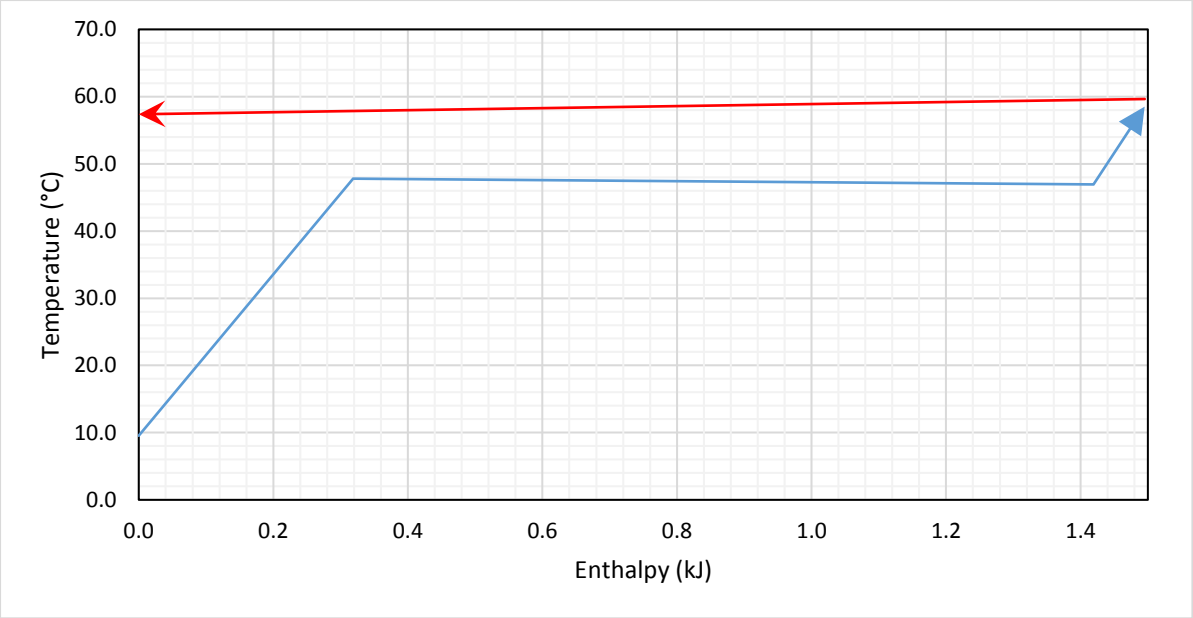

Figure 5.18: Pinch Point Diagram for the evaporator at a heat source temperature of 60°C for a non-regenerative cycle at a pump speed of 20Hz.

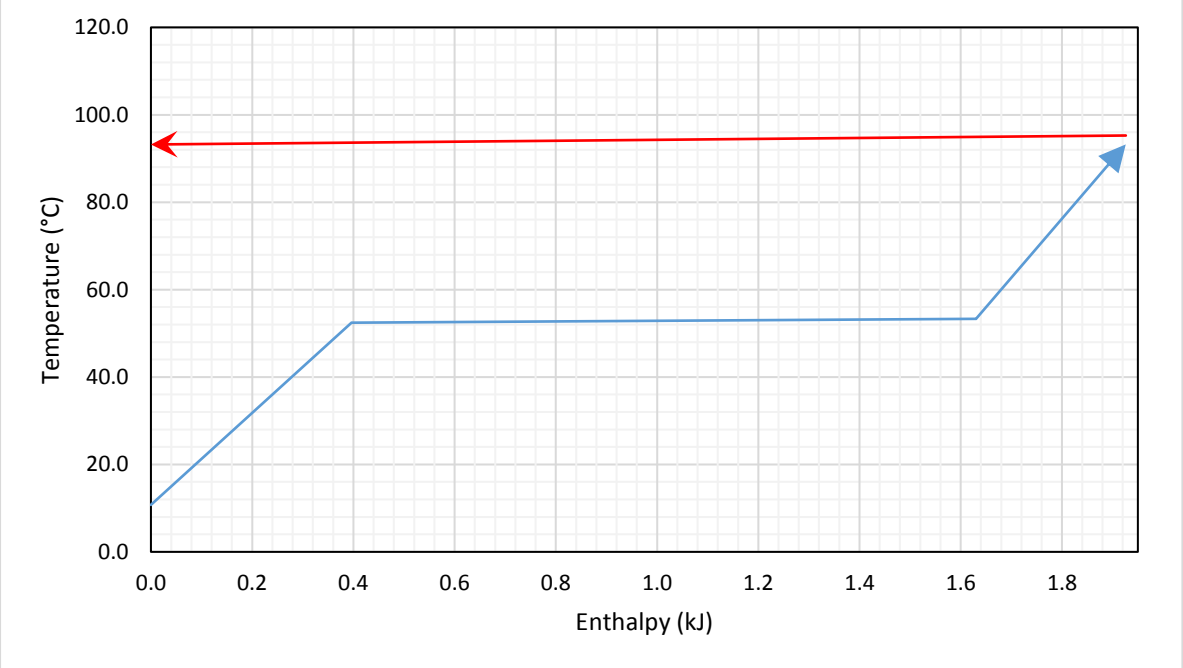

Figure 5.19: Pinch Point Diagram for the evaporator at a heat source temperature of 95°C for a non-regenerative cycle at a pump speed of 20Hz.

Figure 5.18 and Figure 5.19 show pinch point diagrams for the evaporator, for heat source temperatures of 60°C and 95°C respectively. Several things can be observed on these plots. Firstly, the effects of pressure changes in the evaporator can be seen. The upper figure features a slight drop in the temperature of the working fluid during phase change due to the pressure loss in the evaporator, whereas the lower figure shows a slight increase in temperature during phase change, due to the increase in pressure in the evaporator at these higher heat source temperatures. Secondly, the change in the temperature of the thermal fluid (hot water) in both cases is extremely small, and the pinch point at the working fluid outlet is very narrow, 2.2°C for the 95°C case, and just 1.2°C for the 60°C case. This is with the circulation pump for the hot water set to its lowest speed, so the lack of temperature drop in the thermal fluid implies that the hot water circulation pump or the evaporator is oversized for its task. Thirdly, the increased temperature at the expander inlet has increased the expander work slightly, but this increase is limited by the fact that the scroll expander is a positive displacement device, so much of the advantage that could have been gained by an increased heat source temperature has gone into adding superheat to the fluid. These pinch point diagrams will later be compared to similar plots for zeotropic working fluid blends so the performance of both classes of fluid can be analysed and contrasted.

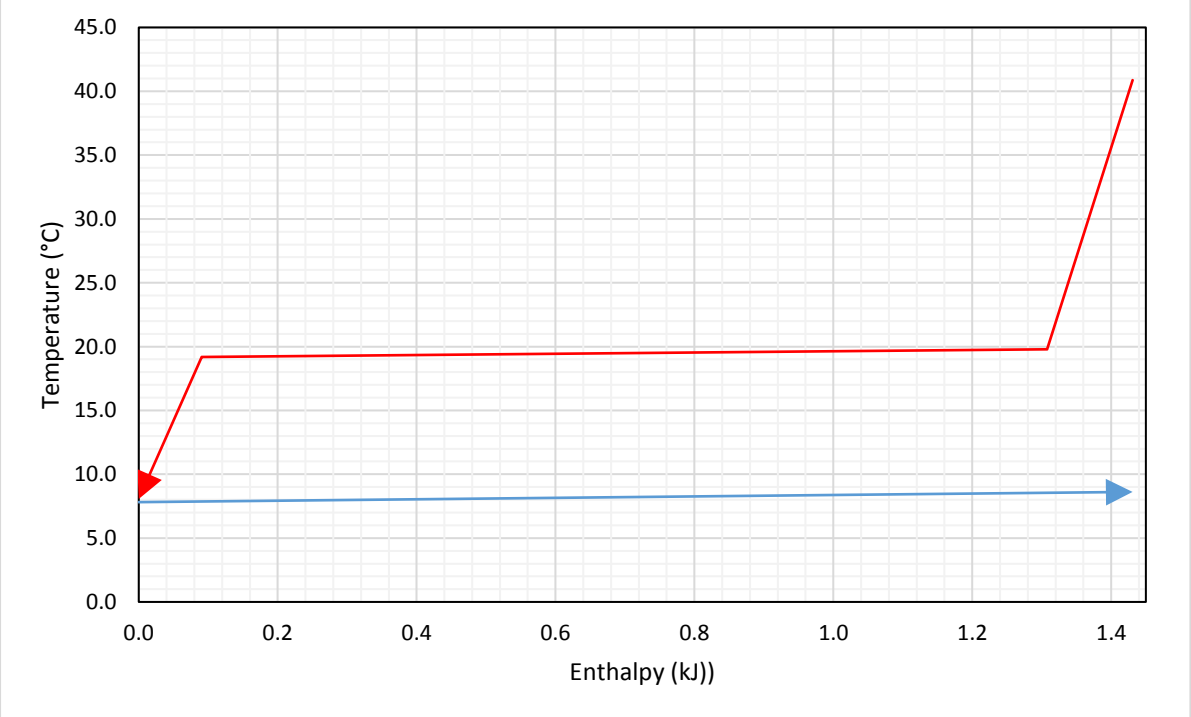

Figure 5.20: Condenser pinch point diagram for a heat source temperature of 60°C for a non-regenerative cycle with a pump speed of 20Hz.

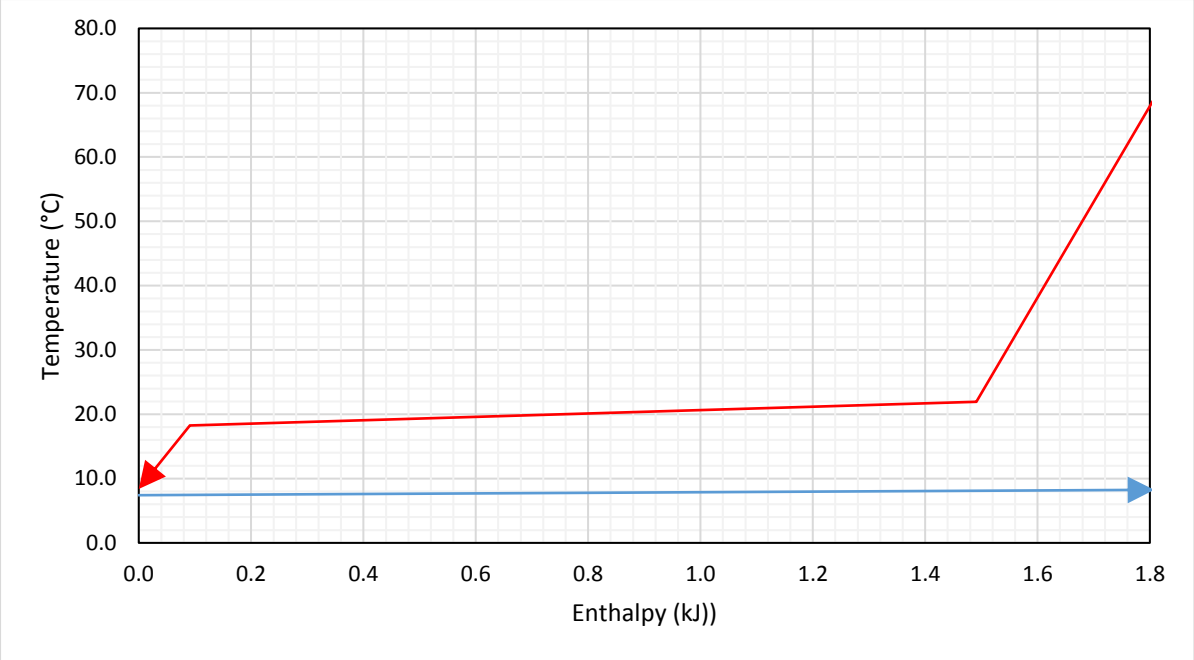

Figure 5.21: Condenser pinch point diagram for a heat source temperature of 95°C for a non-regenerative cycle with a pump speed of 20Hz.

Figure 5.20 and Figure 5.21 show the pinch point diagrams for the condenser at two different heat source temperatures. It can be noted that once more the pinch point temperature difference at the working fluid outlet is very narrow, and the change in the temperature of the cooling fluid, in this case a water/ethylene glycol mixture from the building's chiller, is very small. Again, this implies that the heat exchanger and the cooling system are oversized for this particular application. Also, an increased temperature at the condenser inlet can be observed in Figure 5.21. This is due to the increased superheat at the expander inlet, which can itself be seen in Figure 5.19. The effects of the pressure losses in the heat exchanger can once again be seen here. The temperature at the bubble point is in both cases lower than that at the dew point, as both the flow losses and the condensation process will tend to result in a drop in temperature during phase change.

The next section will look at the effects of increasing the speed of the working fluid pump on the non-regenerative cycle.

5.5.1.1 Pump Speed 40Hz

At the higher working fluid pump speed of 40Hz it was found that the lack of superheat due to the higher expander inlet temperature, combined with the heat losses from the expander, meant that the working fluid left the expander as a saturated mixture for heat source temperatures lower than 75°C. Having temperature and pressure information is insufficient to calculate the

enthalpy and entropy of such a mixture, so the calculated efficiency could not be obtained for these values. This is shown in the T-s diagram in Figure 5.22. This can be contrasted with the T-s diagram of the cycle presented in Figure 5.23, which uses a higher heat source temperature, and expands into the superheated region. Furthermore, with the higher evaporator pressure, the heat source temperature of 60°C was insufficient to fully vaporise the working fluid, leading to a saturated mixture at the expander inlet. Additionally, due to the higher working fluid mass flow rate and power output of the cycle, the water heater was not capable of providing enough energy to the working fluid to maintain the heat source temperature above 75°C for the non-regenerative cycle. Therefore the results for this pump speed are considerably sparser than for the lower value. However, a comparison between the two data sets is still presented as it reveals some interesting results

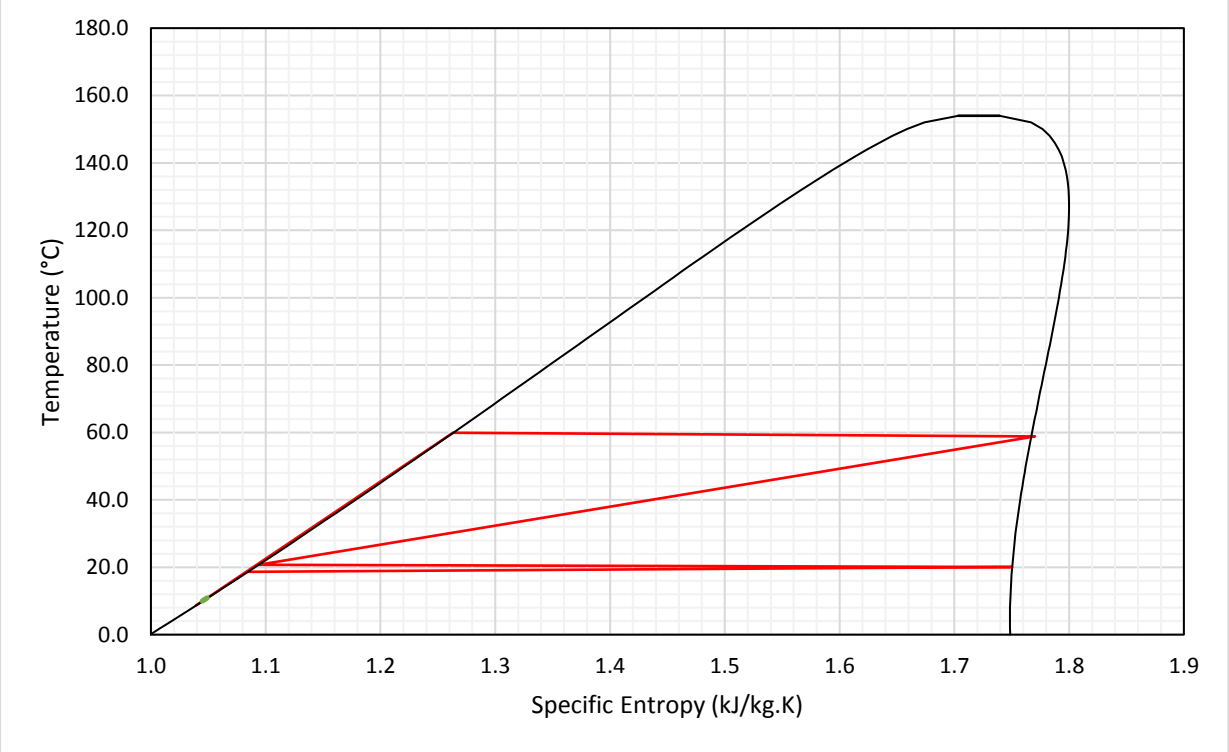

Figure 5.22: T-s diagram for a non-regenerative cycle, a pump speed of 40Hz and a heat source temperature of 65 °C, showing the state at the outlet of the expander under the saturation dome.

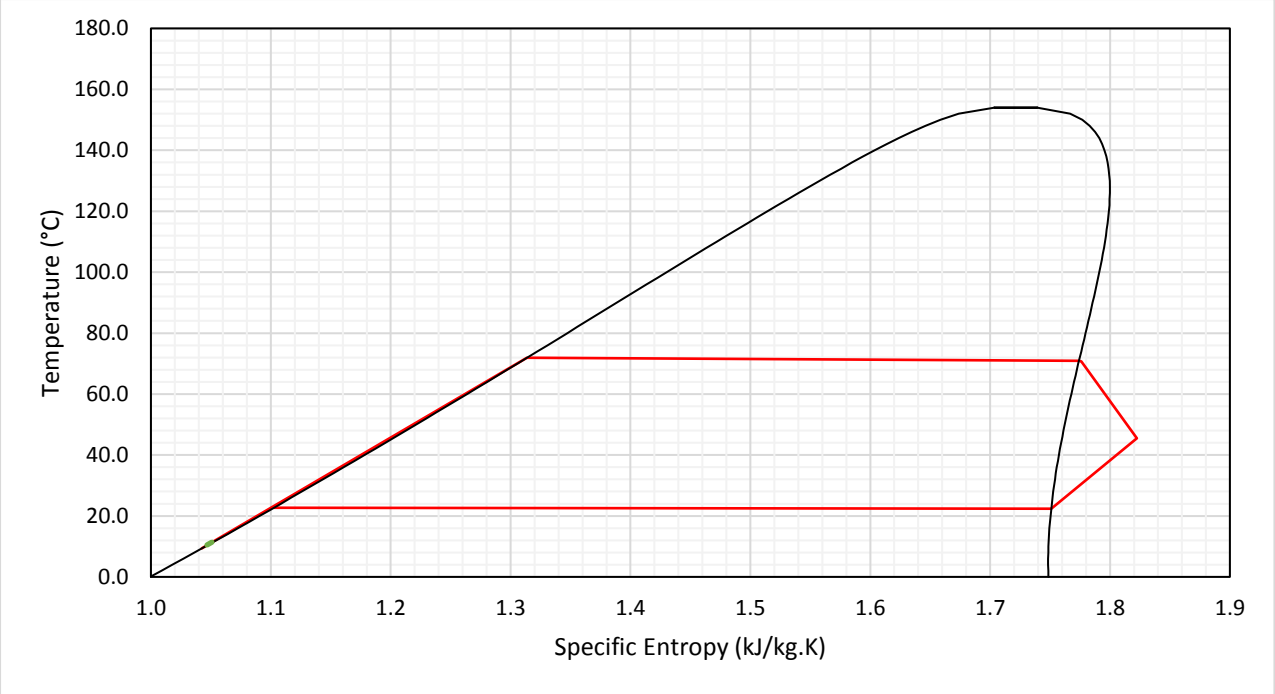

Figure 5.23: T-s diagram for a non-regenerative cycle, a pump speed of 40Hz and a heat source temperature of 75 °C, showing the state at the outlet of the expander as a superheated vapour.

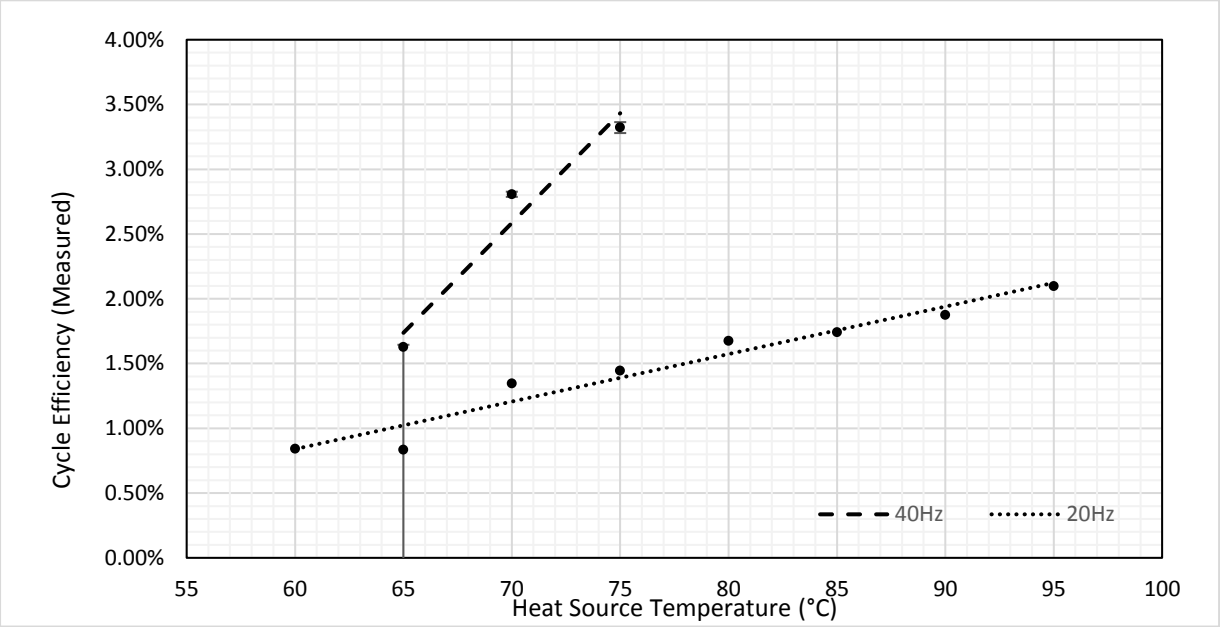

Figure 5.24: Variation in measured efficiency with changing heat source temperature for a non-regenerative cycle and two pump speeds of 20Hz and 40Hz. The extremely large error bar for the 65°C heat source temperature is due to the lower bound of the temperature measurement falling below the saturation dome.

Figure 5.24 shows how the measured efficiency varies with changing heat source temperature for this pump speed, compared to the data previously presented for the pump speed of 20Hz. It can be seen that there is an increasing trend in the value for 40Hz, but that for the lower heat source temperatures the 20Hz pump speed produced a comparable result in terms of efficiency. The highest measured efficiency recorded was 3.32%. Over the next few figures, the possible causes for these effects will be investigated.

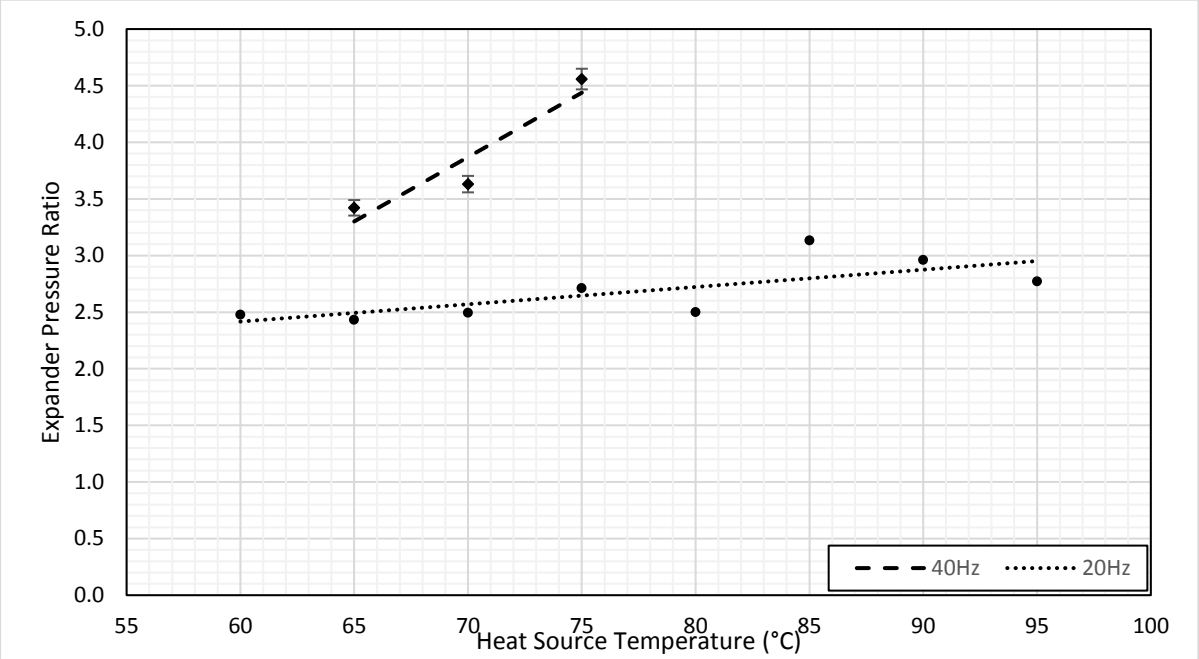

Figure 5.25: Comparison of the expander pressure ratios for two pump speeds over a range of heat source temperatures for the non-regenerative cycle

Figure 5.25 shows the variation in the cycle pressure ratio as the heat source temperature varies for the 20Hz and 40Hz pump speeds. It can be seen that the 40Hz pump speed gives a higher pressure ratio, which was expected. This pressure ratio is, for the heat source temperature of 65°C, closer to the in-built volume ratio of the expander, which reduces over- and under-expansion losses. The same trend of increasing pressure ratio with increasing heat source temperature can be observed in both plots as the vapour pressure increases.

One possible cause for the relatively low efficiency of the 40Hz cycle compared to the 20Hz cycle at the lower heat source temperatures in the considered range was increased pressure losses in heat exchangers and pipework due to the increased flow rate. This increase in working fluid mass flow rate is shown in Figure 5.26.

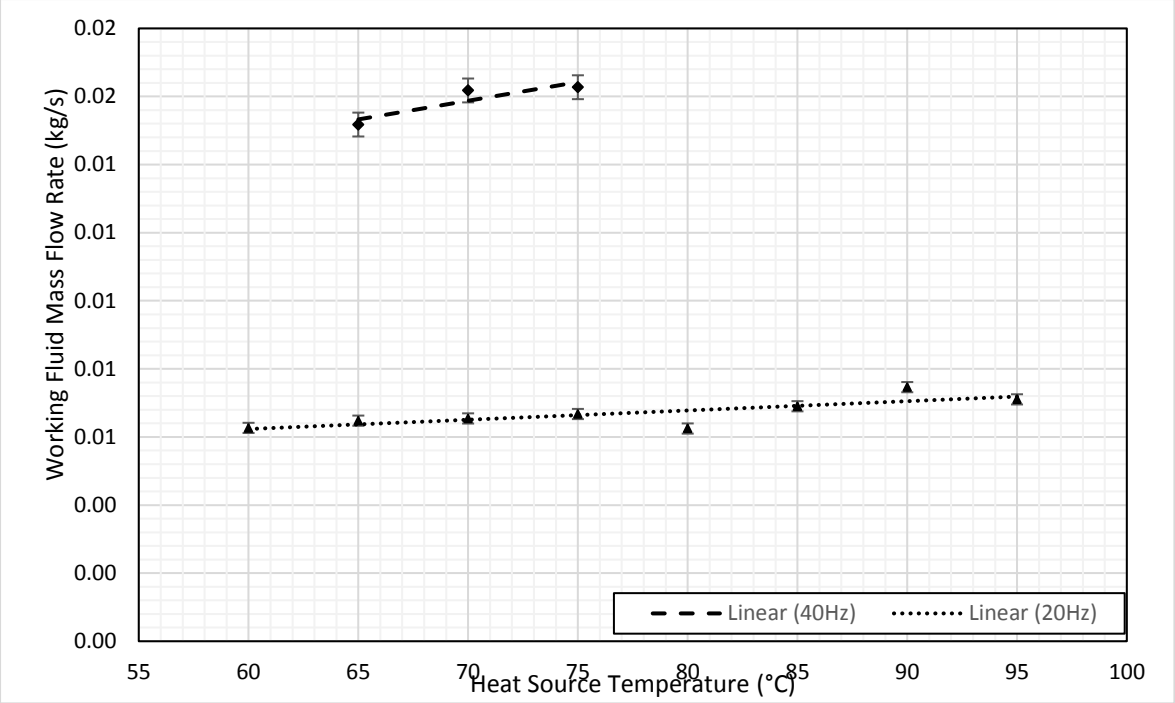

Figure 5.26: Variation in cycle mass flow rate with changing heat source temperature for two pump speeds, for a non-regenerative cycle

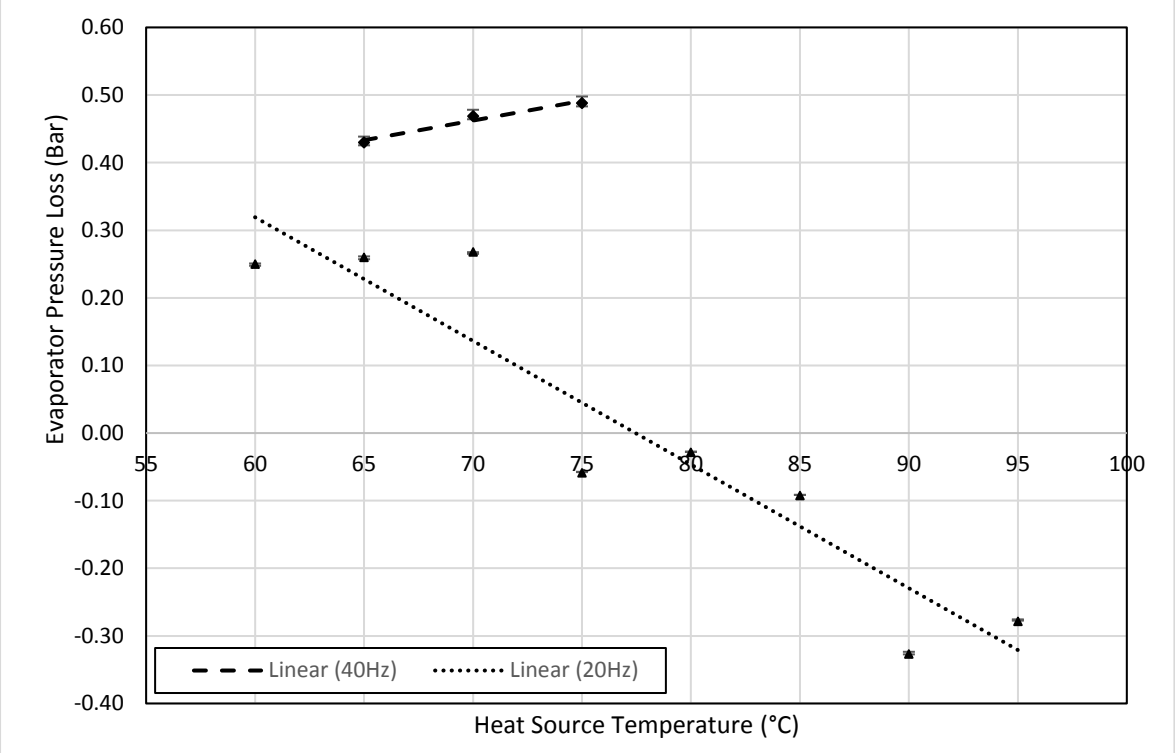

Figure 5.27: Variation in expander pressure losses for two pump speeds across a range of heat source temperatures for a non-regenerative cycle

Figure 5.27 shows the variation in the evaporator pressure loss with varying heat source temperature for the two pump speeds considered. It can be seen that the lower line, representing 20Hz, drops with increasing heat source temperature, but, over the small range considered, the upper line representing the 40Hz pump speed increases. For all heat source temperatures for which a comparison was possible, the 40Hz pump speed produced a higher pressure drop in the evaporator. This increased pressure drop could be part of the reason for the lower-than-expected improvement in the efficiency of the cycle for certain heat source temperatures.

Without being able to analyse the expander work and losses due to the fluid exiting the expander as a saturated mixture, it is impossible to say with a high degree of certainty what exactly is causing the observed trends.

There was sufficient useable data to analyse the temperature profiles inside the heat exchangers. This data is presented in Figure 5.28 and Figure 5.29 for the evaporators.

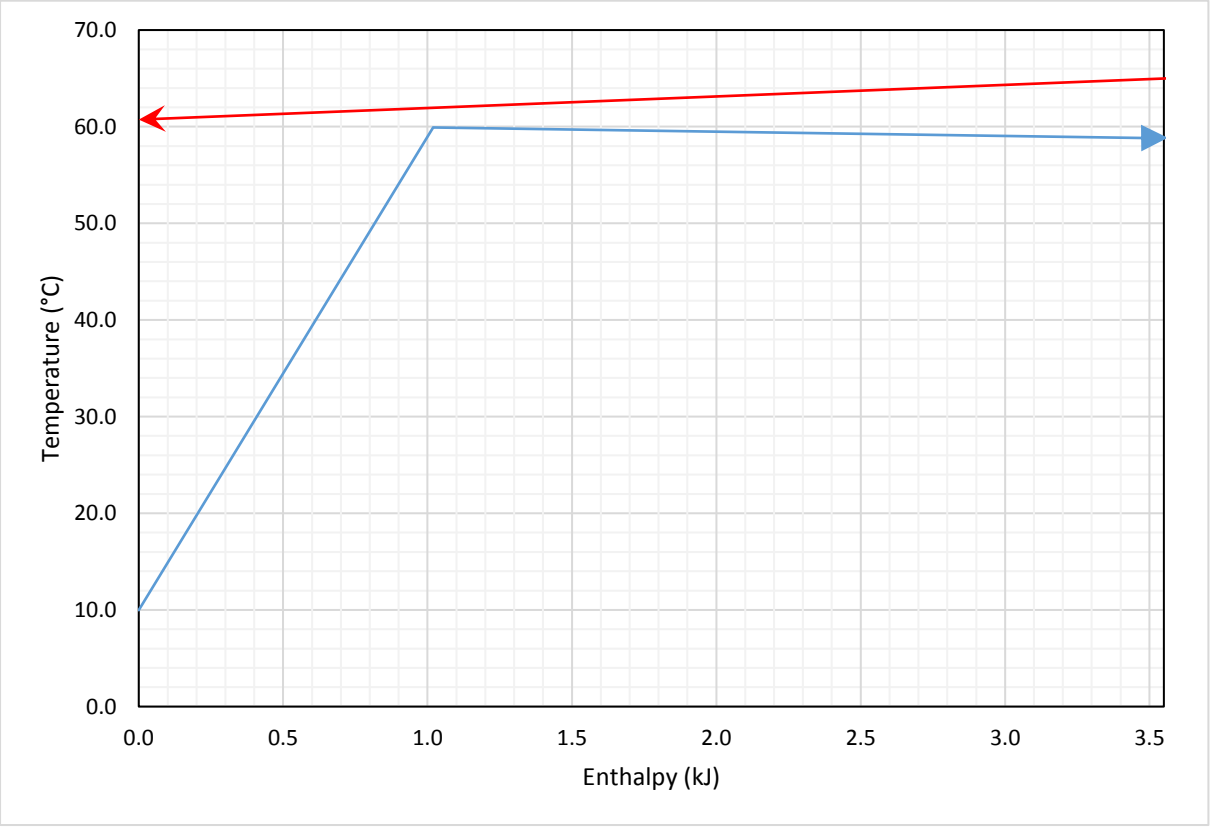

Figure 5.28: Pinch point diagram for the evaporator of a non-regenerative cycle for a pump speed of 40Hz and a heat source temperature of 65°C

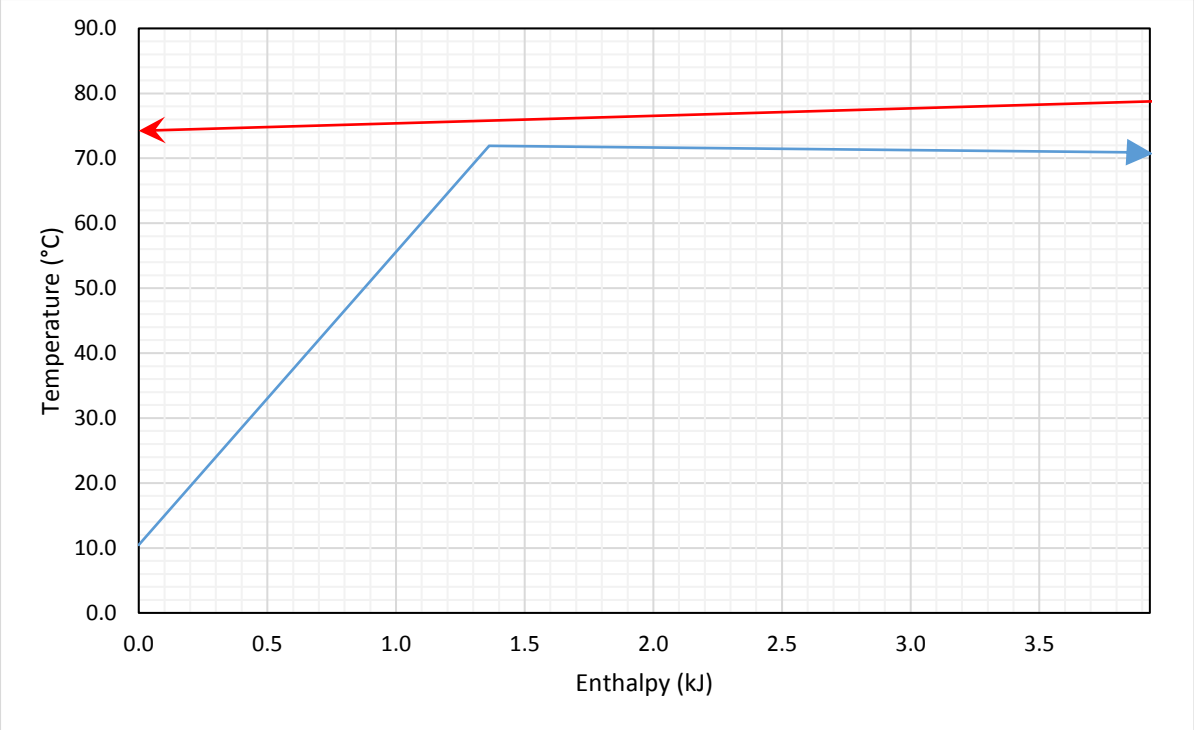

Figure 5.29: Pinch point diagram for the evaporator of a non-regenerative cycle for a pump speed of 40Hz and a heat source temperature of 75°C

It can be seen that in contrast to the same plots for a pump speed of 20Hz (Figure 5.18 and Figure 5.19), the pinch point has shifted from the thermal fluid inlet on the right hand side of the plot to the bubble point, towards the left hand side of the plot. This is due to the higher evaporator pressure resulting in zero superheat at the expander inlet. The pinch point temperature difference is now 2.1°C for the heat source temperature of 65°C and 4.1°C for the heat source temperature of 75°C. This second value is close to the range of pinch point temperature differences commonly found in literature, which means that the heat exchanger is not as oversized for the higher pump speed. This result was expected, as the heat input to the cycle is higher with the greater mass flow rate and higher evaporator pressure.

Condenser pinch points could not be effectively analysed for the cycle as the condenser inlet lay underneath the saturation dome, meaning it could not be properly characterized using REFPROP with only temperature and pressure information available.

In the next section, the effect of a regenerator on the cycle will be analysed and compared with the performance of the non-regenerative cycle.

5.6 Regenerative Cycles

The flow of working fluid in the cycle could be passed through a regenerator to recover heat energy from the expander exhaust and use it to preheat the working fluid prior to it entering the evaporator, thus reducing the load on the water heater. Here, the results of the rig running in a regenerative configuration are presented and compared with the non-regenerative results.

5.6.1 Pump Speed 20Hz

Figure 5.30 and Figure 5.31 show the variation in calculated and measured cycle efficiency with changing heat source temperature. As for the non-regenerative cycles, the trend is for both the calculated and measured cycle efficiencies to increase with increasing heat source temperatures.

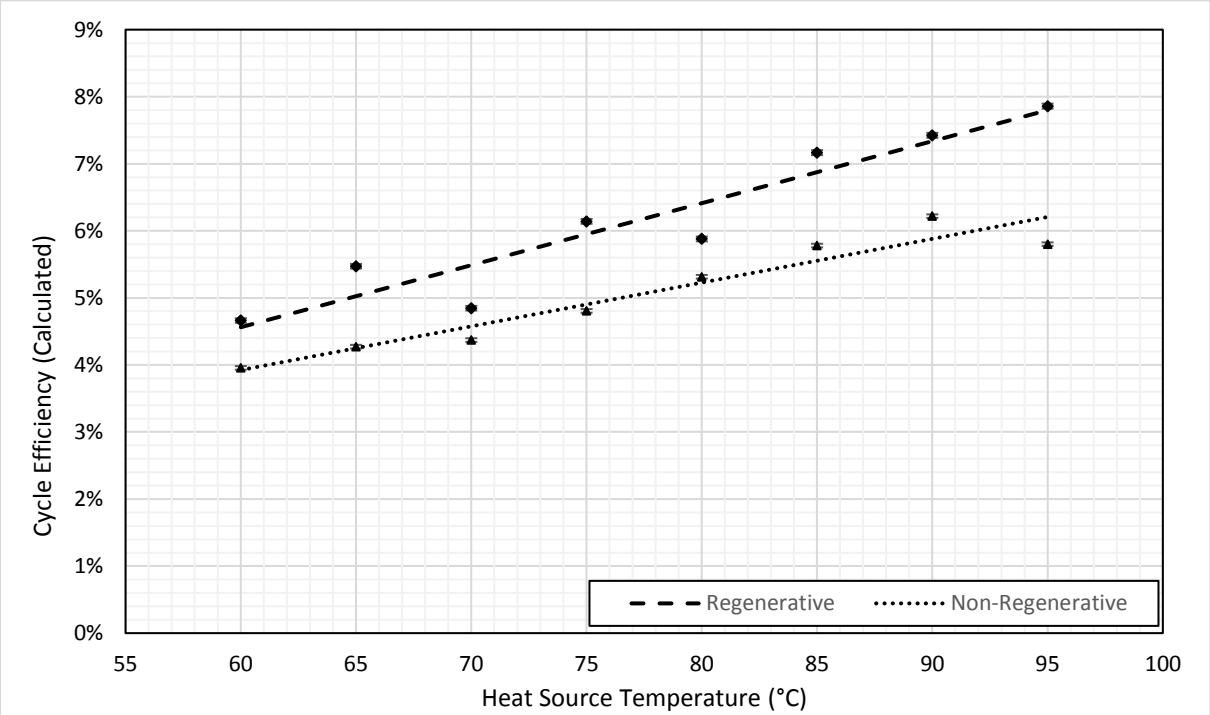

Figure 5.30: Variation in calculated cycle efficiency for a regenerative cycle with pump speed 20Hz across a range of heat source temperatures

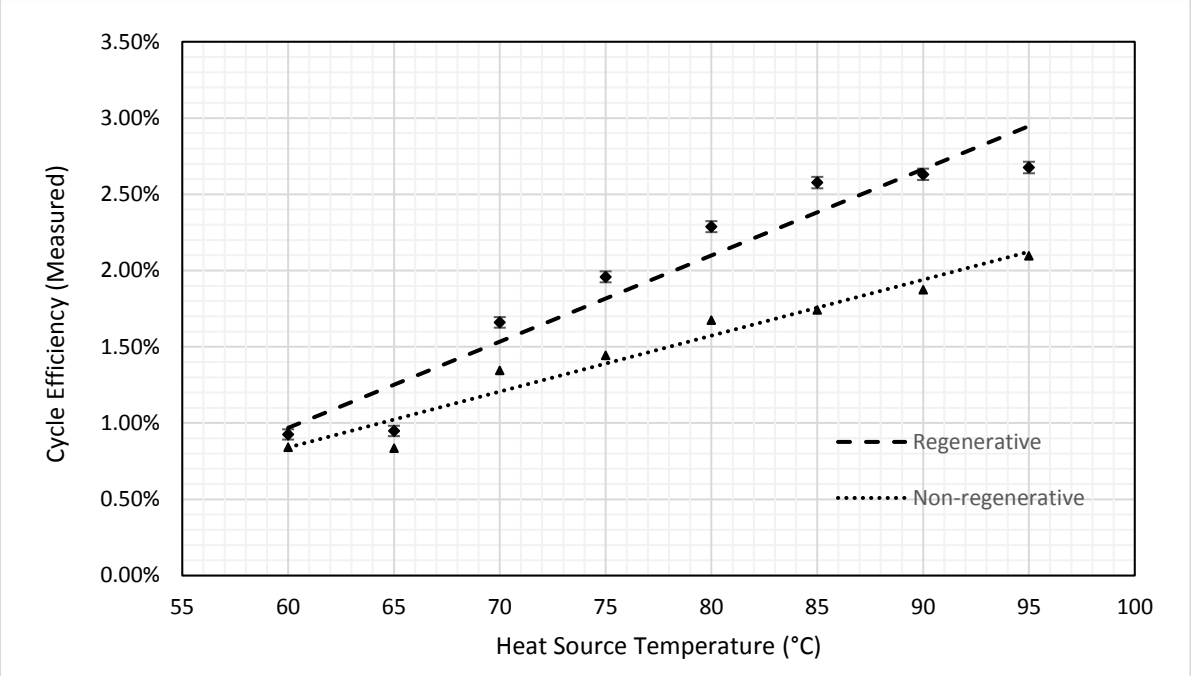

Figure 5.31: Variation in measured cycle efficiency for a regenerative cycle with pump speed 20Hz across a range of heat source temperatures

In both the calculated and measured cases the regenerative cycle results in a greater first law efficiency than the corresponding non-regenerative cycle. The maximum calculated efficiency of the regenerative cycle is 7.86% (compared to 6.22% for the non-regenerative cycle, and the maximum measured efficiency is 6.42% (compared to 4.61% for the non-regenerative cycle. As for the non-regenerative cycle, the regenerative cycle exhibits an increasing trend in expander losses with increasing heat source temperature, probably due to increased thermal losses from the expander through conduction into the body of the expander and through the scrolls. The variation in the expander losses is plotted in Figure 5.32, showing that there is a general increasing trend in losses with increasing temperature, although there is quite a large amount of scatter in the recorded data.

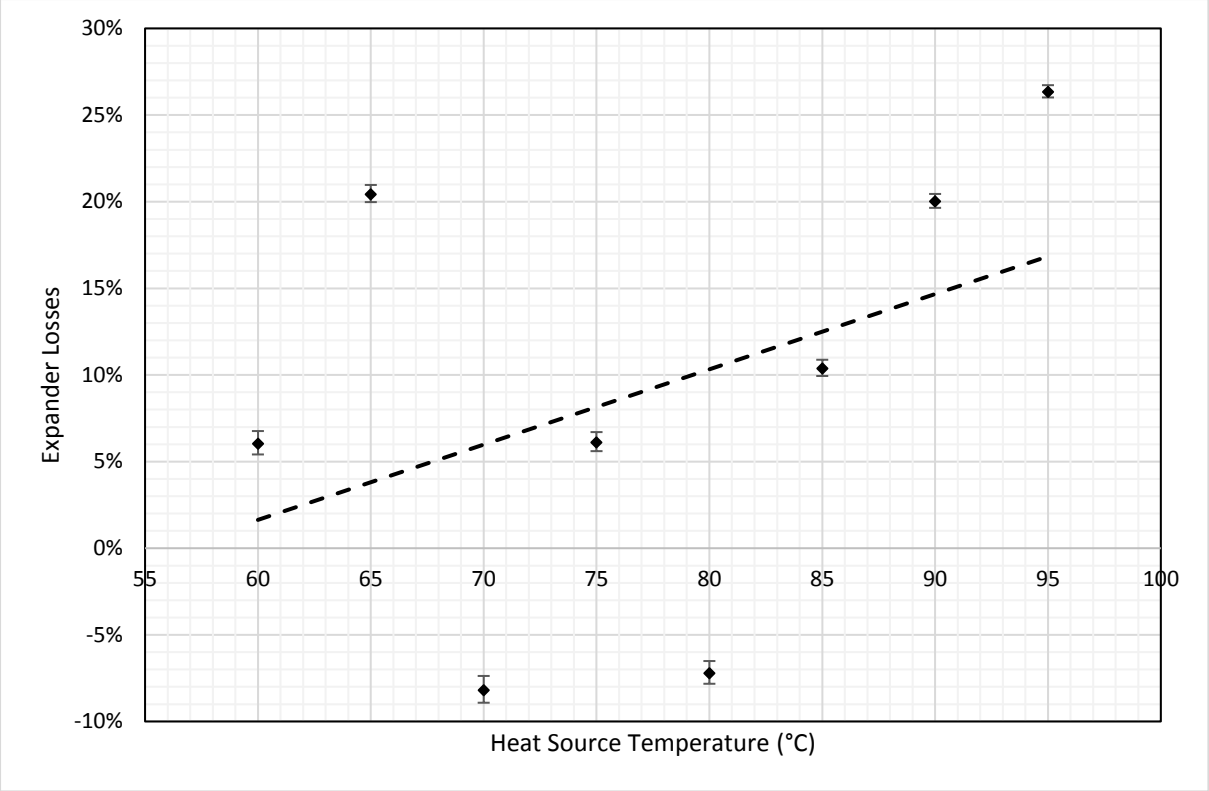

Figure 5.32: Variation in expander losses with varying heat source temperature for a regenerative cycle and a pump speed of 20Hz

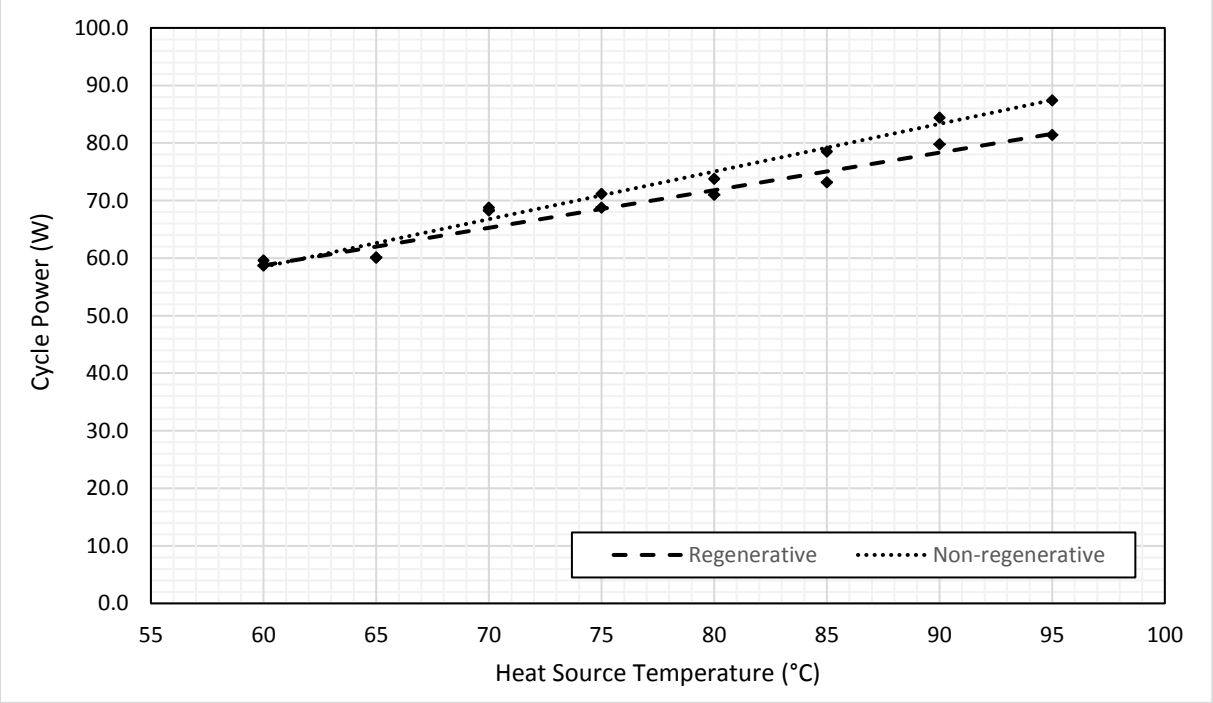

Figure 5.33: Variation in cycle output power for regenerative and non-regenerative cycles, at a pump speed of 20Hz across a range of heat source temperatures

Figure 5.33 shows the variation in the output power of the cycle with changing heat source temperature for both the regenerative and non-regenerative cycles. Both cycles shown an increasing trend, but the power output from the regenerative cycle is in fact lower than that of the non-regenerative cycle, in spite of the regenerative cycle's higher efficiency.

The possibility that this was due to pressure drops and thermal losses in the regenerator was considered. However, Figure 5.34 shows that at this pump speed, there is actually a slight increase in pressure across the regenerator, again most likely due to the increased vapour pressure caused by heating up the fluid. This is supported by Figure 5.35, which shows that there is no significant difference between the expander inlet pressures for the regenerative and non-regenerative cycles.

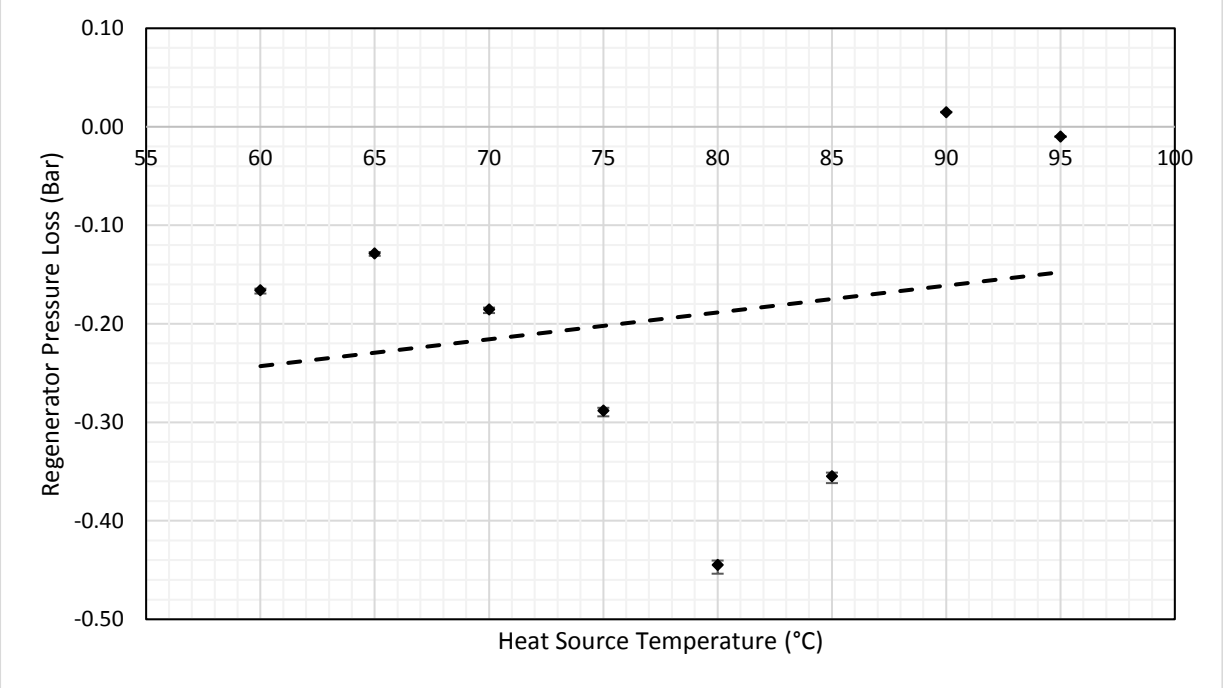

Figure 5.34: Variation in Regenerator Pressure Drop with changing heat source temperature for a pump speed of 20Hz

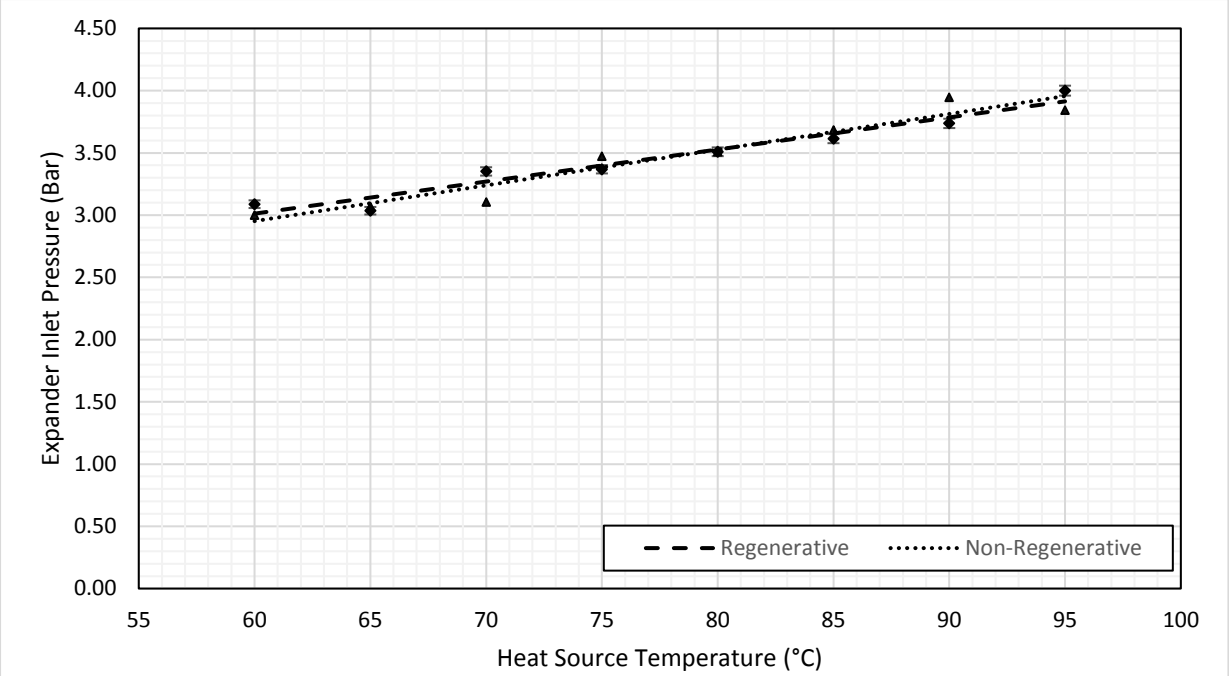

Figure 5.35: Comparison of Expander Inlet Pressure between regenerative and non-regenerative cycles for a pump speed of 20Hz

Another possible explanation is that the working fluid mass flow rate is lower for the regenerative cycle due to the greater resistance provided by the extra heat exchanger. Figure 5.36 shows that the mass flow rate of working fluid gradually increases with increasing heat source temperature for the non-regenerative cycle, but remains relatively constant for the regenerative cycle. This trend broadly matches the increasing gap between the power output of the regenerative and non-regenerative cycles observed in Figure 5.33.

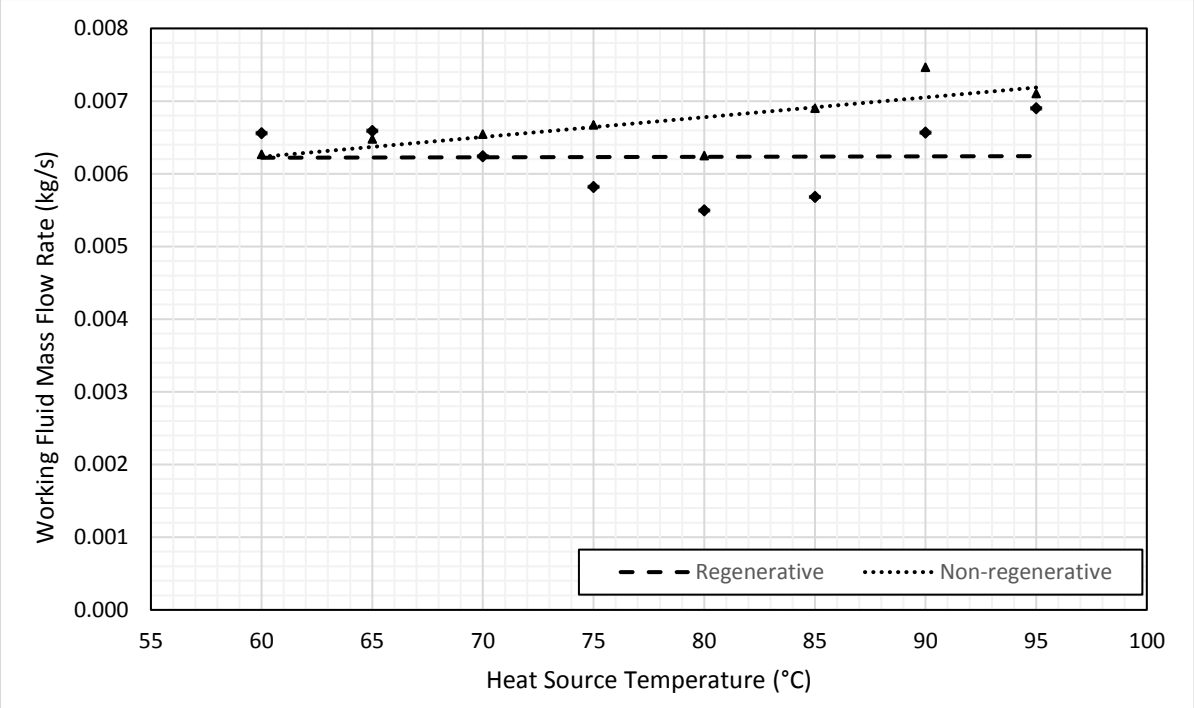

Figure 5.36: Comparison of working fluid mass flow rate for regenerative and non-regenerative cycles for a pump speed of 20Hz over a range of heat source temperatures

Figure 5.37 shows the variation in the enthalpy transfer in the regenerator with changing heat source temperature. There is a clear increasing trend in the amount of enthalpy transfer as the heat source temperature increases.

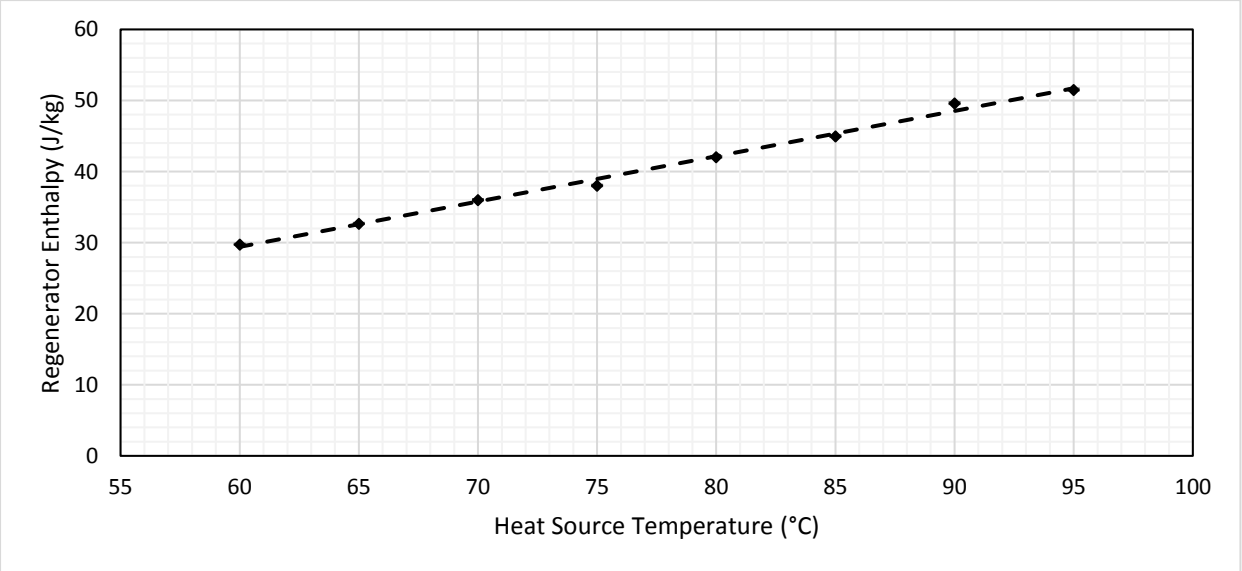

Figure 5.37: Variation in regenerator enthalpy for a pump speed of 20Hz across a range of temperatures

Figure 5.38 and Figure 5.39 show the temperature profiles of the hot and cold sides of the regenerator for two different heat source temperatures. For a heat source temperature of 60°C, there is 19.4°C of superheat at the expander outlet, which allows 29.7kJ/kg of specific enthalpy to be transferred from the hot side to the cold side. The pinch point is located at the dew point on the hot side and its temperature difference is 2.6°C, which is lower than the usual range of values found in literature, indicating that, at least for this set of conditions, the regenerator is slightly oversized.

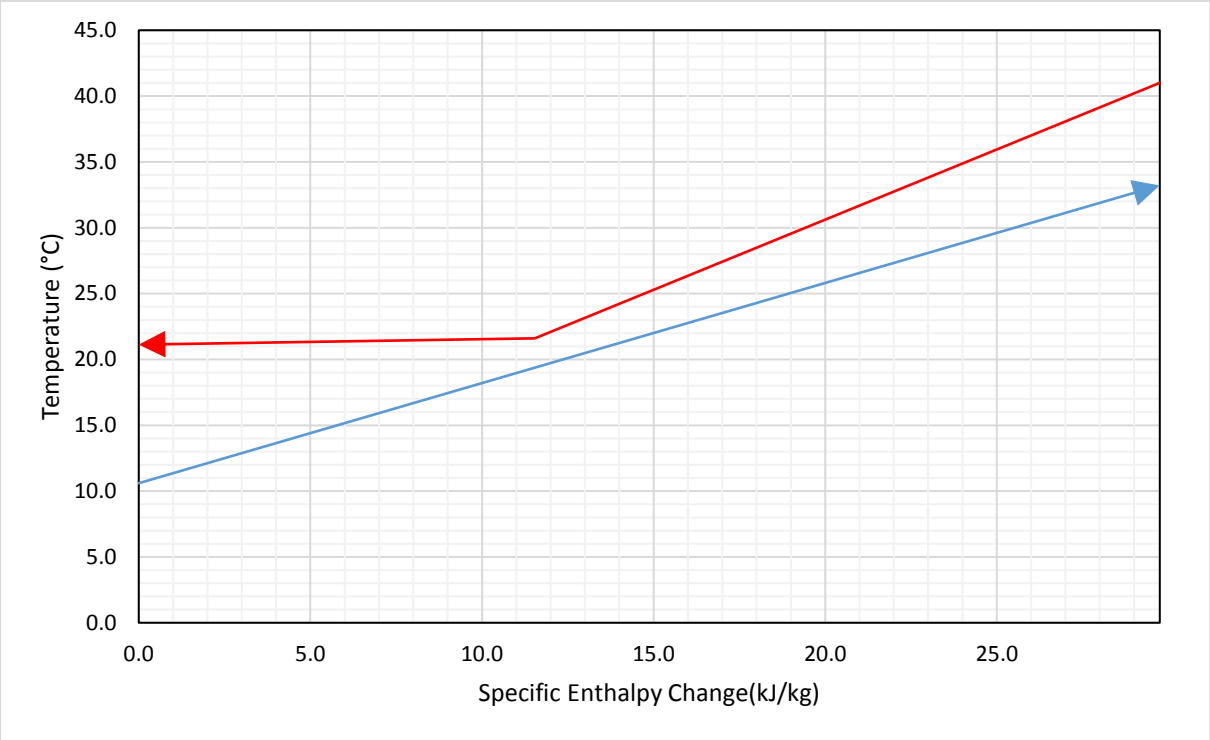

Figure 5.38: Regenerator Pinch Point Diagram for a heat source temperature of 60°C and a pump speed of 20Hz

For the heat source temperature of 95°C, the superheat at the expander outlet is 46.3°C and the specific enthalpy transferred from the hot side to the cold side is 51.5 kJ/kg. The pinch point is still located at the dew point on the hot side, but a much greater proportion of the heat transferred in the regenerator now comes from cooling the fluid to its dew point, as opposed to from a phase change inside the regenerator. The pinch point temperature difference in this case is 5.8°C, which is within the range found in literature, indicating that the regenerator is neither over- nor under-sized for these conditions.

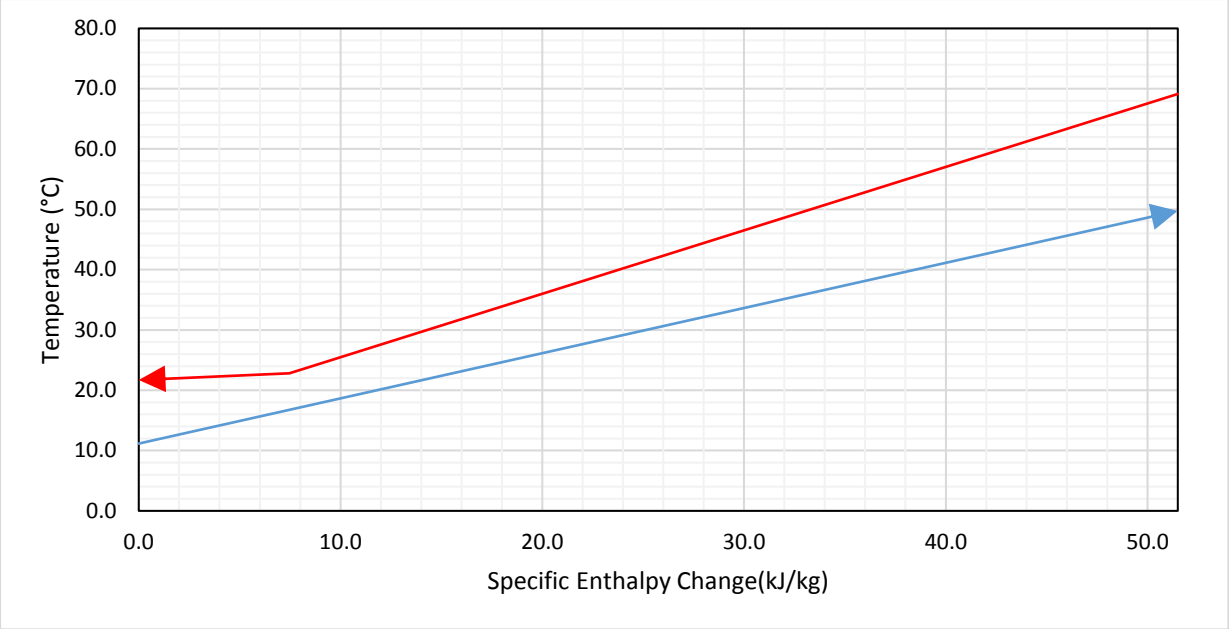

Figure 5.39: Regenerator Pinch Point Diagram for a heat source temperature of 95°C and a pump speed of 20Hz

The presence of a regenerator has an effect on the heat transfer processes in the other heat exchangers of the cycle. Figure 5.40 and Figure 5.41 show evaporator pinch point diagrams for the regenerative cycle for heat source temperatures of 60°C and 95°C.

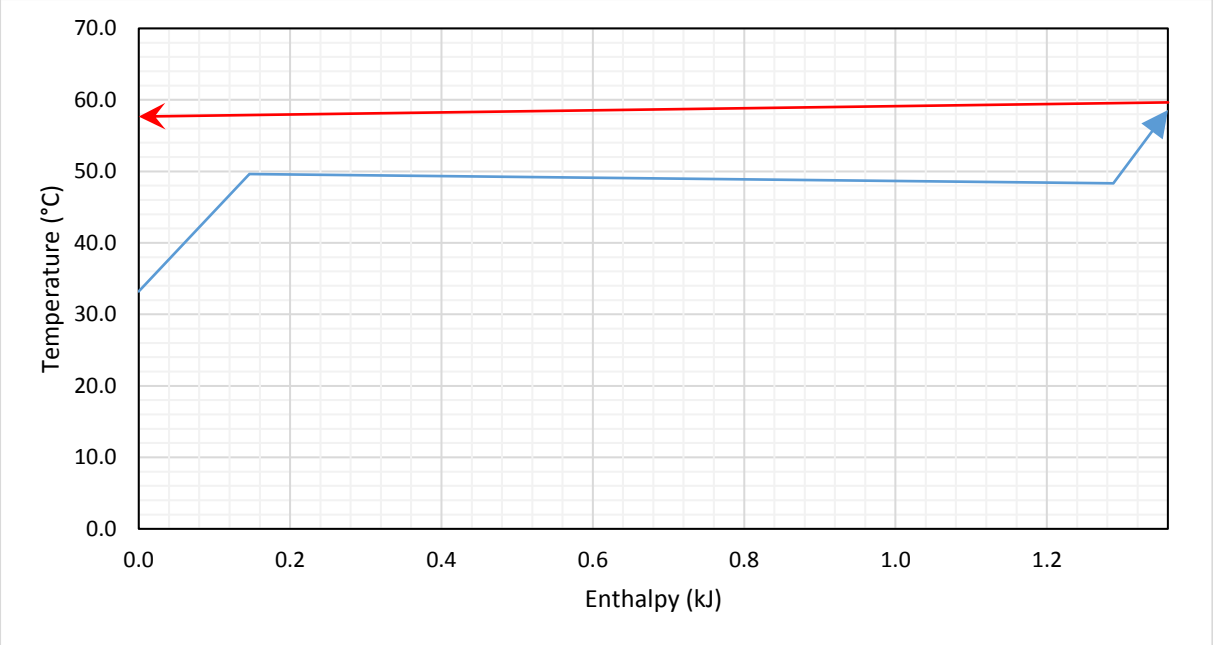

Figure 5.40: Evaporator pinch point diagram for a regenerative cycle with a heat source temperature of 60°C and a pump speed of 20Hz

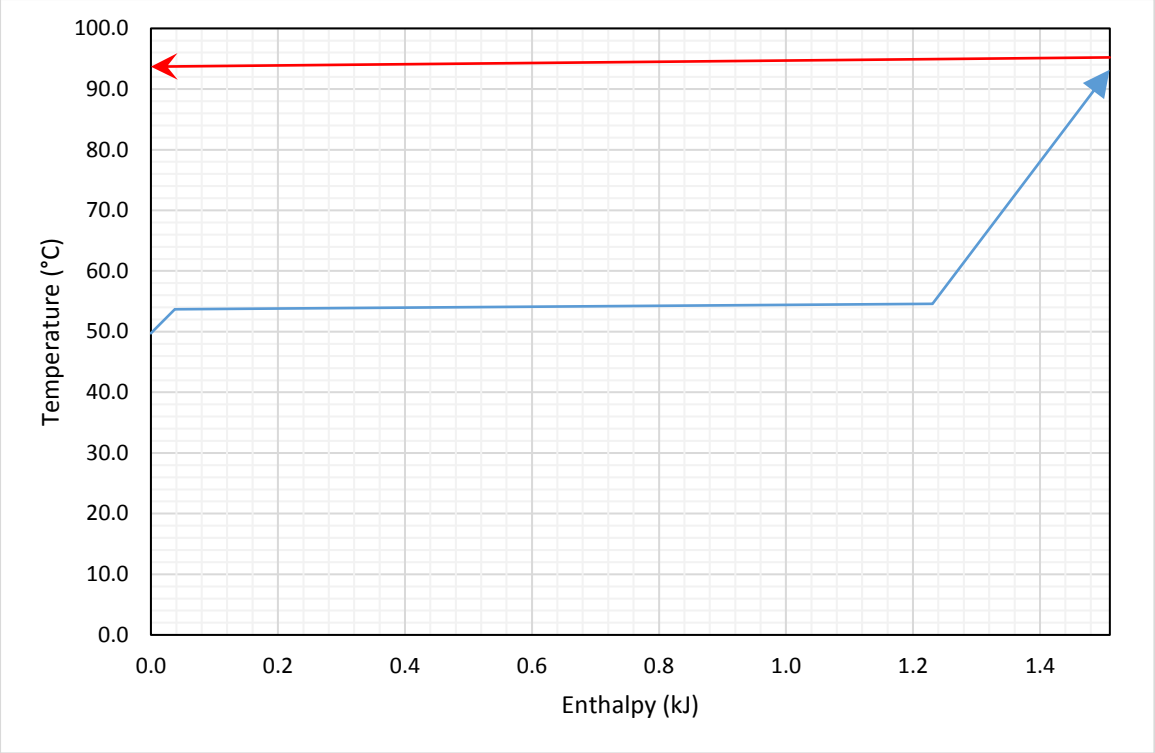

Figure 5.41: Evaporator pinch point diagram for a regenerative cycle with a heat source temperature of 95°C and a pump speed of 20Hz

5.6.1.1 Pump Speed 40Hz

As for the non-regenerative cycle, increasing the pump speed to 40Hz increased the evaporator pressure of the cycle. Combined with heat losses from the expander, this led to the state of the working fluid at the expander outlet being underneath the saturation dome, meaning that it could not be accurately calculated. However, the measured efficiency of the cycle could still be obtained.

Additionally, the presence of the regenerator significantly reduced the heat requirements in the evaporator, which meant that the electric heater was able to supply the heat requirements for the higher heat source temperatures that were not possible with the non-regenerative cycle.

In this section the results of the regenerative cycle for a pump speed of 40Hz will be presented and compared with the corresponding results for both the regenerative cycle at 20Hz and the non-regenerative cycle at 40Hz.

Figure 5.42 shows the comparison between the regenerative cycle for a pump speed of 20Hz and a pump speed of 40Hz. It can be seen that the two series start out at a similar efficiency,

then diverge as the measured efficiency for the 40Hz series increases more quickly, reaching a maximum value of 8.64% for a heat source temperature of 95°C.

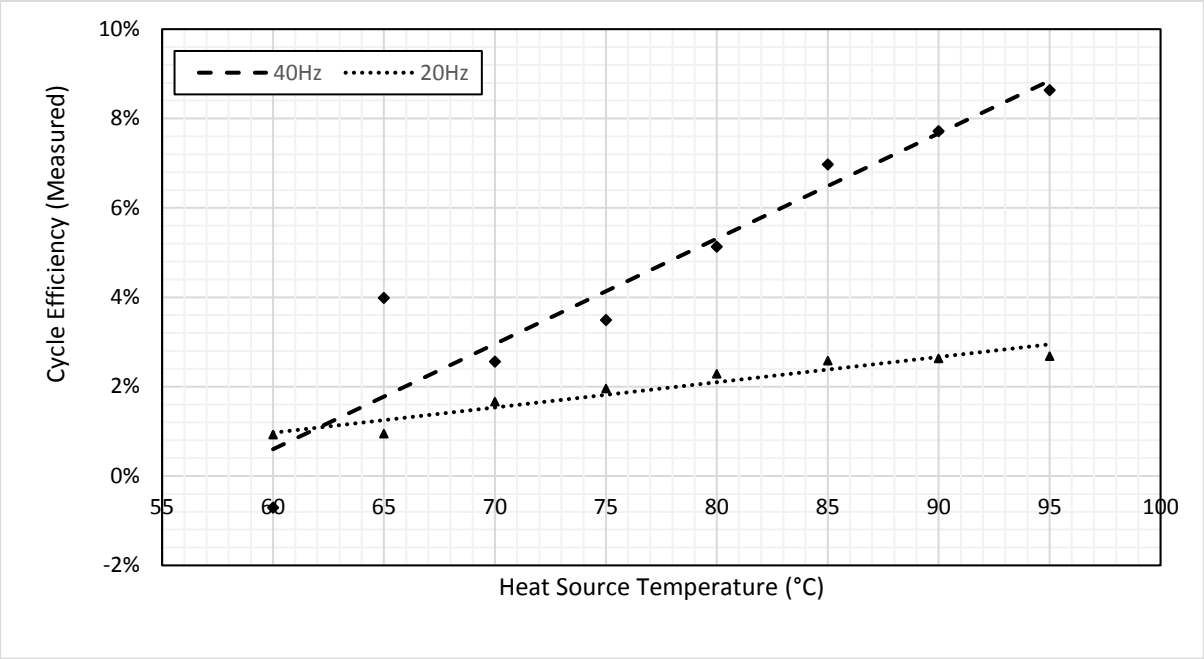

Figure 5.42: Comparison of measured efficiencies for the regenerative cycle at pump speeds of 20Hz and 40Hz

There are several potential reasons for this trend, which will be investigated over the following figures.

The first is that the heat demand in the evaporator is relatively lower for the 40Hz cycle than for the 20Hz cycle. Figure 5.43 compares the specific enthalpy change in the evaporator for the two different pump speeds. It can be seen that the specific enthalpy change for the 20Hz cycle steadily increases with increasing heat source temperature, whereas the specific enthalpy change for the 40Hz cycle shows a slight decreasing trend with a large amount of variation in specific enthalpy change between heat source temperatures. Also to note is the fact that the overall variation in the specific enthalpy change is quite small over the range of temperatures considered. Therefore it can be inferred that the change in evaporator specific enthalpy is not responsible for the trend observed in Figure 5.42.

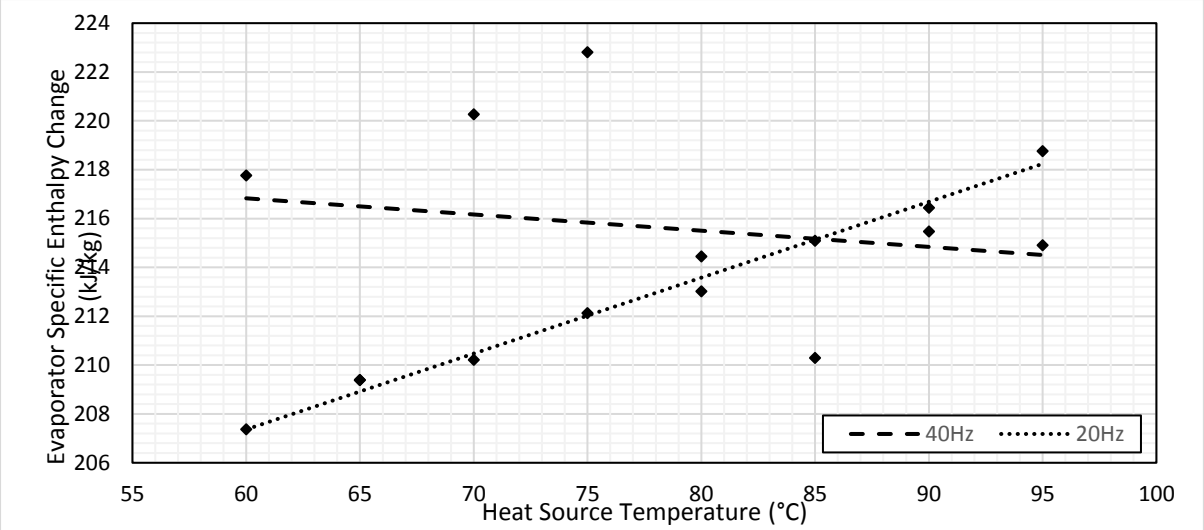

Figure 5.43: Comparison of the change in specific enthalpy in the evaporator for two regenerative cycles at pump speeds of 20Hz and 40Hz

The second possible cause is that the measured power increases for the 40Hz cycle more quickly than for the 20Hz cycle. Figure 5.44 shows a comparison between the measured powers of the cycle for pump speeds of 20Hz and 40Hz. It can be seen that the trend in this plot is similar to the trend observed in Figure 5.42, with the plots for the 40Hz and 20Hz cycles diverging, with the 40Hz cycle reaching a power output of 355W, and the 20Hz cycle only reaching a power output of 87W, in spite of the two pump speeds producing almost identical power outputs at a heat source temperature of 60°C. Possible reasons for the trends observed in Figure 5.42 and Figure 5.44 will be investigated over the following several figures.

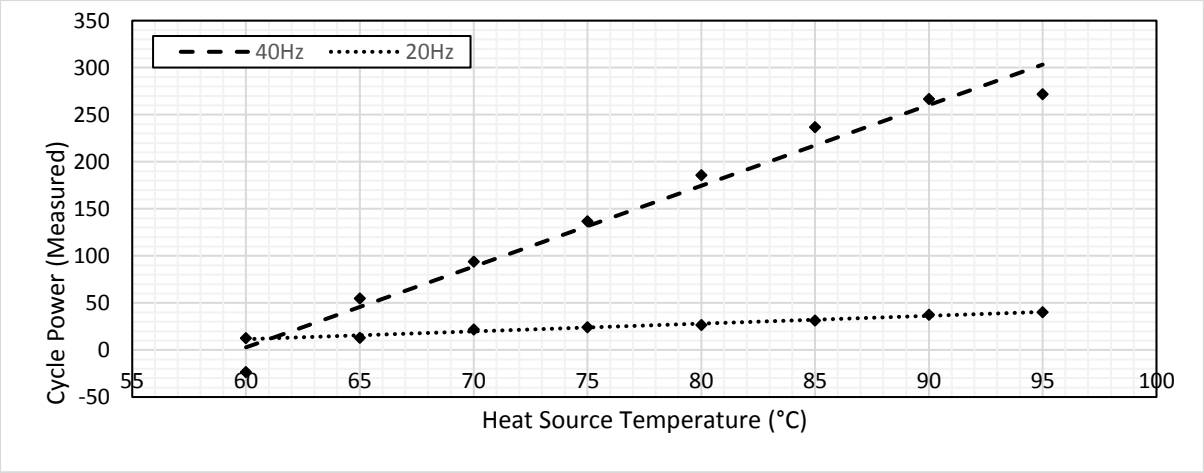

Figure 5.44: Comparison of the measured cycle power for regenerative cycles at pump speeds of 40Hz and 20Hz

Figure 5.45 compares the regenerator specific enthalpy change between the two pump speeds as the heat source temperature is varied. Both pump speeds show an increasing trend as the heat source temperature increases, but the 20Hz pump speed actually shows a greater regenerator heat load than the 40Hz pump speed.

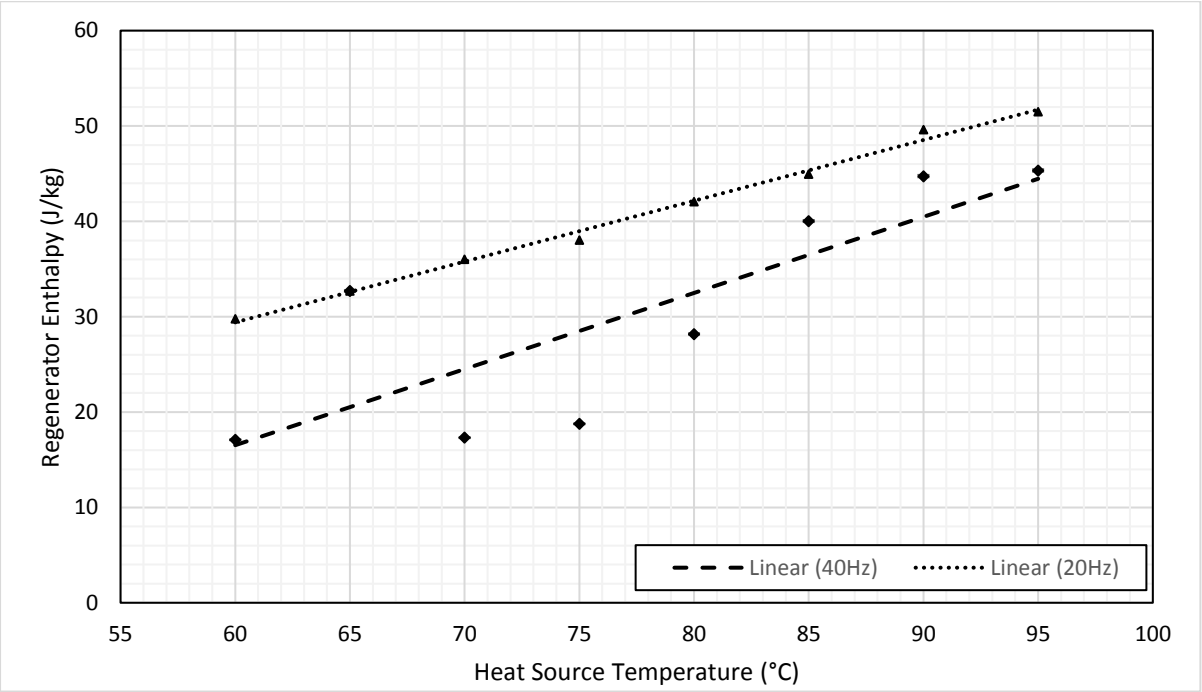

Figure 5.45: Comparison of Regenerator Enthalpy Change between the 20Hz and 40Hz cycles

Figure 5.46 and Figure 5.47 compare the expander inlet and outlet superheat, respectively, for the 20Hz and 40Hz pump speeds. Figure 5.46 shows a greater expander inlet superheat for the 20Hz cycle, which is to be expected due to the lower evaporator pressure depressing the dew point. For the 40Hz pump speed the superheat is far lower, the higher evaporator pressure meaning that the heat source temperature is not far above the dew point of the working fluid until the highest heat source temperatures are reached. This affects the expander outlet superheat, as seen in Figure 5.47. The higher expander inlet superheat results in a correspondingly higher expander outlet superheat, increasing the driving temperature difference available to the regenerator and increasing its specific enthalpy change. This holds true both for increasing heat source temperature for both pressures, and also for the increased expander inlet superheat with reduced pump speed.

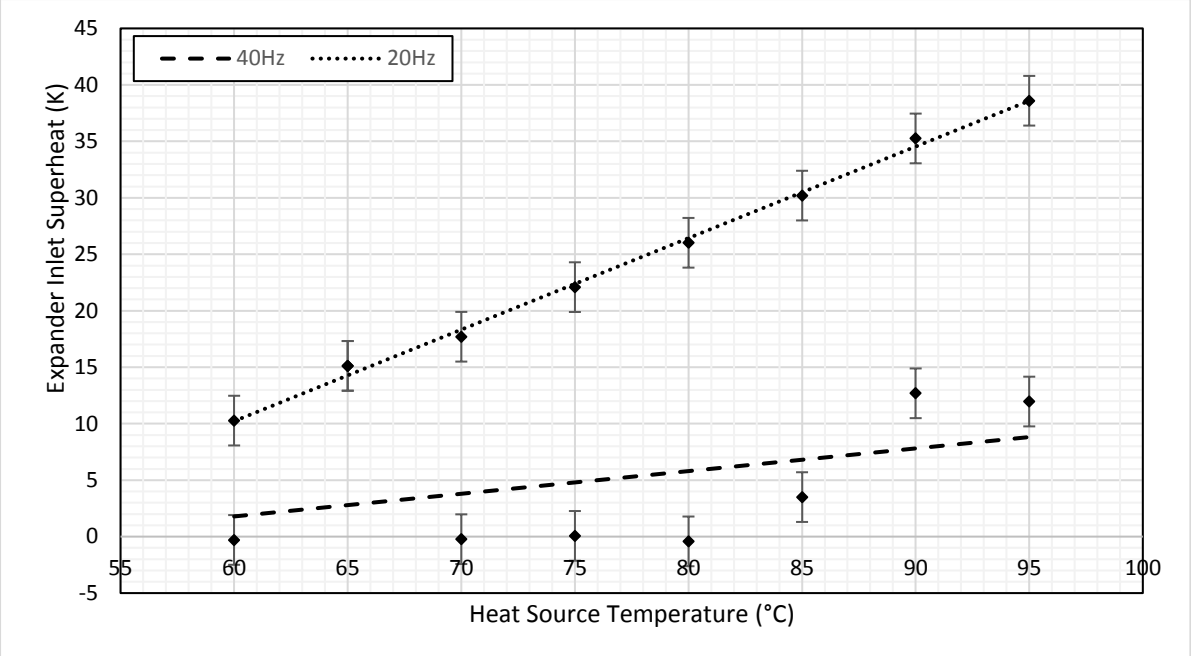

Figure 5.46: Comparison of Expander Inlet Superheat for regenerative cycles and pump speeds of 20Hz and 40Hz

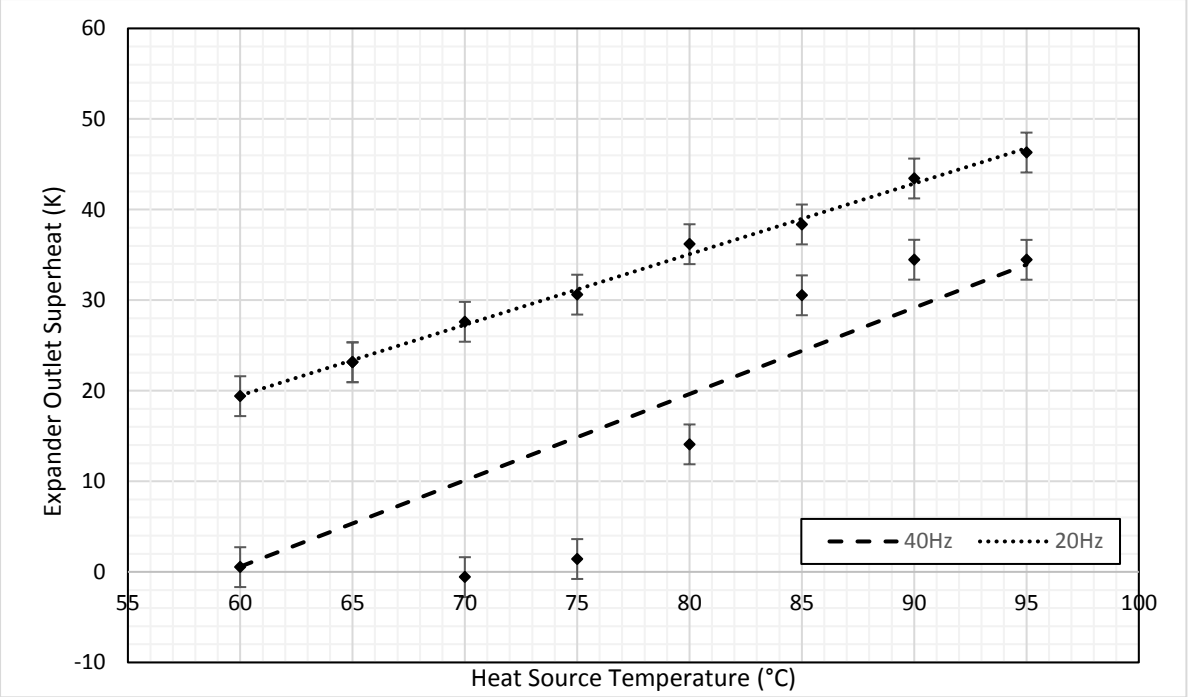

Figure 5.47: Comparison of Expander Outlet Superheat for regenerative cycles and pump speeds of 20Hz and 40Hz

The trend of increasing regenerator power with increasing heat source temperature can explain the trend observed in Figure 5.43. The following figures will attempt to account for the trend

of diverging cycle power seen in Figure 5.44. There are two possible causes, the cycle pressure ratio and the mass flow rate of working fluid in the cycle.

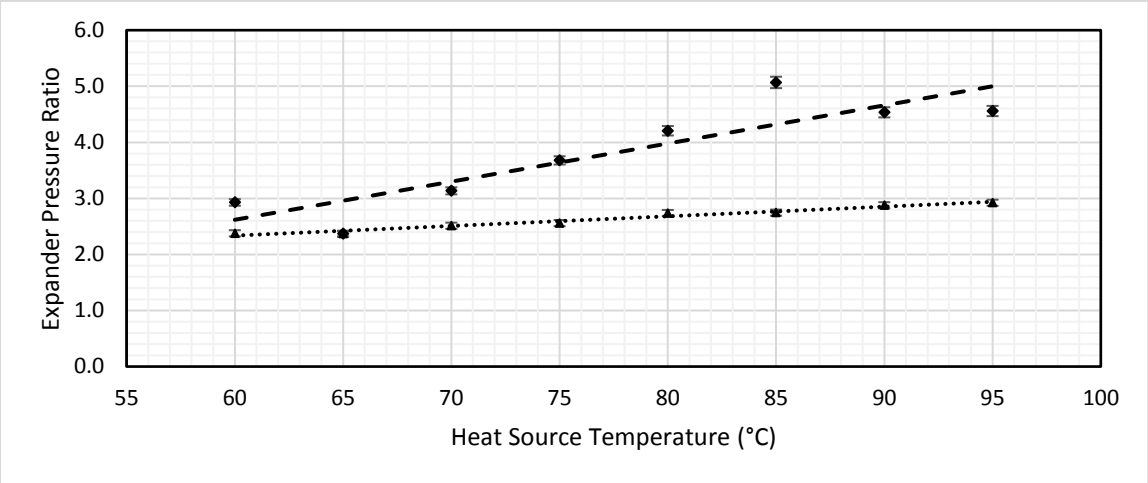

Figure 5.48: Comparison of the expander pressure ratio between the 20Hz and 40Hz cycles

Figure 5.48 shows how the expander pressure ratio varies with changing heat source temperature between the 20Hz and 40Hz pump speeds. The 40Hz pump speed shows a consistently higher pressure ratio and also a steeper slope with increasing heat source temperature. While this could in itself account for the diverging trend in Figure 5.43, for completeness the working fluid mass flow rate should also be examined. This is presented in Figure 5.49. Again a diverging trend can be seen between the mass flow rates for the 20Hz and 40Hz. Therefore it is reasonable to conclude that the trend of increasing power in Figure 5.43 is caused by a combination of increased cycle pressure ratio and increased mass flow rate of the working fluid.

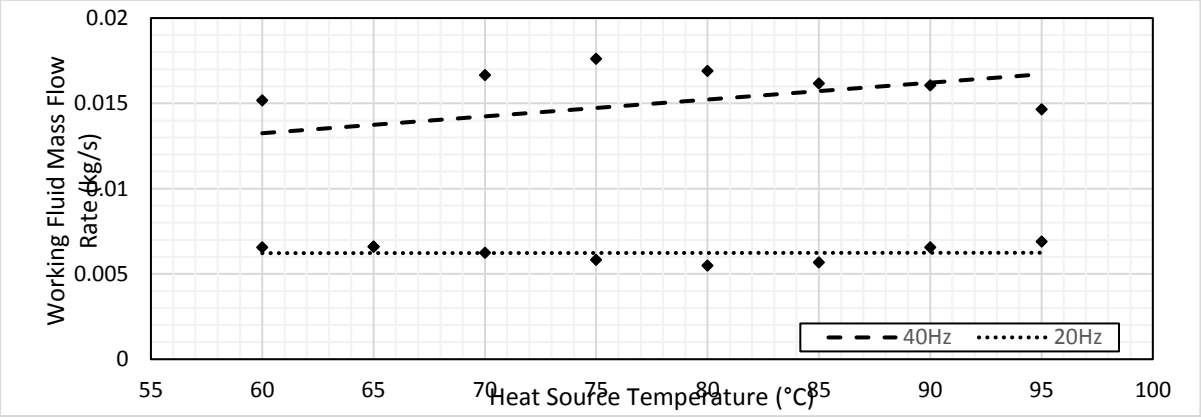

Figure 5.49: Comparison of working fluid mass flow rates between the two pump speeds of 20Hz and 40Hz

Also of interest is the pressure change in the regenerator. The regenerator pressure changes for the two pump speeds are compared in Figure 5.50. It can be seen that the plot for 40Hz begins with a pressure loss of 0.4 bar, but with increasing heat source temperature, this changes to a net pressure increase as the heat source temperature increases. There is no phase change in the cold side of the regenerator, so this pressure increase could be due to back pressure from the evaporator.

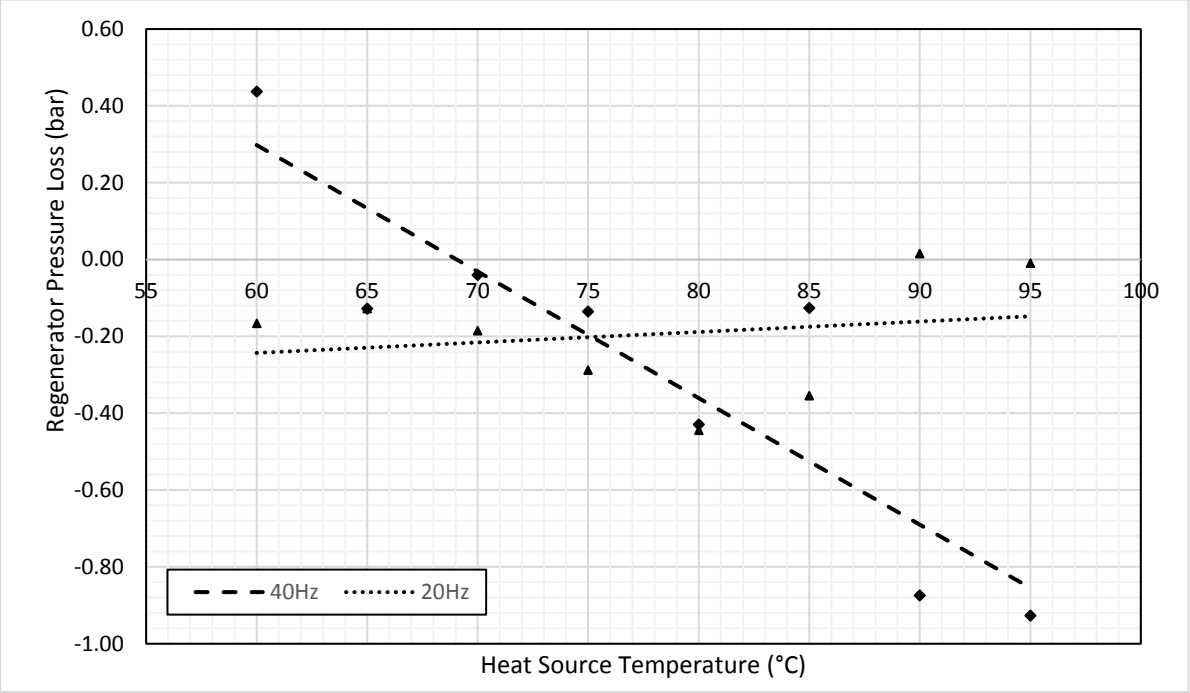

Figure 5.50: Comparison of the pressure change in the regenerator for two pump speeds

Pinch point diagrams for the heat exchangers are presented in the following figures. As the working fluid is in the two-phase region at the expander outlet for the heat source temperature of 60°C, heat source temperatures of 65°C and 95°C were used for comparison. Figure 5.51 shows the pinch point diagram for the evaporator for a heat source temperature of 65°C. It can be seen that the pinch point is located at the expander inlet, and that the pinch point temperature difference is 1.2°C, indicating that the heat exchanger is oversized for this application, and that the thermal fluid mass flow rate could be dropped without violating the pinch point limitation. Figure 5.52 shows the pinch point diagram for the evaporator for a heat source temperature of 95°C. Compared to the corresponding diagram for the lower heat source temperature several things are apparent. Firstly the evaporator enthalpy is greater for the higher heat source temperature. As the specific enthalpy change is broadly similar between the two, this is most likely due to the increased mass flow rate of the working fluid. Secondly the evaporating

temperature of the working fluid is higher and the superheat is lower. The pinch point has reduced to 0.9°C, although it is still located at the expander inlet. The temperature drop in the hot water has increased from 1.8°C to 5.4°C, reflecting the increased enthalpy change in the evaporator. The temperature differential at the bubble point of the working fluid has also decreased from 15°C to 6.9°C, which indicates that the heat exchanger is still slightly oversized.

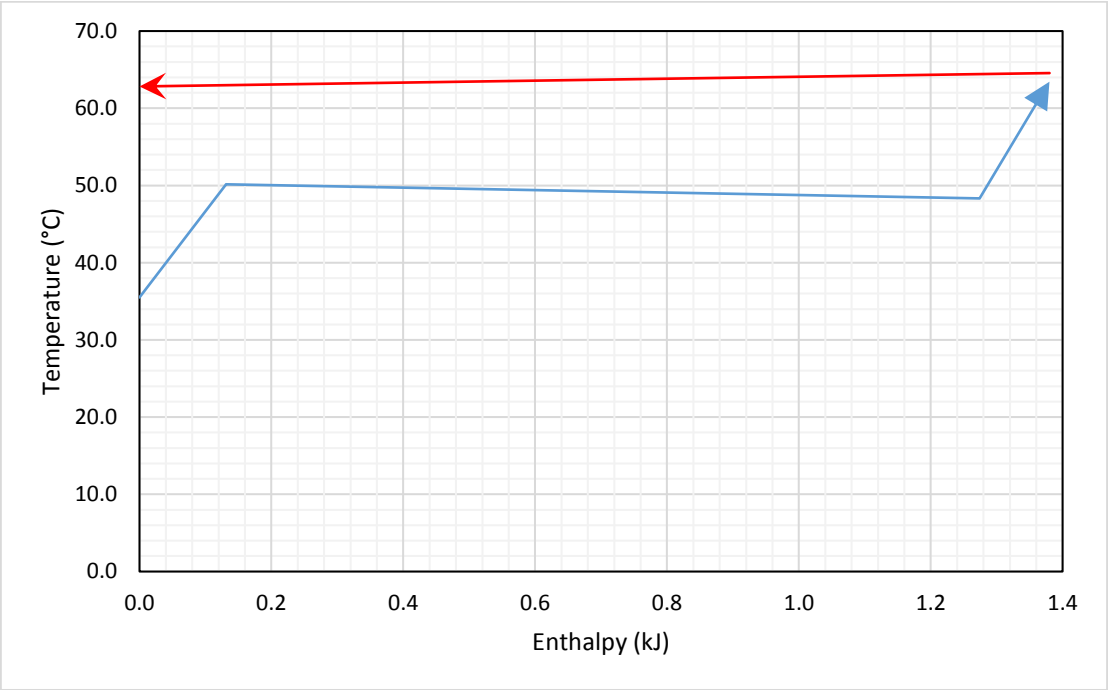

Figure 5.51: Pinch Point Diagram for the evaporator for a heat source temperature of 65°C

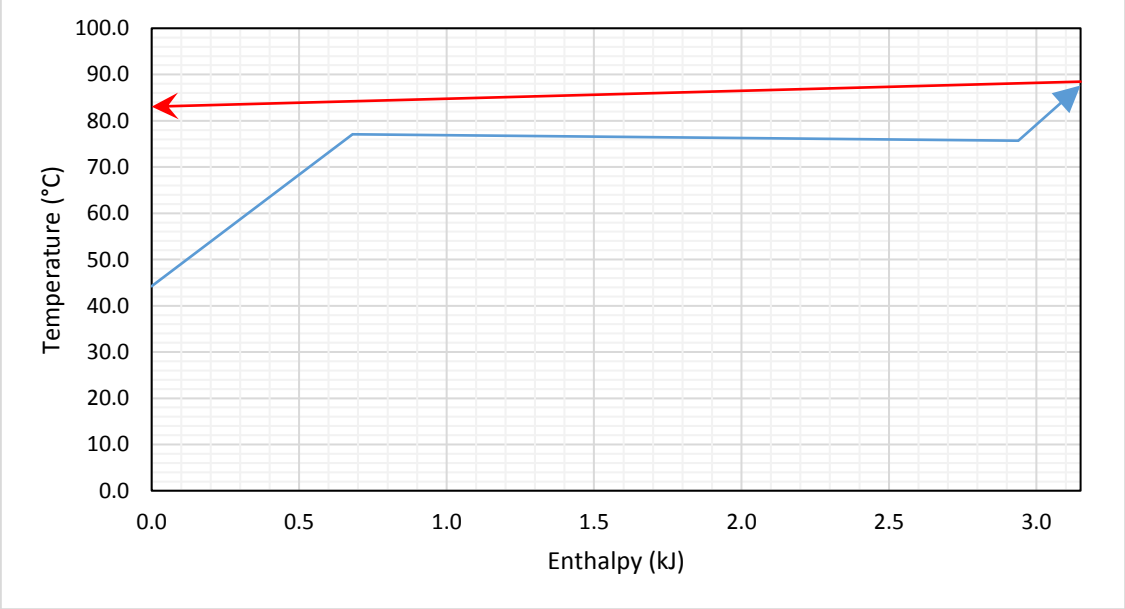

Figure 5.52: Pinch Point Diagram for the evaporator for a heat source temperature of 95°C

Figure 5.53 and Figure 5.54 show the condenser pinch point diagrams for the heat source temperatures of 65°C and 95°C. The shapes of the two plots are similar, with both starting in the two-phase region, and the pinch point lying at the cold side inlet. The enthalpy change is greater for the 95°C heat source temperature, as is to be expected. The greater mass flow rate and heat input results in a greater loading on the condenser.

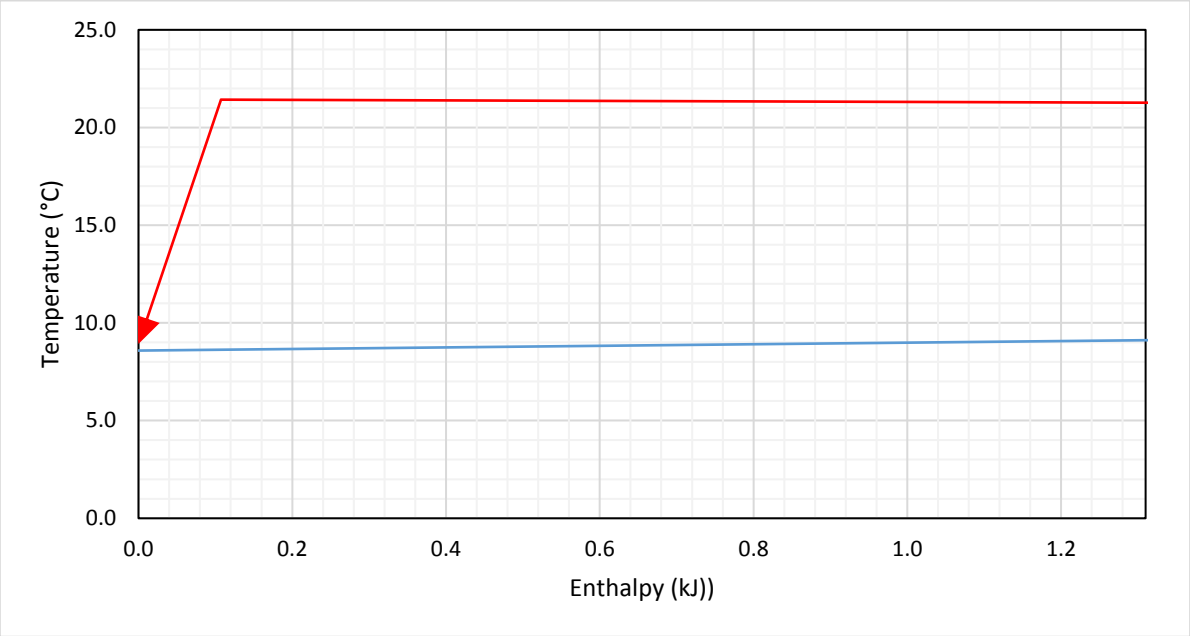

Figure 5.53: Condenser Pinch Point Diagram for a heat source temperature of 65°C

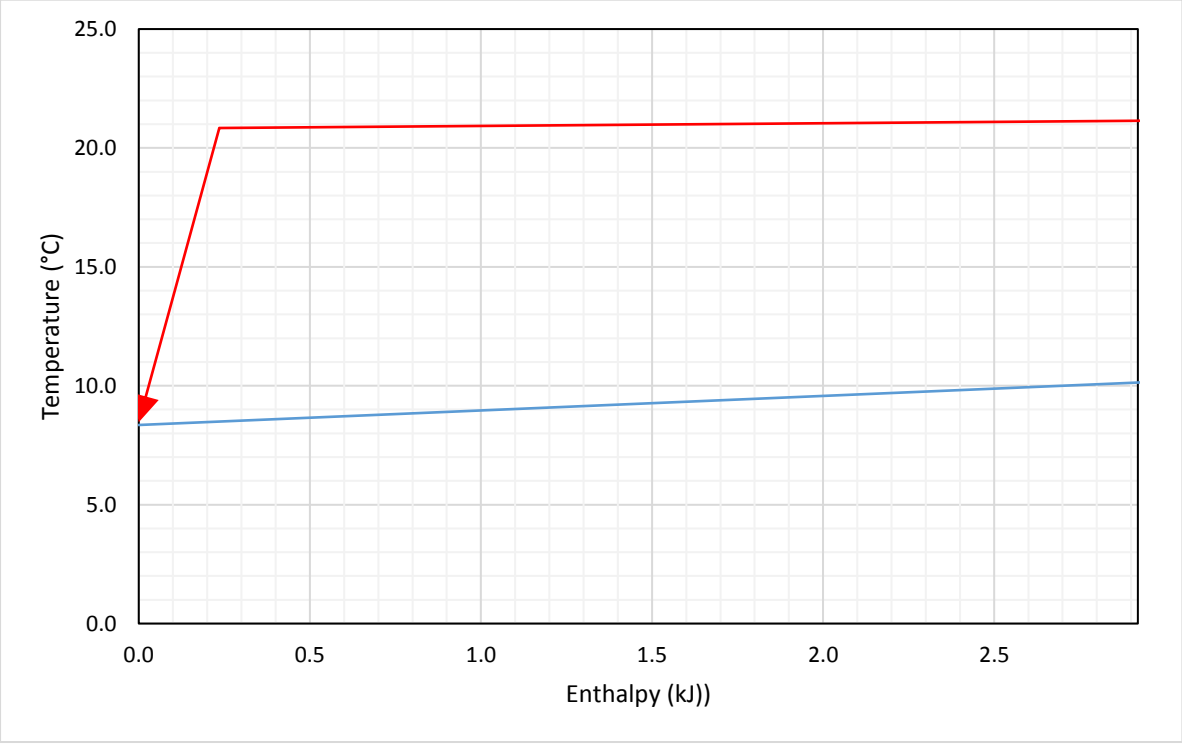

Figure 5.54: Condenser Pinch Point Diagram for a heat source temperature of 95°C

Figure 5.55 and Figure 5.56 show the pinch point diagrams for the regenerator for the heat source temperatures of 65°C and 95°C. In both cases there is a phase change on the hot side of the regenerator but not on the cold side. However, the total specific enthalpy change, and the expander inlet superheat, are greater for the 95°C case.

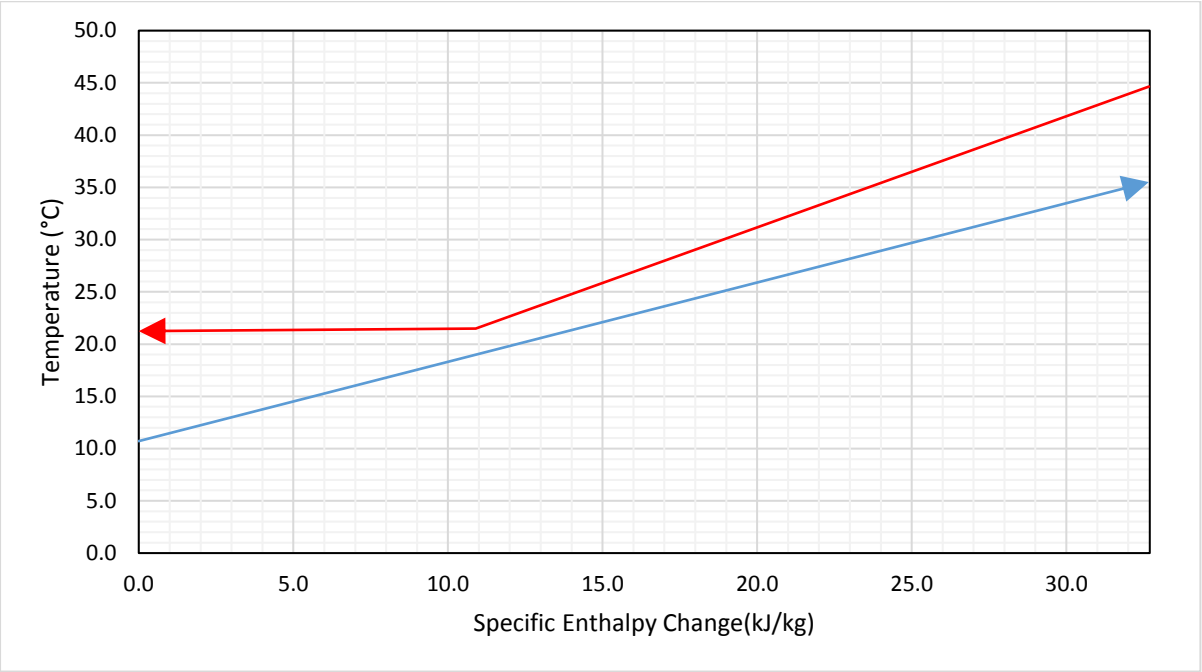

Figure 5.55: Regenerator Pinch Point Diagram for a Heat Source Temperature of 65°C

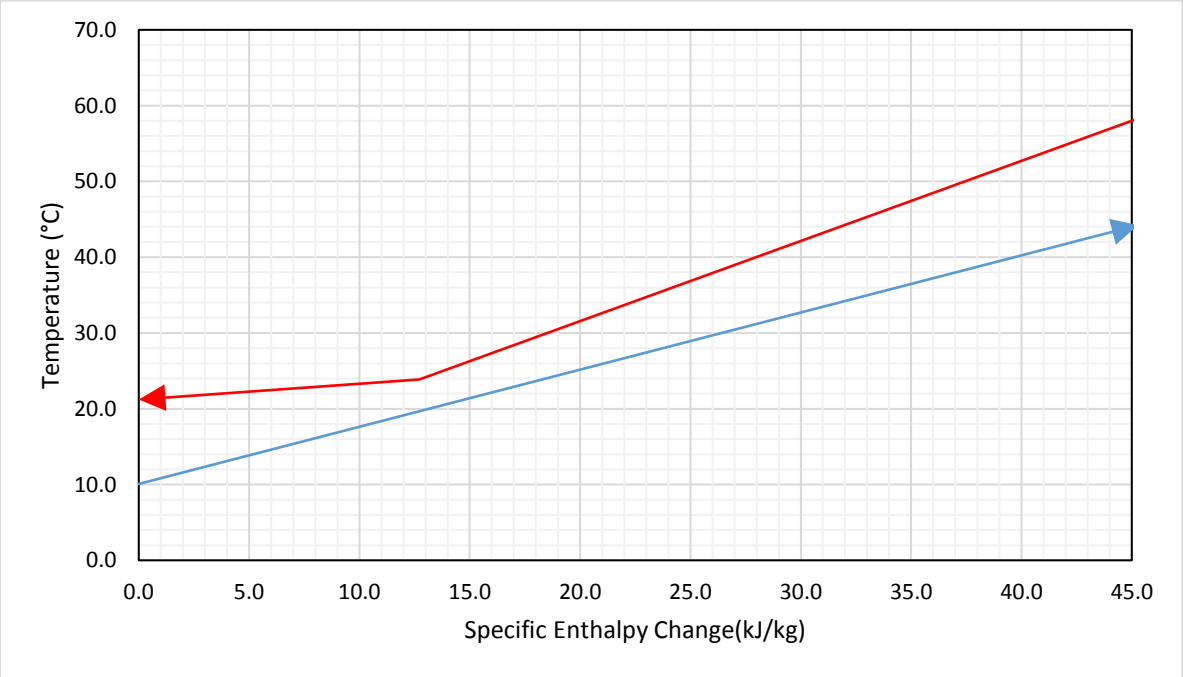

Figure 5.56: Regenerator Pinch Point Diagram for a Heat Source Temperature of 95°C

From these results, it can be determined that increasing the cycle pressure ratio is highly beneficial to the cycle power and the cycle efficiency. The addition of a regenerator has the effect of reducing mass flow rate, which reduces the cycle power, but does substantially reduce the heat demand in the evaporator resulting in a net increase in thermal efficiency. In the next section the effect of changing the working fluid composition will be investigated.

5.7 Zeotropic Cycles

The rig was designed to be easily charged with different blends of working fluid, as well as with pure R245fa. For this thesis, R134a was progressively charged into the rig to create blends with a mass fraction of up to 30% R134a. Above this value, the evaporator pressure rose above the rated pressure of the expander. For each working fluid composition the temperature was varied from 60°C to 95°C and the pump speed was set to both 20Hz and 40Hz.

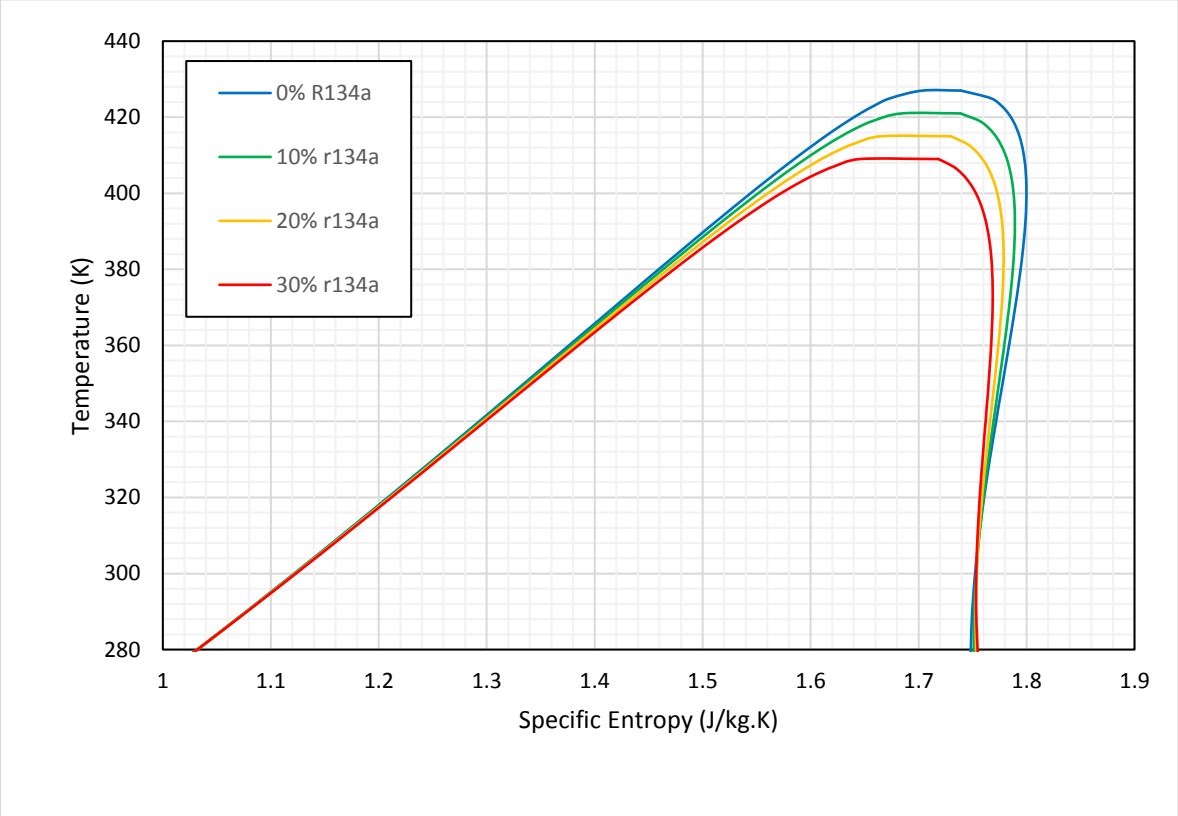

Figure 5.57: Comparison of saturation domes as the working fluid composition changes, calculated using REFPROP.

Figure 5.57 shows how the change in working fluid composition affects the shape of the saturation dome of the cycle. Two effects are obvious. Firstly, increasing the mass fraction of r134a lowers the critical temperature of the cycle. Secondly, increasing the mass fraction of r134a also lowers the specific entropy at the critical point. This has the effect of changing the

fluid from noticeably dry to near-isentropic. In theory this will increase the overall efficiency of the cycle due to a larger specific enthalpy drop during the expansion process, but also reduce the effect of the regenerator due to a reduced expander inlet superheat. These two effects, as well as the effect of introducing glide into the phase changes in the cycle, will be discussed in this section.

5.7.1 Non-regenerative cycles

This section analyses the performance of the non-regenerative cycle as the working fluid composition changes. The explanation for these observed trends is presented in terms of the thermodynamic data that can be determined from the measured parameters. A pump speed of 20Hz was used for all cases, as the capacity of the water heater was insufficient to maintain a constant heat source temperature for higher pump speeds.

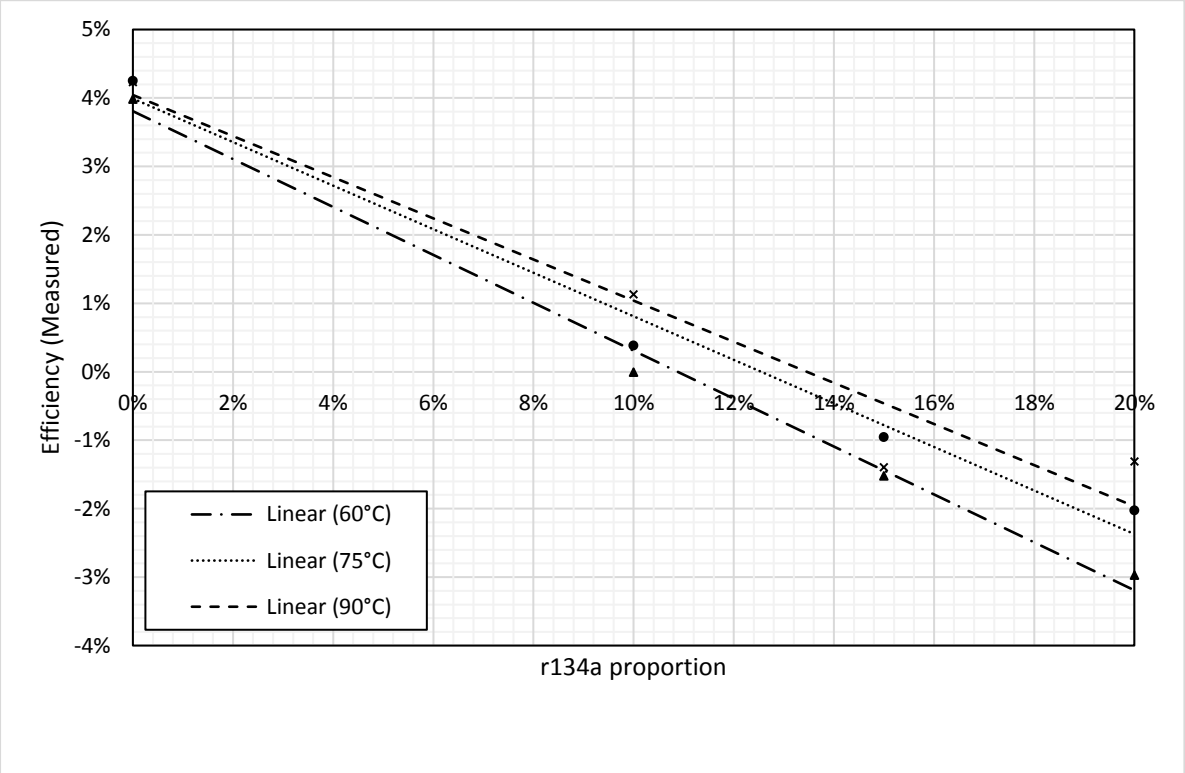

Figure 5.58: Variation in the measured efficiency of the dynamic cycle with varying mixture composition for three different heat source temperatures and a pump speed of 20Hz

These results are plotted in Figure 5.58. There is an obvious trend of decreasing first law efficiency with increasing proportion of r134a in the working fluid. For proportions of r134a above 20% the power was too low for the generator to synchronise, so no tests could be carried

out. The decrease in efficiency must be due to either an increase in the required power for the decrease in the output power of the cycle.

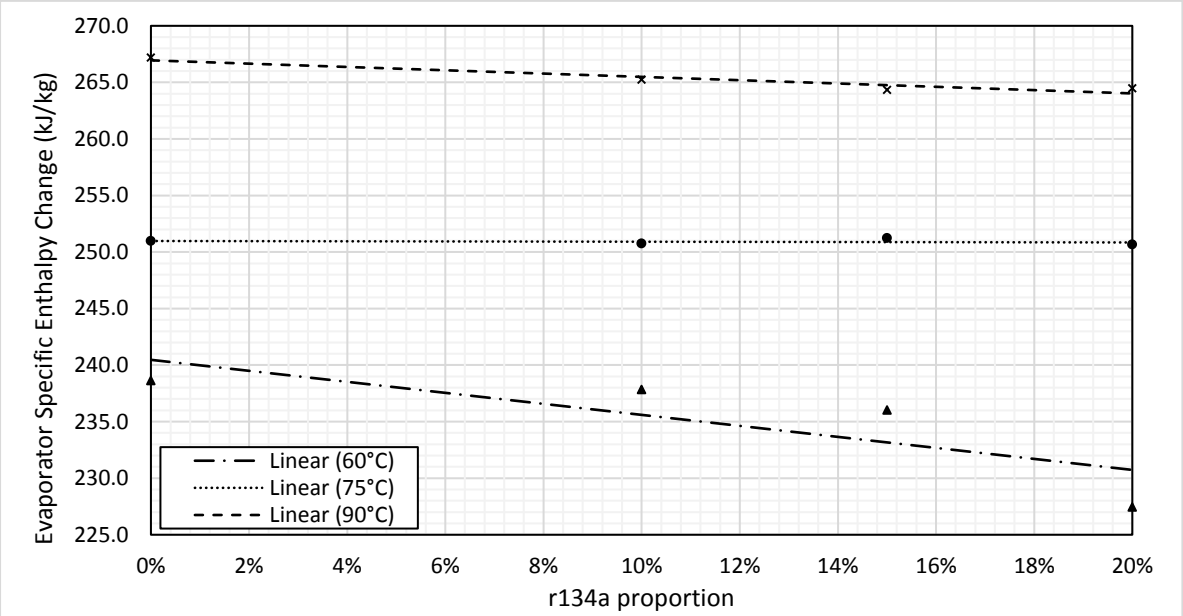

Figure 5.59: Variation in evaporator specific enthalpy change with changing proportion of r134a in the working fluid.

Figure 5.59 shows how the evaporator specific enthalpy change varies as the working fluid composition changes. It can be seen that for the higher heat source temperatures there is no distinct trend in the evaporator specific enthalpy change, and that at the lowest heat source temperature considered, the specific enthalpy change only decreased from 238kJ/kg to 227kJ/kg, a decrease of only 4.6%. Therefore the decrease in efficiency cannot be caused primarily by a change in the evaporator enthalpy.

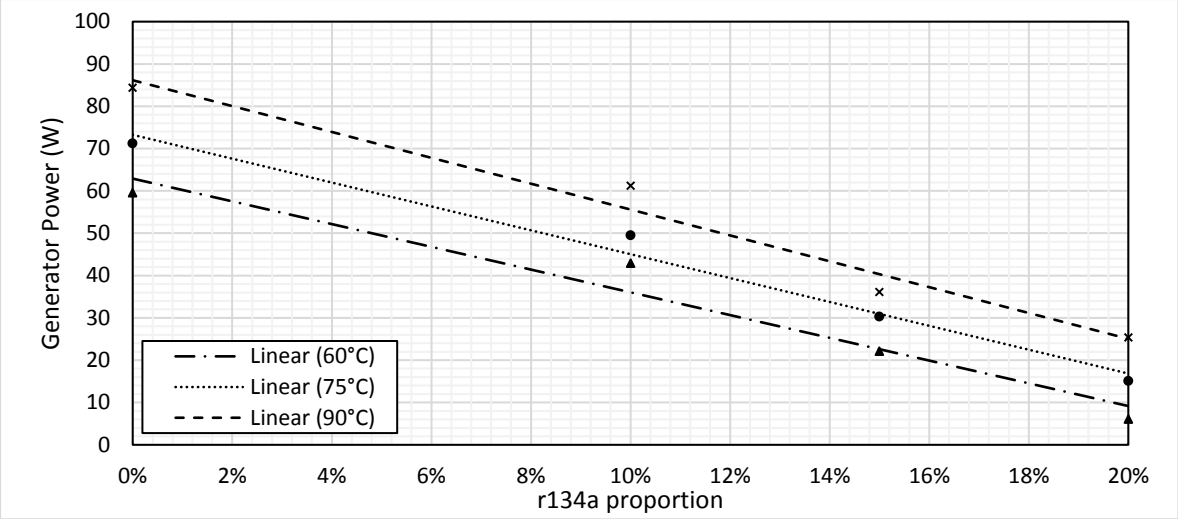

Figure 5.60: Variation in generator power with varying working fluid composition for a non-regenerative cycle and a pump speed of 20Hz

Figure 5.60 shows the variation in the generator power as the working fluid composition changes. Here, it can be seen that there is a clear downward trend in the generator power as the working fluid composition shifts towards a higher proportion of r134a. Possibly reasons for this trend will be investigated over the following few figures.

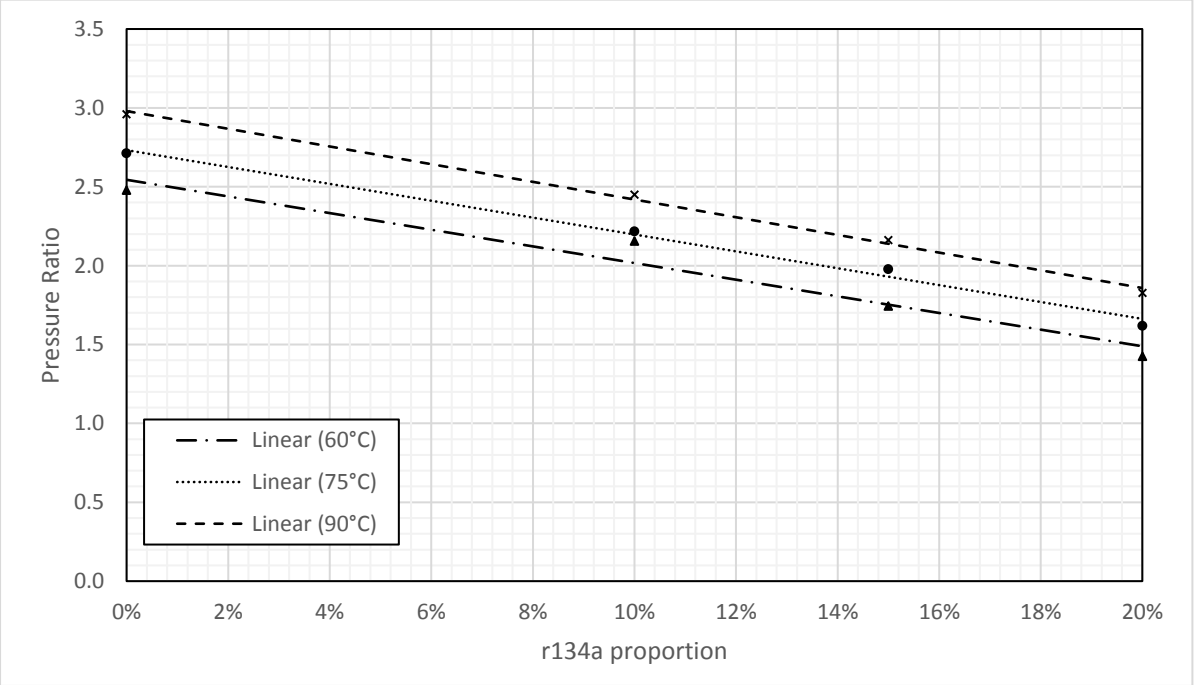

Figure 5.61: Variation in cycle pressure ratio with increasing proportion of r134a for a non-regenerative cycle and a pump speed of 20Hz

Figure 5.61 shows how the pressure ratio in the cycle varies as the working fluid composition changes for three different heat source temperatures. There is a clear decrease in the pressure ratio of the cycle as the composition shifts towards r134a. Figure 5.62 and Figure 5.63 show the evaporator pressure is more or less constant as the composition changes, and that for all compositions, it is higher for the higher heat source temperatures. Figure 5.63 shows a noticeable increase in the condenser pressure as the working fluid composition shifts towards r134a. This is due to the lower boiling point of r134a compared to r245fa, giving a correspondingly higher vapour pressure. This increase in condenser pressure, and corresponding reduction in cycle pressure ratio, is the most likely explanation for the decrease in cycle efficiency observed as the proportion of r134a in the working fluid increases.

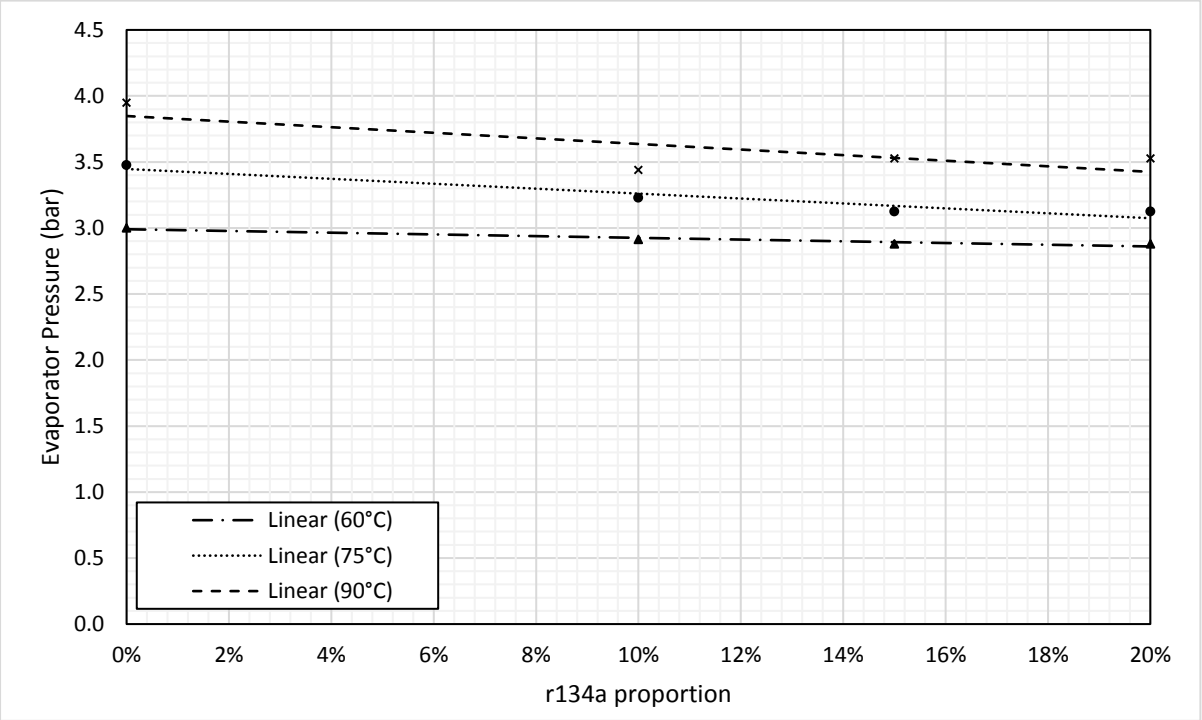

Figure 5.62: Variation in the evaporator pressure of the cycle as the working fluid composition changes for a non-regenerative cycle and a 20Hz pump speed.

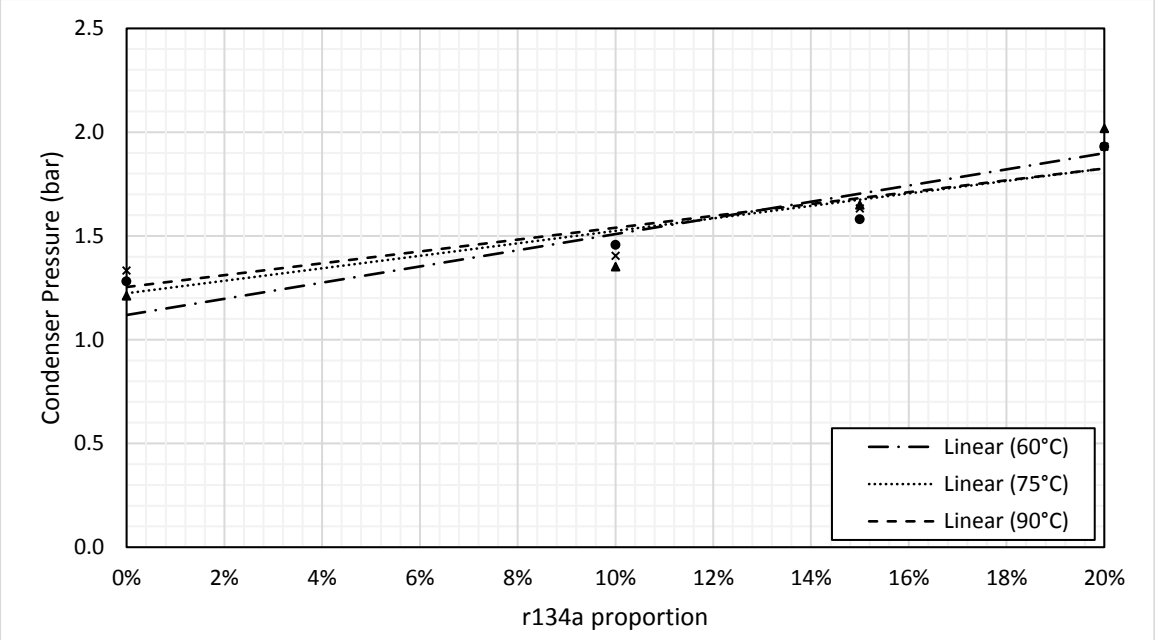

Figure 5.63: Variation in the condenser pressure of the cycle as the working fluid composition changes for a non-regenerative cycle and a 20Hz pump speed.

Apart from its effect on the efficiency of the cycle the zeotropic mixture has several other effects due to its introduction of a temperature glide into the phase change.

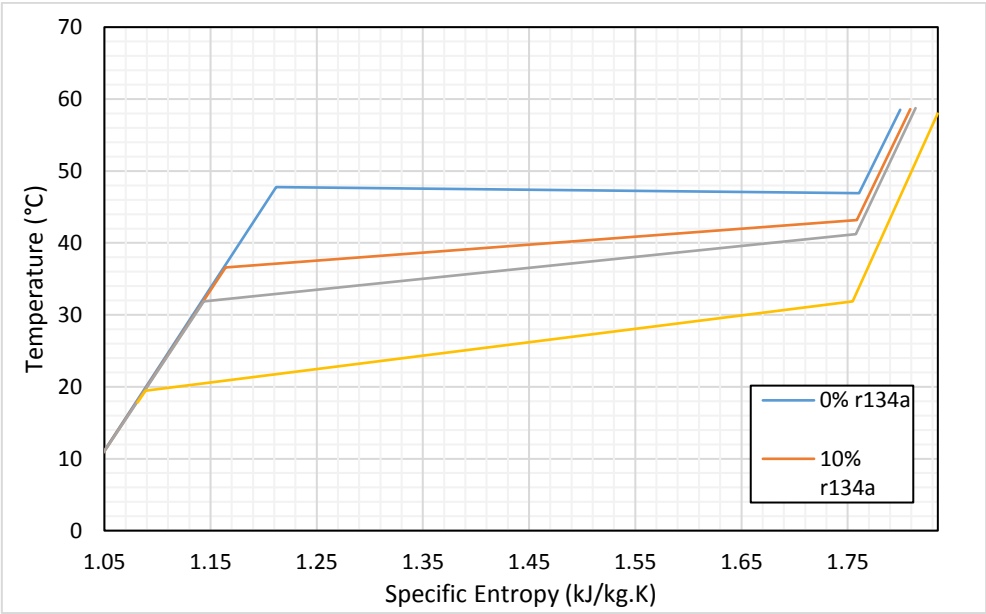

Figure 5.64: T-s diagram of the evaporating process for a non-regenerative cycle, heat source temperature of 60°C and a pump speed of 20Hz, for four different working fluid compositions

Figure 5.64 shows T-s diagrams of the evaporating process for a pump speed of 20Hz and a heat source temperature of 60°C. It can be seen that whereas the the phase change process is near-isothermal for the pure r245fa, represented by the blue line in the plot, with increasing r134a proportion in the working fluid the evaporating temperature decreases, and the level of temperature glide increases. The same trend of decreasing evaporating temperature and increasing temperature glide is evident in Figure 5.65 and Figure 5.66, which plot the same data for heat source temperatures of 75°C and 90°C.

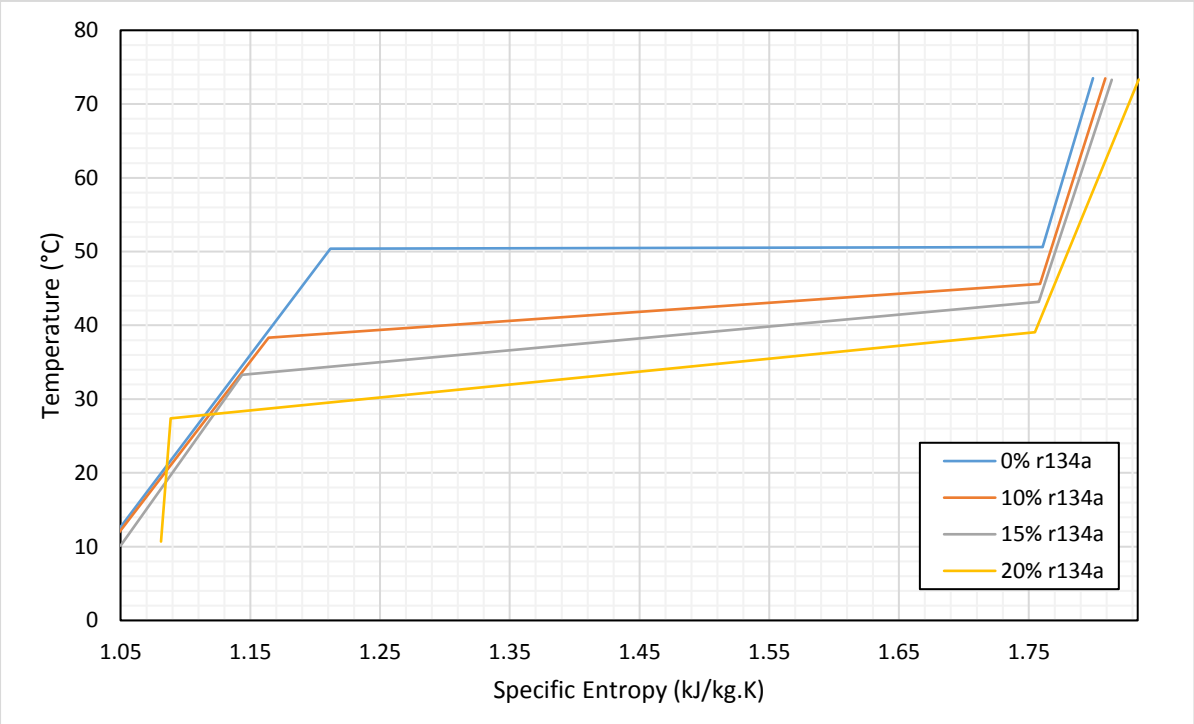

Figure 5.65: T-s diagram of the evaporating process for a non-regenerative cycle, heat source temperature of 75°C and a pump speed of 20Hz, for four different working fluid compositions

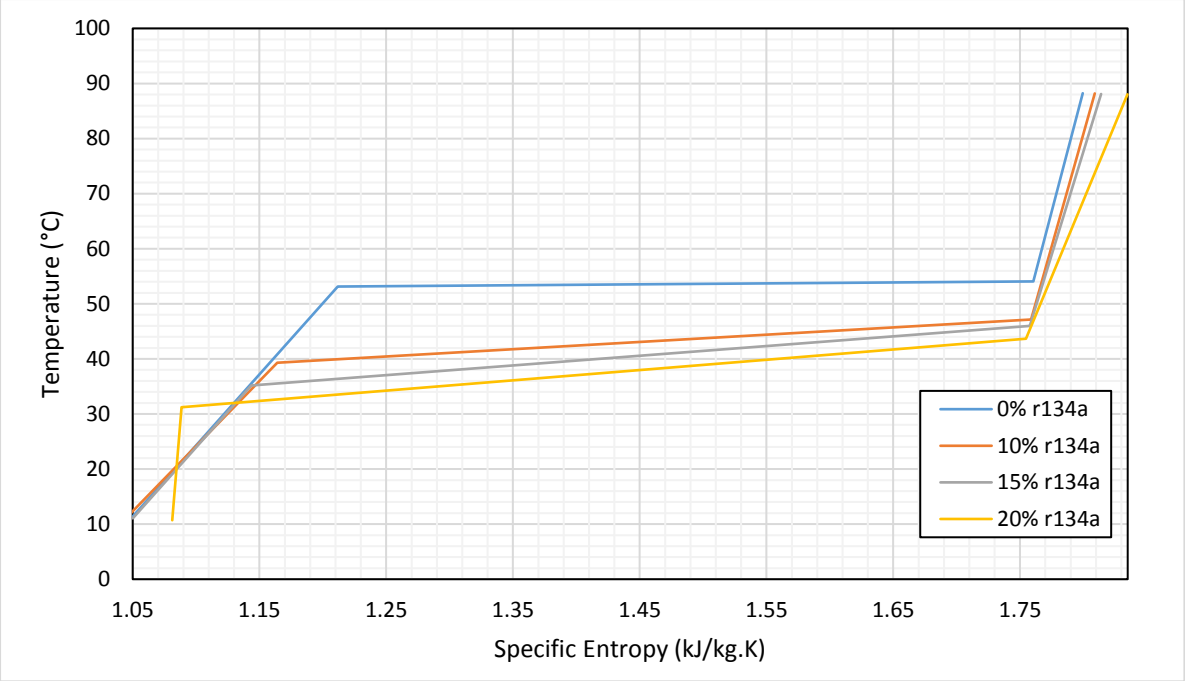

Figure 5.66: T-s diagram of the evaporating process for a non-regenerative cycle, heat source temperature of 90°C and a pump speed of 20Hz, for four different working fluid compositions

Figure 5.67 shows how the temperature glide during the evaporation process changes with varying working fluid composition for three difference heat source temperatures. Along with an increasing temperature glide as the working fluid composition shifts towards r134a, another trend can be observed, which is an increase in the temperature glide as the heat source temperature increases.

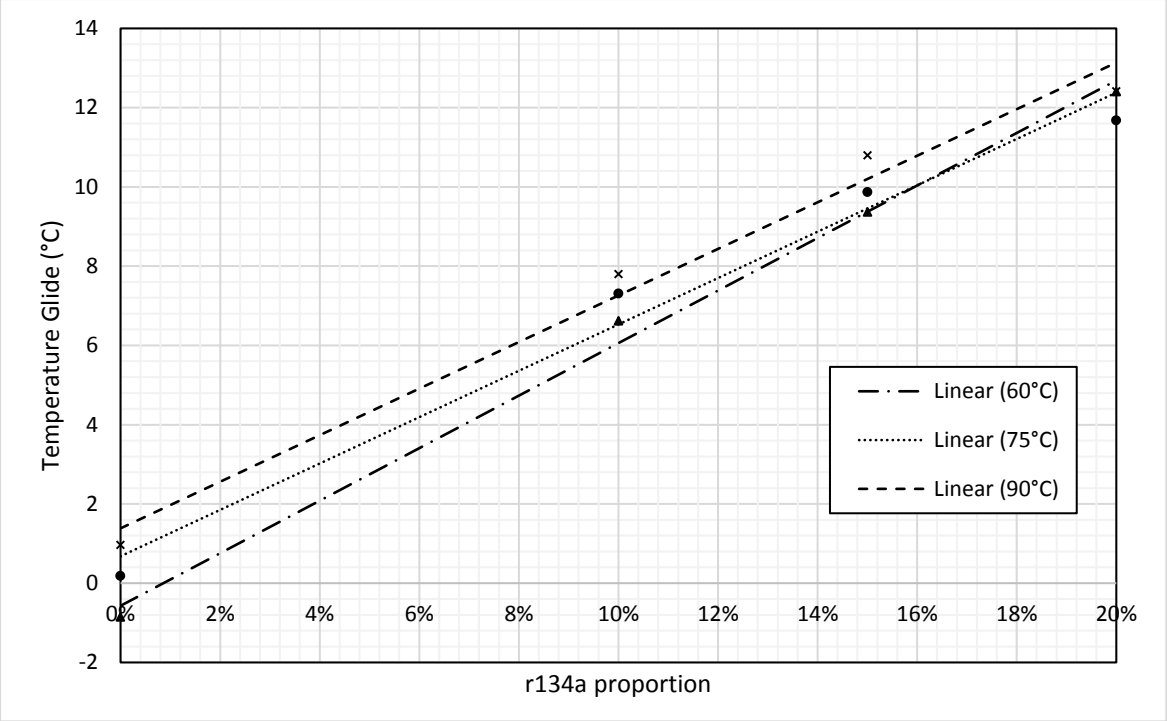

Figure 5.67: Variation in temperature glide for three heat source temperatures with varying working fluid composition, for a non-regenerative cycle and 20Hz pump speed.

This increase in temperature glide with increasing heat source temperature is thought to be a result of the pressure variations in the evaporator, which are plotted in Figure 5.68. At lower heat source temperatures there is a pressure drop of between 0.1 and 0.2 bar across the evaporator. For the 90°C heat source temperature, this has changed to an increase in pressure across the evaporator of 0.1 to 0.3 bar. This is thought to be due to the change in the specific volume of the fluid as it changes phase, and the vapour as it heats up and expands, with these effects being more significant, and overriding the effects of friction, entry and exit losses in the heat exchanger as the heat source temperature rises further.

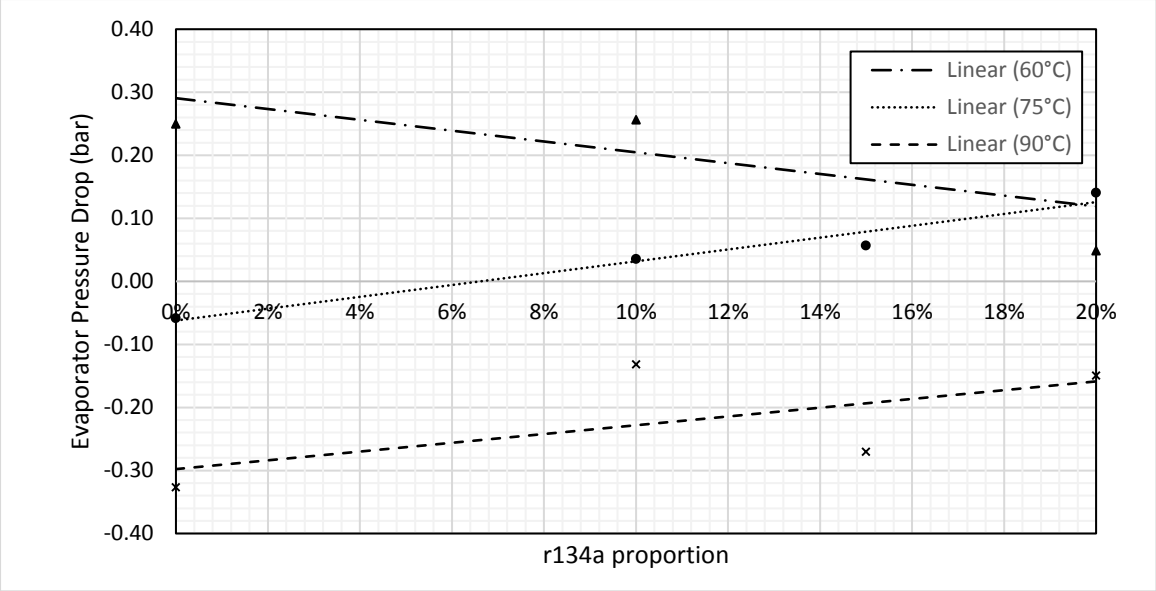

Figure 5.68: Variation in Evaporator Pressure Drop with varying r134a proportion in the working fluid for a non-regenerative cycle with a pump speed of 20Hz.

The expected effect of this temperature glide is to allow a greater temperature change in the thermal fluid as it passes through the hot side of the evaporator, giving higher thermal fluid utilisation.

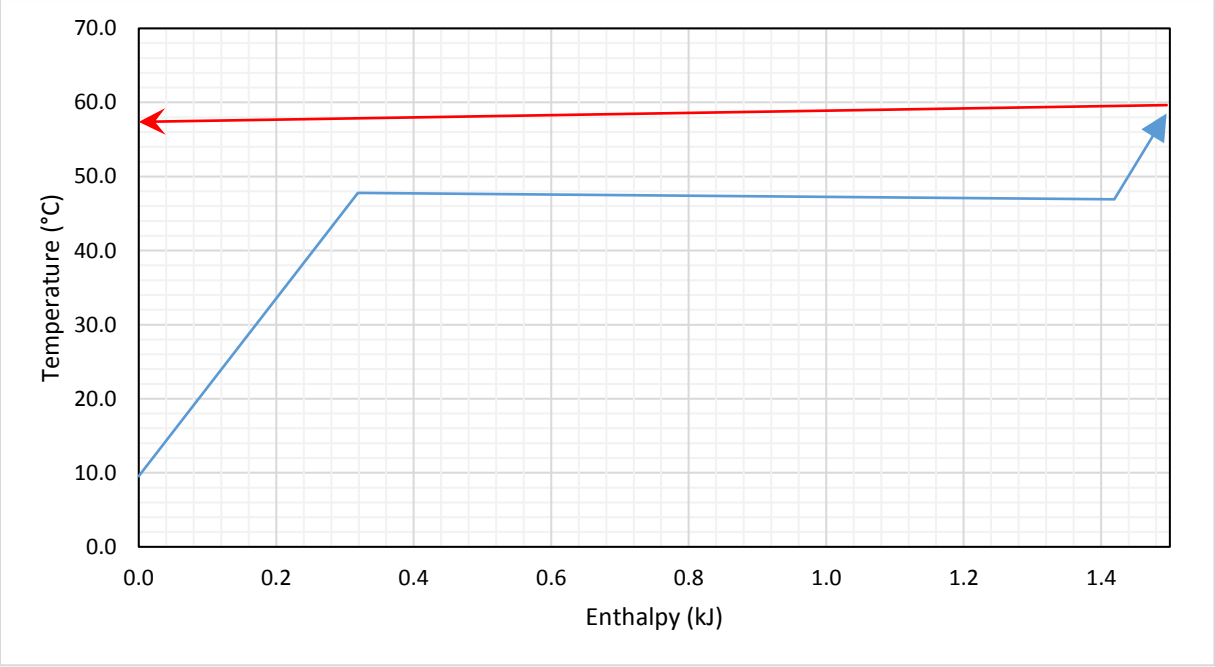

Figure 5.69: Pinch point diagram for the evaporator for a heat source temperature of 60°C and a working fluid composition of 100% r245fa, for a pump speed of 20Hz

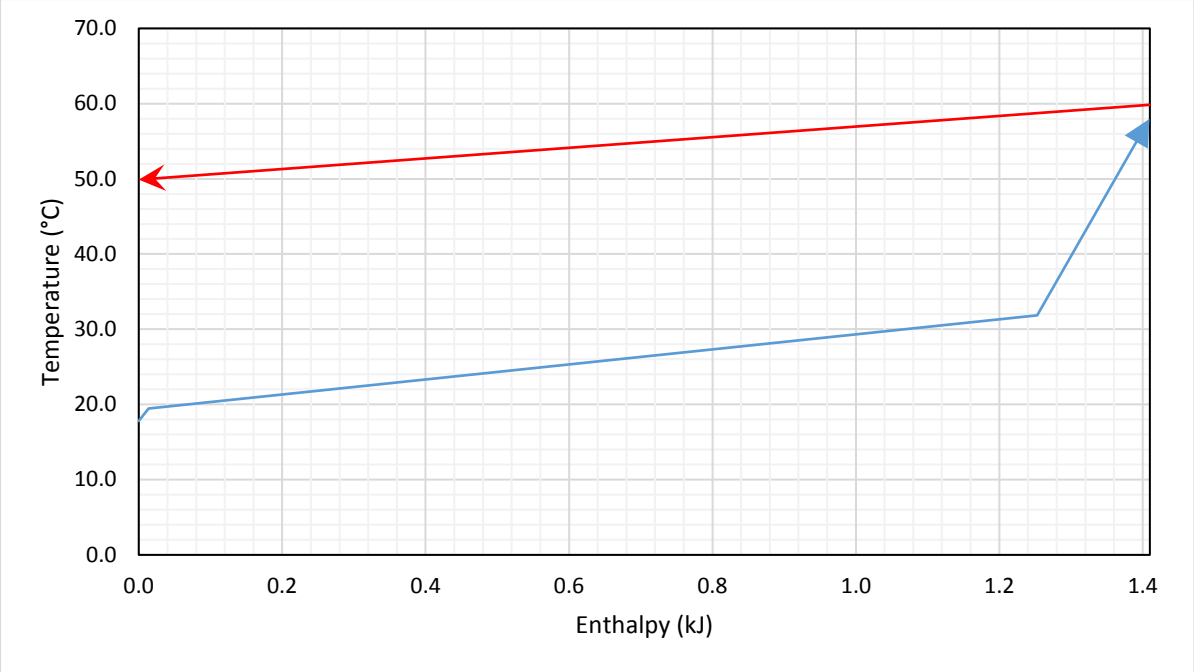

Figure 5.70: Pinch point diagram for the evaporator for a heat source temperature of 60°C and a working fluid composition of 80% r245fa:20%r134a, for a pump speed of 20Hz

Figure 5.69 and Figure 5.70 show the evaporator pinch point diagrams for the cycle with a heat source temperature of 60°C, for two different working fluid compositions. For the 100% r245fa case, there is no obvious temperature glide as the working fluid changes phase, and the thermal fluid undergoes a temperature change of 2.2°C. For the 20% r134a case, the plot has a different shape. There is now an obvious temperature glide as the working fluid changes phase of 12.4°C. The temperature change in the thermal fluid has increased to 9.9°C, due to the greater temperature difference between the hot and cold sides of the evaporator. This represents better utilisation of the heat source available. The pinch point temperature difference is still, however, relatively wide due to the limited degree to which the speed of the thermal fluid circulation pump could be decreased. For future research, even lower thermal fluid flow rates should be possible for zeotropic working fluids while still maintaining an acceptable pinch point temperature difference.

5.7.1.1 Regenerative Cycles

In this section, the effect of the zeotropic fluids on regenerative cycles will be discussed. The overall performance of the regenerative cycles will be presented, and compared with both similar cycles using a pure working fluid, and the corresponding non-regenerative cycles using a working fluid blend.

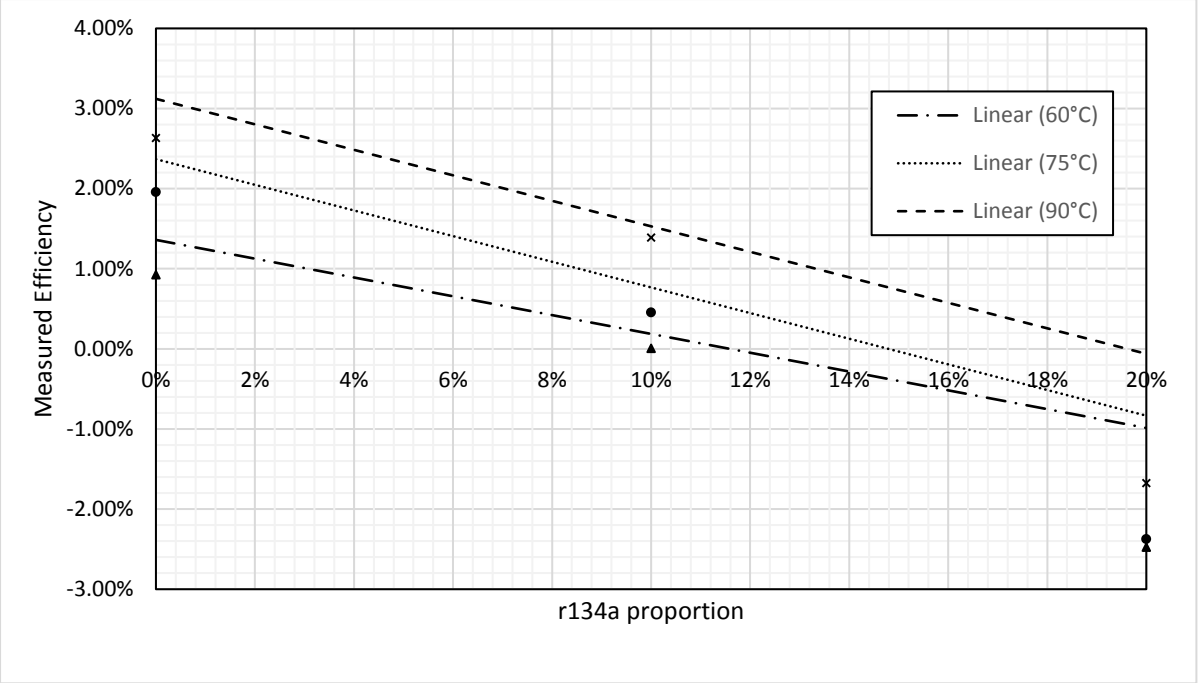

Figure 5.71: Variation in measured cycle efficiency with varying working fluid composition for three different heat source temperatures, for a regenerative cycle with a pump speed of 20Hz.

Figure 5.71 shows how the efficiency of the regenerative cycle varies with changing working fluid composition. Although the values for the efficiency are higher, they show the same general trend of decreasing efficiency with increasing proportion of r134a in the working fluid.

As for the non-regenerative case the evaporator enthalpy change and the generator power were plotted against the fluid composition to ascertain whether the drop in efficiency was due to an increase in the energy requirements of the cycle or a falling expander output as the proportion of r134a in the cycle increased. This data is presented in Figure 5.72 and Figure 5.73.

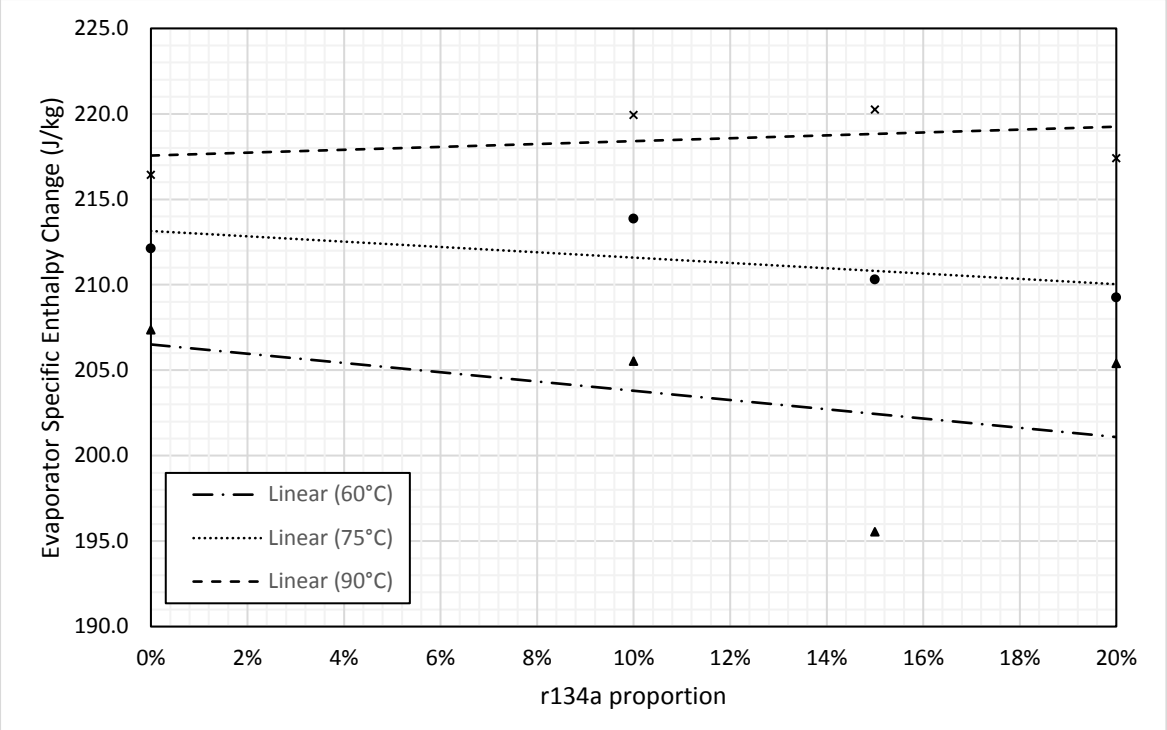

Figure 5.72: Variation in evaporator specific enthalpy change with varying working fluid composition for a regenerative cycle and a pump speed of 20Hz

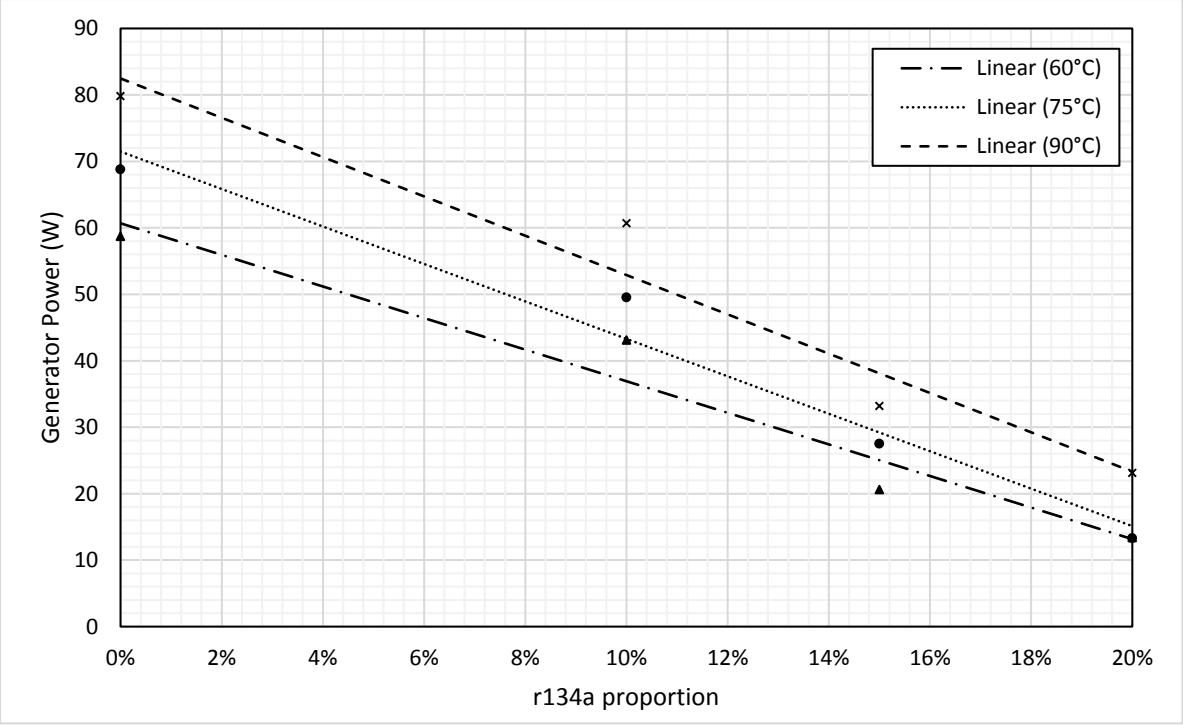

Figure 5.73: Variation in generator output power with varying working fluid composition for a regenerative cycle and a pump speed of 20Hz

Compared with the data presented in Figure 5.59 and Figure 5.60 for the non-regenerative cycle, several things are apparent. Firstly the evaporator enthalpy is lower, due to the influence of the regenerator. Secondly, the generator power is comparable, although slightly lower for the regenerative case, most likely due to the reduced flow rate with the cycle in this configuration, as was the case of the pure working fluid. Thirdly, the general trend of both the evaporator enthalpy and the generator power are the same for both the regenerative and non-regenerative cases, with the evaporator enthalpy remaining more or less constant as the working fluid composition changes, whereas the generator power decreases with increasing r134a in the working fluid.

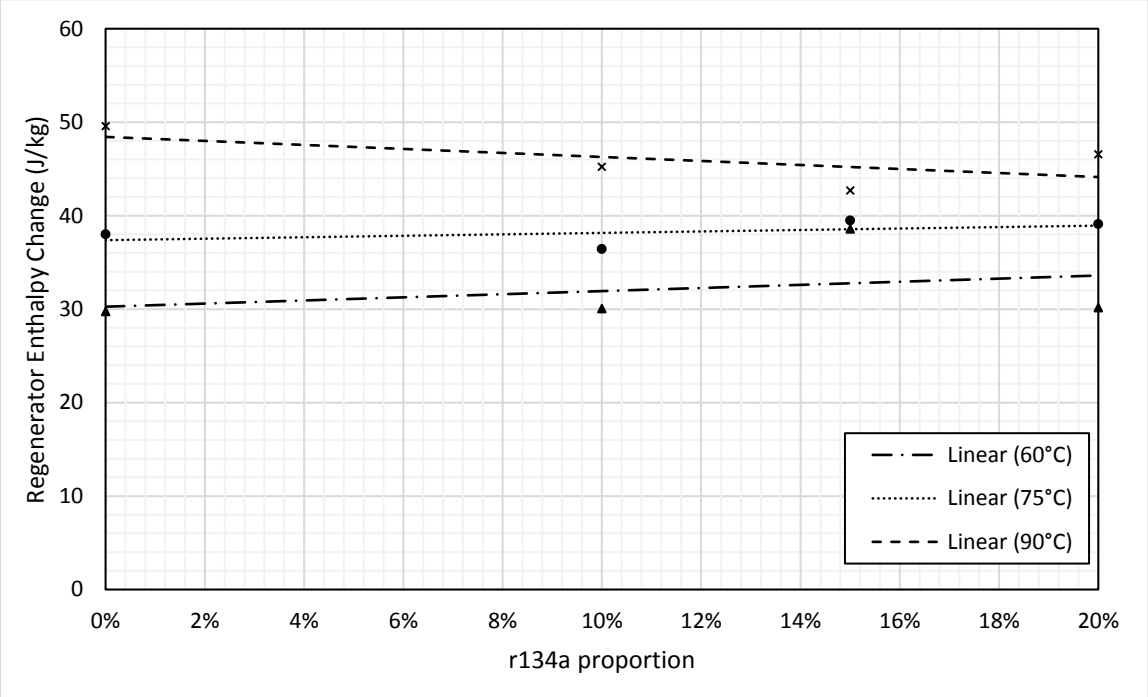

Figure 5.74: Variation in regenerator enthalpy change with changing working fluid composition for a regenerative cycle and a pump speed of 20Hz

Figure 5.74 shows how the specific enthalpy change in the regenerator varies with changing working fluid composition. The expectation was that with increasing proportion of r134a in the fluid, the regenerator enthalpy change would increase. However, the results shown in Figure 5.74 show no clear trend in the enthalpy change in the regenerator. To determine the cause of this, the T-h diagrams of the regenerator are examined in the following figures.

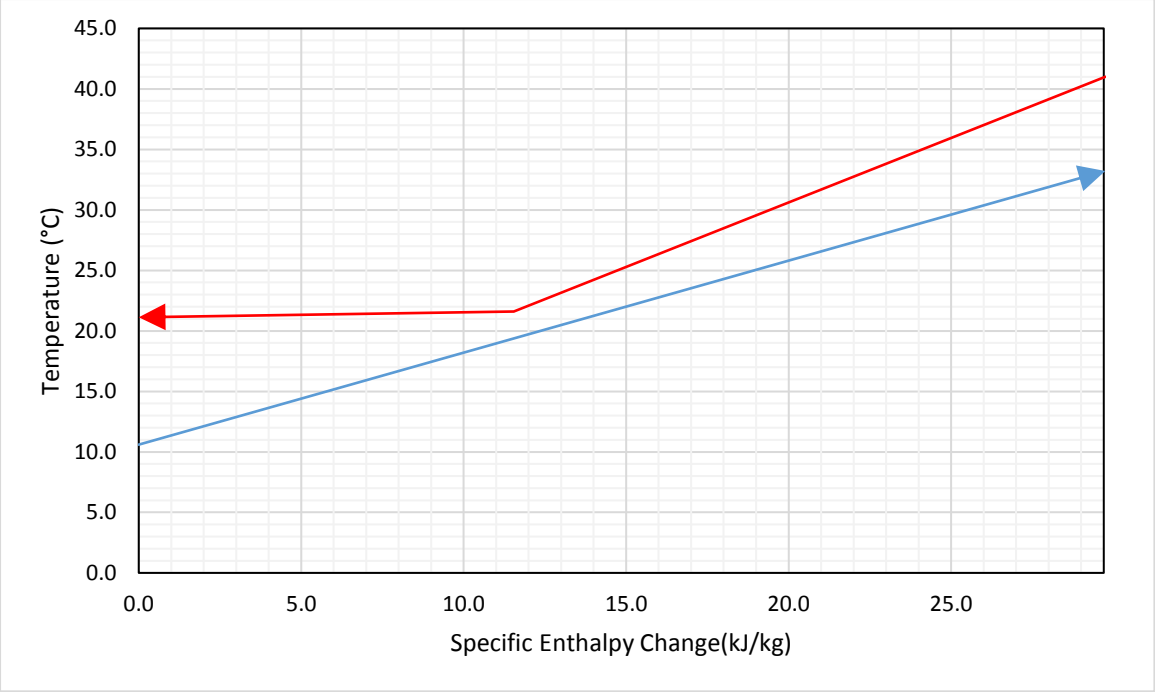

Figure 5.75: Regenerator pinch point diagram for a heat source temperature of 60°C and a working fluid composition of 100% r245fa.

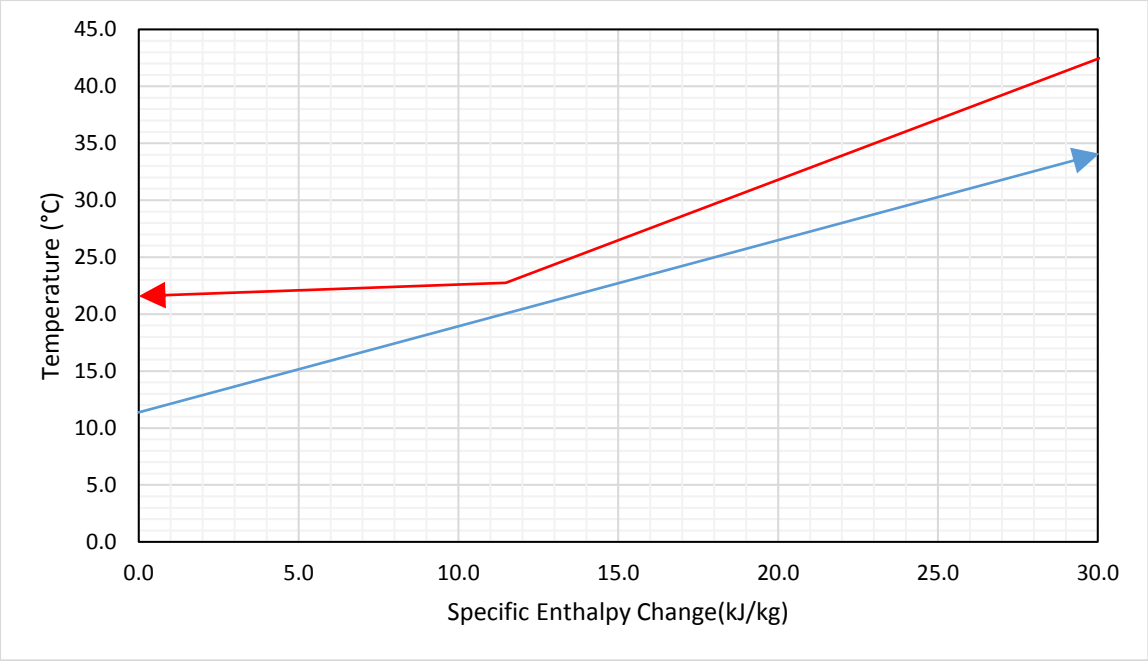

Figure 5.76: Regenerator pinch point diagram for a heat source temperature of 60°C and a working fluid composition of 90% r245fa:10%r134a

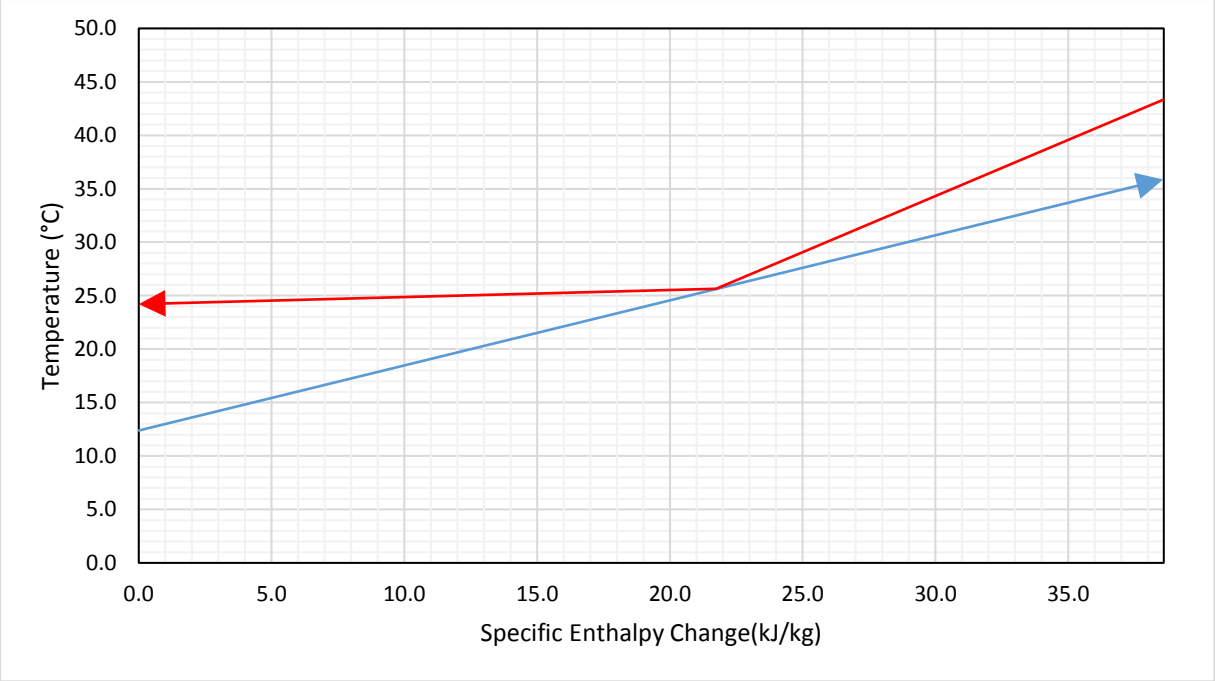

Figure 5.77: Regenerator pinch point diagram for a heat source temperature of 60°C and a working fluid composition of 85% r245fa:15%r134a

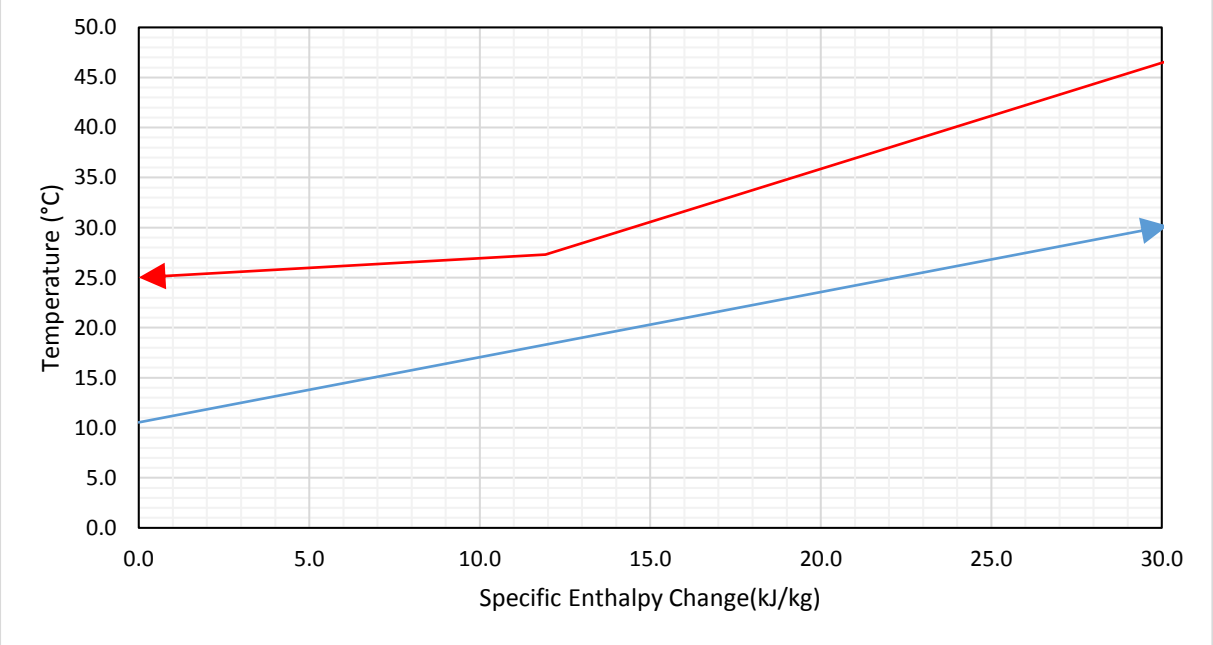

Figure 5.78: Regenerator pinch point diagram for a heat source temperature of 60°C and a working fluid composition of 80% r245fa:20%r134a

Figure 5.75 to Figure 5.78 show the T-h diagrams for the regenerator for a heat source temperature of 60°C. The evaporator hot side inlet temperature increases from 41.1°C to 46.7°C, and the dew point increases from 21.1°C to 27.3°C. These changes are likely to be a result of both the changing working fluid composition and the increasing condenser pressure. This would tend to increase the driving temperature difference in the heat exchanger. However, the pinch point temperature difference increases from 2.1°C for the 100% r245fa case to 10.2°C for the 80% r245fa:20%r134a case. The increasing pinch point temperature difference would seem to indicate a reduction in the effectiveness of the heat exchanger. This is consistent with the results reported in the literature, which indicate a decreased heat transfer coefficient for working fluid mixtures.

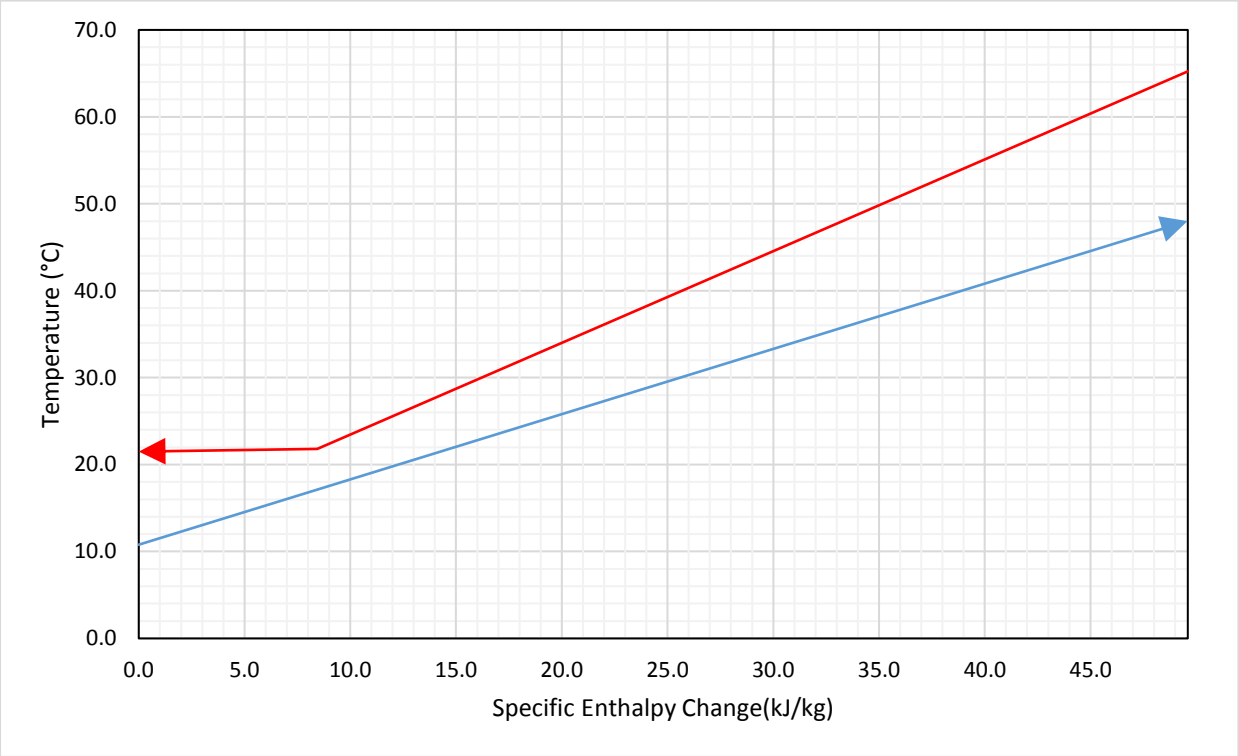

Figure 5.79: Regenerator pinch point diagram for a heat source temperature of 90°C and a working fluid composition of 100% r245fa

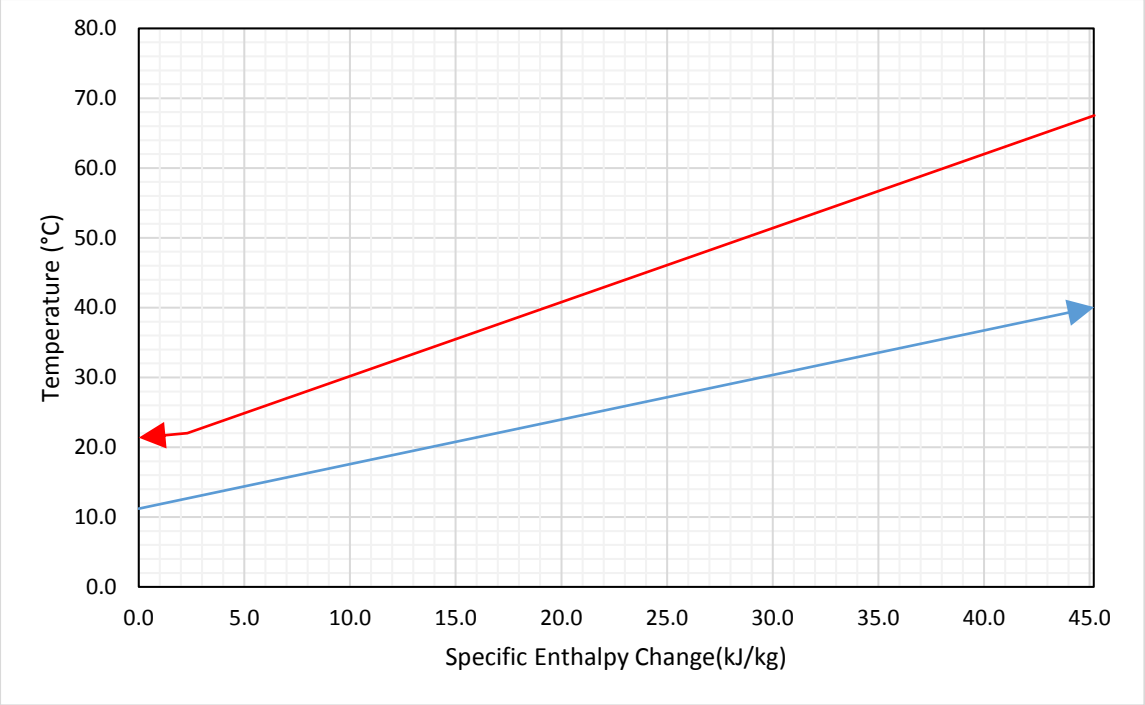

Figure 5.80: Regenerator pinch point diagram for a heat source temperature of 90°C and a working fluid composition of 100% r245fa:10% r134a

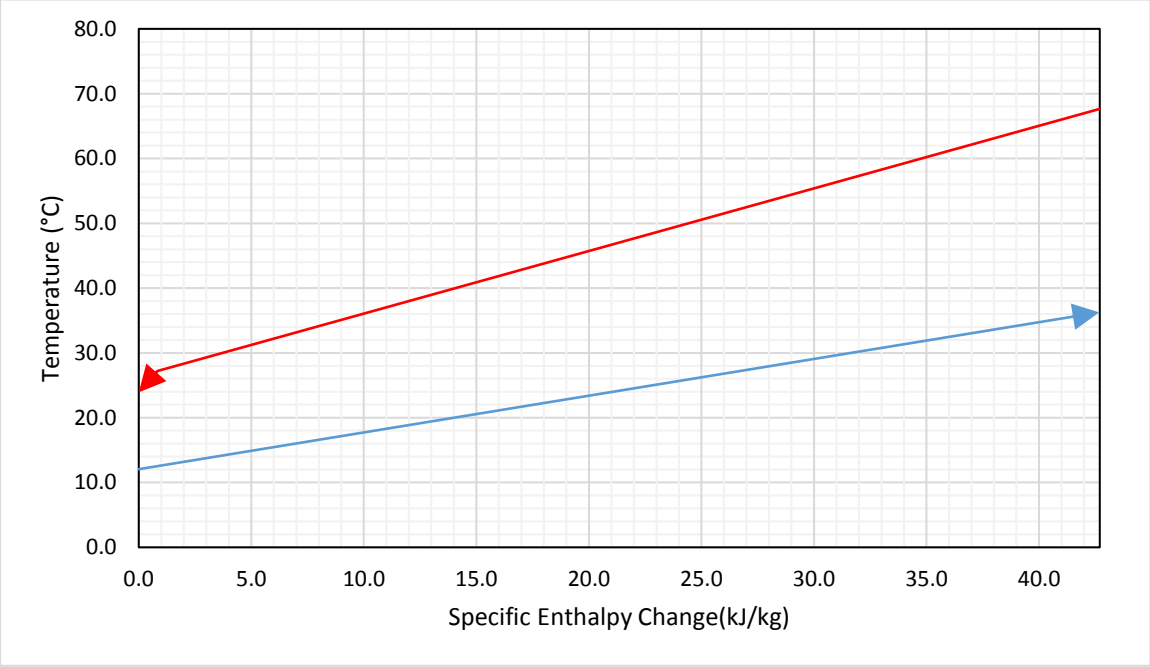

Figure 5.81: Regenerator pinch point diagram for a heat source temperature of 90°C and a working fluid composition of 85% r245fa:15% r134a

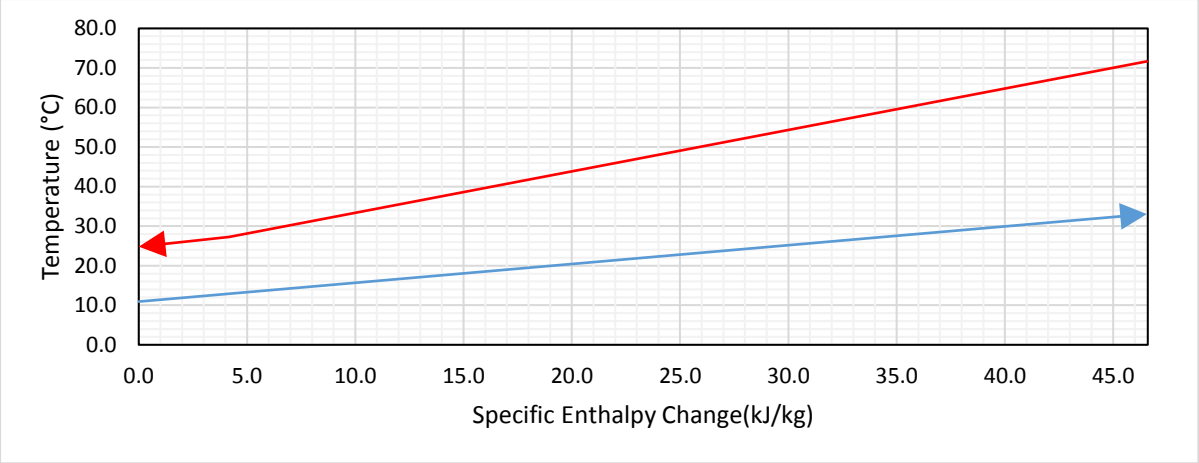

Figure 5.82: Regenerator pinch point diagram for a heat source temperature of 90°C and a working fluid composition of 80% r245fa:20% r134a

Figure 5.79 to Figure 5.82 present the same data for a heat source temperature of 90°C. Again there is no overall trend in the specific enthalpy change in the regenerator and the pinch point temperature difference rises from 3.9°C to 13.9°C, while also shifting from the dew point of the hot side to the hot side outlet, due to the glide increasing the slope of the T-h plot in the two-phase region. As for the case of the 60°C heat source temperature, this implies that the heat transfer process in the heat exchanger is becoming less efficient with increasing proportion of r134a in the working fluid.

5.8 Summary

In this section the experimental results of the Organic Rankine Cycle rig are presented and discussed for both zeotropic and non-zeotropic fluids, and regenerative and non-regenerative cycles. For all cycles, increasing heat source temperature resulted in increasing cycle efficiency, as expected. Regenerative cycles demonstrated increased cycle efficiency, due to the reduced heat requirement in the evaporator, but the extra flow resistance from the additional heat exchanger reduced the mass flow rate of the working fluid, reducing the cycle power. Zeotropic cycles showed increased condenser pressure, which reduced the efficiency of the cycle. The working fluid blend seemed to reduce the efficiency of the heat transfer processes in the heat exchangers, meaning that the expected improvement in regenerator enthalpy change and cycle specific power was not observed.

In the next chapter, the dynamic Organic Rankine Cycle concept will be presented and explored.

CHAPTER 6- DYNAMIC ORGANIC RANKINE CYCLE

In this section, the concept of the Dynamic Organic Rankine Cycle is presented. The justification for the concept is outlined, as is the MATLAB model used to analyse the cycle. The thermodynamic results of the analysis for a range of heat source temperatures, heat sink conditions, and cycle configurations are also laid out.

6.1 Performance of conventional ORCs with varying heat sink temperatures

As laid out previously, the efficiency of a heat engine depends heavily on the temperature differential between the hot and cold reservoirs between which it operates. Organic Rankine Cycles tend to operate with lower temperature heat sources than other thermal cycles, but they still use the same heat sinks. This means that the driving temperature differential available to them is relatively small. This makes them sensitive to changing coolant temperatures [175]. At the same time, air-cooled condensers are commonly used in ORC plants where cooling water is unavailable or too costly [176]. They can also make systems more modular and portable, negating the need for them to be plumbed into a cooling water supply. However, the fact that they use ambient air on their cold side introduces its own set of problems. In continental climates, ambient temperatures can vary from -30°C to +35°C or more. For a low-temperature heat source, say 100°C, this represents a doubling in the driving temperature differential of the system between summer and winter. The annual variation in average monthly temperature for several continental climates is shown in Figure 6.1.

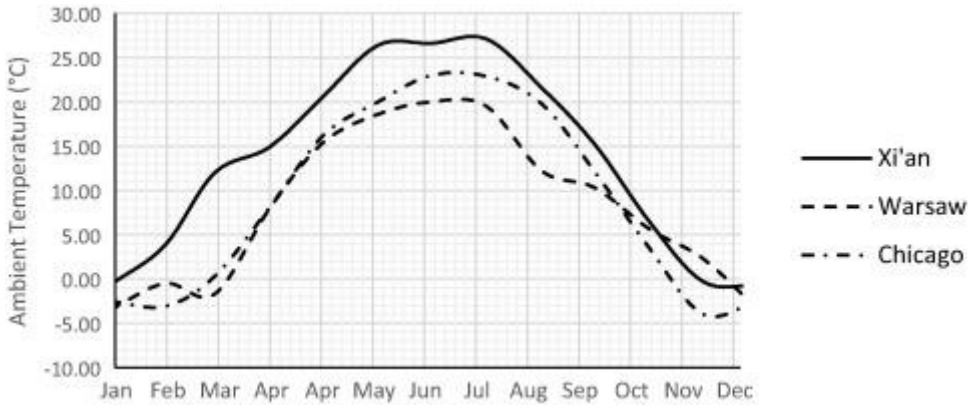

Figure 6.1: The variation in average monthly temperature over the course of the year for three different continental climates; Xi'an (China), Warsaw (Poland) and Chicago (USA) [177].

However, an ORC power plant must maintain a liquid condition at the pump inlet to ensure correct operation of the cycle, avoiding damage to the pump and great losses in pumping

efficiency [178]. Therefore, the cycle itself must be designed with adequate condenser pressure to provide the working fluid to the pump in the liquid phase, even on the hottest day of the year. This means that for much of the year, the cycle will be operating at off-design conditions, not fully utilising the colder heat sink available to it in the winter months [179]. Gu et al [22] observed this in practice, noting that the changing temperature of coolant can result in changing power outputs from the cycle over the course of the year.

6.2 Dynamic ORC Concept

As outlined in Chapter 1, zeotropic working fluids exhibit bubble and dew points between those of their two component fluids. It follows that a working fluid mixture with a specific bubble point within this range can be created by mixing together the two component fluids in the right proportions. This means that if there is control over the working fluid composition, the working fluid can always be set to match a varying coolant temperature. Such a system has been proposed for a heat pump in the past [180] but has not to date been applied to ORC systems [177].

For a practical system, this principle could be used as follows to increase the efficiency of a cycle operating in real-world ambient conditions. Firstly, for clarity, the two working fluid components are denoted A for the working fluid with the higher boiling point, and B for the fluid with the lower boiling point. On the hottest day of the year, the system can be set up with a condenser pressure sufficient to ensure that a working fluid charge composed entirely of Fluid A will be liquid when fed into the pump. Conventional ORC systems must be designed in this way to ensure they are capable of operating year-round without causing damage to their pumps.

As the ambient temperature drops as the season changes from summer to autumn, the temperature of coolant available to the system drops, but the system is not fully utilising this cooler heat sink now available to it. The reduced temperature of the coolant will result in excessive subcooling, increasing the evaporator and condenser loading without increasing the expander work, reducing efficiency, unless the flow rate of coolant through the cold side of the condenser is reduced. The composition of the working fluid is therefore shifted to contain more of Component B. This lowers the bubble point of the resulting working fluid mixture used in the system, until it once more is low enough to just ensure the working fluid is fed into the pump as a liquid.

This continues as the temperature falls, until either the coldest day of the year is reached, or the composition of the working fluid is 100% Component B, in which case the composition

can no longer be adjusted to track the falling ambient temperature. As the temperature begins to rise again when winter changes to spring, the condenser pressure will no longer be high enough to keep a fluid composed of 100% component B liquid at the higher ambient temperatures. Now the working fluid composition is shifted back towards component A to raise the boiling point and ensure the working fluid enters the pump as a liquid. This process is shown in Figure 6.2.

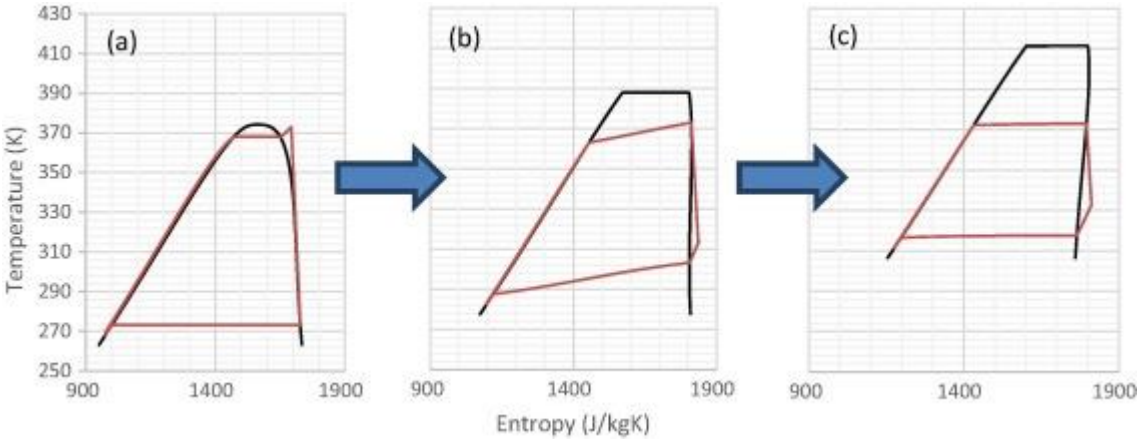

Figure 6.2: Change in the cycle as the composition of the working fluid is tuned to a changing heat sink temperature, while the heat source temperature remains the same. (a) 100% R134a, (b) a 50%:50% mixture of R245fa and R134a and (c) 100% R245fa [177]

This process can be carried out to keep track of seasonal variation in temperature, or with more frequent composition changes, to adjust for varying temperatures over the day-night cycle.

For initial analysis and proof-of-concept, R245fa and R134a were selected as the fluids for use in the Dynamic ORC. These fluids were chosen because they are commonly used in Organic Rankine Cycles [181] [182] [183] [184] [62], are miscible with each other [185] [186]and the difference between their boiling points is similar to the annual temperature variation in a continental climate, meaning that the bubble and dew points of a mixture of these two components can be adjusted over a sufficiently large range to compensate for the changing ambient temperature.

Two broad cases were then considered and analysed. In both cases, the bubble point temperature in both the condenser and the evaporator tends to drop as more of Component B is added. The first case is that the cycle is capable of operating at a variable pressure ratio, so

a variable displacement expander, or momentum based device is assumed. The assumption that the isentropic efficiency does not vary with changing pressure ratio for such devices is supported by Wang et al [187] for a turbine and by Wu et al [111] for a variable-displacement volumetric expansion device. In this case, the evaporator pressure can be controlled by increasing the pump speed and the load on the expander, increasing the flow resistance of the system. This increases the pressure ratio of the system and therefore the expander work, increasing its efficiency. The second case is that the pressure ratio of the cycle is fixed, so a positive displacement device with no capacity to adjust its in-build volume ratio. In this type of cycle, the evaporator pressure cannot be varied without a severe negative effect on the isentropic efficiency of the expander, and therefore changing the working fluid composition instead results in an increase in the superheat at the expander inlet.

6.3 Optimal Distillation Frequency

The frequency at which distillation is carried out has important implications for the performance of the cycle. More frequent distillation means that the working fluid composition can be tuned more accurately to match the changing ambient temperature, while increasing the energy requirements and parasitic power. It also increases the theoretical capital cost of the distillation equipment. Whether the power required for distillation represents a true loss to the system depends on the particular heat source and application of the cycle. If the thermal fluid is not recirculated then it can be used as an energy source for distillation without parasitic loss to the system

Figure 6.3 shows the variation in the average effective efficiency $\eta_{effective}$ with a varying sampling interval for distillation. The climate data fed to the MATLAB program was modified to contain only the highest temperature value within the specified interval. Temperatures over a shorter time period than 24 hours were inferred using the daily maximum and minimum temperatures, and the assumption that the temperature varied sinusoidally over the course of the day, as shown in Chapter 3.

Figure 6.3 shows that the effective efficiency is highest for the case where distillation is carried out once every 12 hours. For shorter time periods, the extra energy required to distil the working fluid reduces the overall cycle efficiency. For longer time periods, the cycle is unable to keep up with the changing ambient temperature, particularly the day-night cycle. 12 hours allows for the cycle to adjust for the fact that temperatures are cooler during the night time with the minimum of parasitic power required to perform distillation.

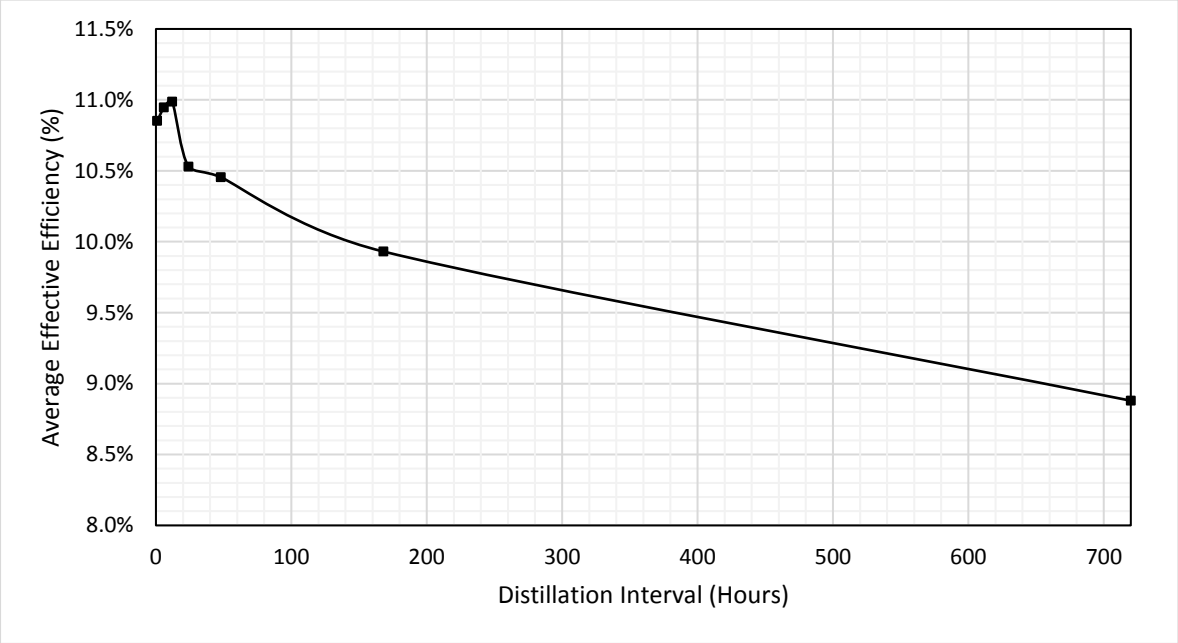

Figure 6.3: Variation in year-round effective efficiency with varying sampling interval. The heat source temperature is 100°C

Figure 6.4 shows the variation in annual average first law efficiency with changing distillation interval. As the interval decreases from months to weeks to days, the efficiency rises slowly as the cycle is able to take into account slow changes in temperature. There is a particularly rapid increase as the distillation interval changes from 24 hours to 12 hours, as now the cycle is able to change its composition to match the day-night temperature variation as well as the longer term seasonal trends. Further reductions in the distillation interval result only in small increases in the efficiency, as the cycle can better match the daily temperature variation. If the energy required for distillation is "free", as is the case for non-cogenerating waste heat and bottoming cycles, this is the figure that best demonstrates the effect of the distillation period. While shorter distillation intervals may result in marginal increases in the cycle efficiency, the decrease from a 24 hour interval to a 12 hour one is the most significant.

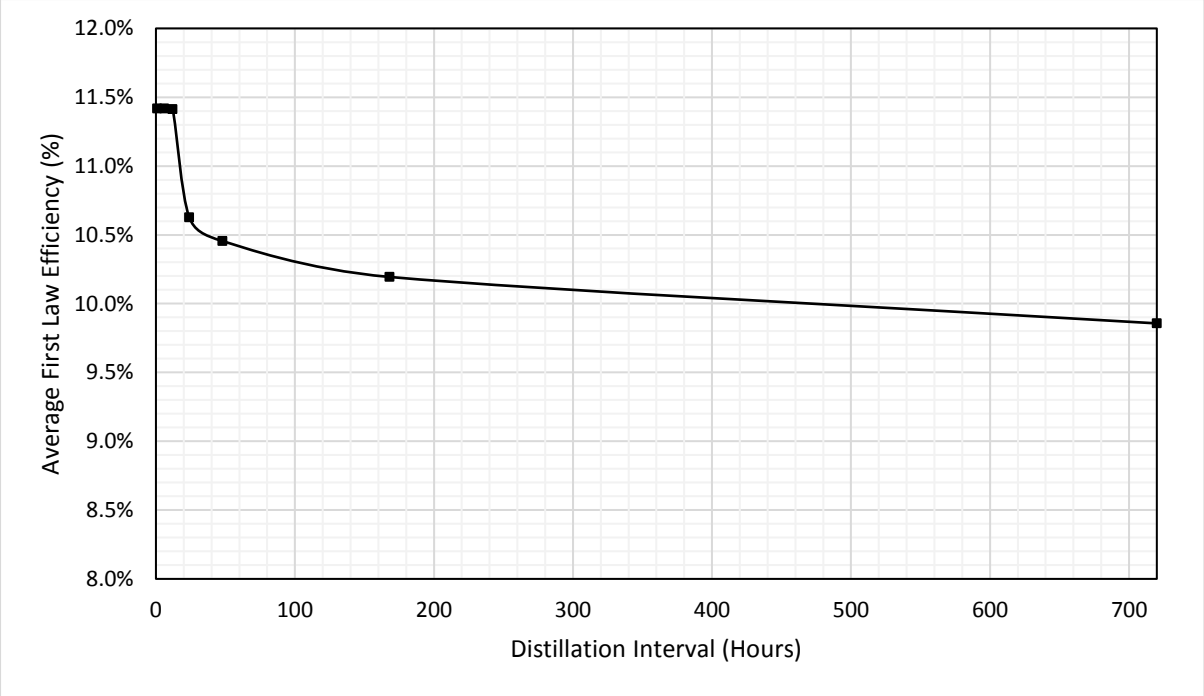

Figure 6.4: Variation in annual average first law efficiency with changing interval of distillation

Figure 6.5 shows the variation in parasitic power caused by the distillation system. The power is low at long intervals, just 220W on average for a monthly distillation, but rising steadily to 680W for weekly distillation and reaching 5kW for daily distillation. There is then a large and abrupt increase as the distillation interval is further reduced to 12 hours. This is again due to the fact that intervals shorter than 24 hours allow for the day-night variation in temperature to be accounted for by the distillation system, and intervals longer than this do not. Reducing the interval to less than 24 hours results in a large amount more distillation being carried out over the course of the year. Decreasing the distillation interval further results in a kink in the graph. The reduced interval results in more distillation being carried out, and in a shorter time, but there is not the same sharp increase observed when the day-night temperature variation is first introduced.

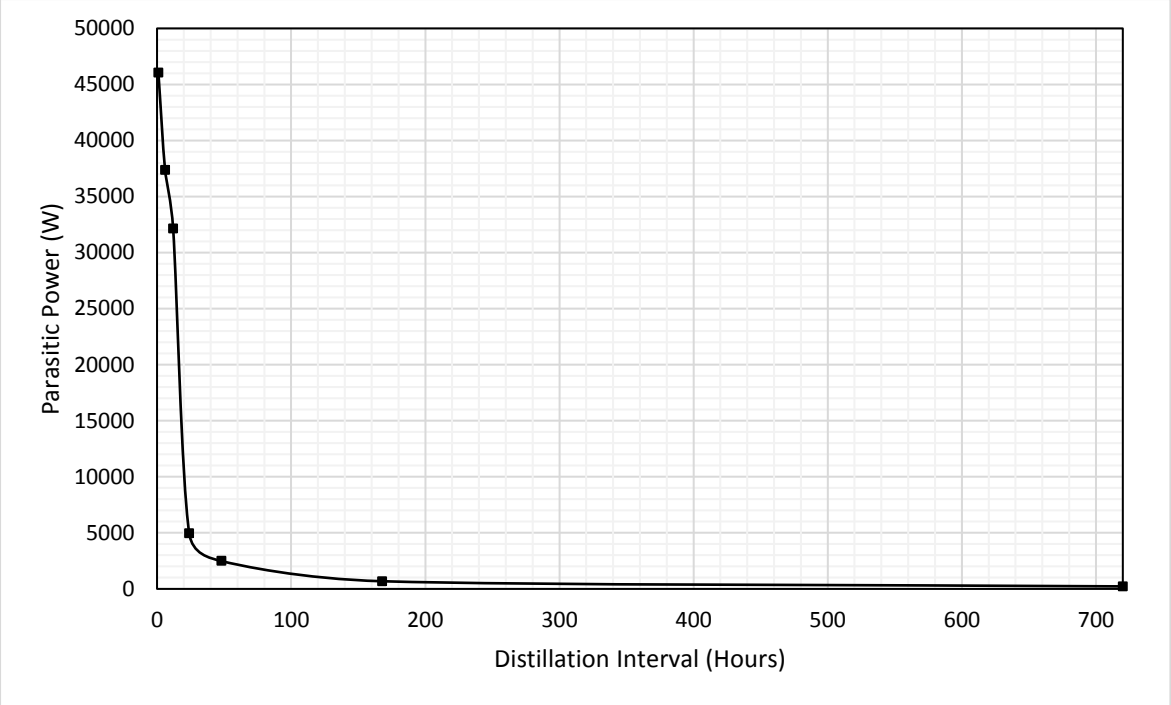

Figure 6.5: Variation in Parasitic Distillation Power with varying distillation interval

As a result of this analysis, it was decided that a 12-hour distillation interval would be used for future comparison of cycles.

6.4 Performance Metrics

6.4.1 Improvement in Annual Energy Generation ψ

This parameter was developed to analyse the effectiveness of the Dynamic Organic Rankine Cycle. It is defined as the increase in the amount of energy generated over the course of the year by the dynamic cycle, compared to that which would be produced by a conventional cycle operating under the same conditions. It was assigned the Greek letter ψ and was given by:

$$\psi = \frac{\bar{\eta}_{dynamic} - \bar{\eta}_{conventional}}{\bar{\eta}_{conventional}}$$

Where the efficiency of the conventional, non-dynamic cycle was taken as the efficiency of the cycle on the hottest day of the year.

6.5 Dynamic Organic Rankine Cycle Simulation Results

The following sections present the results of the theoretical analysis of the Organic Rankine Cycle. Two main categories of cycle are considered, these being fixed-displacement and variable-displacement cycles. Regenerative and non-regenerative variations of each of these

cycles are considered for a range of heat sources and heat sinks. The results are analysed and the trends explained in the context of the available data.

6.5.1 Variable Displacement Cycle

Two broad categories of cycle configuration were considered when analysing the dynamic cycle, those with an expander capable of variable displacement, for example, turbines within a specified range, or positive displacement devices with variable geometry, such as slideable exit ports, and those with a fixed displacement. For each of these cases, regenerative and non-regenerative configurations were also considered. A number of parameters were varied, including the heat source temperature for the cycle and the ambient conditions.

6.5.1.1 Varying Ambient Temperature

Using the climate conditions for Beijing, the heat source temperature of the cycle was varied in 10°C intervals from 60°C to 250°C and the effects on the dynamic cycle were observed.

6.5.1.2 Response Curves

The response curve of the efficiency of the non-regenerative cycle to changing ambient temperature can be seen in Figure 6.6. At low temperatures, the composition of the working fluid can be 100% R134a, and still have a high enough bubble point that the feed of working fluid to the pump inlet is liquid at condenser pressure. As the temperature is increased, there is initially no change in the efficiency of the cycle, as the ambient temperature remains low enough to ensure this liquid pump inlet condition. However, as the temperature difference between the coolant and the condenser temperature drops, this results in an increase in the flow rate of the coolant, as shown in Figure 6.7. This is due to the fact that the reduced allowable rise in temperature of the coolant necessitates a greater flow rate to maintain the required pinch point temperature difference in the condenser.

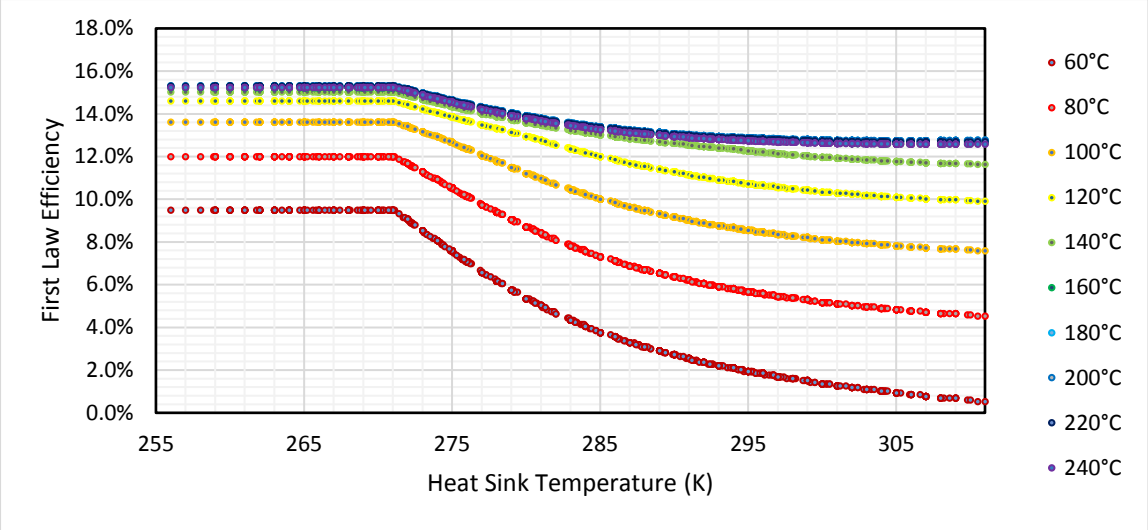

Figure 6.6: Response Curves of first law efficiency for the non-regenerative cycle with varying heat source temperature

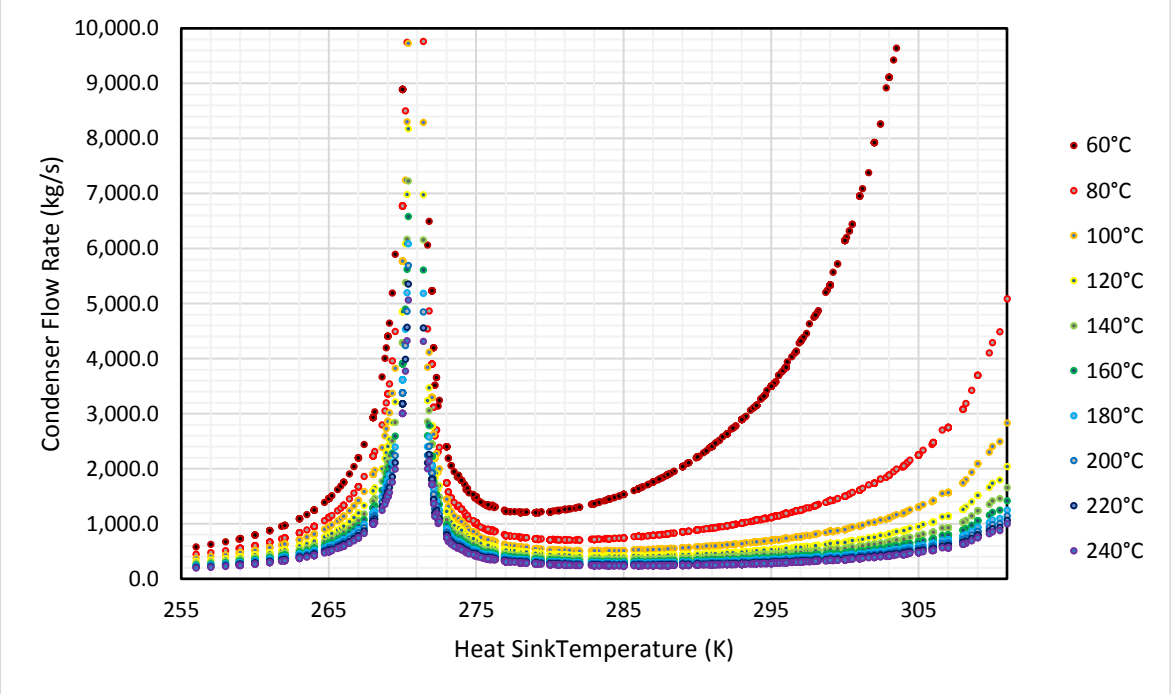

Figure 6.7: Variation in Coolant flow rate for varying heat sink temperature

As the temperature continues to rise, eventually the pure R134a will not be a liquid at the pump inlet. At this point, the bubble point of the cycle can be raised by shifting the composition of the working fluid to contain more R245fa. This has several effects.

-The bubble point of the cycle increases slightly due to the introduction of the higher boiling point fluid.

-The dew point of the cycle increases to a greater degree, in accordance with the glide curve diagram shown in Chapter 3.

-This introduces a temperature glide into the cycle. The glide means that the dew point is raised in relation to the bubble point, and therefore the coolant can undergo a greater temperature change as it passes through the cold side of the condenser. This results in the condenser flow rate decreasing again.

-The efficiency of the cycle begins to decrease. This is primarily due to the reduction in temperature difference between the hot and cold sides of the cycle, and the decrease in the bubble point of the cycle. While this helps to keep the fluid a liquid at the pump inlet, it also means that the evaporator pressure must be dropped to ensure that the working fluid is fully vaporized and subcritical at the expander inlet, reducing the pressure ratio of the cycle. There is also the fact that R245fa is a drier fluid than R134a, which results in a greater superheat at the expander inlet, increasing condenser loading without improving expander output, which results in slightly reduced efficiency.

As the flow rate continues to increase, the efficiency of the cycle continues to drop. However, the shape of the curve is not the linear response of the Carnot efficiency to a changing heat sink temperature. Instead this is convex, which has to do primarily with the shape of the glide curves.

It can be seen in Figure 3.2 that when R245fa is first added to the system, there is a large change in the dew point, and only a relatively small change in the bubble point. This means that the working fluid composition must be shifted towards r245fa by a relatively large amount. The greater rise in dew point temperature than bubble point temperature means that the pressure ratio of the cycle changes particularly quickly in this region, with a correspondingly sharp change in the efficiency of the cycle.

As the temperature continues to increase, the proportion of R245fa becomes higher and higher, and the system moves into a different region of the glide curve. In this region, the bubble point is changing more quickly than the dew point with changing temperature, and so the pressure ratio changes far more slowly as the composition is adjusted to maintain the liquid condition as the pump inlet. This results in the overall concave shape of the curve.

Meanwhile, the condenser flow rate decreases as the glide increases, which was expected, as the increased temperature of the dew point in the condenser allows a greater temperature change while still maintaining the desired pinch point temperature difference. This process is demonstrated in Figure 6.8. At a certain point, maximum glide is reached, after which the glide begins to decrease, and the coolant flow rate begins to increase accordingly, before reaching a local maximum when the working fluid is 100% r245fa, and the glide is once more zero.

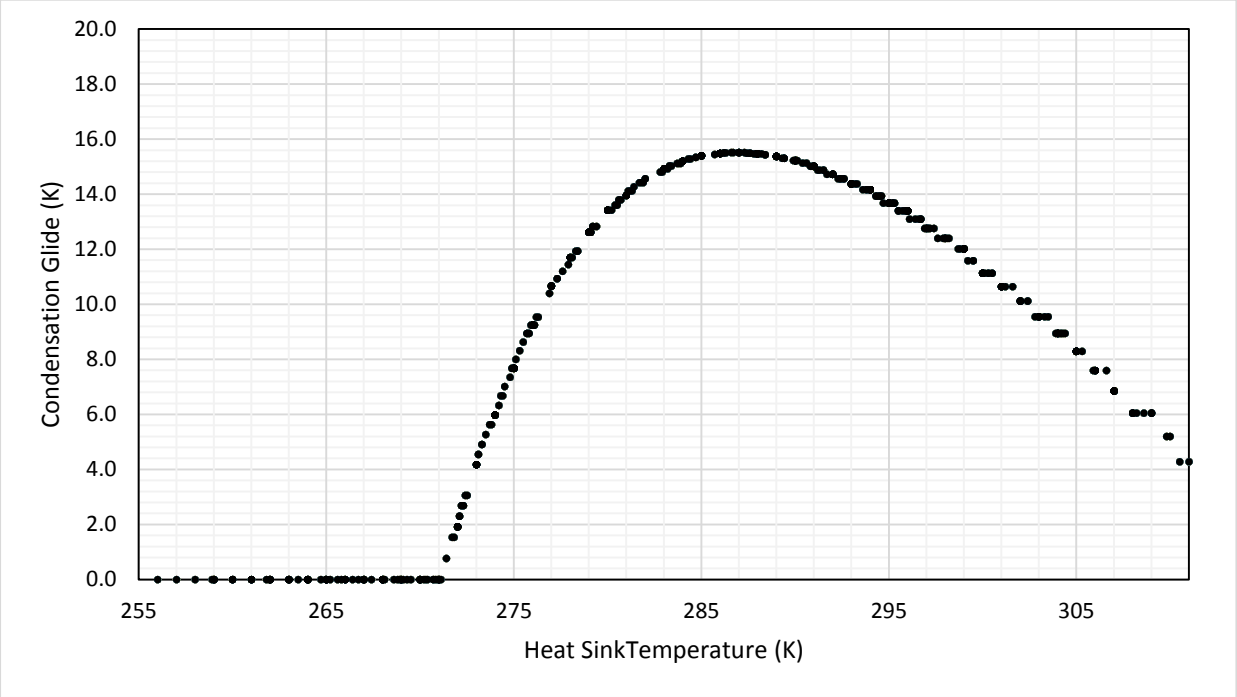

Figure 6.8: Condenser glide variation with changing ambient temperature

Meanwhile the evaporator flow rate also varies with varying ambient temperature, as shown in Figure 6.9. The exact shape of the response curve depends on the heat source temperature.

For all heat source temperatures, the evaporator flow rate remains constant in the colder regions of the year, as would be expected due to the fact that the cycle itself does not change in response to changing ambient conditions in this region.

When the working fluid composition reaches the point at which it begins to change in response to changing ambient conditions, the response in the evaporator flow rate begins to differ for different heat source temperatures. This is due to a number of factors, primarily a combination of expander inlet superheat, temperature glide and working fluid mass flow rate.

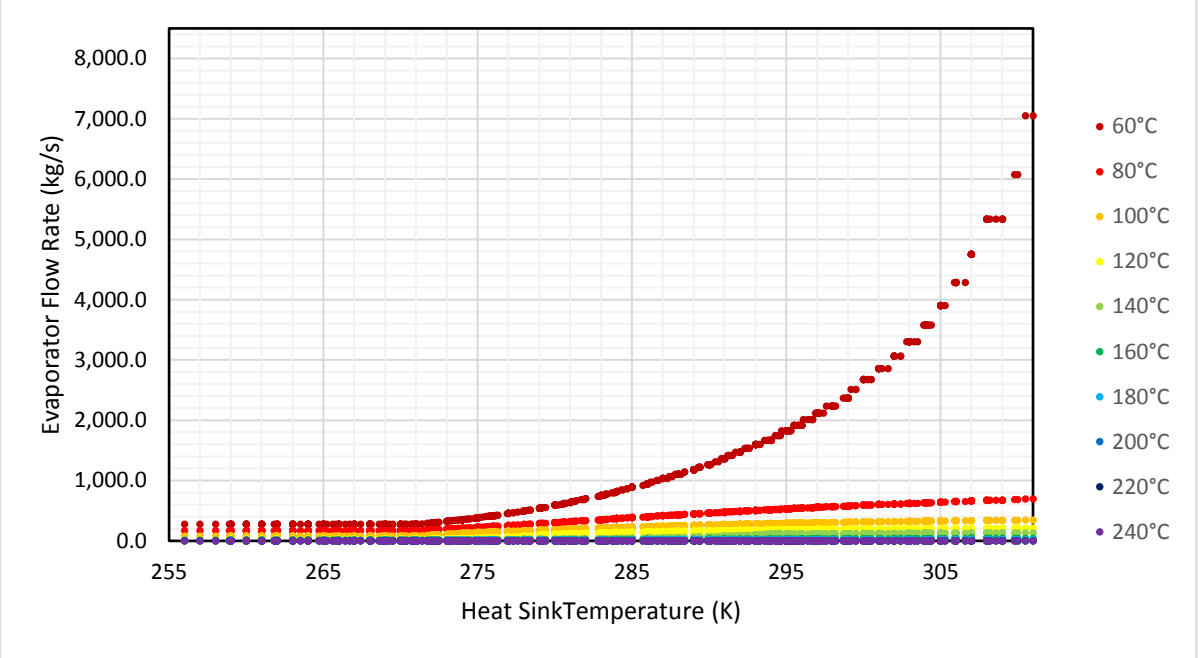

Figure 6.9: Variation in Evaporator Flow Rate with Varying Ambient Temperature

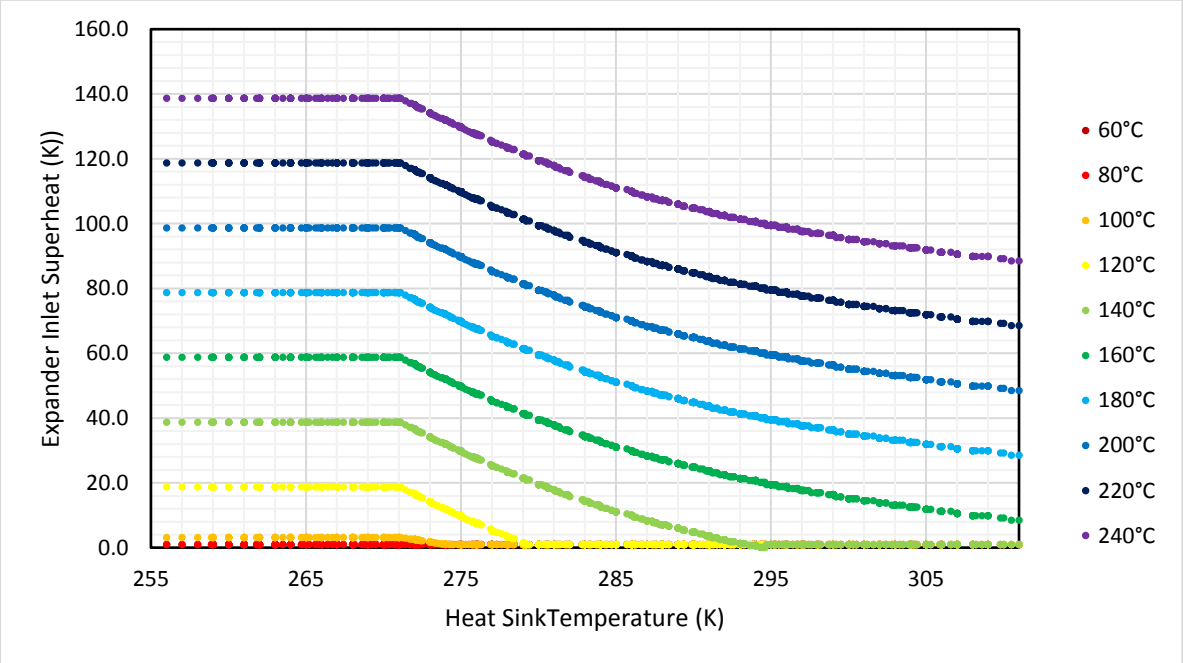

Figure 6.10: Variation in Expander Inlet Superheat with varying ambient temperature

Figure 6.10 shows the variation in expander inlet superheat as the ambient temperature varies. For lower heat source temperatures, the evaporator pressure can always be increased to such a degree that there is no superheat without making the cycle supercritical for any working fluid.

The MATLAB model holds the evaporating temperature 15K below the critical temperature, and the critical temperature of R134a is 101°C, so as the heat source temperature is increased, the first superheat seen at the expander inlet occurs when the heat source temperature is 90°C. For higher heat source temperatures, the superheat begins to appear at warmer and warmer ambient conditions. The shape of the curves for superheat against ambient temperature have the same shape as the dew curve on the glide curve diagram shown in Figure 3.2.

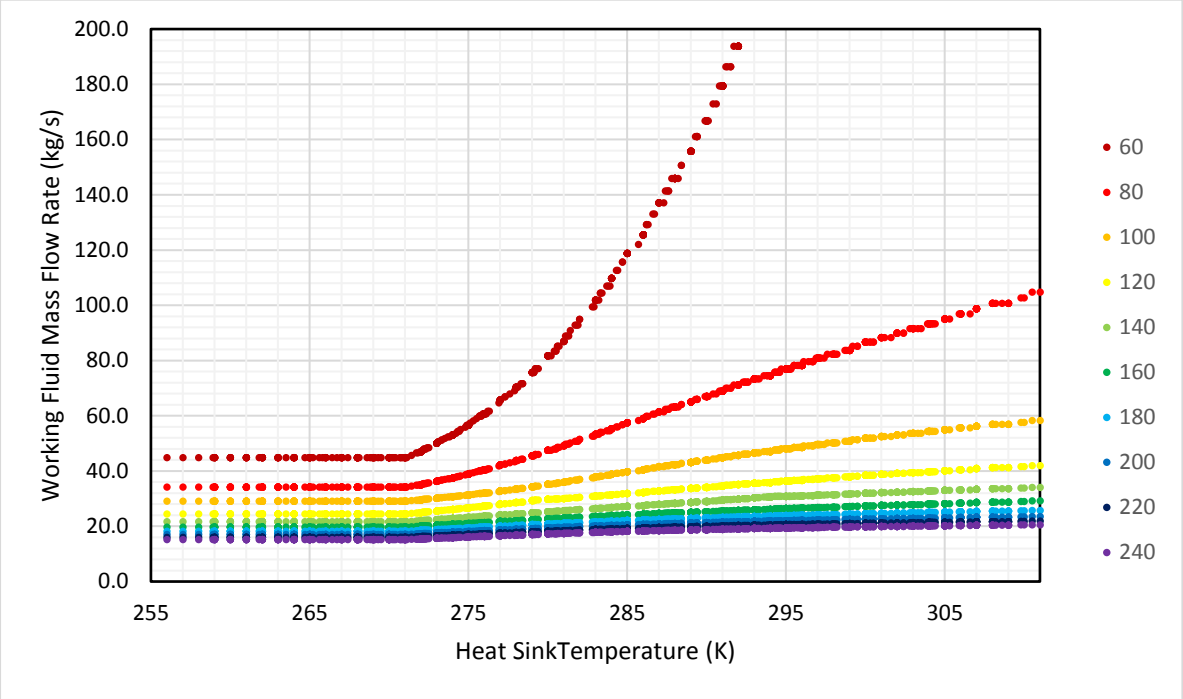

Figure 6.11: Variation in Working Fluid Mass Flow Rate with changing ambient temperature

Figure 6.11 shows the working fluid mass flow rate and how it varies with changing ambient temperature. It increases rapidly with decreasing temperature after the working fluid composition begins to change at 274K. This is due to the specific enthalpy drop of r245fa, which is lower than that of r134a, partly due to the fact that r245fa is a dryer fluid, meaning that more heat is rejected through the condenser after expansion. It is highest for the lower temperatures, as these are the temperatures with the lowest specific enthalpy change of the working fluid as it passes through the expander.

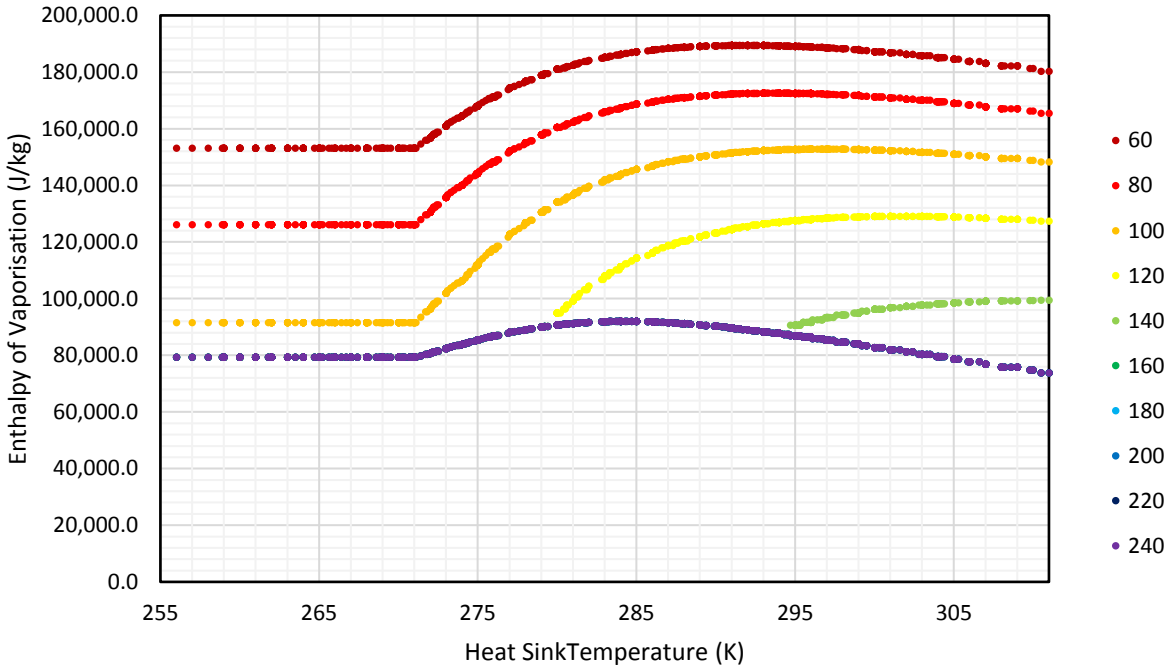

Figure 6.12: Variation in Enthalpy of Vaporisation in the evaporator with varying heat sink temperature

The enthalpy of vaporisation of the working fluid in the evaporator s shown in Figure 6.12. Again, there is no change in the region in which the working fluid is 100% r134a. For low temperature heat sources below 90°C the enthalpy of vaporization rises slowly as the fluid becomes zeotropic, then drops off slightly, which is the expected behaviour for the fluid. The enthalpy of vaporization drops for higher heat source temperatures as the working fluid shifts its operating region closer to the critical point, into a narrower section of the saturation dome. However, the subcritical limitation of the cycle leads to some interesting behaviour as the heat source temperature rises.

With the heat source temperature above 100°C, the 100% r134a section of the plot, i.e. the coldest part of the year, does not change, as to increase the pressure and change the temperature of the phase change would bring the cycle into the supercritical region. For the highest heat source temperatures, those above 150°C, there is no point in the year when the evaporator pressure does not have to be reduced to keep the cycle subcritical. For heat source temperatures between 90°C and 140°C, i.e. those between the critical temperatures of r134a and r245fa, the plot initially follows the same plot as those for higher temperature heat sources, but then detach

as the critical temperature of the working fluid mixture surpasses the heat source temperature and allows a change in the bubble and dew points once more.

For the lowest heat source temperatures, there is no superheat at any point during the cycle, so the flow rate in the hot side of the evaporator is determined by the glide of the working fluid as it changes phase, the latent heat of vaporisation, and the working fluid mass flow rate. Figure 6.9 shows that for the lowest heat source temperatures, the shape of the curve for the evaporator flow rate matches the curve for the working fluid mass flow rate. For the higher heat source temperatures, the overall increase is still dominated by the increase in working fluid mass flow rate, but with a sharp change where the enthalpy of vaporization detaches from the curve for the highest temperatures. The flow rate is lower for higher heat source temperatures, which corresponds to both a higher degree of superheat and a lower enthalpy of vaporization

6.5.1.3 Working Fluid Pump

Figure 6.13 shows the variation in the enthalpy change in the pump as the ambient temperature changes. This is primarily due to the increasing evaporator pressure, which, when combined with the constant condenser pressure, results in an increase in the pressure ration the pump needs to supply. The variation in evaporator pressure can be seen in Figure 6.14. It can be seen that the shapes of the graphs are highly similar for all heat source temperatures, indicating that pressure ratio is the driving force behind the pump enthalpy requirements.

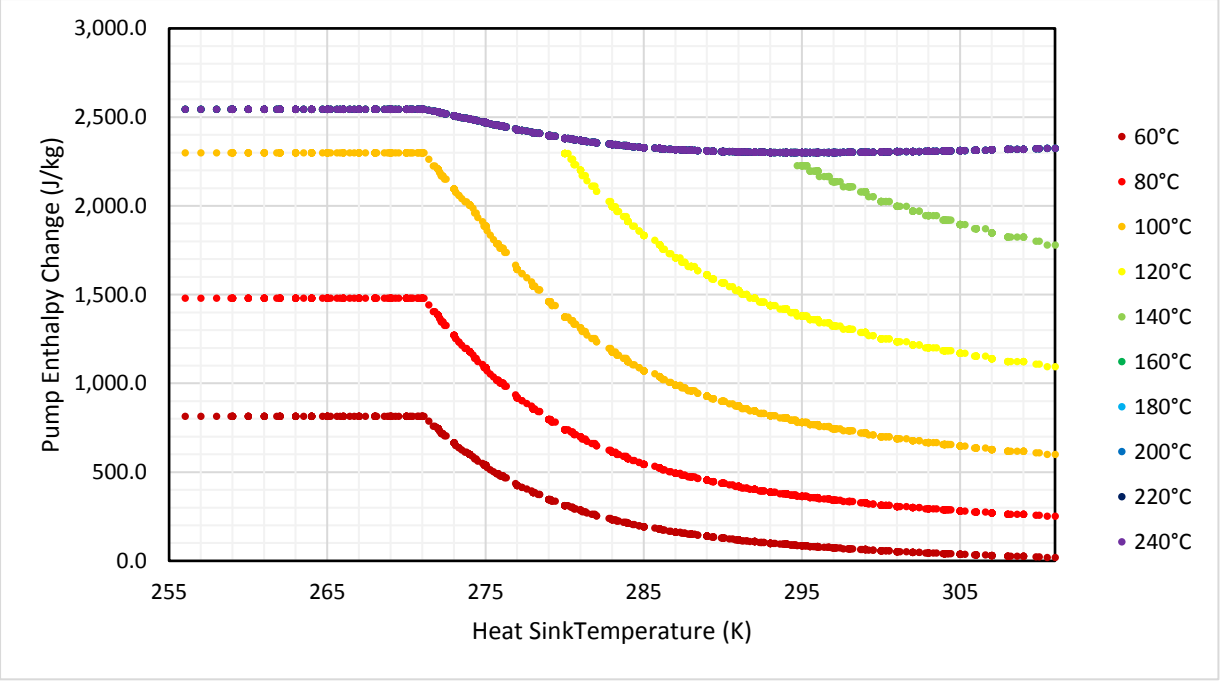

Figure 6.13: Variation in Pump Enthalpy Change with varying ambient temperature

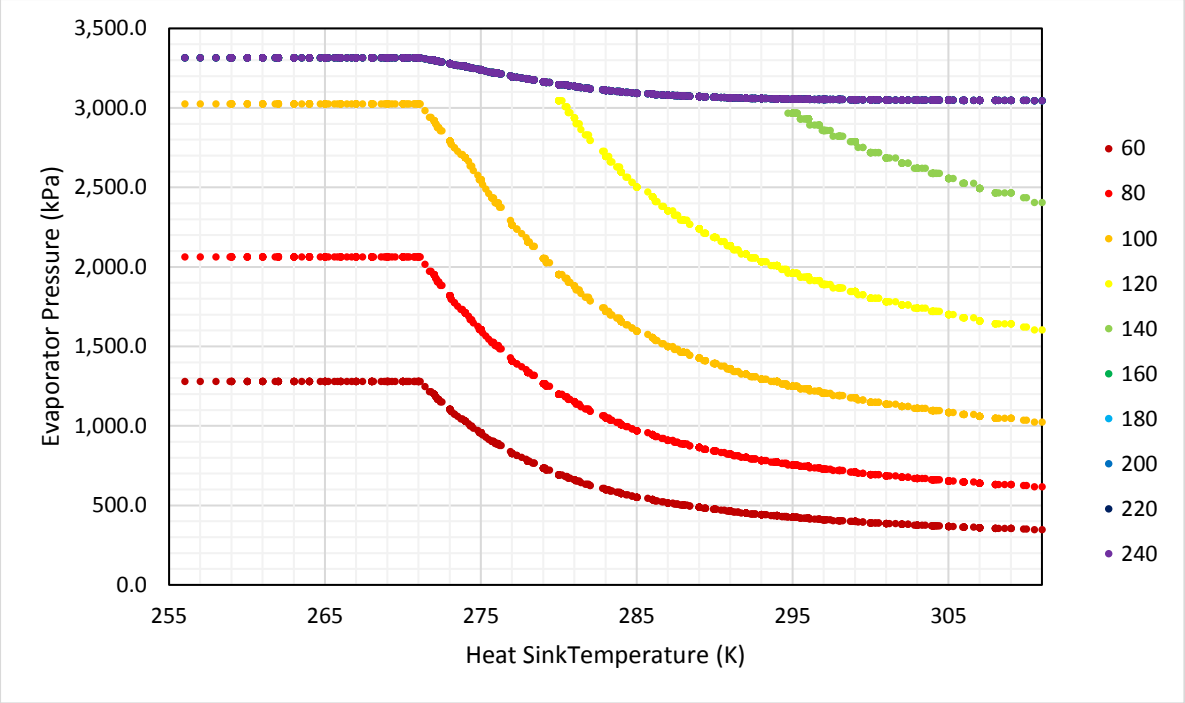

Figure 6.14: Variation in evaporator pressure with varying heat sink temperature

6.5.1.4 Evaporator

The variation in the evaporator enthalpy with varying heat sink temperature is shown in Figure 6.15. It can be seen that this variation is slightly more complex than the corresponding plot for the working fluid pump. For higher heat source temperatures, it appears as though the evaporator enthalpy is primarily driven by the superheat at the expander inlet, as the graph follows the same trend as that observed in Figure 6.10. However, this is not the full story, as the profile of the plots is different, and the correlation does not hold for lower heat source temperatures, when the turbine inlet temperature is not high enough to introduce superheat into the cycle.

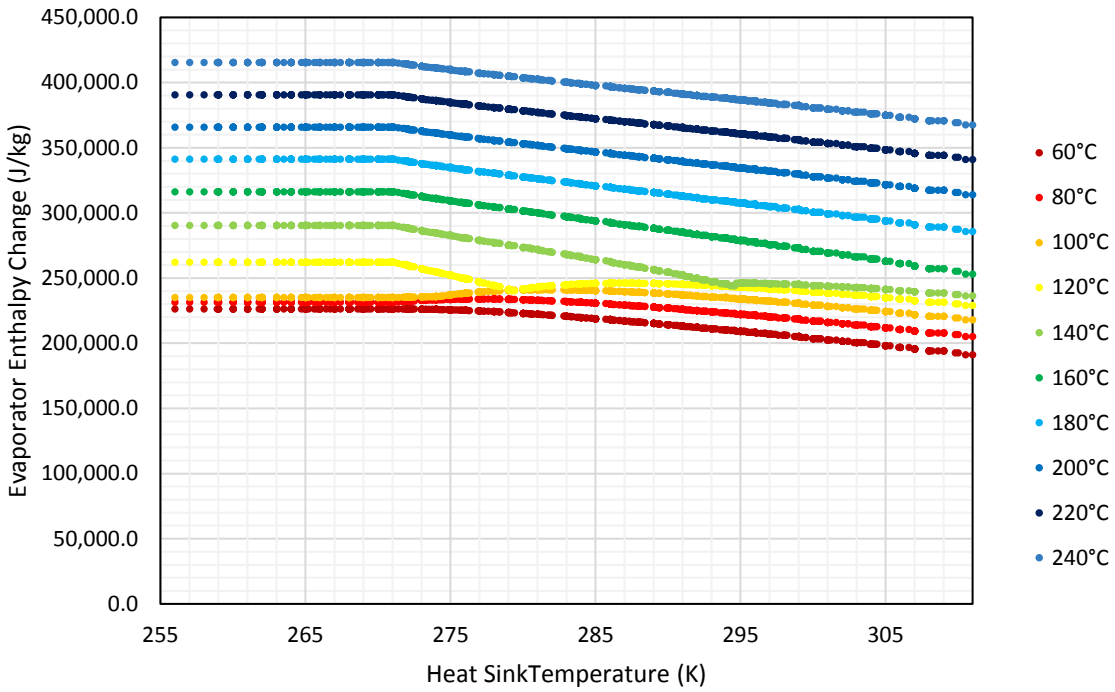

Figure 6.15: Variation in evaporator enthalpy change with changing heat sink temperature

In the case of lower temperature, the response curve for evaporator enthalpy follows the general shape of the enthalpy of vaporization curve observed in Figure 6.12.

The other influencing factor is the energy required to bring the fluid up to its bubble point, which is shown in Figure 6.16. Two distinct regions of behaviour can be seen. At lower heat source temperatures, the pressure ratio is still increasing with decreasing heat sink temperature, and so the evaporator inlet subcooling also increases, as the temperature of the bubble point will increase. However, at higher heat source temperatures, the subcritical limitation placed on the cycle comes into play, and the evaporator pressure cannot be increased any more. In this region, the specific heat capacity of the working fluid is more important. The specific heat capacity of the working fluid mixture decreases with decreasing temperature. The convex shape of the response curves for the enthalpy of vaporization and the evaporator inlet subcooling could help to cancel out the concave shape of the response curve for expander inlet superheat, resulting in the straight line seen towards the right hand side of the response curve for the higher heat source temperatures in Figure 6.15.

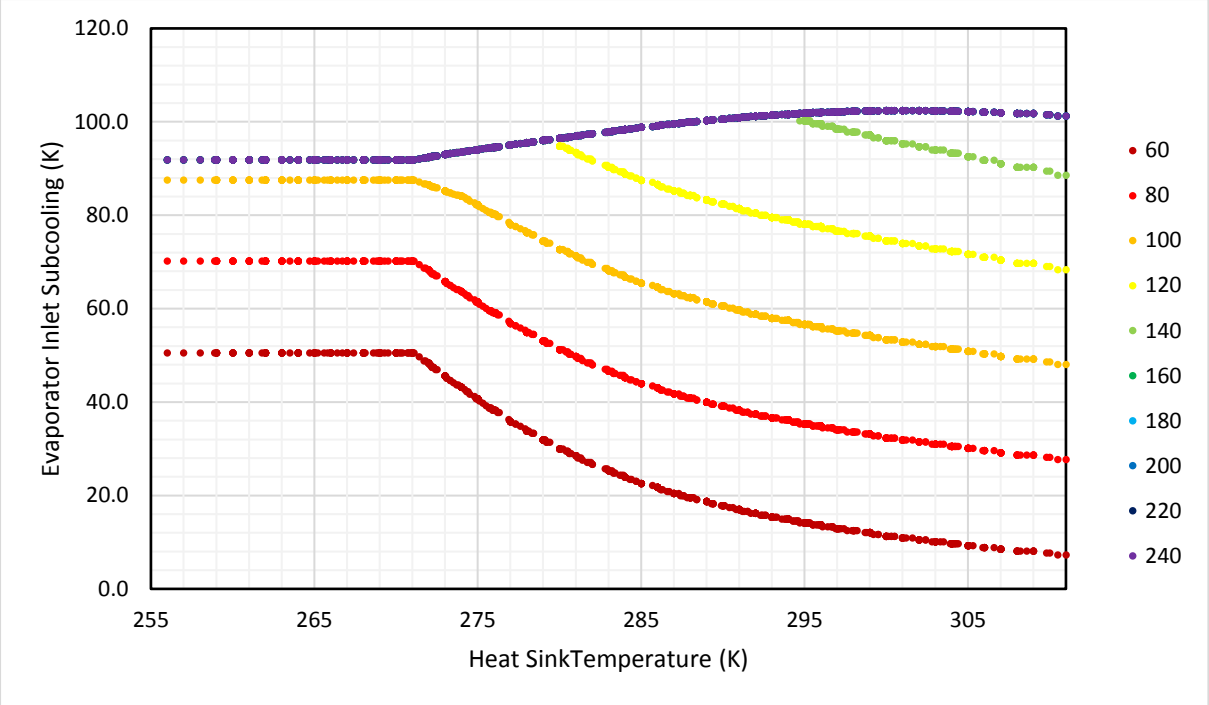

Figure 6.16: Variation in Evaporator Inlet Subcooling with varying ambient temperature

6.5.1.5 Expander

The variation in the enthalpy drop across the expander is shown in Figure 6.17. It can be seen that the shape of the response curves is concave, and corresponds roughly to the evaporator pressure, at least for the lower temperature cycles. Kinks can be seen in some of the response curves for heat source temperatures between 100 and 150°C, as the evaporator pressure hits the critical pressure for the fluid mixture. However, unlike the response curve for evaporator pressure, the enthalpy change curve continues to increase with increasing heat source temperature. This is primarily due to the diverging isobaric lines on the vapour side of the saturation dome, which means that the expander enthalpy change will increase with increasing superheat. The higher specific enthalpy drops for working fluid blends rich in R134a result in lower working fluid mass flow rates than for working fluid blends more rich in R245fa.

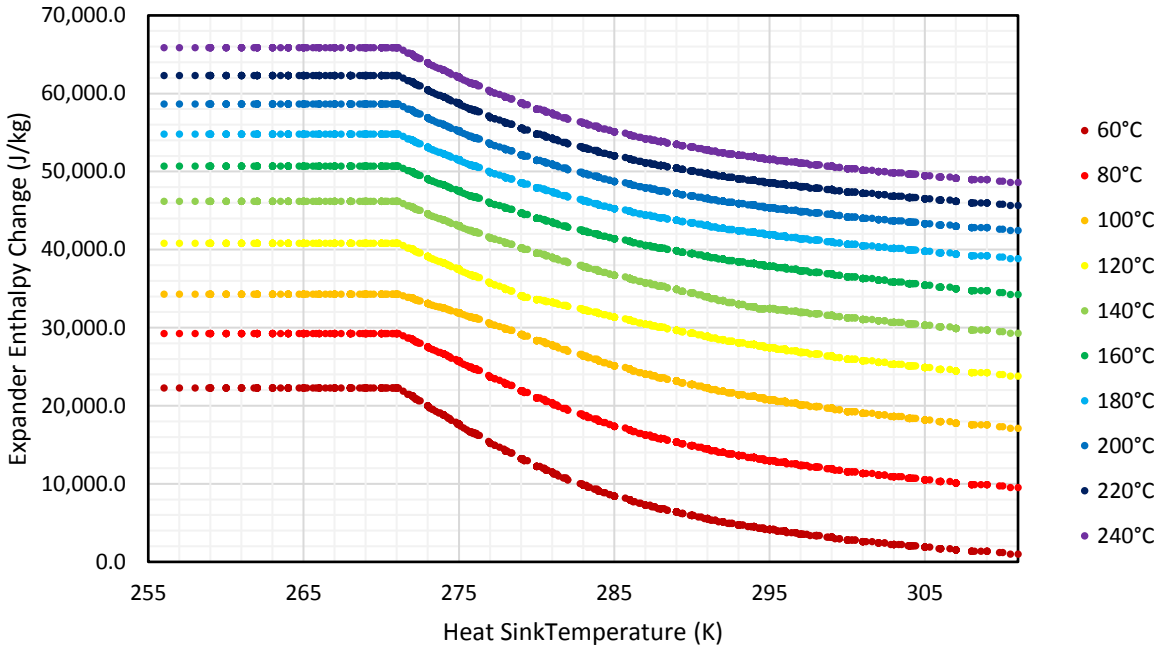

Figure 6.17: Variation in enthalpy change across the expander with varying heat sink temperature

6.5.1.6 Condenser

Figure 6.18 shows the variation in the condenser enthalpy change as the ambient temperature changes. It is visually very similar to the corresponding plot for the variation in evaporator enthalpy change given in Figure 6.15.

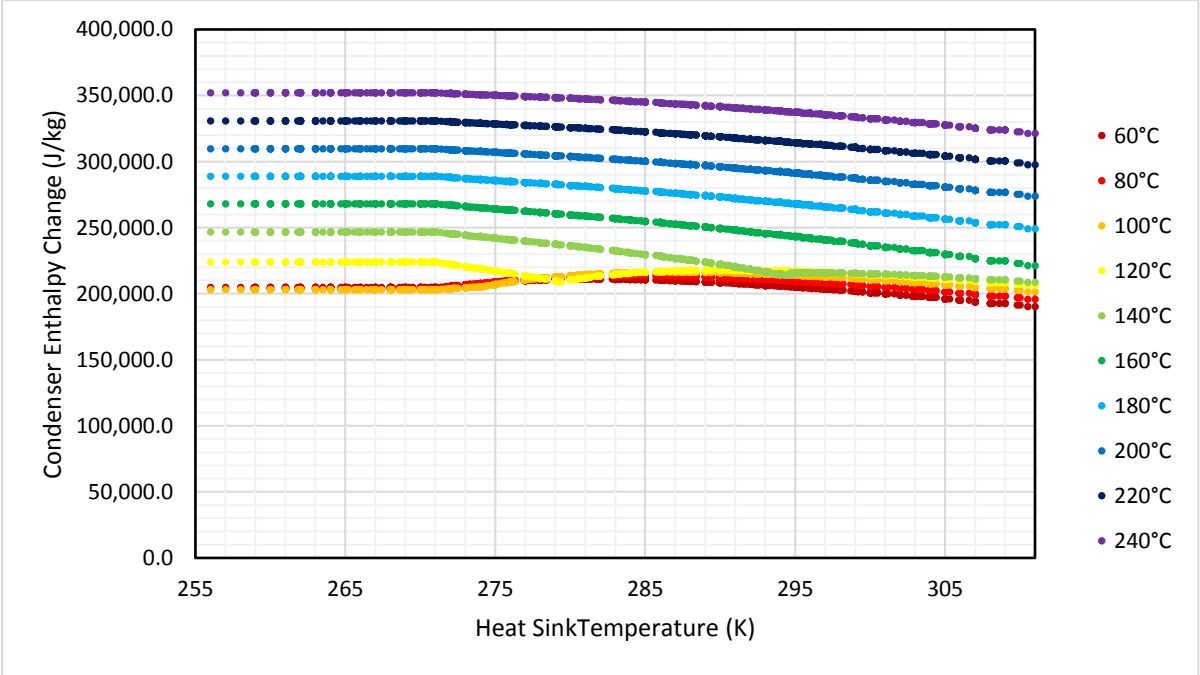

Figure 6.18: Variation in condenser enthalpy change with varying heat sink temperature

The effect all of these varying responses have on the performance of the cycle over the course of a year in a continental climate is shown below.

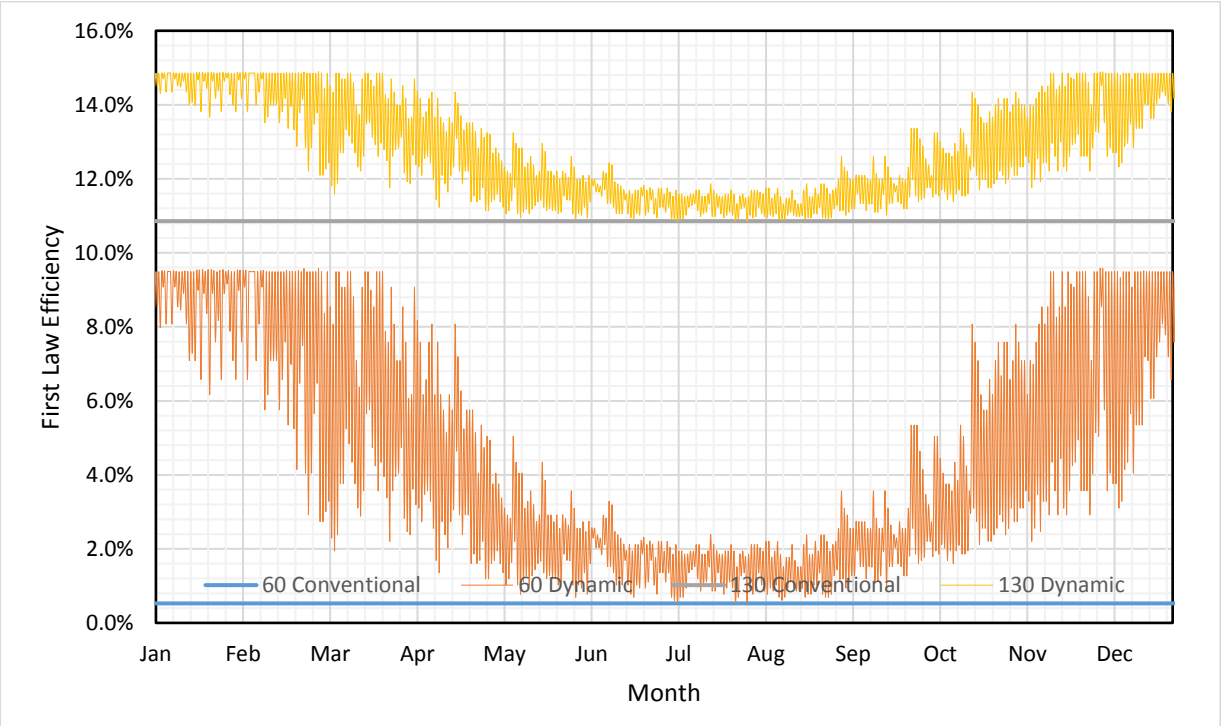

Figure 6.19: Year-round efficiency of the dynamic Organic Rankine Cycle under Beijing's ambient conditions

Figure 6.19 shows the variation in first law efficiency over the course of the year for Beijing's ambient conditions for two heat source temperatures, 60°C and 130°C. The efficiency of an equivalent non-dynamic cycle is shown for each of these cases. For both of these cases, the efficiency of the cycle is clearly higher in the winter months due to the ability of the dynamic cycle to compensate for changing ambient conditions, with the colder winter conditions. It can also be seen that in both cases, there is a sharp cutoff in the efficiency increase during the winter months, as the cycle reaches 100% r134a and enters the horizontal region of its response curve as seen in Figure 6.6. This demonstrates the potential for further improvement of the cycle by selecting working fluids with a greater difference between their heat source temperatures if the variation in the heat sink temperature is great enough to justify this. There is also a significant amount of noise in the signal, caused by the temperature variation from day to night as well as between seasons. This is most obvious in the spring and autumn months, when the intermediate temperatures put it in the region of the response curve in Figure 6.6 with the steepest slope.

6.5.1.7 Effect of Heat Source Temperature

The heat source temperature of the Organic Rankine Cycle is a parameter that has been identified as having a major effect on its efficiency.

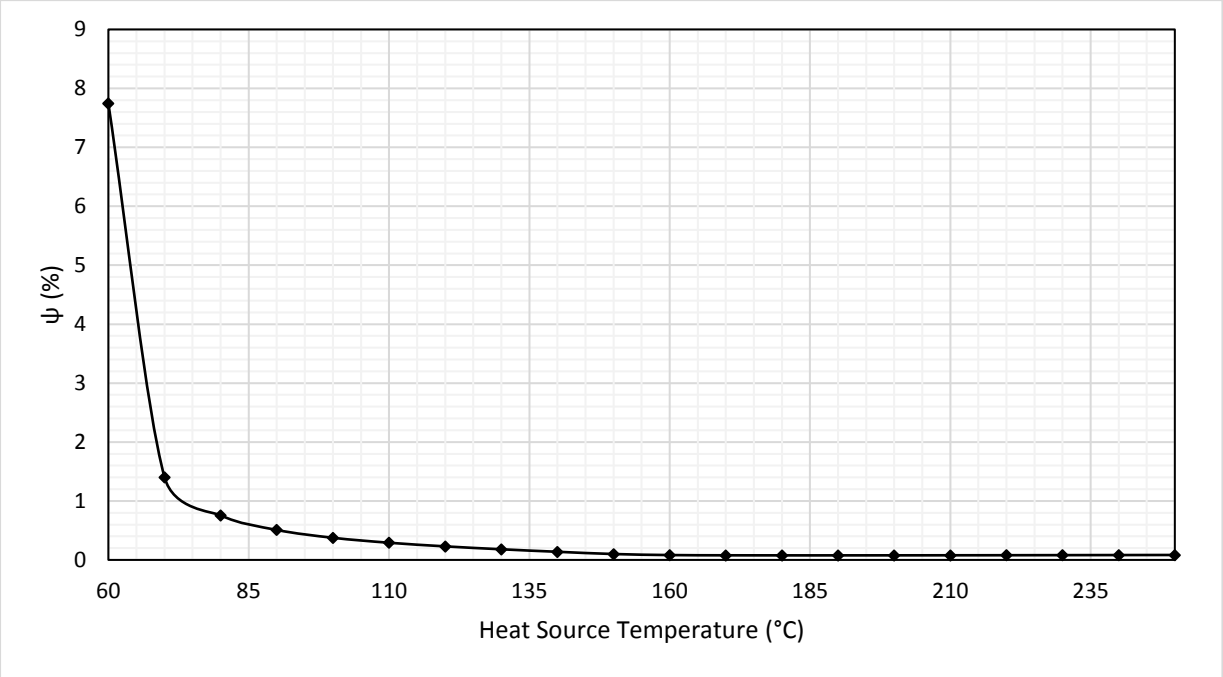

Figure 6.20: Variation in ψ for Beijing's ambient conditions with changing heat source temperature

Figure 6.20 shows the variation in the parameter ψ, which is a measure of the improvement in year-round energy generation, as the heat source temperature changes. At lower heat source temperatures, the dynamic cycle results in a very large value of ψ, which gradually decreases and stabilizes at a constant value for further increases in heat source temperature. This is consistent with the response curves generated in Figure 6.6, in which the higher the heat source temperature, the sooner the changing working fluid composition causes the cycle to reach the critical point as R134a is added, at which no further increase in pressure ratio can be achieved. For a heat source temperature above the critical point of R245fa, which is 154°C, further increases in the value of ψ are not observed. This process can be seen in Figure 6.21. For lower heat source temperatures, the evaporator pressure increases as the ambient temperature increases, and the curve follows the same shape as the dew curve of the saturation diagram in Figure 3.13. However, for heat source temperatures above the critical temperature of R134a, working fluid mixtures containing higher percentages of R134a will not be able to be pressurized to such a degree that there is no superheat at the expander inlet without causing the

cycle to become supercritical. Under these conditions, the pressure will increase until it hits the blue line, which represents the critical pressure of the working fluid at that particular composition. For higher heat source temperatures, the line starts at a higher level, and therefore hits the critical pressure curve sooner, until at heat source temperatures above the critical point of r245fa the entire curve is superimposed on the critical pressure curve.

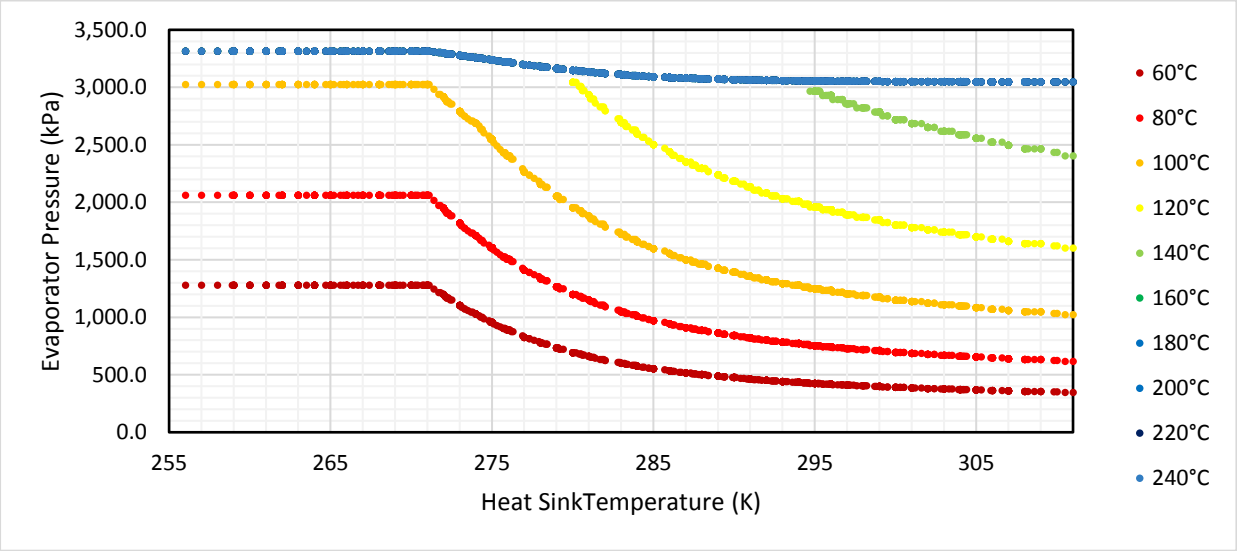

Figure 6.21: Variation in Evaporator Pressure with varying heat sink temperature for a variety of heat sources under Beijing's ambient conditions

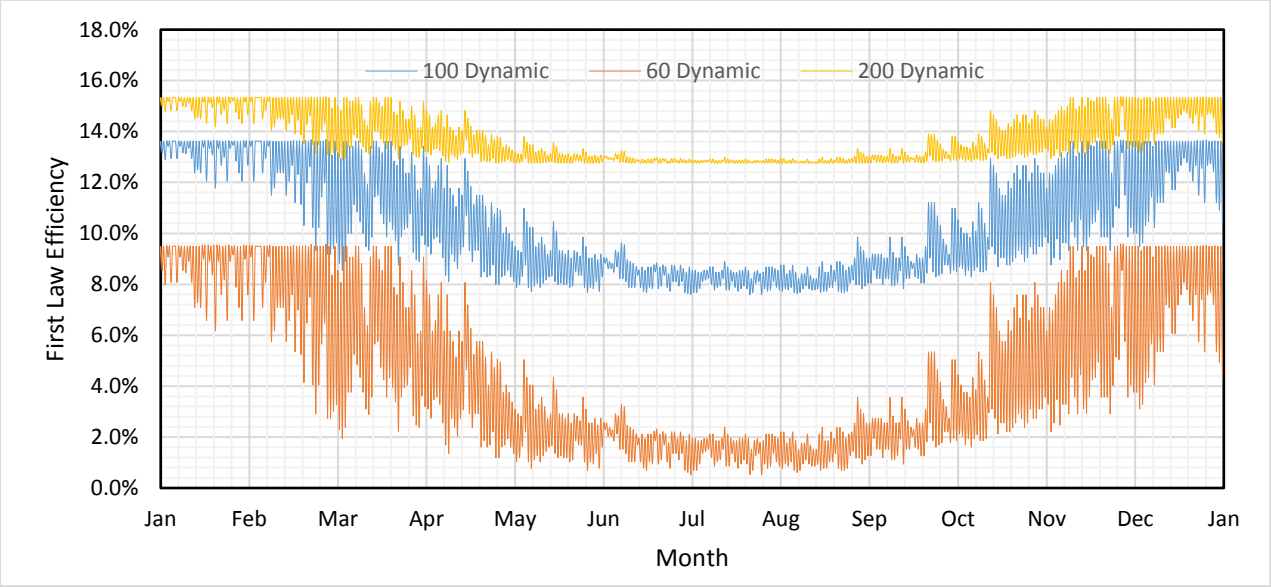

Figure 6.22: Comparison of Annual Efficiency of the dynamic ORC for three different heat source temperatures (60°C, 100°C and 200°C), under Beijing's ambient conditions

The effect of this on the year-round performance of the cycle is demonstrated in Figure 6.22.

6.5.2 Effect of a Regenerator

The presence of a regenerator in the cycle has large effects on the response of the cycle to changing ambient conditions. First, looking at the effect on the response curve as shown in Figure 6.23, several of these effects can be seen.

6.5.2.1 Response Curves for the Regenerative Cycle

Firstly, the efficiency of the cycle continues to increase as the heat source temperature rises past 140°C, unlike the situation for the non-regenerative cycle observed in Figure 6.6. This is due to the fact that even though the evaporator pressure will no longer increase, due to the subcritical limitation placed on the cycle, the regenerative cycle can use the increased superheat at the expander outlet to reduce the evaporator loading by preheating the working fluid. As the heat source temperature increases it causes the superheat at the expander inlet to increase, even without an increase in evaporator pressure. The spacing between subsequent series does decrease with increasing heat source temperature, however, as the cycle runs into diminishing returns. This raises the temperature of the hot side of the regenerator relative to the cold side.

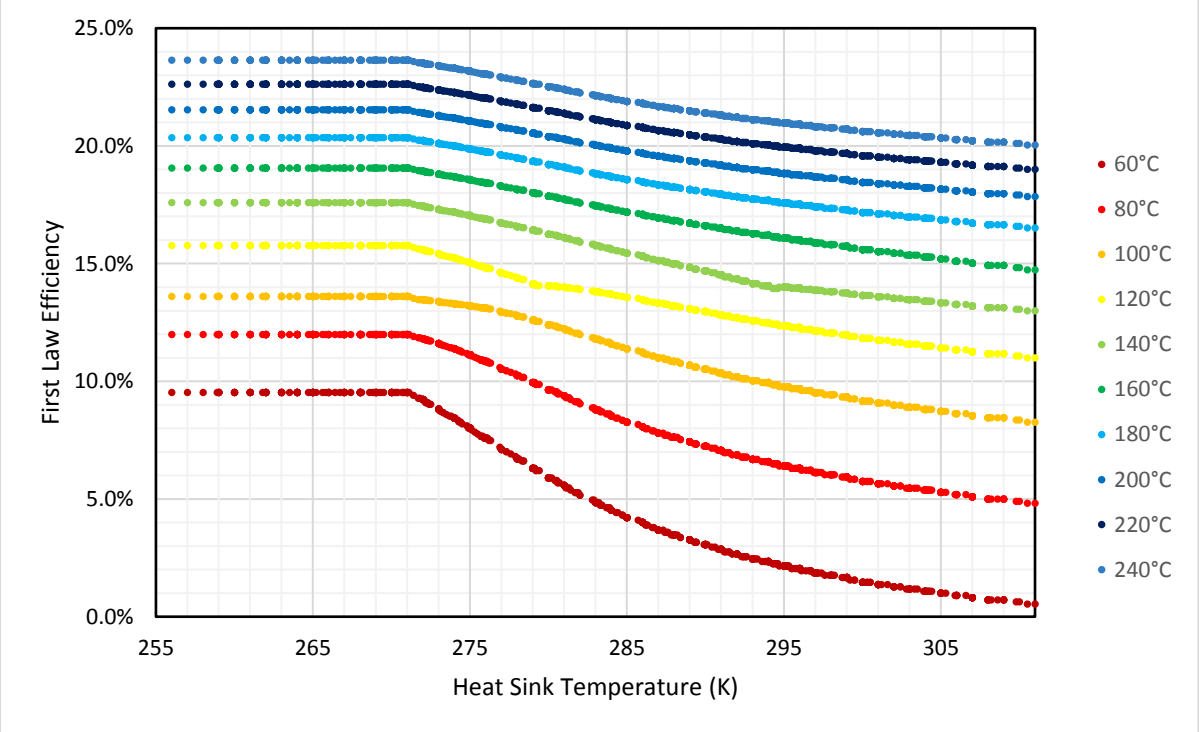

Figure 6.23: Response curves of the regenerative cycle for a variety of heat source temperatures

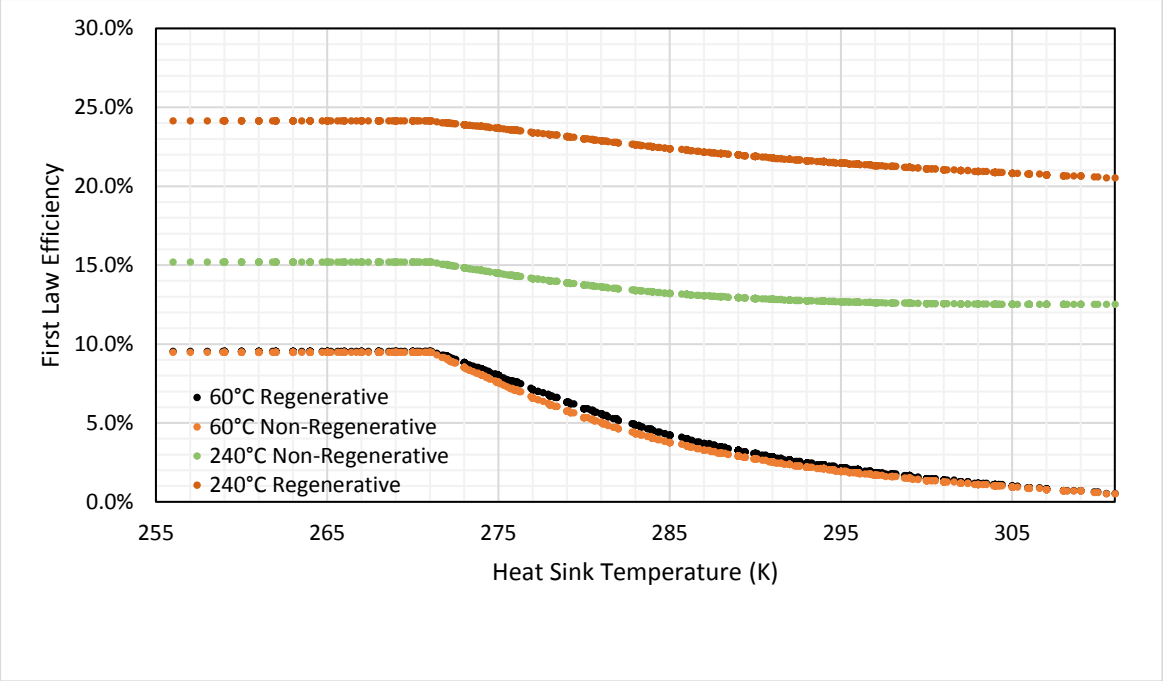

Figure 6.24: Comparison of response curves for regenerative and non-regenerative cycles from two different heat source temperatures

At lower temperatures, the two curves follow a relatively similar profile, as shown in Figure 6.24. At low ambient temperatures, the regenerative and non-regenerative cycles have the same efficiency, as R134a is a wet fluid. This means that if there is no superheat at the expander inlet, there will likely be no heat at the expander outlet, unless the expander has a particularly low isentropic efficiency. This results in there being no driving temperature differential for the regenerator to exploit, rendering it ineffective. However, the curves do diverge slightly at temperatures towards the middle of the range. This is partly due to the fact that the working fluid blend becomes drier as the composition shifts towards R245fa, but as the curves for the regenerative and non-regenerative cycles converge at higher temperatures when the composition shifts back towards 100% R245fa, this cannot be the sole reason for the increase. Instead, the temperature glide of the working fluid is most likely responsible for this, as the glide introduced by the working fluid mixture raises the dew point with respect to the bubble point. This makes a greater driving temperature differential available to the regenerator, counteracting the effects that led to the concave shape of the response curve for the non-regenerative cycle.

At higher temperatures, the two curves have significantly diverged. The lower curve for the non-regenerative cycle has stuck at a certain level of efficiency, unable to increase any more,

whereas the curve for the regenerative cycle has continued to rise. The difference in shape between the curves has remained, with the non-regenerative curve being more concave. The effect of all of this is that the regenerative cycle causes a particularly large increase in efficiency in the spring and autumn, when the response curves for regenerative and non-regenerative cycles are at their most divergent.

A third effect that can be seen in the response curves in Figure 6.23 is a slight kink in the curves for heat source temperatures between 100°and 140°C. As with several previously identified effects on the cycle, this is due to the subcritical limitation placed on it. The kinks in the response curves correspond to the point at which the cycle would need to become supercritical in order to avoid a superheat at the expander inlet, and therefore any further shift in working fluid composition towards R134a will result in an increase in superheat, which will in turn result in an increase in energy transferred by the regenerator. For heat source temperatures outside this range, the kink is not apparent, as for lower heat source temperatures, there is no superheat at the expander inlet at any point, and for higher heat source temperatures, the evaporator pressure cannot be increased further due to the subcritical limitation, meaning that the entire cycle is operating in the region where changes in ambient temperature simply result in increased or decreased regenerator loading.

6.5.2.2 Pump

For the regenerative cycle, the pump enthalpy change is the same as for the non-regenerative cycle, as shown in Figure 6.13.

6.5.2.3 Regenerator

Figure 6.25 shows the variation in the enthalpy change in the regenerator with varying heat sink temperature. At high heat source temperatures, the regenerator profiles are very similar to each other, with an increase as the fluid composition begins to shift from R134a to R245fa, and a temperature glide is introduced into the system raising the dew point with respect to the bubble point with respect to the dew point and increasing the driving temperature differential available to the heat exchanger. This peaks at a heat sink temperature of 285K, which is the point of maximum glide observed in Figure 6.8.

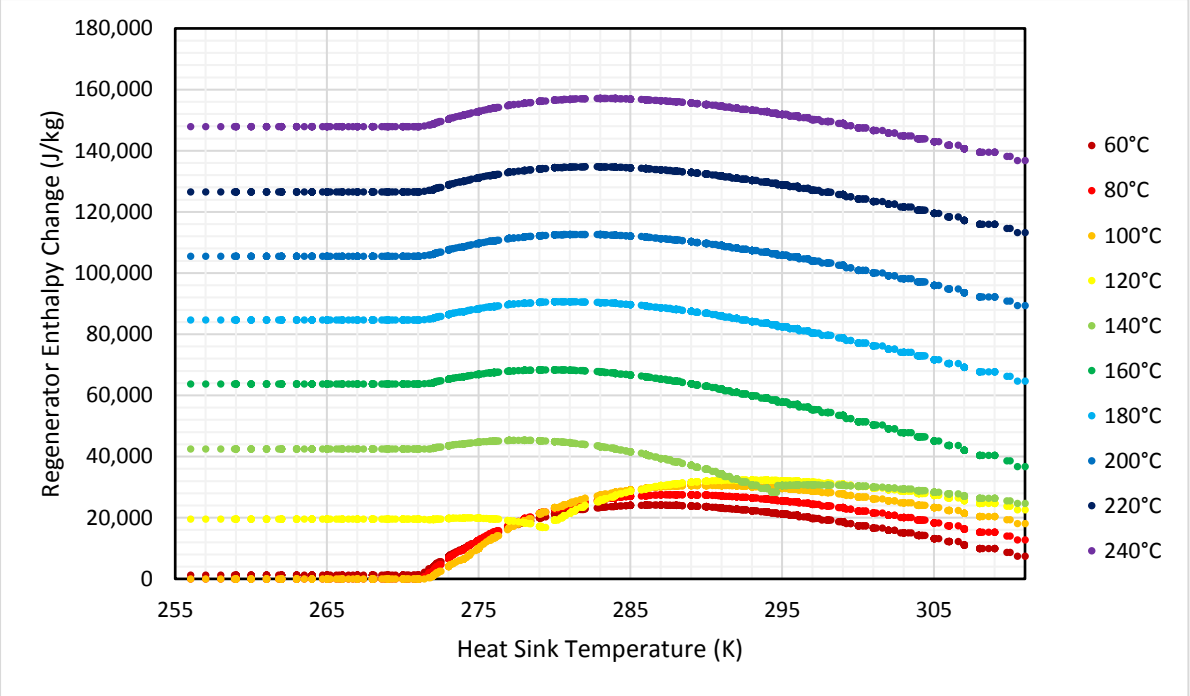

Figure 6.25: Variation in Regenerator Enthalpy with varying heat sink temperature

At lower heat source temperatures, the subcritical limitation of the cycle again has a strong effect on the shape of the response curve for the regenerator enthalpy. When the heat source temperature is low, the supercritical limitation is not necessary, as the evaporator pressure can be raised high enough to eliminate the expander inlet superheat without causing the cycle to become supercritical. R134a is a slightly wet fluid, so if there is no superheat at the expander inlet, any expander with a reasonably high isentropic efficiency will not have any superheat at the expander outlet. With no glide, this means there is no driving temperature differential for the regenerator. As R245fa is introduced into the system, it has two effects. Firstly it introduces glide, which raises the temperature of the dew point relative to the bubble point, and secondly, being a dryer fluid than R134a, it makes the resulting working fluid blend dryer, which tends to increase the amount of superheat at the expander inlet. Both of these increase the regenerator enthalpy change. As the ambient temperature increases further and the working fluid tends towards 100%R245fa, the increase in regenerator enthalpy due to glide disappears, but the increase caused by the greater dryness of R245fa remains. These effects are not seen at higher heat source temperatures when the superheat at the expander inlet leads to a corresponding superheat at the expander outlet, meaning that the regenerator is always able to transfer some enthalpy, even when the working fluid is composed of mostly R134a.

6.5.2.4 Evaporator

Although the profile of the evaporation process will be the same in the regenerative cycle as in the non-regenerative one, due to the evaporator pressure being the same in both cycles, the enthalpy change in the evaporator itself will vary as the regenerator accounts for a varying amount of the heating required. This is shown in Figure 6.26. When compared with the non-regenerative case (Figure 6.15), several things can be seen. Firstly, the behaviour of the cycle in the high R245fa region at lower temperatures follows the same profile as the higher temperatures, even though the same subcritical limitation applies to the cycle. Looking at Figure 6.25, which plots the regenerator enthalpy change, it can be seen that the increased evaporator enthalpy in this region in the non-regenerative case is being taken up by the regenerator in the regenerative case, due to the temperature glide and increased dryness of the working fluid. This gives a much smoother profile to the plot, as there is no point when the subcritical limitation suddenly begins to apply. Secondly the plots for the higher heat source temperatures have a more concave shape than for the non-regenerative cycle, due to the convex shape of the plot for the regenerator enthalpy change. When subtracted from the relatively straight plot observed in Figure 6.15 it results in the concave plot observed in Figure 6.26. Finally, the different plots for varying heat source temperatures are far closer together than for the non-regenerative plot, as the increase observed in Figure 6.15 between plots of increasing heat source temperature was mainly caused by increasing superheat at the expander inlet, especially at higher heat source temperatures. This results in more energy being captured by the regenerator at these temperatures, reducing the spacing between the plots.

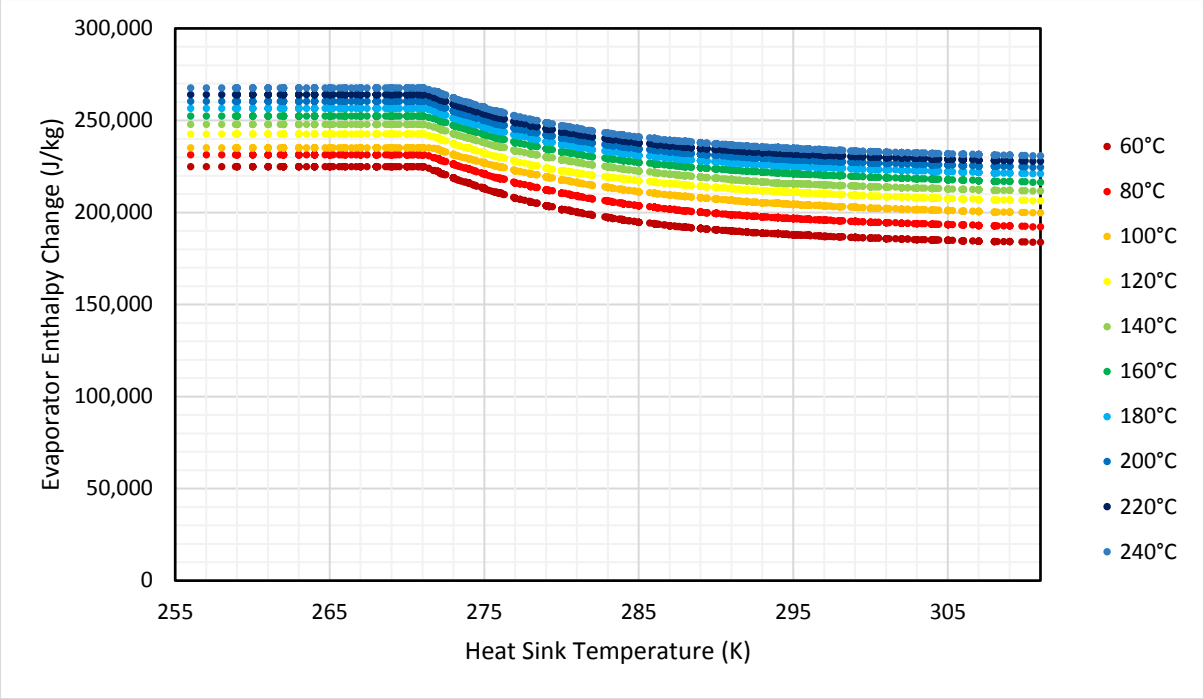

Figure 6.26: Variation of evaporator enthalpy change with varying ambient temperature

6.5.2.5 Expander

As with the pump, the expander has the same response in the regenerative and non-regenerative cycles, due to the same working fluid, maximum cycle temperature and pressure ratio.

6.5.2.6 Condenser

The plot for the condenser in the regenerative case is similar to that for the evaporator. The plots for different heat source temperatures are concave, smooth, and closely-packed due to the effects of the regenerator.

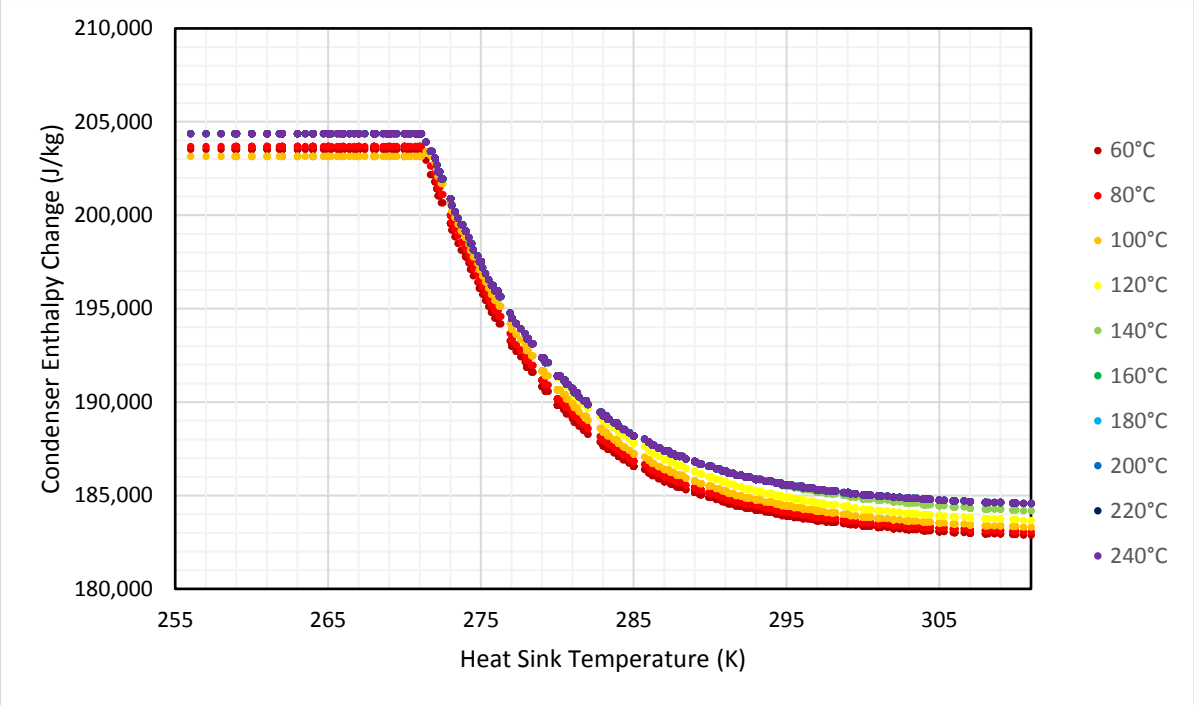

Figure 6.27: Variation in condenser enthalpy change with varying heat sink temperature

6.6 Fixed Displacement Cycle

A fixed-displacement cycle, in contrast to the variable-displacement cycles considered in the previous section, has a displacement that is constrained by its geometry, so for example, the stroke of a piston using a transverse crankshaft, or a scroll expander with a fixed outlet port. These cycles will suffer a sharp decrease in isentropic efficiency if they are operated at a pressure ratio too far from the natural volume ratio imposed by their displacement. As for the variable-displacement cycles, the fixed-displacement cycles were analysed over the course of the year under varying conditions of heat source temperature, and with and without a regenerator.

6.6.1 Non-regenerative Cycles

6.6.1.1 Response Curves

Figure 6.28 shows the response curves of the cycle for varying ambient temperature, under a variety of heat source temperatures. When compared to Figure 6.6, which shows the same response curves for the variable-displacement cycle, the results are very different. Figure 6.6 showed a sharp increase in the efficiency for lower heat source temperatures as the heat sink temperature dropped, an increase that became less noticeable for higher heat source temperatures. In Figure 6.28, the opposite effect can be seen. Lower heat source temperatures

show little to no increase in efficiency with decreasing ambient temperature without an increase in pressure ratio. Higher heat source temperatures, however, do show a slight increase, although not to the same degree as that observed in Figure 6.6. This initially appeared consistent with the research of Saleh et al [48] who noted that the first law efficiency of the cycle does increase with increasing expander inlet superheat. However, Figure 6.30 shows the variation in expander inlet superheat with varying heat sink temperature, and there is no observable difference in the profile of the superheat curve with varying temperature between the curves for low and high temperature heat sources.

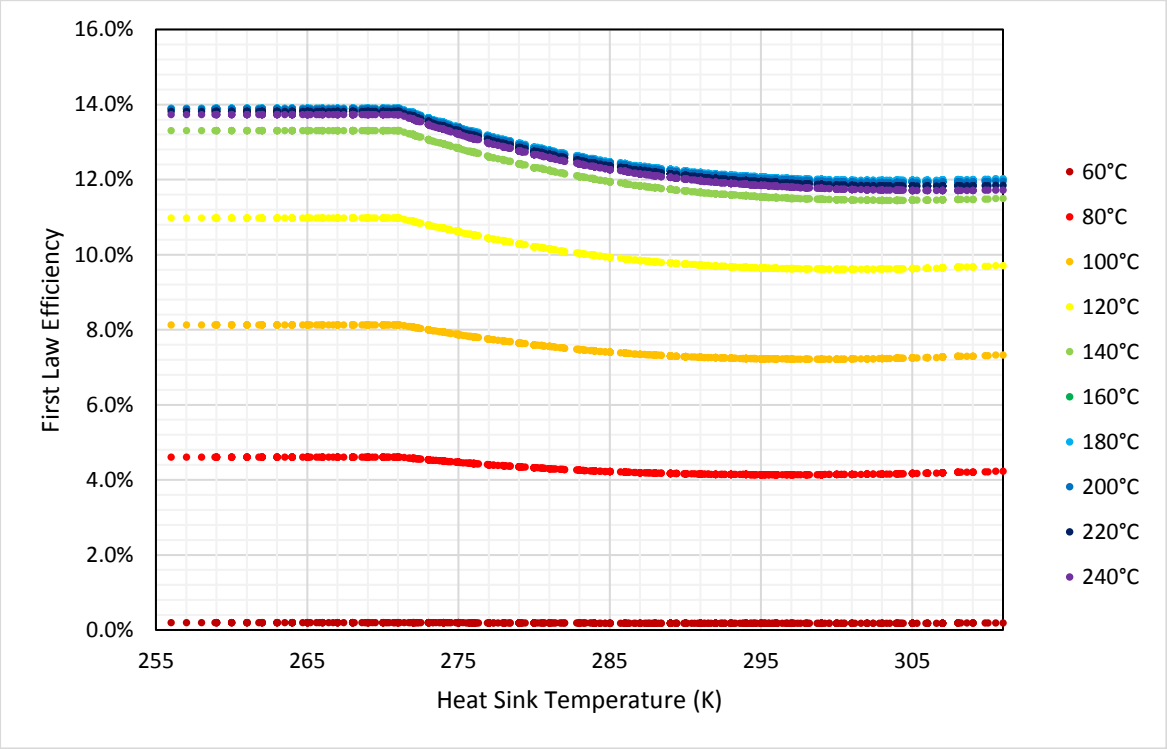

Figure 6.28: Response Curve of first law efficiency with varying heat sink temperature for a variety of heat source temperatures

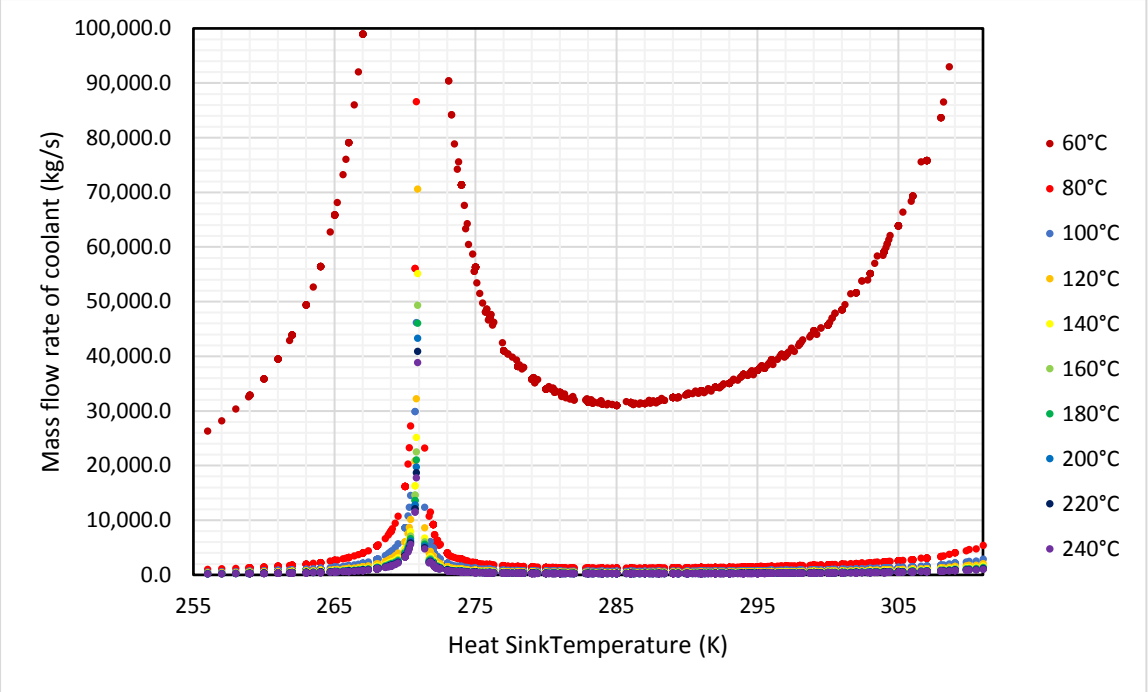

Figure 6.29: Variation in coolant mass flow rate with varying heat sink temperature for a variety of heat source temperatures

Figure 6.29 shows the variation in the mass flow rate of the coolant on the cold side of the condenser. The same trend as observed in Figure 6.11, which shows the corresponding data for the variable-displacement cycle, can be seen. At high temperatures the mass flow rate is at a local maximum, before decreasing as the temperature glide of the fluid increases when the composition shifts towards R134a. It reaches a trough at the point of maximum glide, before increasing again as the glide reduces when the working fluid composition approaches pure R134a. At temperatures colder than this, the cycle itself does not change, so the only effect of reducing coolant temperature is to increase the temperature difference at the condenser cold side inlet, increasing the acceptable rise in temperature on the cold side of the condenser while still maintaining the required pinch point temperature difference. The effect of this is that the required mass flow rate for removing the same amount of energy from the system can be lower, and the required coolant mass flow rate can be seen to drop as the temperature decreases beyond this point.

It can also be seen that the mass flow rate of the coolant is higher for lower heat source temperatures, dropping off rapidly as the heat source temperature increases. While this may initially seem counterintuitive, it can be attributed to the changes in the mass flow rate of the

system, as shown in Figure 6.31. The lower the heat source temperature, the lower the pressure ratio in the cycle, and the lower the expander output. Therefore the higher the necessary mass flow rate of working fluid to achieve the required 1MW power output.

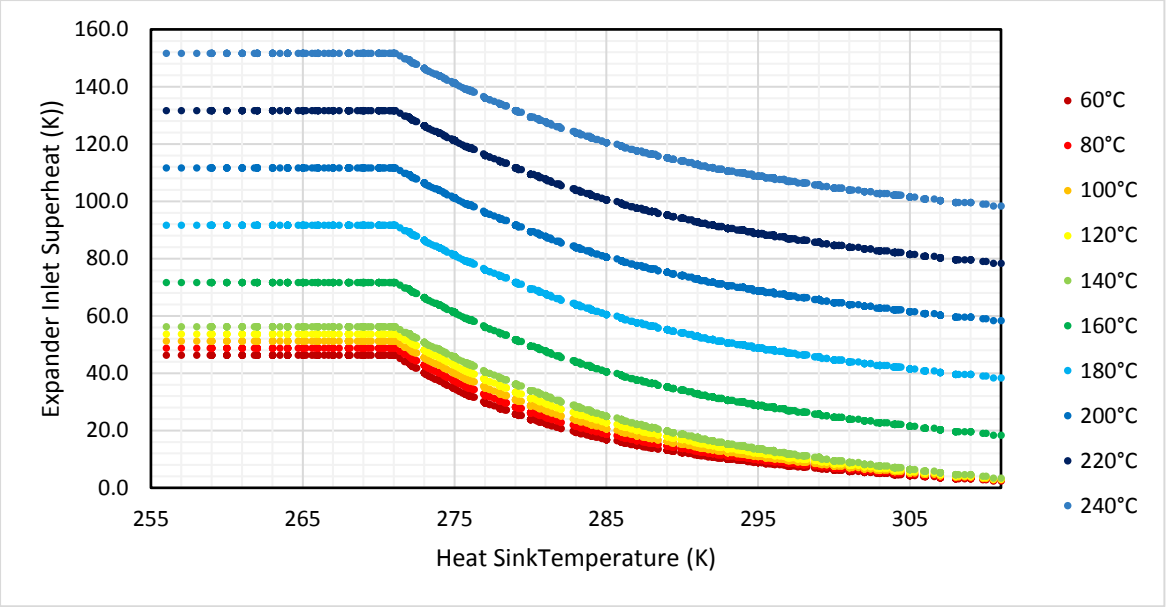

Figure 6.30: Variation in Expander Inlet Superheat with changing ambient temperature for a non-regenerative, positive displacement cycle for a variety of heat source temperatures

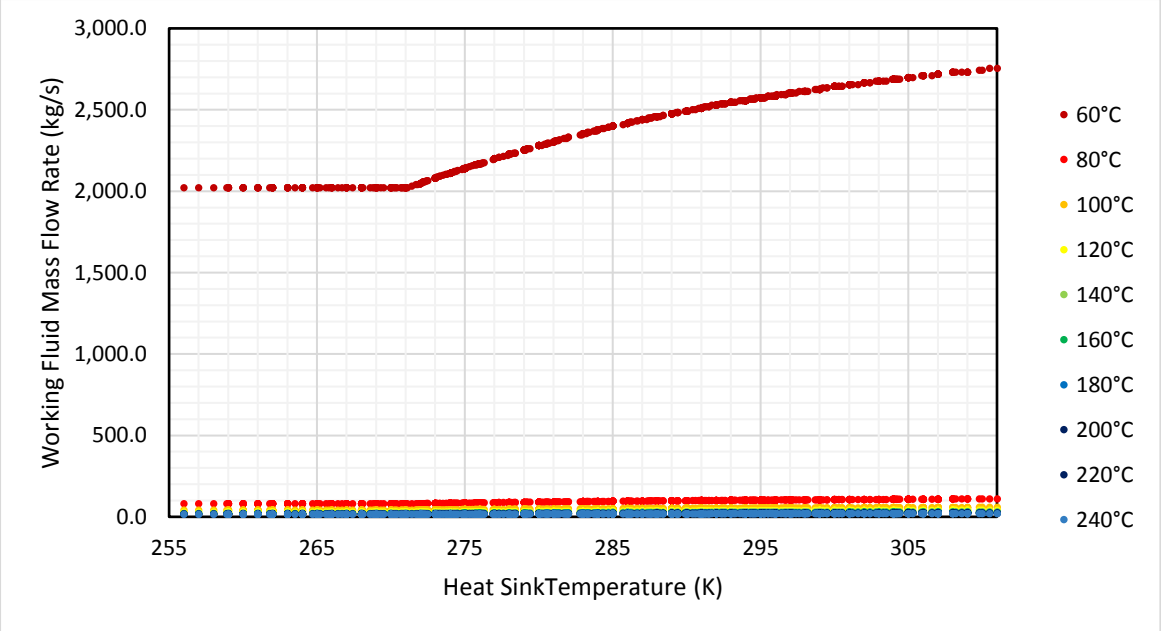

Figure 6.31: Variation in Working Fluid Mass Flow Rate with Varying Ambient Temperature for a non-regenerative, positive displacement cycle for a variety of heat source temperatures

6.6.1.2 Pump

Figure 6.32 shows the variation in pump enthalpy change with varying heat sink temperature. As the pressure ratio is fixed over the course of the year, it can be seen that the pump enthlalpy varies very little as the heat sink temperature changes. In the mid-temperature range, when the fluid has the highest glide, there is a slight dip in the plot. The shape of the curves in Figure 6.32 does not match those of the mass flow rate in Figure 6.31. There is no change in the pump enthalpy change above a heat source temperature of 140°C, due to the subcritical limitation on the cycle. Above this heat source temperature, the pressure ratio cannot be increased any further without violating this limitation.

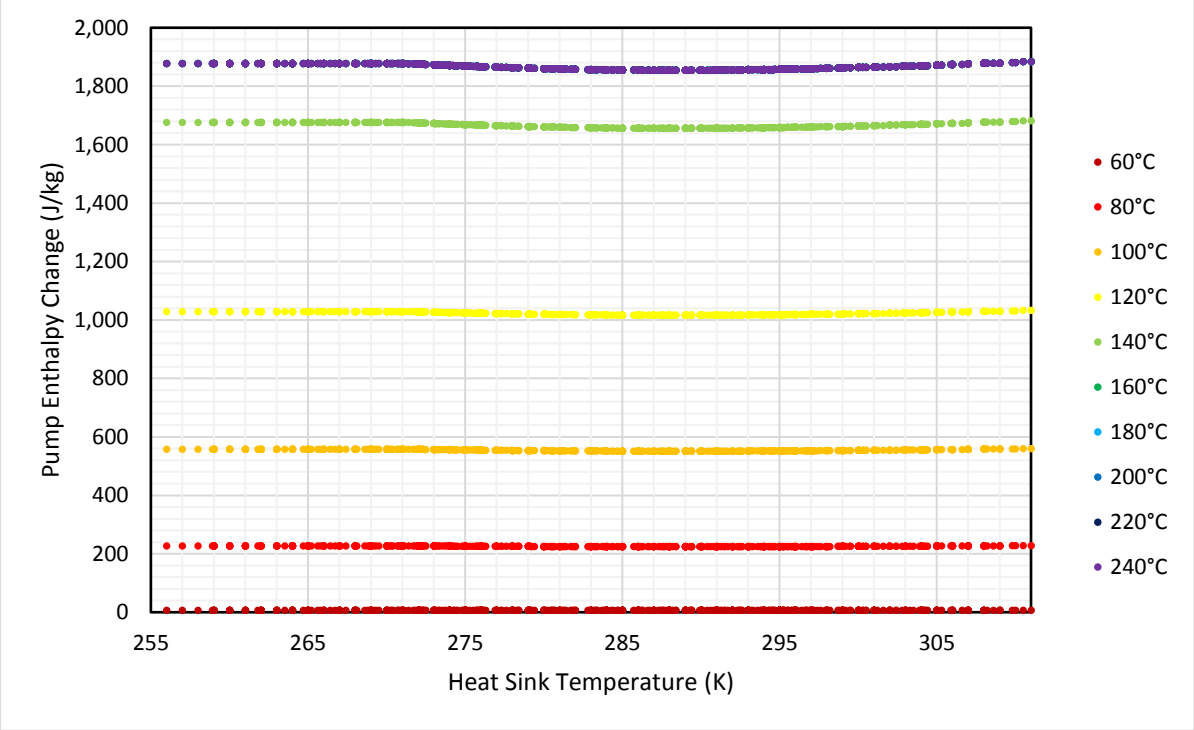

Figure 6.32: Variation in Pump Enthalpy with Varying Ambient Temperature for a non-regenerative, positive displacement cycle for a variety of heat source temperatures

6.6.1.3 Evaporator

Figure 6.33 shows the variation in the evaporator enthalpy change as the heat sink temperature changes, for a variety of heat source temperatures. It can be seen that the evaporator enthalpy increases in a linear manner as the temperature drops, before plateauing when the heat sink temperature drops below 271K, the working fluid composition is 100% R134a, and cannot be shifted any more.

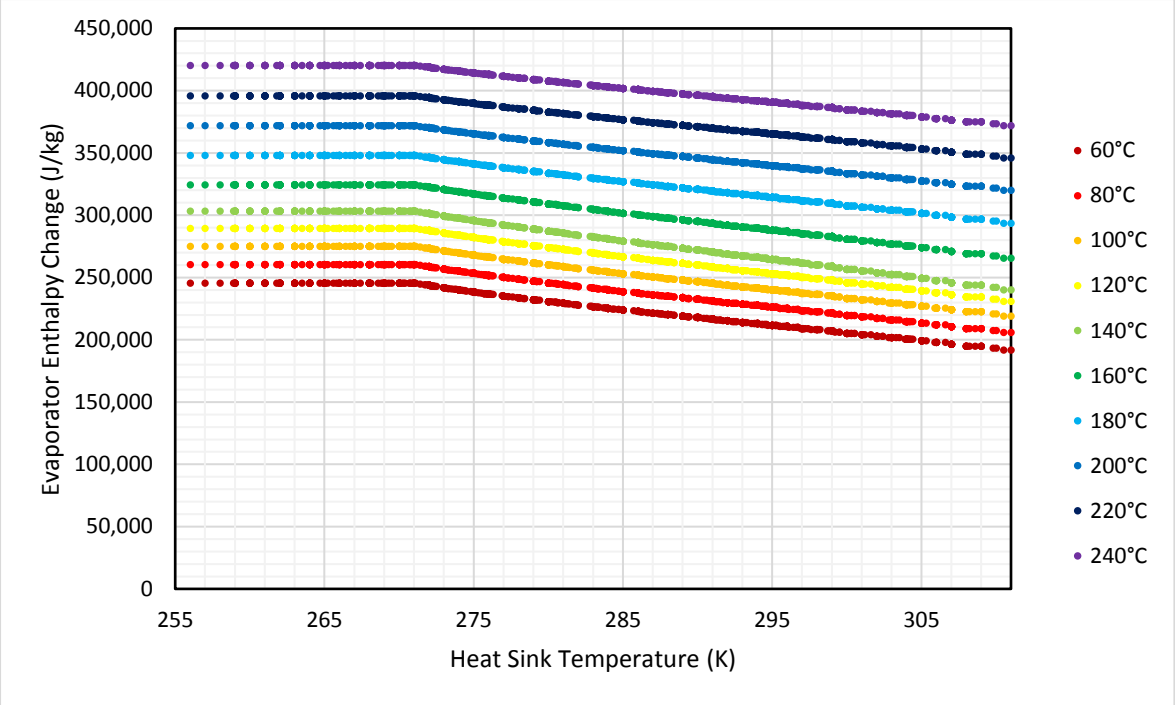

Figure 6.33: Variation in Evaporator Enthalpy Change with varying heat sink temperature for a non-regenerative, positive displacement cycle for a variety of heat source temperatures

When compared to Figure 6.15, which is the corresponding graph for the variable displacement cycle, this figure is much simpler. There is no change in evaporator pressure, which means there are no sudden changes in the profile of the graph caused by the subcritical limitation on the cycle. The plots for all heat source temperatures simply rise linearly as the heat sink temperature decreases, and more energy is required to bring the working fluid up to expander inlet temperature.

6.6.1.4 Expander

Figure 6.34 shows the variation in the enthalpy drop across the expander as the heat sink temperature changes. It can be seen that the trend of the plots is very similar to those seen in Figure 6.28, which shows the variation in the overall cycle efficiency. This implies that the change in the cycle efficiency under these conditions is primarily due to the change in the expander enthalpy, which will increase with increasing superheat as the constant pressure lines on the vapour side of the saturation dome diverge. The greater the superheat at the expander inlet, the greater the enthalpy drop across the expander, whether this superheat is a result of an increasing heat source temperature, or an increasing proportion of R134a in the working fluid.

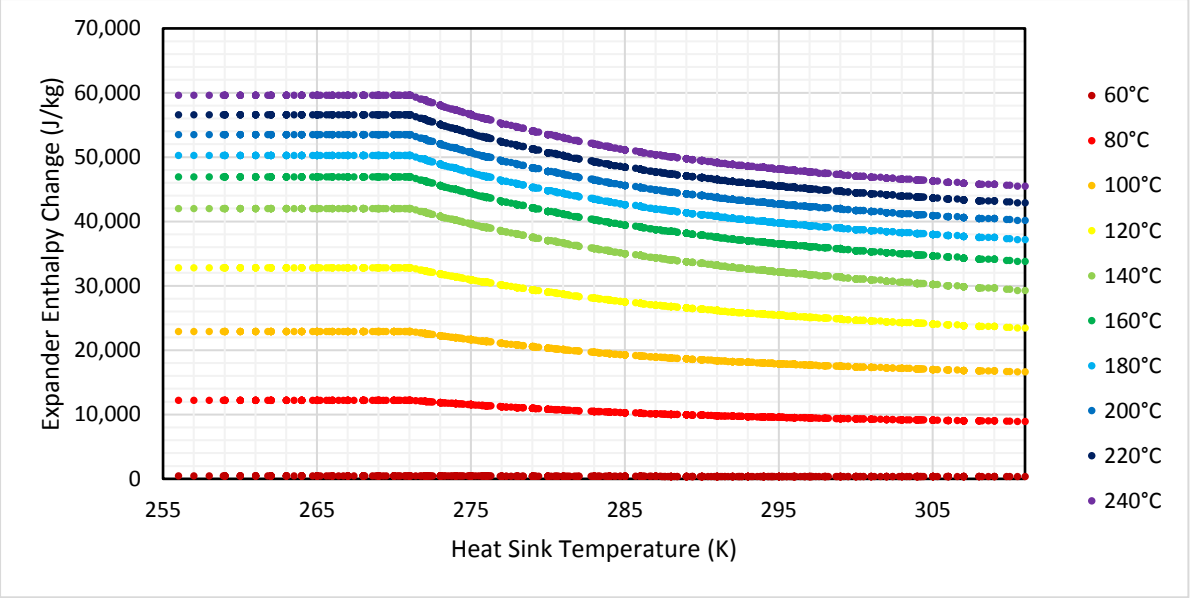

Figure 6.34: Variation in Expander Enthalpy Change with Varying Heat Sink Temperature for a non-regenerative, fixed-displacement cycle with various heat source temperatures

6.6.1.5 Condenser

Figure 6.35 shows the variation in the enthalpy change in the condenser as the ambient temperature varies. It is largely similar to the shape of the corresponding graph for the evaporator shown in Figure 6.33, but with a slightly convex shape at higher heat source temperatures, corresponding to the concave shape of the curves for the expander shown in Figure 6.34 being subtracted from the relatively linear curves for the evaporator.

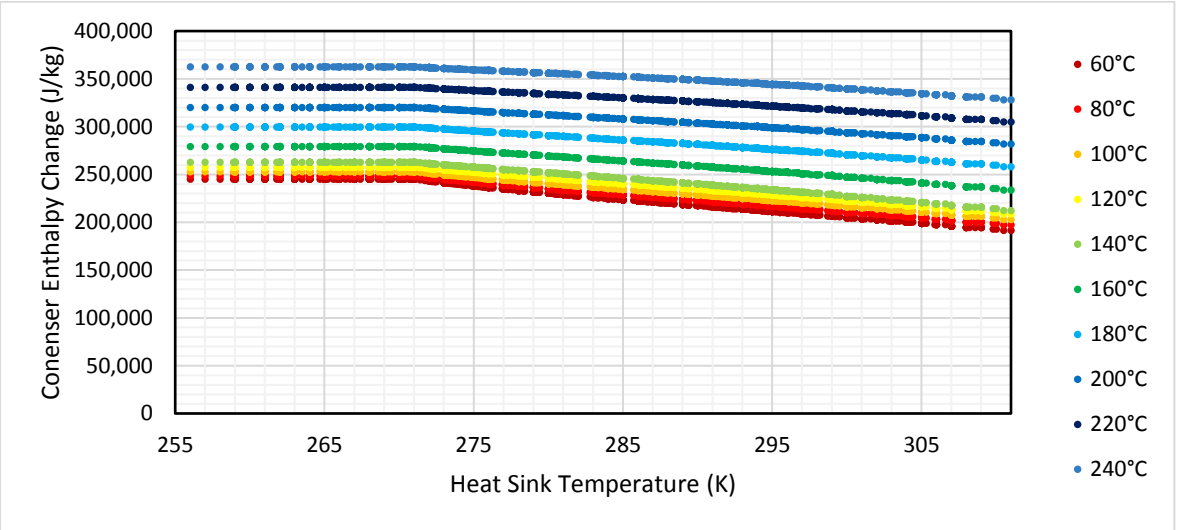

Figure 6.35: Variation in Condenser Enthalpy Change with varying heat sink temperature for a non-regenerative, fixed-displacement cycle for a variety of heat source temperatures

6.6.2 Regenerative Cycles

As with the variable-displacement cycle, a regenerator can be applied to the fixed-displacement cycle to recover energy from the expander exhaust and use it to preheat the working fluid before it enters the evaporator.

6.6.2.1 Response Curves

Figure 6.36 shows the variation in the first law efficiency of the regenerative fixed displacement cycle as the ambient temperature varies. When compared to the values shown in Figure 6.28, which plots the same data for the corresponding non-regenerative, fixed displacement cycles. Several differences can be seen.

At low heat source temperatures, the cycles have relatively similar performances. This could be due to the fact that due to the low heat source temperature there is minimal superheat at the expander inlet, especially for the wet fluid r134a. This means that there is only a small driving temperature differential for the regenerator to utilise, reducing its effectiveness. For the regenerative cycle, a slight increase can be seen over the middle range of ambient temperatures, between about 280 and 290K. This corresponds with the maximum temperature glide experienced by the cycle, and is consistent with the theory that the glide increases the temperature of the dew point relative to the bubble point, increasing the temperature differential available to the regenerator.

Figure 6.28 shows no noticeable increase in first law efficiency with increasing heat source temperature above a heat source temperature above 150°C, as the subcritical limitation placed on the cycle comes into effect, even for a working fluid composition of 100% R245fa, meaning further increases in heat source temperature simply increase the expander inlet superheat without large increases in the expander work. However, in Figure 6.36 there is still a noticeable increase in the efficiency of the cycle with increasing heat source temperature, even at higher heat source temperatures.

Also, as seen in the related plots for the variable-displacement cycle, the plots for the regenerative cycle seen in Figure 6.36 are less concave than those seen in the non-regenerative cycle seen in Figure 6.28, due to the fact that the regenerator enthalpy change is higher in mid-temperature regions due to the temperature glide, counteracting the factors which cause the concavity in Figure 6.28.

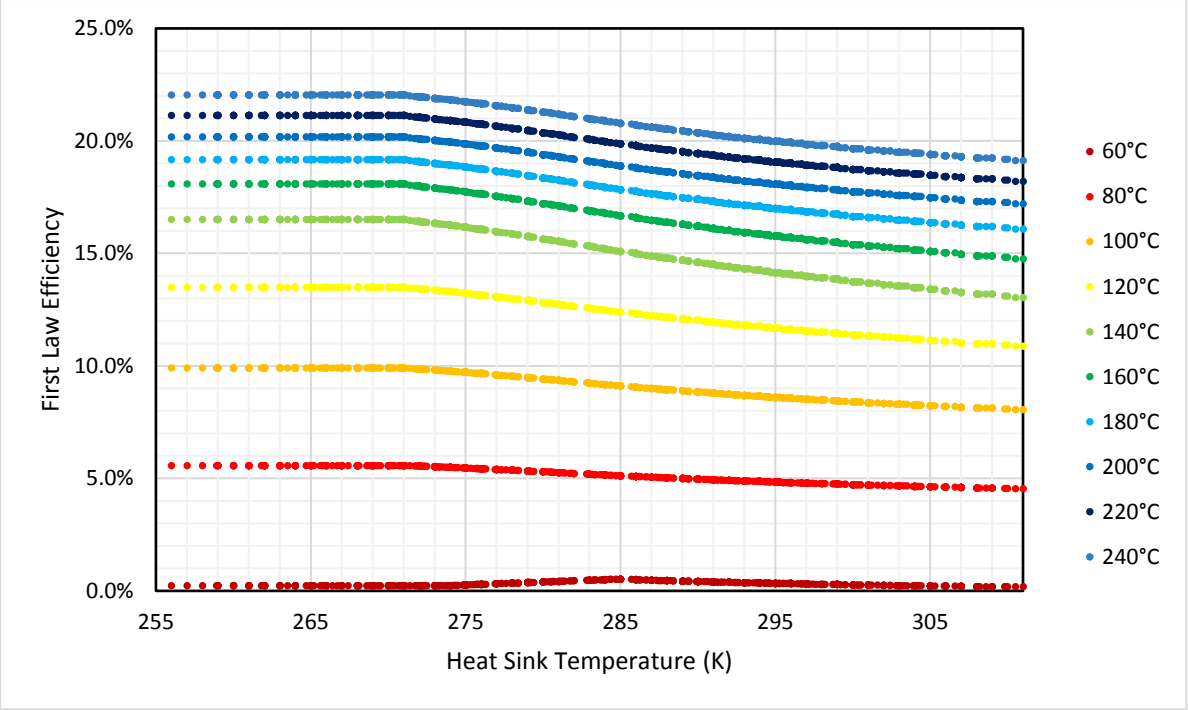

Figure 6.36: Variation in First Law Efficiency with varying ambient temperature for a regenerative, fixed displacement cycled over a variety of heat source temperatures

As for the variable-displacement cycle, the working fluid mass flow rate to produce the required 1MW of power does not change with the addition of a regenerator, as the enthalpy drop across the expander remains the same.

6.6.2.2 Pump

The response curve for the pump for the regenerative, fixed-displacement cycle is shown in Figure 6.37. It is identical to the corresponding plot for the non-regenerative cycle given in Figure 6.32. This was an expected result, as the pressure ratio and input temperature to the pump are exactly the same in both regenerative and non-regenerative cases.

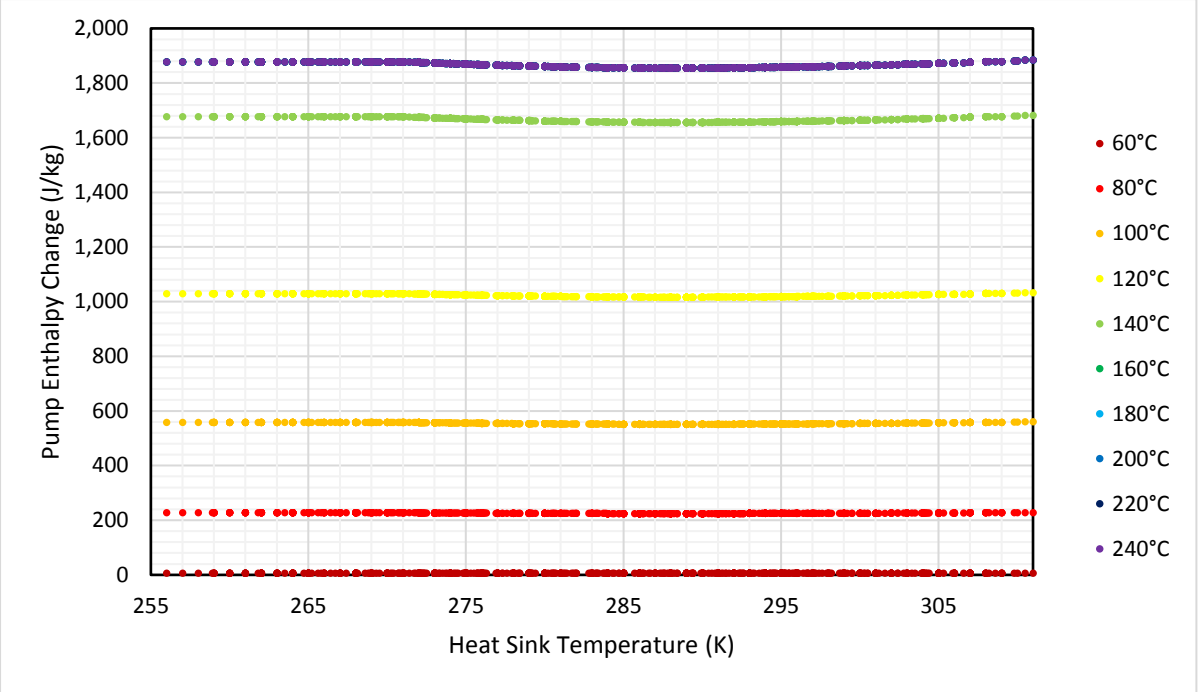

Figure 6.37: Variation in Pump Enthalpy Change with varying ambient temperature for a fixed-displacement regenerative cycle for a range of heat source temperatures

6.6.2.3 Regenerator

Figure 6.38 shows the variation in the regenerator enthalpy with varying heat sink temperature for the regenerative, fixed-displacement cycle. As for previous graphs, the coldest portion of the year, when the working fluid is 100% R134a, shows no change with changing ambient temperature for all of the heat source temperatures. As the temperature increases to such a point where R245a must be added, the regenerator enthalpy begins to increase due to the temperature glide this introduces raising the dew point relative to the bubble point and making a greater driving temperature difference available for the regenerator to exploit. The regenerator enthalpy peaks at the point of maximum glide, at 282K, and then begins to drop off as the amount of glide reduces. The final regenerator enthalpy at the highest temperatures when the working fluid composition is 100% R245fa is lower than the initial regenerator enthalpy when the working fluid is 100% R134a. This is expected due to the lower temperature difference between the hot and cold reservoirs, and counteracts any tendency for R245fa to have a higher regenerator enthalpy due to it being a drier working fluid.

There is also a noticeable trend with changing heat source temperature. Initial rises in heat source temperature cause a slight initial rise in the regenerator enthalpy, although this is limited, because the amount of superheat at the expander inlet and outlet can be controlled by

increasing the evaporator pressure. Above a heat source temperature of 140°C the subcritical limitation on the cycle takes effect and the evaporator pressure cannot be increased any more. Above this temperature the spacing between the lines in Figure 6.38 increases, corresponding to a greater increase in regenerator enthalpy. Without the ability to control the superheat at the expander inlet by increasing the evaporator pressure, the superheat will rise rapidly with increasing heat source temperature after this point, increasing the enthalpy change in the regenerator.

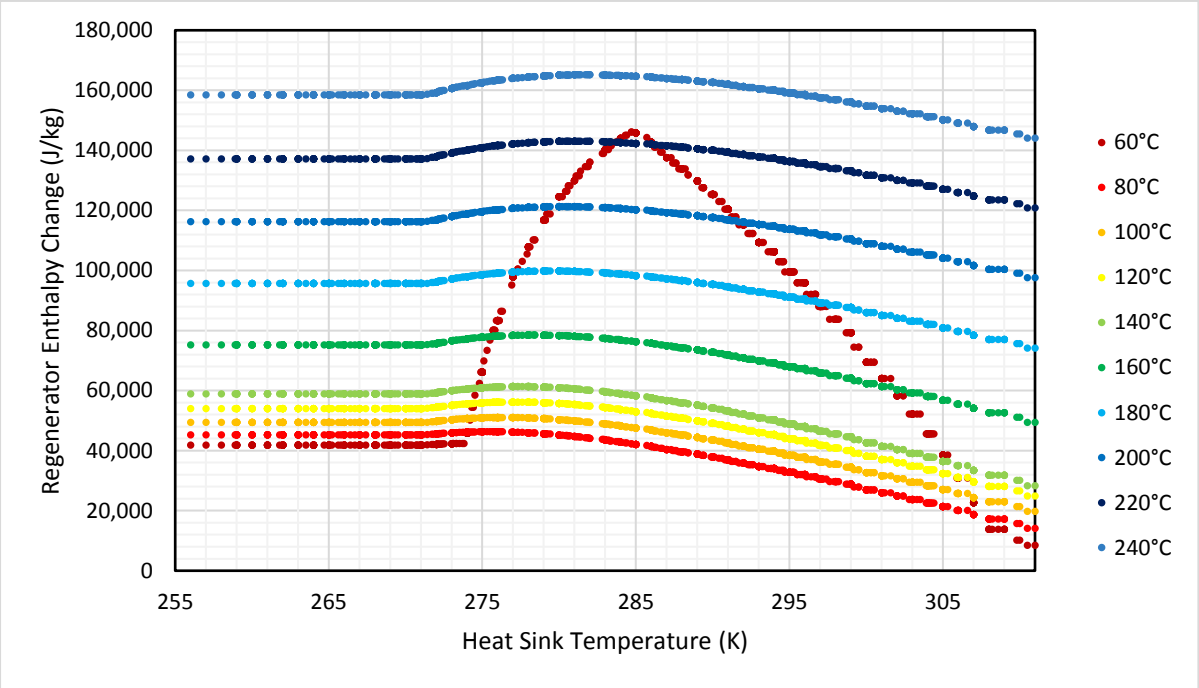

Figure 6.38: Variation in Regenerator Enthalpy Change with varying ambient temperature for a regenerative fixed-displacement cycle over a range of heat source temperatures

The one anomalous result that can be seen in Figure 6.38 is the dark red series representing a heat source temperature of 60°C. This rises sharply above the corresponding plots for other heat source temperatures, and peaks at the point of maximum glide, at 285K. This would suggest that the effect is being caused at least in some capacity by the glide of the fluid. Figure 6.39 shows T-s diagrams for three cycles, with heat source temperatures of 60°C, 70°C and 80°C. It can be seen that the condensation lines for all three plots are the same, as the condenser pressure and fluid compositions are determined by the maximum and current heat sink temperatures, not by the heat source temperature. However, the evaporating lines vary considerably between the three plots. For a heat source temperature of 60°C, the two lines almost overlap, and there is only a 2°C difference between the temperature of the working fluid

in the evaporator and the condenser. For the heat source temperature of 70°C this increases to 12°C. The 14.7°C of glide in the evaporator and the 15.4°C in the condenser are more proportionally significant in the 60°C case than in the 70°C case. The marks on the T-s plots underneath the saturation domes show the state of the working fluid after exiting the regenerator. The evaporator temperature is so low in the 60°C case that even a small amount of superheat at the expander outlet, combined with the small amount of glide, can cause a significant proportion of the working fluid to undergo a phase change, greatly increasing the amount of energy transferred in the regenerator. In the 60°C case, working fluid leaves the cold side of the regenerator with a quality of 71%. In the 70°C case, the quality at this point is 8.4%. In the 80°C case, this has further dropped to 3.8%.

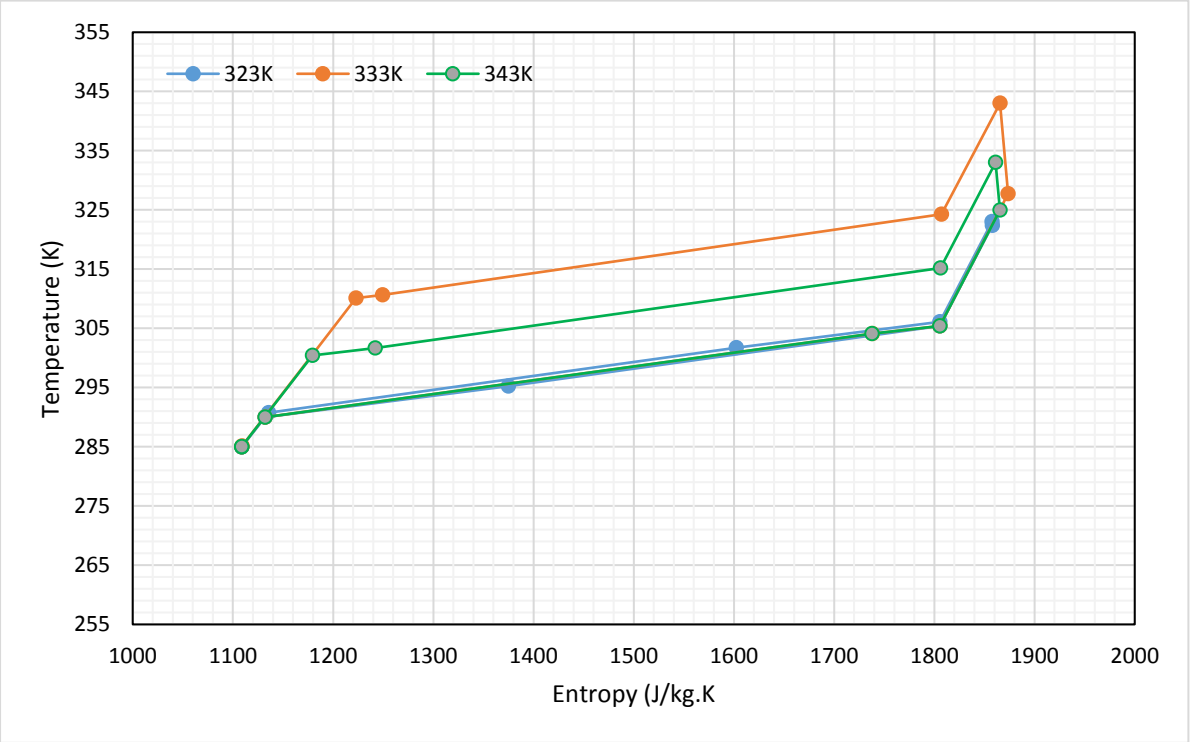

Figure 6.39: T-s diagram for three cycles, with a heat sink temperature of 285K, and heat source temperatures of 323K, 333K and 343K

6.6.2.4 Evaporator

Figure 6.40 shows the variation in the evaporator enthalpy change as the ambient temperature changes. It can be seen that the enthalpy change increases as the heat source temperature increases, and also as the heat sink temperature drops. Both of these were expected, as intuitively the amount of enthalpy transferred in the evaporator would be expected to rise with the increasing temperature differential between its two ends.

When compared to the corresponding plot for the non-regenerative fixed-displacement cycle, given in Figure 6.33, several differences are apparent. Firstly, the values for evaporator enthalpy are lower for the regenerative cycle, again, this was expected due to the fact that the regenerator is now taking up some of the heating duty previously accounted for by the evaporator in the non-regenerative cycle. Secondly, the plot for the regenerative cycle is noticeably more concave than the plot for the non-regenerative cycle. This can be explained by the plot for the regenerator given in Figure 6.38. The shape of this plot is clearly convex, being higher at mid-range temperatures when the temperature glide is the highest. Subtracting this convex shaped curve from the relatively linear curve observed for the non-regenerative case seen in Figure 6.33 gives the concave shape seen in Figure 6.40.

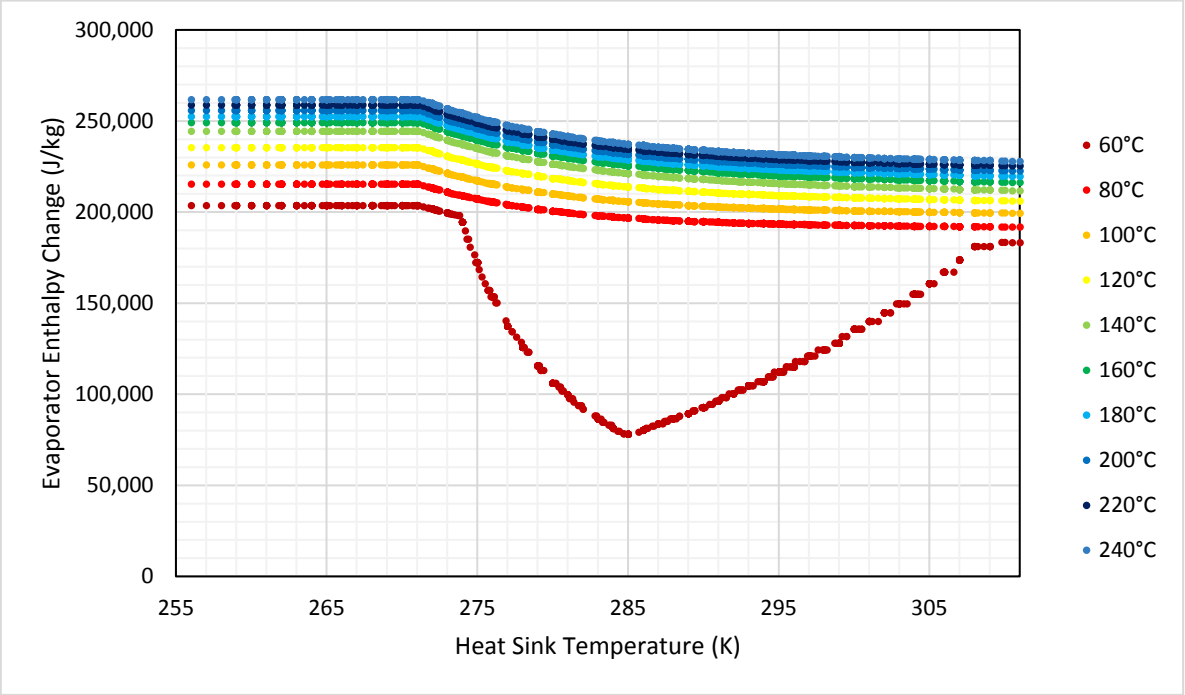

Figure 6.40: Variation in Evaporator Enthalpy Change with varying ambient temperature for a fixed displacement regenerative cycle over a range of heat source temperatures

The evaporator enthalpy change is again an anomaly for the 60°C heat source case. The spike in regenerator enthalpy caused by the greater phase change in this case, and demonstrated graphically in Figure 6.38 and Figure 6.39, subtracts from the external energy required to bring the working fluid up to the condition at the expander inlet.

6.6.2.5 Expander

Figure 6.41 shows the variation in the enthalpy drop across the expander with varying ambient temperature. It is identical to the corresponding plot shown in Figure 6.34, for the non-regenerative case. Again, this result was expected, as the pressure ratio, inlet temperature, and working fluid composition are identical between the two cases. The plot has a concave shape which corresponds reasonably well with the concave shape of the plot for the evaporator. This means that the curve for first law efficiency, shown in Figure 6.36 is relatively linear.

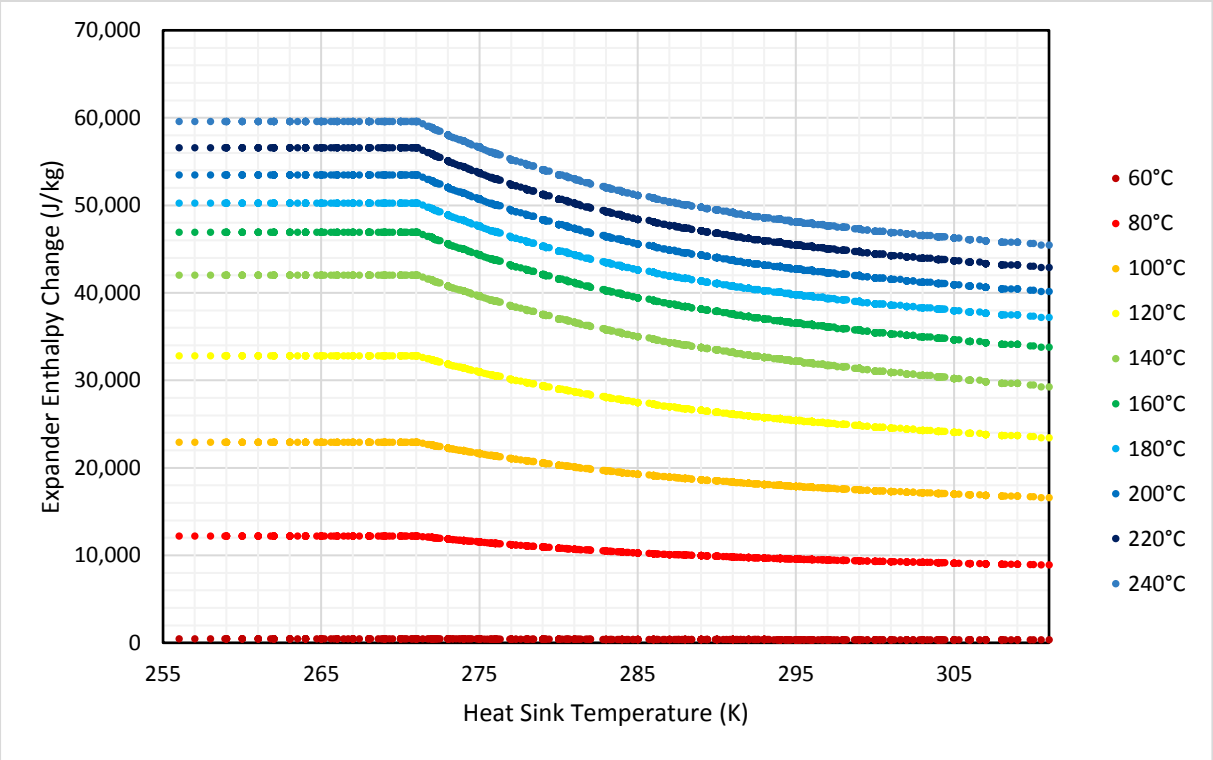

Figure 6.41: Variation in Expander Enthalpy Change with varying ambient temperature for a regenerative, fixed-displacement cycle over a range of heat source temperatures

6.7 Comparison of Performance Metrics

The response curves to varying ambient and heat source temperatures generated in the previous section can be used to analyse the variation in the performance parameter ψ discussed in Chapter 3. This parameter is the improvement in annual energy generation that can be achieved with the use of the dynamic cycle.

6.7.1 Variation in ψ with changing Heat Source Temperature

Figure 6.42 shows the variation in ψ for four different cycle configurations, regenerative and non-regenerative, and positive displacement and variable displacement. The four plots show different trends, which can primarily be explained using the response curves shown previously.

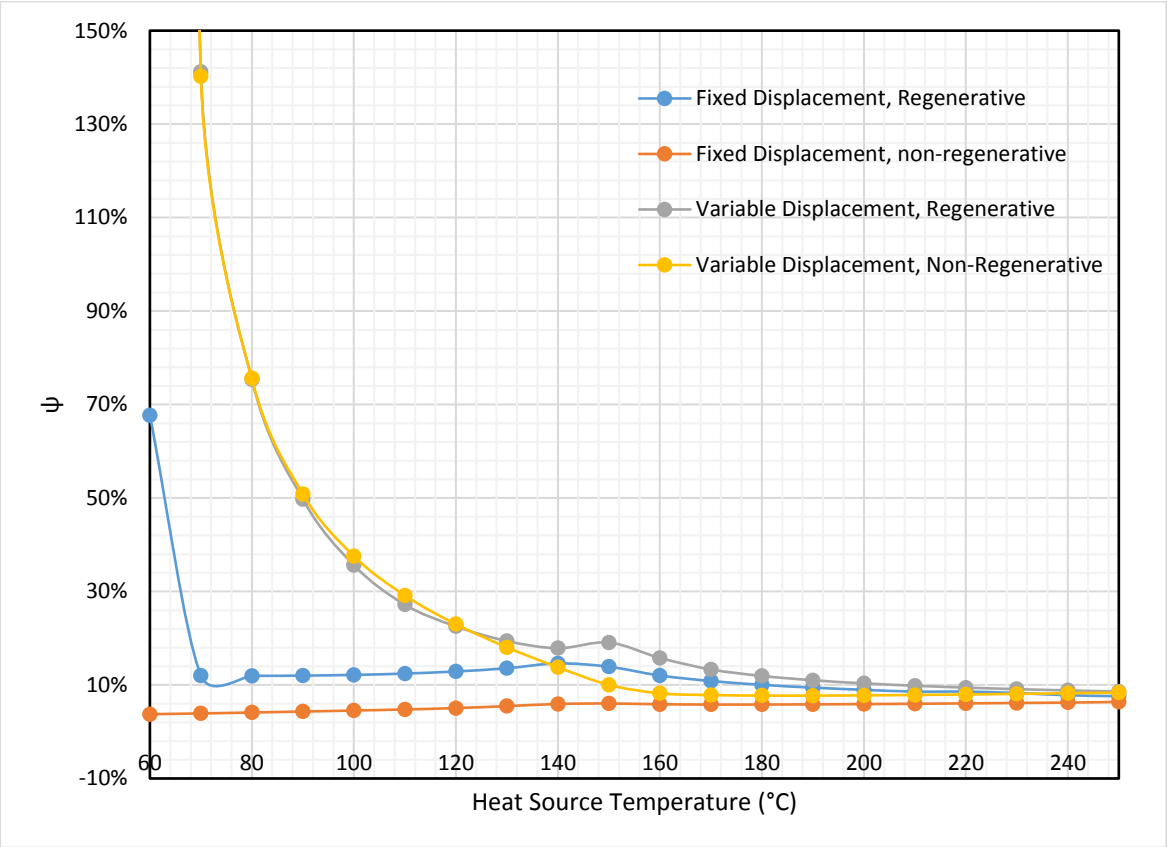

Figure 6.42: Variation in ψ for 4 different cycle configurations with varying heat source temperatures for Beijing's ambient conditions.

Firstly, the curve for the Fixed Displacement, regenerative cycle. This begins at a relatively high value of 60% at a heat source temperature of 60 °C. This is significantly higher than the corresponding value for the non-regenerative fixed displacement cycle, primarily because of the effects discussed in section 6.6.2.3, namely the extremely low pressure ratio allowing for a very large amount of heat to be transferred in the regenerator, improving the cycle efficiency by a large amount, as shown in Figure 6.39. As the heat source temperature increases, the energy transferred in the regenerator drops off sharply, as shown in Figure 6.38, due to the rapidly-increasing difference in temperature between the hot and cold sides of the regenerator. However, the value of ψ for the regenerative cycle is still higher than the value of ψ for the non-regenerative cycle. This was to be expected, considering the response curves shown in

Figure 6.28 and Figure 6.36. The response curve in Figure 6.28 shows a far greater increase in First Law Efficiency over all heat sink temperatures, but particularly for heat sink temperatures at the higher end of the temperature range, or those necessitating a higher proportion of R245fa in the working fluid, because of the ability of the regenerator to scavenge heat from the fluid exiting the expander.

After the initial drop-off with increasing heat source temperature, the value of ψ for the regenerative fixed displacement cycle begins to increase, until it reaches a peak at a heat source temperature of 150°C. This heat source temperature corresponds to the critical temperature of R245fa, which is significant, because it means that above this heat source temperature the evaporator pressure of the cycle cannot be increased any more without violating the subcritical condition imposed on the cycle in the MATLAB model. As the cycle approaches this condition, the value of ψ increases as the slopes of the response curves shown in Figure 6.36 increase. This could be partially explained by the fact that above this temperature, a phase change will no longer occur in the regenerator, as shown in Figure 6.38. However, as the same trend is observed, albeit to a lesser degree, in the same plot in Figure 6.42 for the non-regenerative fixed displacement cycle, there must be another factor at work.

After this point, the value of ψ decreases with increasing heat source temperature for both cycles as the improvement caused by the dynamic cycle decreases in significance compared to the base efficiency of the cycle, which itself increases due to the increased Carnot efficiency resulting from the greater difference in temperature between the heat source and sink.

6.7.2 Variation in ψ with changing heat sink conditions

The main driver of the improvement in annual energy generation ψ was the variation in heat sink temperature. A larger annual variation in the ambient temperature, the larger the theoretical improvement in the energy generation of the cycle due to the implementation of the dynamic cycle.

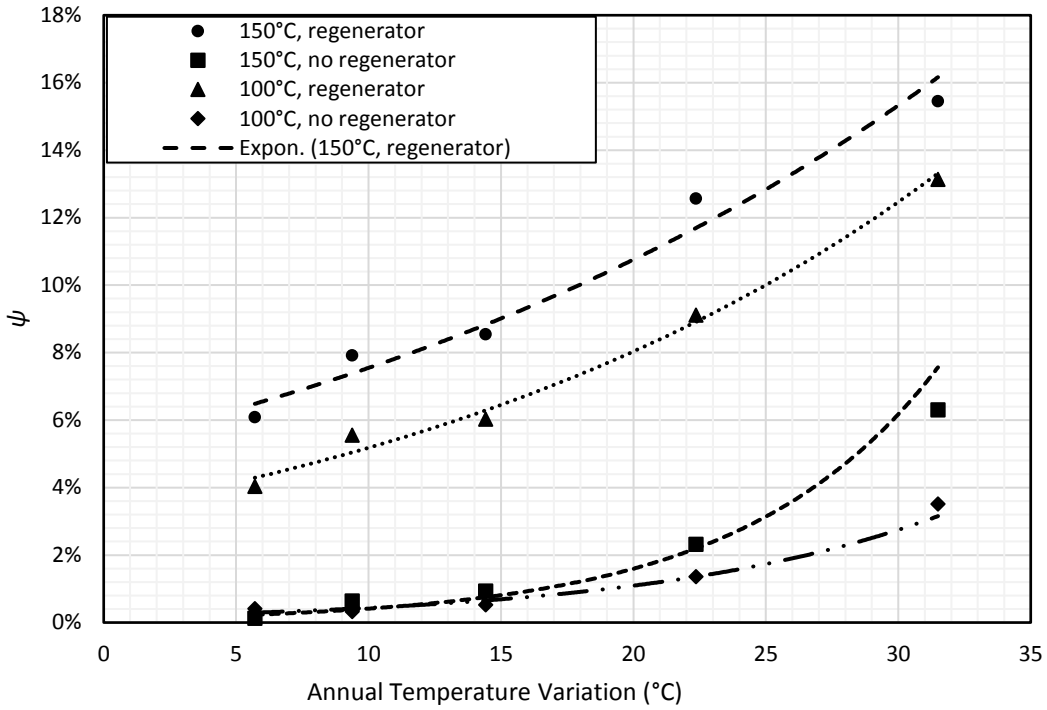

Figure 6.43: Variation in ψ for five case studies for annual temperature variation. From left to right, Mumbai, Ushuaia, Glasgow, Phoenix, Beijing.

The MATLAB routine was run using climate data from several locations worldwide, for heat source temperatures of 100 °C and 150 °C and the results plotted in Figure 6.43. A steady increase in ψ can be seen as the amplitude of the temperature variations increases. This is to be expected, as the greater the temperature variation, the greater the difference between the hot and cold reservoirs, and therefore the greater the Carnot efficiency. The plot deviates slightly from the linear increase in Carnot efficiency, however, due to several factors, most notably the composition of the working fluid. When the temperature variation is small, only a small amount of R134a is needed to keep up with the changing heat sink temperature. When the temperature variation is much larger, the working fluid can be 100% R134a, and still have excess cooling capacity it is not utilising. Some small deviations from the theoretical smooth increase can be seen. For example, Phoenix has a higher average temperature than any of the other locations, and therefore a reduced conventional cycle efficiency. This means that the dynamic cycle is slightly more effective here than the idealised case would predict.

The trend for the non-regenerative cycles is of a slightly different shape, rising slowly at first, then increasing in slope. This is because, as shown in Figure 6.28, the efficiency of non-

regenerative cycles only increase very slowly when the ambient temperature decreases from the annual maximum. At lower annual temperature variations, the heat sink temperature never becomes cold enough to cause the non-regenerative cycle to enter the region of its response curve where a sharp increase in efficiency can be seen.

6.8 Summary

In this section the concept of the Dynamic Organic Rankine Cycle has been expanded upon, and the results of the theoretical analysis of this cycle presented.

Firstly the optimum frequency of distillation to maximise the net power output of the cycle was calculated. This showed that the greatest net power output is obtained if distillation is carried out at a 12-hourly interval, allowing the cycle to adjust to the day-night cycle. With this information, the performance of the dynamic cycle in response to real-world ambient temperature conditions could be determined.

Two broad classes of cycles were considered for this analysis; those in which the evaporator pressure can vary, and those in which the evaporator pressure is fixed. Within these categories the heat source temperature was varied, as well as the cycle configuration, regenerative or non-regenerative.

It was found that the dynamic cycle has the potential to improve the annual power generation of an ORC by a significant amount, greater at lower heat source temperatures. For the variable-displacement cycle, this increase is possible for both regenerative and non-regenerative cycles, as the pressure ratio of the cycle can increase with changing working fluid composition. However, for the fixed-displacement cycle, a regenerator is needed to see significant improvement in the annual power generation of the cycle.

The response of the dynamic cycle to changing ambient conditions was also discussed. It was found that, as expected, increasing annual temperature variation, such as those encountered in continental climates, resulted in an increased effect of the dynamic cycle.

In the next chapter the overall conclusions from this thesis will be discussed, and suggestions for further work made.

CHAPTER 7- CONCLUSIONS AND FURTHER WORK

In this section the overall conclusions of each previous chapter are presented and discussed. Suggestions for further work building on that carried out for this thesis are also given.

7.1 Previous Literature and Motivation

A review of the existing literature on the Organic Rankine Cycle was carried out, and several trends were identified. Current research appeared to be focused on the areas of cycle optimisation using theoretical methods, expander selection and development, and specification of working fluids. It was noticed that although there exists a body of research on the response of ORCs to varying heat source temperatures, there is almost no research, either theoretical or experimental, on the response of an ORC to changing heat sink temperatures. This gap in the previous research was addressed by building a theoretical model to analyse both the response of an ORC to changing heat source temperatures, and also by developing the novel concept of the Dynamic Organic Rankine Cycle, which is capable of changing its working fluid composition in response to changing ambient conditions to maximise the use of a variable heat sink.

Also noted was the lack of practical research on certain aspects of the Organic Rankine Cycle. Although there is a body of research on such topics as working fluid, heat source temperature and expander selection, little experimental research could be found on the effect of zeotropic working fluid mixtures on the performance of a cycle, or on the effect of a regenerator on the cycle's performance. Therefore a 1kW lab-scale ORC rig was designed and fabricated. The results of this rig fill a substantial hole in the pre-existing literature.

7.2 Design of the ORC Rig

A 1kWe experimental rig was developed, build around an off-the-shelf scroll expander from AirSquared. Key parameters to be investigated by this rig were as follows:

- Working fluid composition, which could be adjusted by manually charging the rig with varying amounts of the two selected working fluids; r245fa and r134a.
- Heat Source Temperature, which could be varied between ambient and 100°C by changing the set point of the electric water heater used to simulate a geothermal or waste heat source.

- Mass flow rate, which could be changed by adjusting the speed of the inverter that supplied the positive displacement pump.
- Cycle pressure ratio, which could be varied by a combination of changing the speed of the working fluid pump, the temperature of the heat source and the shaft load on the expander. In practice a specific evaporator pressure was hard to obtain, so results were categorised in terms of pump speeds and heat source temperatures, then analysed in respect of the resulting pressure ratios.
- Cycle configuration, which could be changed from a non-regenerative to a regenerative configuration by redirecting the flow using several valves in the system's pipework.

A series of tests investigating the effect of all of these parameters on cycle performance was carried out, and the results presented and analysed.

7.3 Experimental Results

A series of tests was carried out using the experimental rig, varying the heat source temperature, pump speed, cycle configuration and working fluid composition.

The results of these experimental tests can be summarised as follows.

Increasing heat source temperature increased the power output and efficiency of the cycle in all cases, increasing both the evaporator pressure and specific enthalpy at the evaporator inlet, resulting in greater expander specific enthalpy drop relative to the evaporator heat demand. This was consistent with previous theoretical analysis of ORCs.

Increasing the pump speed increased both the mass flow rate of working fluid, as the positive displacement pump's volume flow rate is a direct function of its speed and stroke. The greater flow rate causes greater resistance from the expander, increasing the back-pressure and therefore the pressure in the evaporator. Increasing the pressure ratio over the expander increases the specific enthalpy drop across the expander, without a proportionally greater heat demand in the evaporator, thereby increasing the cycle efficiency.

Regenerative cycles resulted in a decreased cycle power output, due to the greater flow resistance caused by the additional heat exchanger reducing the mass flow rate of the working fluid in the cycle. However, the recovery of heat from the working fluid stream at the expander

outlet results in a significantly reduced heat demand in the evaporator, increasing the overall cycle efficiency.

The working fluid composition was varied from 100% r245fa to [70%r245fa:30%r134a]. The expected result based on the literature was that the temperature glide would increase as the working fluid composition shifted towards r134a. However, the experimental results showed that the expected increase in glide did not appear, most likely due to the pressure drops in the heat exchangers counteracting the effect. The introduction of r134a, which has a higher vapour pressure than r245fa, into the working fluid increased the pressure in the condenser, reducing the pressure ratio in the cycle, and decreasing the power output and the efficiency of the cycle. The zeotropic fluid also exhibited evidence of decreased heat transfer coefficient within the heat exchanger, namely a widening of the pinch points in the heat exchangers. This is an effect that has previously been reported in the literature.

Overall, a maximum cycle power of 640W was obtained from the cycle, although this was not sustainable with the electrical power available in the heater. The maximum sustained power output was 421W for a regenerative cycle with a pump speed of 40Hz. A maximum cycle efficiency of 5.5% was observed for the non-regenerative cycle and 11.3% for the regenerative cycle.

7.4 Simulation Results

A MATLAB model was built to analyse the Dynamic Organic Rankine Cycle and its response to varying ambient temperature across a range of heat source temperatures. Two broad cases were taken, that of a cycle with a fixed pressure ratio, and that in which the pressure ratio can be varied without a significant loss in the isentropic efficiency of the expander.

Firstly, the optimum interval for changing the composition of the working fluid was found to be 12 hours, which can account for changes in temperature due to the day/night cycle. Shorter intervals than this were found to consume more power for distillation than they gained in increased power generation.

For the variable pressure-ratio cycle the dynamic cycle was found to cause a significant increase in the year-round power production of the cycle. Both the regenerative and non-regenerative cases showed an extremely large improvement, of several hundred percent, for the lowest heat source temperature of 60°C, primarily due to the extremely low efficiency of the non-dynamic cycle making the proportional gains due to the dynamic cycle very large. This

decreased to a stable level of roughly 8% for heat temperatures above 140°C for both regenerative and non-regenerative cycles.

For the fixed pressure-ratio cycle the same effect was not observed in the non-regenerative cycle. Only a small increase was observed with the application of the dynamic cycle, as the change in working fluid composition only resulted in an increased superheat at the expander inlet, not an increased output from the expander. However, the regenerative case of this cycle resulted in an increase of roughly 10% across a wide range of heat source temperatures. The increased superheat at the expander inlet in this case means that more energy is available for the regenerator to use to preheat the working fluid before the evaporator, decreasing evaporator heat loading and increasing the cycle efficiency.

Finally, the response of the cycle to five real-world heat sinks was presented. The greater the annual temperature variation, the greater the effect that could be obtained with the use of the dynamic cycle. This makes it more applicable to continental climates such as Beijing, Chicago and Berlin than to temperate, tropical and maritime climates.

7.5 Recommendations for Further Work

The work carried out for this thesis has revealed several areas of interest for future research work, which are detailed in this chapter section, separated into experimental work and analysis of the dynamic cycle.

7.5.1 Experimental work

-The concept of the dynamic Organic Rankine Cycle, which has been analysed theoretically, can be further demonstrated by the introduction of an online composition tuning system for the experimental rig. Along with a method for setting the coolant temperature this would provide experimental verification of the theoretical work already carried out.

-A reliable method of changing the shaft load of the expander would allow the pressure ratio of the cycle to be changed while maintaining the mass flow rate of the cycle. This is not possible with the current arrangement whereby the pressure ratio is changed using the pump speed.

-The effect of different working fluids can be easily investigated, as the rig is designed to be charged and discharged.

-An expander rated to a higher pressure and a heater using thermal oil instead of water would allow higher heat source temperatures and cycle pressure ratios to be investigated, expanding the body of experimental data in the literature.

-A more powerful heater could be used to run the pump at higher speeds and obtain more results from the current experimental rig, as the current heater was only powerful enough to provide a sufficient level of heat across 50% of the speed range of the working fluid pump.

-A smaller pump for the water from the heater would allow the heat source utilisation of the cycle to be determined, as the current pump is oversized, which limits the temperature drop in the evaporator.

7.5.2 Theoretical Analysis

-Different pairs of working fluids other than the r245fa/r134a pair considered in this paper could be taken. Over the temperature range of continental climates a working fluid composition of 100% r134a is reached before the minimum ambient temperature. A greater difference in the boiling temperatures of the working fluids would allow an even greater improvement in annual power generation. Different working fluids could also have lower power requirements for distillation, increasing the net efficiency of the cycle.

-Similarly, selecting a pair of working fluids with a greater difference between their boiling points would allow the cycle to operate at a different point on the operating curve. The concave shape of the efficiency vs. temperature plot means that the dynamic cycle is more responsive to changing ambient temperature in certain temperature ranges.

-The validation of the theoretical model showed that, contrary to the assumption that the isentropic efficiency of the expander remaining constant for a constant pressure ratio, it was subject to a wide range of factors, including heat source temperature, flow rate and working fluid composition. A more detailed expander model, taking into account these variables, would allow for a more in-depth analysis of the dynamic cycle to be carried out.

REFERENCES

1. UK Government: Climate Change Act. (Accessed 2008) Available at: www.parliament.uk

2. UK Government: The UK Low Carbon Transition Plan. (Accessed 2009) Available at: https://www.gov.uk

3. Larjola, J.: Electricity from Industrial Waste Heat using High-Speed Organic Rankine Cycle (ORC). International Journal of Production Economics 41, 227-235 (1995)

4. Tartiere, T., Astolfi, m.: A World Overview of the Organic Rankine Cycle Market. Energy Procedia 129, 2-9 (September 2017)

5. Energy, E.: The Potential for Recovering and Using Surplus Heat from Industry., UK Department of Energy and Climate Change, London (2014)

6. Cayer, E., Galanis, N., Nesreddine, H.: Parametric Study and Optimisation of a Transcritical Power Cycle Using a Low-Temperature Heat Source. Applied Energy 87, 1349-1367 (2010)

7. Hung, T.-C.: Waste Heat Recovery of Organic Rankice Cycle Using Dry Fluids. Energy Conversion and Management 42(5), 539-553 (2001)

8. Hung, T. C., Shai, T. Y., Wang, S. K.: A review of Organic Rankine cycles (ORCs) for the recovery of low-grade waste heat. Energy 22(7), 661-667 (July 1997)

9. Budislistyo, D., Krumdieck, S.: A novel design methodology for waste heat recovery systems using organic Rankine cycle. Energy Conversion and Management 142, 1-12 (2017)

10. Wang, Y., Tang, Q., Wang, M., Feng, X.: Thermodynamic Performance Comparison between ORC and Kalina Cycles for Multi-Stream Waste Heat Recovery. Energy Conversion and Management 143, 482-492 (2017)

11. Zhang, X., Yamaguchi, H., Fujima, K., Enomoto, M.: Theoretical Analysis of a Thermodynamic Cycle for Power and Heat Production Using Supercritical Carbon Dioxide. Energy 32(4), 591-599 (April 2007)

12. Papadimitratos, A., Sobhansarbandi, S., Pozdin, V., Zakhidov, A., Hassanipour, F.: Evacuated Tube Solar Collectors Integrated with Phase Change Materials. Solar Energy 129, 10-19 (May 2016)

13. Wu, D., Aye, L., Ngo, T., Mendis, P.: Optimisation and Financial Analysis of an Organic Rankine Cycle Cooling System Driven by Facede Integrated Solar Collectors. Applied Energy 185, 172-182 (2017)

14. Zhang, J., Zhao, L., Wen, J., Deng, S.: An Overview of 200kW Solar Power Plant Based on Organic Rankine Cycle. Energy Procedia 88, 356-362 (2016)

15. Helvaci, H. U.: Thermodynamic Modelling and Analysis of a Solar Organic Rankine Cycle Employing Thermofluids. Energy Conversion and Management 138, 493-510 (April 2017)

16. Walraven, D., Laenen, B., D'haeseleer, W.: Minimising the levelised cost of electricity production from low-temperature geothermal heat sources with ORCs: Water or air cooled? Applied Energy 142, 144-153 (2015)

17. Liu, X., Zhang, Y., Shen, J.: System Performance Optimisation of ORC-based geo-plant with R245fa under different geothermal water inlet temperatures. Geothermics 66, 134-142 (2017)

18. Astolfi, M., Romano, M., Bombarda, P., Macchi, E.: Binary ORC (organic Rankine cycles) power plants for the exploitation of medium-low temperature geothermal sources - Part A: Thermodynamic optimisation. Energy 66, 423-434 (2014)

19. Cammarata, G., Cammarata, L., Petrone, G.: Thermodynamic Analysis of ORC for energy production from geothermal resources. Energy Procedia 45, 1337-1343 (2014)

20. Barbier, E.: Geothermal Energy Technology and Current Status: an Overview. Renewable and Sustainable Energy Reviews 6(1-2), 3-65 (2002)

21. Subbiah, S., Natarajan, R.: Thermodynamic Analysis of Binary-Fluid Rankine Cycles for Geothermal Power Plants. Energy Conversion and Management 28(1), 47-52 (1988)

22. Gu, Z., Sato, H.: Performance of Supercritical Cycles for Geothermal Binary Design. Energy Conversion and Management 43(7), 961-971 (May 2002)

23. Franco, A.: Power Production from a Moderate Temperature Geothermal Resource with a Regenerative Organic Rankine Cycle. Energy for Sustainable Development 15 (2011)

24. Chen, T., Zhuge, W., Zhang, Y., Zhang, L.: A novel casade organic Rankine cycle (ORC) system for waste heat recovery of truck diesel engines. Energy Conversion and Management 138, 210-223 (2017)

25. Michos, C., Lion, S., Vlaskos, I., Taccani, R.: Analysis of the backpressure effect of an Organic Rankine Cycle (ORC) evaporator on the exhaust line of a turbocharged heavy duty diesel power generator for marine applications. Energy Conversion and Management 132, 347-360 (2017)

26. Yang, M.-H., Yeh, R.-H.: Economic research of the transcritical Rankine cycle systems to recover waste heat from the marine medium-speed diesel engine. Applied Thermal Engineering 114, 1343-1354 (2017)

27. Yang, F., Zhang, H., Song, S., Bei, C., Wang, H., Wang, E.: Thermoeconomic Multi-Objective Optimisation of an Organic Rankine cycle for Exhaust Waste Heat Recovery of a Diesel Engine. Energy 93(2), 2208-2228 (2015)

28. Carcasci, C., Winchler, L.: Thermodynamic Analysis of an Organic Rankine Cycle for Waste Heat Recovery from an Aeroderivative Intercooled Gas Turbine. Energy Procedia 101, 862-869 (November 2016)

29. Eveloy, V., Rodgers, P., Qiu, L.: Hybrid gas turbine-organic Rankine cycle for seawater desalination by reverse osmosis in a hydrocarbon production facility. Energy Conversion and Management 106, 1134-1148 (December 2015)

30. Strzalka, R., Eicker, U.: Analysis and Optimisation of a Cogeneration System based on Biomass Combustion. In : 2nd European Conference on Polygeneration, Tarragona, Spain (2011)

31. Al-Sulaiman, F., Dincer, I., Hamdullahpur, F.: Energy and Exergy Analyses of a Biomass Trigeneration System using an Organic Rankine Cycle. Energy 45(1), 975-985 (September 2012)

32. Jradi, M., Riffat, S.: Experimental investigation of a biomass-fuelled micro-scale tri-generation system with an organic Rankine cycle and liquid desiccant cooling unit. Energy 71, 80-93 (July 2014)

33. Uris, M., Linares, J., Arenas, E.: Size Optimisation of a Biomass-Fired Cogeneration Plant CHP/CCHP (Combined Heat and Power/Combined Heat, Cooling and Power) based on Organic Rankine Cycle for a District Network in Spain. Energy 88, 935-945 (August 2015)

34. Tańczuk, M., Ulbrich, R.: Implementation of a biomass-fired co-generation plant supplied with an ORC (Organic Rankine Cycle) as a heat source for small-scale heat distribution system - A comparative analysis under Polish and German conditions. Energy 62, 132-141 (December 2013)

35. Maraver, D., Royo, J.: Efficiency enhancement in existing biomass organic Rankine cycle plants by means of thermoelectric systems integration. Applied Thermal Engineering 119, 396-402 (June 2017)

36. Obi, J.: State of art on ORC applications for waste heat recovery and micro-cogeneration for installations up to 100kWe. Energy Procedia 82, 994-1001 (2015)

37. Karellas, S., Braimakis, K.: Energy-Exergy Analysis and Economic Investigation of a Cogeneration and Trigeneration ORC-VCC Hybrid System Using Biomass Fuel and Solar Power. Energy Conversion and Management 107, 103-113 (January 2016)

38. Guo, T., Wang, H. X., Wang, S. J.: Selection of working fluids for a novel low-temperature geothermally-powered ORC based cogeneration system. Energy Conversion and Management 52(6), 2384-2391 (June 2011)

39. Bianchi, M., Pascale, A.: Bottoming Cycles for Electric Energy Generation: Parametric Investigation of Available and Innovative Solutions for the Exploitation of Low and Medium Temperature Heat Sources. Applied Energy 88(5), 1500-1509 (May 2011)

40. Zephyris, U. In: The English Language Wikipedia. Available at: https://commons.wikimedia.org/w/index.php?curid=5283208

41. Cotana, F., Messineo, A., Petrozzi, A., Coccia, V., Cavalaglio, G., Aquino, A.: Comparison of ORC Turbine and Stirling Engine to Produce Electricity from Gasified Poultry Waste. Sustainability 6, 5714-5729 (2014)

42. Wang, E., Yu, Z.: A numerical analysis of a composition-adjustable Kalina Cycle power plant for power generation fron low-temperature geothermal heat sources. Applied Energy 180, 834-848 (2016)

43. Nemati, A., Nami, H., Ranjbar, F., Yari, M.: A Comparative Thermodynamic Analysis of ORC and Kalina Cycles for Waste Heat Recovery: A Case Study for CGAM Cogeneration System. Case Studies in Thermal Engineering 9, 1-13 (March 2017)

44. Lin, D., Zhu, Q., Li, X.: Thermodynamic ComparativE Analyses between (organic) Rankine cycle and Kalina Cycle. Energy Procedia 75, 1618-1623 (August 2015)

45. Zare, V., Mahmoudi, S. M. S.: A Thermodynamic Comparison Between Organic Rankine and Kalina Cycles for waste heat recovery from the Gas-Turbine-Modular Helium Reactor. Energy 79, 398-406 (January 2015)

46. DiPippo, R.: Second Law Assessment of Binary Plants Generating Power from Low-Temperature Geothermal Fluids. Geothermics 33(5), 565-586 (2004)

47. Fu, W., Zhu, J., Li, T., Zhang, W., Li, J.: Comparison of a Kalina Cycle Based Cascade Utilisation System with an Existing Organic Rankine Cycle based Geothermal Power System in an Oilfield. Applied Thermal Engineering 58(1-2), 224-233 (September 2013)

48. Saleh, B., Koglbauer, G., Wendland, M., Fisher, J.: Working Fluids for Low-Temperature Organic Rankine Cycles. Energy 32(7), 1210-1221 (2007)

49. Bruno, J., Lopez-Villada, J., Letelier, E., Romera, S., Coronas, A.: Modelling and optimisation of solar organic rankine cycle engines for reverse osmosis desalination. Applied Thermal Engineering 28 (2008)

50. Kosmadakis, G., Manolakos, D., Kyritsis, S., Papadakis, G.: Economic assessment of a two-stage solar organic Rankine cycle for reverse osmosis desalination. Renewable Energy 34 (2009)

51. Drescher, U., Bruggemann, D.: Fluid Selection for the Organic Rankine Cycle (ORC) in Biomass Power and Heat Plants. Applied Thermal Engineering 27 (2007)

52. Dai, Y., Wang, J., Gao, L.: PArametric Optimisation and Comparative Study of Organic Rankine Cycle (ORC) for Low Grade Waste Heat Recovery. Energy Conversion and Management 50(3), 576-582 (March 2009)

53. Liu, L., Zhu, T., Ma, J.: Working Fluid Charge Oriented Off-Design Modelling of a Small-Scale Organic Rankine Cycle System. Energy Conversion and Management 148, 944-953 (September 2017)

54. Shao, L., Zhu, J., Meng, X., Wei, X., Ma, X.: Experimental Study of an Organic Rankine Cycle System with Radial Inflow turbine and R123. Applied Thermal Engineering 124, 940-947 (September 2017)

55. Miao, Z., Xu, J., Zhang, K.: Experimental and Modeling Investigation of an Organic Rankine Cycle System Based on the Scroll Expander. Energy 134, 35-49 (September 2017)

56. Muratori, M., Ledna, C., McJeon, H., Kyle, P., Patel, P., Kim, S., Wise, M., Kheshgi, H., Clarke, L., Edmonds, J.: Cost of Power or Power of Cost: A U.S. Modeling Perspective. Renewable and Sustainable Energy Reviews 77, 861-874 (September 2017)

57. Quoilin, S., Broek, M., Declaye, S., Dewaller, P., Lemort, V.: Techno-economic survey of Organic Rankine Cycle (ORC) Systems. Renewable and Sustainable energy Reviews 22, 168-186 (2013)

58. Angelino, G., Paliano, P.: Multicomponent Working Fluids for Organic Rankine Cycles (ORCs). Energy 23 (1998)

59. Shangjun, Z., Huaixin, W., Tao, G.: Performance Comparison and Parametric Optimisation of Subcritical Organic Rankine Cycle (ORC) and Transcritical Power

Cycle System or Low-Temperature Geothermal Power Generation. Applied Energy 88(8), 2740-2754 (2011)

60. Lakew, A., Bolland, O.: Working Fluids for Low-Temperature Heat Sources. Applied Thermal Engineerin 30(10), 1262-1268 (2010)

61. Baik, Y.-J., Kim, M., Chang, K., Kim, S.: Power-based Performance Comparison between Carbon Dioxide and R125 Transcritical Cycles for a Low-Grade Heat Source. Applied Energy 88(3), 892-898 (March 2011)

62. Baik, Y.-J., Kim, M., Chang, K.-C., Lee, Y.-S., Yoon, H.-K.: Power Enhancement Potential of a Mixture Transcritical Cycle for A Low-Temperature Geothermal Power Generation. Energy 47(1), 70-76 (November 2012)

63. Wang, X. D., Zhao, L.: Analysis of Zeotropic Mixtures Used in Low-Temperature Solar Rankine Cycles for Power Generation. Solar Energy 83(5), 605-613 (2009)

64. Lemmon, E. W., , H., McLinden, M. O.: NIST Standard Reference Database 23: Reference Fluid Thermodynamic and Transport Properties-REFPROP, Version 9.1, National Institute of Standards and Technology, Standard Reference Data Program., Gaithersburg (2013)

65. Oberle, W.: Monte Carlo Simulations: Number of Iterations and Accuracy. Technical Note ARN-TN-0684, US Army Research Laboratory (2015)

66. Afanasyeva, S., Saari, J., Kalkofen, M., Partanen, J., Pyrhönen, O.: Technical, economic and uncertainty modelling of a wind power project. Energy Conversion and Management 107, 22-33 (January 2016)

67. Agency, U.: Guiding Principles for Monte Carlo Analysis., Washington, DC (1997)

68. Lipton, J., Shaw, W., Holmes, J., Patterson, A.: Short Communication: Selecting Input Distributions for Use in Monte Carlo Simulations. Regulatory Toxicology and Pharmacology 21, 192-198 (1994)

69. Zhang, T., Zhu, T., An, W., Song, X., Liu, L., Liu, H.: Unsteady Analysis of a Bottoming Organic Rankine Cycle for Exhaust Heat Recovery from and Internal Combustion

Engine using Monte Carlo Simulation. Energy Conversion and Management 124, 357-368 (2016)

70. Frutigera, J., Andreasen, J., Liu, W., Spliethoff, H., Haglin, F., Abildskov, J., Sin, G.: Working Fluid Selection for Organic Rankine Cycles - Impact of Uncertainty of Fluid Properties. Energy 109, 987-997 (2016)

71. Momen, M., Shirinbakhsh, M., Baniassadi, A., Behbahani-nia, A.: Application of Monte Carlo method in economic optimisation of cogeneration systems - Case study of the CGAM system. Applied Thermal Engineering 104, 24-41 (July 2016)

72. Osaki, M., Jr., P.: Bioethanol and power from integrated second generation biomass: A Monte Carlo simulation. Energy Conversion and Management 141, 274-284 (2017)

73. Xi, H., Li, M.-J., Xu, C., He, Y.-L.: Parametric optimisation of regenerative organic Rankine cycle (ORC) for low grade waste heat recovery using genetic algorithm. Energy 58, 473-482 (September 2013)

74. Wang, J., Yan, Z., Wang, M., Li, M., Dai, Y.: Multi-Objective optimisation of an organic Rankine cycle (ORC) for low grade waste heat recovery using evolutionary algorithm. Energy Conversion and Management 71, 146-158 (July 2013)

75. Kai, Z., Mi, Z., Yabo, W., Zhili, S., Shengchun, L., Jinghong, N.: Parametric Optimisation of Low Temperature ORC System. Energy Procedia 75, 1596-1602 (2015)

76. Feng, Y., Zhang, Y., Li, B., Yang, J., Shi, Y.: Sensitivity analysis and thermoeconomic comparison of ORCs (organic Rankine cycles) for low temperature waste heat recovery. Energy 82, 664-677 (March 2015)

77. Sadeghi, M., Nemati, A., Ghavimi, A., Yari, M.: Thermodynamic analysis and multi-objective optimisation of various ORC (organic Rankine cycle) configurations using zeotropic mixtures. Energy 109, 791-802 (August 2016)

78. Bao, J., Zhao, L.: A review of working fluid and expander selections for Organic Rankine Cycle. Renewable and Sustainable Energy Reviews 24(1), 325-342 (August 2013)

79. Liu, B.-T., Chien, K.-H., Wang, C.-C.: Effect of Working Fluids on Organic Rankine Cycle for Waste Heat Recovery. Energy 29(8), 1207-1217 (June 2004)

80. Lemmon, E. W., Huber, M. L., McLinden, M. O.: NIST Standard Reference Database 23: Reference Fluid Thermodynamic and Transport Properties-REFPROP, Version 9.1., National Institute of Standards and Technology, Standard Reference Data Program, Gaithersburg (2013)

81. Badr, O., O'Callaghan, P. W., Hussein, M., Probert, S. D.: Multi-vane Expanders as Prime Movers for Low-Grade Energy Organic Rankine Cycle Engines. Applied Energy 16(2), 129-146 (1984)

82. Hung, T. C., Wang, S. K., Kuo, C. H., Pei, B. S., K.F.Tsai: A Study of Organic Working Fluids on System Efficiency of an ORC Using Low-Grade Energy Sources. Energy 35(3), 1403-1411 (March 2010)

83. Macchi, E., Perdichizzi, A.: Efficiency Prediction for Axial-Flow Turbines Operating with Non-Conventional Fluids. Transaction of the ASME Journal of Engineering for Power 103, 718-724 (1981)

84. Chen, Y., Lunchqvist, P., Platell, P.: Theoretical Research of Carbon Dioxide Power Cycle Application in Automobile Industry to Reduce Vehicle's Fuel Consumption. Applied Thermal Engineering 25(14-15), 2041-2053 (2005)

85. Papadopoulos, A., Stijepovic, M., Linke, P.: On the systematic design and selection of optimal working fluids for Organic Rankine Cycles. Applied Thermal Engineering 30, 760-769 (2010)

86. Borsukiewicz-Gozdur, A.: Pumping Work in the Organic Rankine Cycle. Applied Thermal Engineering 51(1-2), 781-786 (March 2013)

87. Invernizzi, C., Iora, P., Silva, P.: Bottoming Micro-Rankine Cycles for Micro-gas Turbines. Applied Thermal Engineering 27(1), 100-110 (January 2007)

88. Heberle, F., Preißinger, M., Bruggemann, D.: Zeotropic Mixtures as Working Fluids in Organic Rankine Cycles for Low-Enthalpy Geothermal Resources. Renewable Energy 37(1), 364-370 (2012)

89. Angelino, G., Paliano, P.: Multicomponent Working Fluids for Organic Rankine Cycles (ORCs). Energy 23(6), 449-463 (1998)

90. Li, W., Feng, X., Yu, L. J., Xu, J.: Effects of Evaporating Temperature and Internal Heat Exchanger on Organic Rankine Cycle. Applied Thermal Engineering 32(17-18), 4014-4023 (2011)

91. Venkatarathnam, G., Murthy, S.: Effect of Mixture Composition on the Formatin of Pinch Points in Condensers and Evaporators for Zeotropic Refrigerant Mixtures. International Journal of Refrigeration 22, 205-215 (1999)

92. Chen, Y., Lundqvist, P., Johansson, A., Platell, P.: A Comparative Study of the Carbon Dioxide Transcritical Power Cycle Compared with an Organic Rankine Cycle with R123 as Working Fluid in Waste Heat Recovery. Applied Thermal Engineering 26(17-18), 2142-2147 (December 2006)

93. Mago, P. J., Chamra, L. M., Srinivasan, K., Somayaji, C.: An Examination of Regenerative Organic Rankine Cycles Using Dry Fluids. Applied Thermal Engineering 28, 998-1007 (2008)

94. Sauret, E., Rowlands, A. S.: Candidate Radial-Inflow Turbines and High-Density Working Fluids for Geothermal Power Systems. Energy 36(7), 4460-4467 (2011)

95. Kang, S.: Design and Preliminary Tests of ORC (Organic Rankine Cycle) with two-stage radial turbine. Energy 96, 142-154 (February 2016)

96. Fiaschi, D., Manfrida, G., Maraschiello, F.: Thermo-fluid dynamis preliminary design of turbo-expanders for ORC cycles. Applied Energy 97, 601-608 (2012)

97. Li, J., Pei, G., Li, Y., Ji, J.: Evaluation of External Heat Loss from a Small-Scale Expander Used in Organic Rankine Cycle. Applied Thermal Engineering 31(14), 2694-2701 (2011)

98. Teng, H., Regner, G., Cowland, C.: Waste Heat Recovery of Heavy-Duty Diesel Engines by Organic Rankine Cycle Part 1: Hybrid Energy System of Diesel and Rankine Engines. SAE Technical Paper 1-637 (2007)

99. Song, J., Gu, C.-w., Xue-Song-Li: Performance Estimation of Tesla Turbine Applied in Small-scale Organic Rankine Cycle (ORC) System. Applied Thermal Engineering 110, 318-326 (2017)

100. Fiashi, D., Innocenti, G., Manfrida, G., Maraschiello, F.: DEsign of Micro Radial Turboexpanders for ORC Power Cycles: From 0D to 3D. Applied Thermal Engineering 99, 402-410 (2016)

101. Wali, E.: Working Fluids for Solar Rankine-Cycle Cooling Systems. Energy 5, 631-639 (1980)

102. Nugyen, V., Doherty, P., Riffat, S.: Development of a prototype low-temperature Rankine cycle electricity generation system. Applied Thermal Engineering 21, 169-181 (2001)

103. Quoilin, S., Broek, M., Declaye, S., Dewaller, P., Lemort, V.: Techno-economic survey of Organic Rankine cycle (ORC) Systems. Renewable and Sustainable Energy Reviews 22, 168-186 (2013)

104. Garg, P., Karthik, G. M., Kumar, P., Kumar, P.: Development of a Generic Tool to Design Scroll Expanders for ORC Applications. Applied Thermal Engineering (2016)

105. Huff, H. J., Radermacher, R.: Experimental Investigation of a Scroll Expander in a Carbon Dioxide Air Conditioning System. In : Proceedings of the 21st International Congress of Refrigeration, Washington, D.C., USA (2003)

106. Lemort, V., Quoilin, S., Cuevas, C., Lebrun, J.: Testing and Modeling a Scroll Expander Integrated into an Organic Rankine Cycle. Applied Thermal Engineering 29(14-16), 3094-3102 (2009)

107. Fukuta, M., Yanagisawa, T., Kosuda, O.: Performance of Scroll Expander for CO2 Refrigeration Cycle. In : 18th International Refrigeration and Air Conditioning Conference at Purdue University, Lafeyette, Indiana (2006)

108. Yanigasawa, T., Fukuta, M., Ogi, Y., Hikichi, T.: Performance of an Oil-Free Scroll-Type Air Expander. In : Proceedings of the iMechE Conference on Compressors and their Systems, pp.167-174 (2001)

109. Zanelli, R., Favrat, D.: Experimental Investigation of a Hermetic Scroll Expander-Generator. In : Proceedings of the International Compressor Engineering Conference at Purdue, pp.459-464 (1994)

110. gborc.eu. Available at: http://www.gborc.eu/sites/default/files/obrazky-gborc/sroubovy_expander.jpg

111. Wu, Y., Zhi, R., Lei, B., Wang, W., Wang, J., Li, G., Wang, H., Ma, C.: Slide Valves for Single Screw Expanders Working Under Varied Operating Conditions. Energis 9 (2016)

112. Tang, H., Wu, H., Wang, X., Xing, Z.: Performance study of a twin-screw expander used in a geothermal organic Rankine cycle power generator. Energy 90, 631-642 (October 2015)

113. Ziviani, D., Gusev, S., Lecompte, S., Groll, E. A., Braun, J. E., Horton, W. T., Broek, M., Paepe, M.: Characterising the Performance of a Single-Screw Expander in a Small-Scale Organic Rankine Cycle for Waste Heat Recovery. Applied Energy 181, 155-170 (November 2016)

114. Giuffrida, A.: Improving the semi-empirical modelling of a single-screw expander for small organic Rankine cycles. Applied Energy 193, 356-368 (May 2017)

115. Zhang, Y.-Q., Wu, Y.-T., Xia, G.-D., Ma, C.-F., Ji, W.-N., Liu, S.-W., Yang, K., Yang, F.-B.: Development and Experimental Study on Organic Rankine Cycle System with Single-Screw Expander for Waste Heat Recovery from Exhaust of Diesel Engine. Energy 77, 499-508 (December 2014)

116. Oudkerk, J. F., Dickes, R., Dumont, O., Lemort, V.: Experimental Performance of a Piston Expander in a Small-Scale Organic Rankine Cycle. In : 9th International Conference on Compressors and their Systems (2015)

117. Zha, S., Ma, Y., Sun, X.: The Development of CO2 Expander in CO2 Transcritical Cycles. In : Proceedings of the 21st International Congress of Refrigeration, Washington, D.C., USA (2003)

118. Zhang, B., Peng, X., He, Z., Xing, Z., Shu, P.: Development of a Double-Acting Free Piston Expander for Power Recovery in Transcritical CO2 Cycle. Applied Thermal Engineering 27(8-9), 1629-1636 (June 2007)

119. Torregrosa, A., Galindo, J., Dolz, V., Royo-Pascual, L., Haller, R., Melis, J.: Dynamic tests and adaptive control of a bottoming organic Rankine cycle of IC engine using swash-plate expander. Energy Conversion and Management 126, 168-176 (October 2016)

120. Kim, H., Kim, H., Kim, Y.: A Steam Expander for a Waste Heat Recovery Cycle. In : International Refrigeration and Air Conditioning Conference (2010)

121. Koç, E., Hooke, C. J.: Considerations in the Design of Partially Hydrostatic Slipper Bearings. Tribology International 30(7) (November 1997)

122. Yang, B., Peng, X., He, Z., Guo, B., Xing, Z.: Experimental Investigation on the Internal Working Process of a CO2 Rotary Vane Expander. Applied Thermal Engineering 29(11-12), 2289-2296 (2009)

123. Badr, O., Probert, S. D., O'Callaghan, P.: Multi-Vane Expanders: Vane Dynamic and Friction Loss. Applied Energy 20(4), 268-286 (1986)

124. mran, M., Usman, M., Park, B.-S., Lee, D.-H.: Volumetric Expanders for Low-Grade Heat and Waste Heat Recovery Applications. Renewable and Sustainable Energy Reviews 57, 1090-1109 (May 2016)

125. Toji, K., Kan, T., Arai, A.: Dynamic Behaviour of Sliding Vane in Small Rotary Compressors. In : Fourth International Refrigeration and Air Conditioning Conference at Purdue University, Lafayette, Indiana, USA (1978)

126. Singh, B., Singh, O.: A Study of Performance Output of a Multivane Air Enginer Applying Optimal Injection and Vane Angles. International Journal of Rotating Machinery (2012)

127. Lai, N. A., Wendland, M., Fischer, J.: Working Fluids for High-Temperature Organic Rankine Cycles., 199-211 (2011)

128. Rayegan, R., Tao, Y. X.: A procedure to select working fluids for solar organic rankine cycles (ORCs). Renewable Energy 36(2), 659-670 (2011)

129. Pasetti, M., Invernizzi, C., Iora, P.: Thermal Stability of Working Fluids for Organic Rankine Cycles: An Improved Survey Method and Experimental Results for Cyclopentane, Isopentane and n-Butane. Applied Thermal Engineering 73(1), 764-774 (December 2014)

130. Drescher, U., Bruggemann, D.: Fluid Selection for the Organic Rankine Cycle (ORC) in Biomass Power and Heat Plants. Applied Thermal Engineering 27(1), 223-228 (2007)

131. Invernizzi, C. M., Bonalumi, D.: 5- Thermal Stability of Organic Fluids for Organic Rankine Cycle Systems. In : Organic Rankine Cycle (ORC) Power Systems. (2017) 121-151

132. Quoilin, S.: Sustainable energy Conversion Through the Use of Organic Rankine Cycles for Waste Heat Recovery and Solar Applications., University of Liège (2011)

133. Gimelli, A., Luongo, A., Muccillo, M.: Efficiency and Cost Optimisation of a Regenerative Organic Rankine Cycle power plant through the multi-objective approach. Applied Thermal Engineering 114, 601-610 (March 2017)

134. Cayer, E., Galanis, N., M.Desilets, Nesreddine, H., Roy, P.: Analysis of Carbon Dioxide Transcritical Power Cycle Usine a Low-Temperature Heat Source. Applied Energy 36, 1055-1063 (2009)

135. Mago, P., Chamra, L., Srinivasan, K., Somayaji, C.: An examination of regenerative Organic Rankine Cycles Using Dry Working Fluids. Applied Thermal Engineering 28(8-9), 998-1007 (June 2008)

136. Peris, B., Navarro-Esbrí, J., Molés, F., Martí, J., Mota-Babiloni, A.: Experimental Characterisation of an Organic Rankine Cycle (ORC) for micro-scale CHP applications. Applied Thermal Engineering 79, 1-8 (March 2015)

137. Wang, X. D., Zhao, L., Wang, J. L., Zhang, W. Z., Zhao, X. Z., Wu, W.: Performance Evaluation of a Low-Temperature Solar Organic Rankine Cycle System utilising R245fa. Solar Energy (2009)

138. Pu, W., Yue, C., Han, D., He, W., Liu, X., Zhang, Q., Chen, Y.: Experimental Study on Organic Rankine Cycle for Low Grade Thermal Energy Recovery. Applied Thermal Engineering 94, 221-227 (February 2016)

139. Yun, E., Kim, D., Yoon, S., Kim, K.: Experimental Investigation of an Organic Rankine Cycle with Multiple Expanders used in Parallel. Applied Energy 145, 246-254 (May 2015)

140. Quoilin, S., Lemort, V., Lebrun, J.: Experimental Study and Modeling of an Organic Rankine Cycle using Scroll Expander. Applied Energy 87(4), 1260-1268 (April 2010)

141. Navarro-Esbri, J., Molés, F., Peris, B., Mota-Babiloni, A., Kontomaris, K.: Experimental Study of an Organic Rankine Cycle with HFO-1336mzz-Z as a low global-warming potential working fluid for micro-scale low temperature applications. Energy 133, 79-89 (August 2017)

142. Eyerer, S., Wieland, C., Vandersickel, A., Spliethoff, H.: Experimental Study of and ORC (Organic Rankine Cycle) and analysis of R1233zd-E as a Drop-in Replacement for R245fa for low-temperature heat utilisation. Energy 103, 660-671 (2016)

143. Muhammad, U., Imran, M., Lee, D., Park, B.: Design and Experimental Investigation of a 1kW organic Rankine cycle system using R245fa as the working fluid for low-grade waste heat recovery from steam. Energy Conversion and Management 103, 1089-1100 (2015)

144. Li, M., Wang, J., He, W., Gao, L., Wang, B., Ma, S., Dai, Y.: Construction and Preliminary Test of a Low-Temperature Regenerative Organic Rankine Cycle (ORC) using R123. Renewable Energy 57, 216-222 (September 2013)

145. Jung, H.-C., Taylor, L., Krumdieck, S.: An Experimental and Modelling Study o a 1kW Organic Rankine Cycle Unit with Mixture Working Fluid. Energy 81, 601-614 (March 2015)

146. Abadi, G., Yun, E., Kim, K.: Experimental Study of a 1kW Organic Rankine Cycle with a Zeotropic Mixture of R245fa/R134a. Energy 93(2), 2363-2373 (December 2015)

147. Garcia, S., Garcia, R., Carril, J., Garcia, D.: Critical Review of the First Law Efficiency in Different Power Combined Cycle Architectures. Energy Conversion and Management 148, 844-859 (September 2017)

148. Zeyghami, M.: Performance Analysis and Binary Working Fluid Selection of Combined Flash-Binary Geothermal Cycle. Energy 88, 765-774 (August 2015)

149. Quoilin, S., Declaye, S., Lemort, V.: Expansion Machine and Fluid Selection for the Organic Rankine Cycle. In : 7th International Conference on Heat Transfer, Fluid Mechanics and Thermodynamics, Antalya, Turkey (2010)

150. Quoilin, S., Lemort, V., Lebrun, J.: Experimental study and modeling of an Organic Rankine Cycle using scroll expander. Applied Energy 87 (2010)

151. Seyedkavoosi, S., Javan, S., Kota, K.: Exergy-Based Optimization of and Organic Rankine Cycle (ORC) for Waste Heat Recovery from and Internal Combustion Engine (ICE). Applied Thermal Engineering 126, 447-457 (November 2017)

152. Dovíc, D., Palm, B., Švaic, S.: Generalised Correlations for Predicting Heat Transfer and Pressure Drop in Plate Heat Exchanger Channels of Arbitrary Geometry. International Journal of Heat and Mass Transfer 52, 4554-4563 (2009)

153. García-Cascales, J. R., Vera-García, F., Corberán-Salvador, J. M., Gonzálvez-Maciá, J.: Assessment of Boiling and Condensation Heat Transfer Correlations in the Modelling of Plate Heat Exchangers. International Journal of Refrigeration 30, 1029-1041 (2007)

154. Chisholm, D., Wanniarachchi, A. S.: Plate Heat Exchangers: Plate Selection and Arrangement. In : Proceedings of the AIChE Meeting, Orlando, Florida (March 18-22, 1990)

155. Kim, Y. S.: An Experimental Study on Evaporation Heat Transfer Characteristics and Pressure Drop in a Plate Heat Exchanger. M.S. Thesis, Yonsei University (1999)

156. Wanniarachchi, A. S., Ratnam, U., Tilton, B. E., Dutta-Roy, K.: Approximate Correlations for Chevron-Type Plate Heat Exchangers. In : Proceedings of the 30th National Heat Transfer Converence, New York, vol. 12, pp.145-151 (1995)

157. Bogaert, R., Bölcs, A.: Global Performance of a Prototype Brazed Plate Heat Exchanger in a Large Reynolds Number Range. Experimental Heat Transfer 8, 293-311 (1995)

158. Yan, Y. Y., Lin, T. F.: Evaporation Heat Transfer and Pressure Drop of Refrigerant R134a in a plate heat exchanger. Journal of Heat Transfer 121, 118-127 (1999)

159. Kilmenko, V. V.: A generalised correlation for two-phase forced flow heat transfer. International Journal of Heat and Mass Transfer 31, 541-552 (1986)

160. Riehl, R. R., Seleghim, P., Ochterbeck, J. M.: Comparison of Heat Transfer Correlations for Single-and Two-Phase Microchannel Flows for Microelectronics Cooling. In : Proceedings of the Sixth Intersociety Conference on Thermal and Thermomechanical Phenomena in Electronic Systems (27-30 May 1998)

161. Guo, D., Sun, D., Li, Z. Y., Tao, W.: Phase Change Heat Transfer Simulation for Boiling Bubbles Arising from a Vapour Film by the VOSET Method. Numerical Heat Transfer, Part A: Applications 59, 857-881 (2011)

162. Kuo, W. S., Lie, Y. M., Hsieh, Y. Y., Lin, T. F.: Condensation Heat Transfer and Pressure Drop of Refrigerant R410a flow in a vertical plate heat exchanger. International Journal of Heat and Mass Transfer 48, 5205-5220 (2005)

163. Hsieh, Y. Y., Lie, Y. M., Lin, T. F.: Condensation Heat Transfer and Pressure Drop of Refrigerant R-410a in a Vertical Plate Heat Exchanger. In : Proceedings of the Third International Symposium on Two-Phase Flow Modelling and Experimentation, Pisa, Italy, vol. 1 (September 22-24, 2004)

164. Han, D. H., Lee, K. J., Kim, Y. H.: The Characteristics of Condensation in Brazed Plate HEat Exchangers with Different Chevron Angles. Journal of the Korean Physical Society 43 (2003)

165. Imran, M., Park, B.-S., Kim, H., Lee, D., Usman, M., Heo, M.: Thermo-economic optimisation of Regenerative Organic Rankine Cycle for Waste Heat Recovery Applications. Energy Conversion and Management 87, 107-118 (November 2014)

166. Plate and Frame Heat Exchangers. In: Thermopedia. Available at: http://www.thermopedia.com/content/1035/

167. Dvořák, V., Vit, T.: Evaluation of CAE Methods used for Plate Heat Exchanger Design. Energy Procedia 111, 141-150 (2017)

168. Fernandes, C., Dias, R., Nóbrega, J., Maia, J.: Friction Factors of Power-Law Fluids in Chevron-Type Plate Heat Exchangers. Journal of Food Engineering 89(4), 441-447 (December 2008)

169. Gorak, A., Sorensen, E.: Distillation: Fundamentals and Principles. Academic Press (2014)

170. Gorak, A., Sorenses, E., eds.: Distillation: Fundamentals and Principles.

171. Kohl, A., Nielsen, R.: Gas Purification 5th edn. (1997)

172. Tutiempo.net. Available at: en.tutiempo.net

173. Honeywell Advanced Materials Inc.: Honeywell Enovate 245fa Technical Information. (2017)

174. Thermometrics Corporation: Tolerance of Thermocouples. In: Thermometrics.com. Available at: http://www.thermometricscorp.com/images/Thermocouples/thermocouple_tolerance.jpg

175. Harinck, J., Calderazzi, L., Colonna, P., Polderman, H.: ORC Deployment Opportunities in Gas Plants. In : 3rd International Seminar on ORC Power Systems, Brussels, Belgium (2015)

176. Usman, M., Imran, M., Yang, Y., Lee, D., Park, B.-S.: Thermo-economic comparison of air-cooled and cooling tower based Organic Rankine Cycle (ORC) with R245fa and R1233zde as candidate working fluids for different geographical climate conditions. Energy 123, 353-366 (March 2017)

177. Collings, P., Yu, Z., Wang, E.: A Dynamic Organic Rankine Cycle using a Zeotropic Mixture as the Working Fluid with Composition Tuning to Match Changing Ambient Conditions. Applied Energy 171, 581-591 (June 2016)

178. Yang, X., Xu, J., Miao, Z., Zou, J., Yu, C.: Operation of an Organic Rankine Cycle dependent on pumping flow rates and expander torques. Energy 90(P1), 864-878 (2015)

179. Harinck, J., Calderazzi, L., Colonna, P., Polderman, H.: ORC deployment opportunities in gas plants. In : 3rd International Seminar on ORC Power Systems, Brussels, Belgium (2015)

180. Rothfleisch, P.: A simple method of composition shifting with a distillation column for a heat pump employing a zeotropic refrigerant mixture., NIST, Maryland, USA (1995)

181. Mohammad, U., Imran, M., Lee, D., Park, B.: Design andd Experimental Investigation of a 1kW Organic Rankine Cycle System Using R245fa as Working Fluid for Low-Grade Heat Recovery From Steam. Energy Conversion and Management 103, 1089-1100 (October 2015)

182. Heberle, F., Schifflechner, C., Bruggemann, D.: Life Cycle Assessment of Organic Rankine Cycles for Geothermal Power Generation Considering Low-GWP Working Fluids. Geothermics 64, 392-400 (November 2016)

183. Invernizzi, C. M., Iora, P., Preissinger, M., Manzolini, G.: HFOs as Substitute for R134a in ORC Power Plants: A Thermodynamic Assessment and Thermal Stability Analysis. Applied Thermal Engineering 103, 790-797 (2016)

184. Holdmann, G.: The Chena Hot Springs 400kW Geothermal Power Plant: Experience Gained During the First Year of Operation. In : GRC Conference 2007

185. Abadi, G., Yun, E., Kim, K.: Experimental Study of a 1kW Organic Rankine Cycle with a Zeotropic Mixture of R245fa/R134a. Energy 93(2), 2363-2373 (December 2015)

186. Abadi, G., Yun, E., Kim, K.: Flow Boiling Characteristics of R134a and R245fa Mixtures in a Vertical Circular Tube. Experimental Thermal Fluid Science 72, 112-124 (2016)

187. Wang, W., Zeng, D., Liu, J., Niu, Y., Cui, C.: Feasibility analysis of changing turbine load in power plants using continuous condenser pressure adjustment. Energy 64, 533-540 (2014)